Rare Earth Electrochemical Property Measurements and Phase Diagram Development in a Complex Molten Salt Mixture for Molten Salt Recycle

Final Report

Project Number: NEUP-14-6489

Project Period:

Principal Investigator: Prof. Jinsuo Zhang (10/2014-09/2017); Prof. Christopher Taylor (10/2017-12/2017)

Research Scientist: Dr. Shaoqiang Guo (VT)

Postdoc: Dr. Adib Samin (OSU), Dr. Wentao Zhou (OSU)

Graduate Student: Evan Wu (Ph.D., OSU), Eric Lahti (M.S., OSU), Brendan Dsouza (Ph.D., VT)

The Ohio State University (OSU), Columbus, OH 43210

Virginia Polytechnic Institute and State University (VT), Blacksburg, VA 24060

Co-Principal Investigator: Prof. Michael Simpson

Graduate Student: Parshant Bagri (Ph.D.)

Undergraduate Student: Lauryn Hansen

University of Utah (UU), Salt Lake City, UT 84112

Collaborator: Dr. James L. Willit

Argonne National Laboratory (ANL), Argonne, IL 60439

March 30th, 2018

Table of Contents

List of Figures

List of Tables

Executive Summary

Pyroprocessing is a promising alternative for the reprocessing of used nuclear fuel (UNF) that uses electrochemical methods. Compared to the hydrometallurgical reprocessing method, pyroprocessing has many advantages such as reduced volume of radioactive waste, simple waste processing, ability to treat refractory material, and compatibility with fast reactor fuel recycle. The key steps of the process are the electro-refining of the spent metallic fuel in the LiCl-KCl eutectic salt, which can be integrated with an electrolytic reduction step for the reprocessing of spent oxide fuels. During the electro-refining process, actinides and active fission products such rare earth (RE) elements are dissolved into the molten salt from the spent fuel at an anode basket. Then U and Pu are electro-deposited on the cathodes while REs with relatively negative reduction potentials are left in the molten salt bath. However, with the accumulation of lanthanides in the salt, the reduction potentials of REs will approach the values for U and Pu, affecting the recovery efficiency of U and Pu. Hence, RE drawdown is necessary to reduce salt waste after uranium and minor actinides recovery, which can also be performed by electrochemical separations. To separate various REs and optimize the drawdown process, physical properties of REs in LiCl-KCl salt and their concentration dependence are essential. Thus, the primary goal of present research is to provide fundamental data of REs and deduce phase diagrams of LiCl-KCl-$RECl_3$ based complex molten salts. La, Nd and Gd are three representative REs that we are particularly interested in due to the high ratio of La and Nd in UNF, highest standard potential of Gd among all REs, and the existing literature data in dilute solution.

Electrochemical measurements are performed to study the thermodynamics and transport properties of $LaCl_3$, $GdCl_3$, $NdCl_3$, and $NdCl_2$ in LiCl-KCl eutectic in the temperature range 723–823 K. Test are conducted in LiCl-KCl melt with concentrations of RE chlorides up to 9 wt% to identify the concentration dependence of the properties. The diffusion coefficients of RE^{n+} in LiCl-KCl melts are determined by cyclic voltammetry (CV), Chronocoulummetry (CC) and Chronopoentiometry (CP). The CV data is analyzed by both conventional methods and a developed BET model that considers the adsorption of RE. In addition to the diffusion coefficient, other properties such as activity coefficient of RE^{n+} in the melt and the apparent standard potential of its reaction are also obtained from the CV analysis. The exchange current density and charge-transfer coefficient for the reduction reactions of La and Gd are determined by various method, including electrochemical spectroscopy (EIS) method, Tafel method, and liner polarization (LP) method. Considering these conventional methods are based on the assumption of no mass-transfer effect, an electrode kinetic model that accounts for the mass transfer effect is developed for the analysis of exchange current density. Correlations of diffusion coefficient, apparent potential, exchange current density with temperature and concentration are developed. In addition, the concentration dependence of activity coefficient and diffusion coefficient of La(III) in LiCl-KCl eutectic are studied using molecular dynamics simulation method.

The effects of an active fission product Cs on the properties of $LaCl_3$, $NdCl_3$, $CeCl_3$, and $GdCl_3$ are studied in LiCl-KCl and LiCl-KCl-CsCl melts. With the design of electromotive force (emf) cell, the activity coefficient for these REs are obtained from the measured open circuit potential (OCP) between the Re electrode and reference electrode. Tests are

conducted at several CsCl concentrations and a group of RE concentrations up to 12 wt%. Correlations between the activity and ionic size of lanthanides have been developed and the effects of CsCl on activity coefficients of $LaCl_3$, $CeCl_3$ and $GdCl_3$ are identified. A novel process using a galvanic couple between a cathode basket made of stainless steel and a Gd rod is investigated in LiCl-KCl-UCl_3-$MgCl_2$. The process shows rapid reduction of UCl_3 to U and $MgCl_2$ to Mg without any co-reduction of $LaCl_3$, $NdCl_3$, or $CeCl_3$ because of the higher standard potential of Gd^{3+}/Gd.

Electrolysis of the molten salt results in a perturbation of the composition, which in turn can affect the equilibrium phase behavior. Studies on phase behavior in more complex salt mixtures as will be encountered in real electrorefiner salt drawdown are very limited. In present research, the solidus and liquidus temperatures for four quaternary LiCl-KCl-CsCl-$RECl_3$ (RE = La, Nd, Ce, and Gd) salt systems are analyzed by differential scanning calorimetry (DSC) measurement. The presence of CsCl causes a slight depression in the liquidus temperature for all of the four rare earth chloride mixtures when compared to the corresponding ternary system liquidus temperatures in the absence of any CsCl.

Thermodynamic assessment for the LiCl-KCl-$LnCl_3$ ternary system(here Gd as a reprehensive of Ln) has been carried out by CALPHAD method using two-sublattice model. From the optimized phase diagram, the solubility of $GdCl_3$ in LiCl-KCl eutectic is obtained. This model can also be applied to other salt system to evaluate the thermodynamic properties of other REs in pyroprocessing salt systems with more components.

In the end, an electrolysis model is developed to predict the electrolysis process for RE drawdown from LiCl-KCl salt. The model considers both the diffusion in electrolyte and Faraday process on the electrode surface and a surface layer is introduced to account for the fact that diffusion current is not necessarily equal to the current due to the Butler-Volmer equation. Using the fundamental data obtained from this study, the proposed model is validated by chronoamperometry and chronopotentiometry experimental data.

1. Introduction and motivation

1.1. Development of pyroprocessing

Electricity generation through nuclear energy reduces the consumption of fossil fuel, thus lowering CO_2 emission. However, there are also some concerns on the using of nuclear energy such as the management of radioactive nuclear waste. The total used nuclear fuel (UNF) as of 2015 is around 266,000 tHM worldwide and is increasing at a rate of 7,000 tHM/year [1]. Currently, 75,000 tHM UNFs [1] are being stored at 75 sites in United States in pools and dry casks and is increasing at a rate of 2000 tHM/year [2]. While being called used nuclear fuel, 96% of the original uranium in fact remains in the UNF [3]. Merits for recycling UNF includes the significant improvement in fuel cycle efficiency, reduction of UNF waste volume, the decrease in radiotoxicity of UNF, the reduction in the time needed for UNF to decay back to normal radiation level from several million years to several hundred years [4]. Before pyroprocessing, PUREX, an aqueous reprocessing method based on liquid-liquid extraction ion-exchange, was the standard method for the recovery of U and Th from UNF. Pyroprocessing is a promising alternative to the aqueous processing method for reprocessing UNF. The technique was originally developed by Argonne National Laboratory (ANL) in late 1990s and then further investigated by the USA, Japan, Korea and Europe [5,6,7,8] in the past two decades.

Pyroprocessing is based on the electrochemical techniques in molten salt electrolyte systems. The process has the capability to deal with hot fissile material and has a potential economic advantage over PUREX; it is also suggested that pyroprocessing can reduce the volume of waste form significantly compared with aqueous fuel reprocessing such as PUREX [9]. The core technology of the process is electrorefining which deals with metallic UNF but it can be applied to oxide UNF by reducing oxide fuels to their metal forms before electrorefining [10]. In the electrorefiner, chopped UNF is put in an anode basket while stainless steel rods or liquid Cd or Bi pool serve as cathodes [11]. During the electrorefining, a current or potential is applied between the anode and cathode, resulting in the occurrence of oxidation of metals (M) at the anode and the reduction of their ions (M^{n+}) at the cathode. In the thermodynamic consideration, metals with lower redox potentials (popularly known as oxidation potential at the anode and reduction potential at cathode) are easier to be oxidized which also means the reduction of their ions (M^{n+}) are more difficult. Hence, by controlling the system potential [12,13] in the electrorefiner, uranium and metals with lower redox potentials (categorized as active elements in this report) are dissolved into the molten salt from UNF at the anode. For the reduction at cathode, uranium will be electro-deposited first due to the higher reduction potential than other dissolved active elements. The reduction potential can be calculated by the standard potential (E^0) and activity (a) according to Nernst equation (1-1). The standard potentials for typical elements at 723 K are given in Figure 1-1.

$$E_{M^{n+}/M} = E^0_{M^{n+}/M} + \frac{RT}{nF} ln \frac{a_{M^{n+}}}{a_M} \quad (1\text{-}1)$$

where n is exchanged electrons, F is faraday constant.

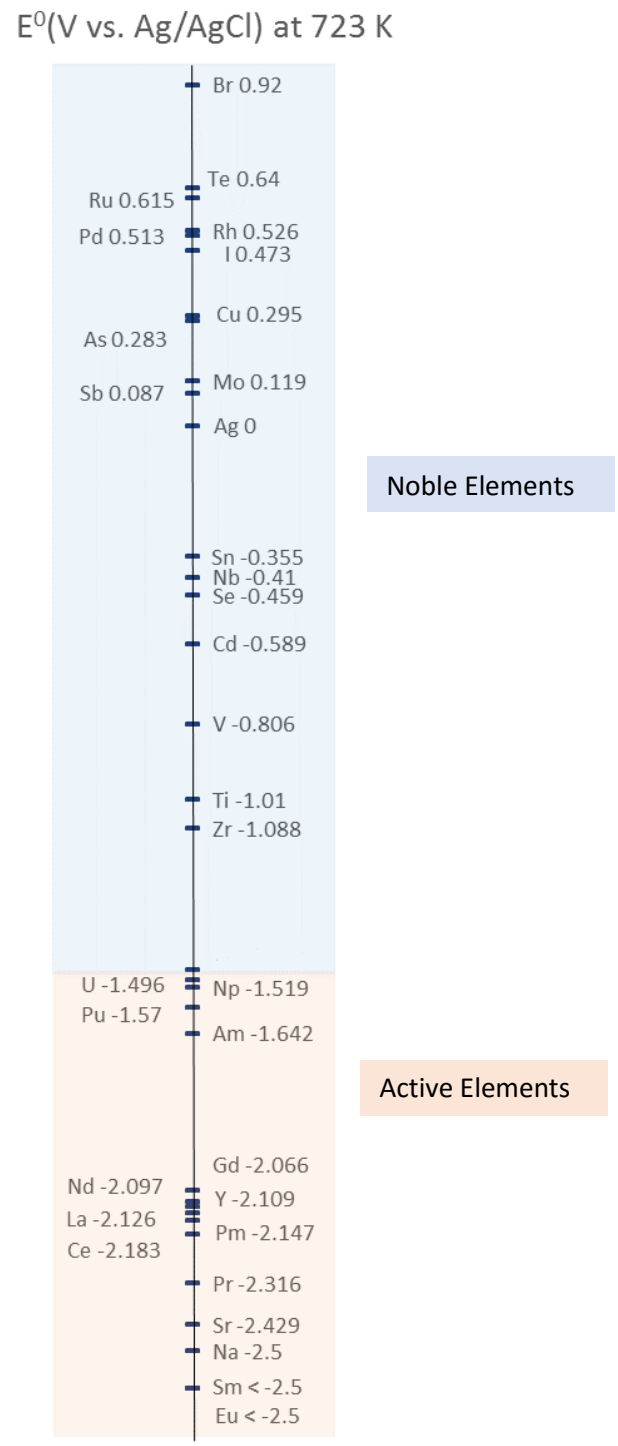

Figure 1-1: Standard potentials of elements in LiCl-KCl salt at 723 K.

During electrorefining, most of the dissolved uranium can be selectively electro-deposited at a solid cathode in the electrorefiner, while other active elements (e.g., Pu, MAs, and rare earth fission products) are either electro-reduced in the liquid Cd or Bi cathode or

remained in the melt and basket [14]. A conceptual figure below describes how electrorefiner works:

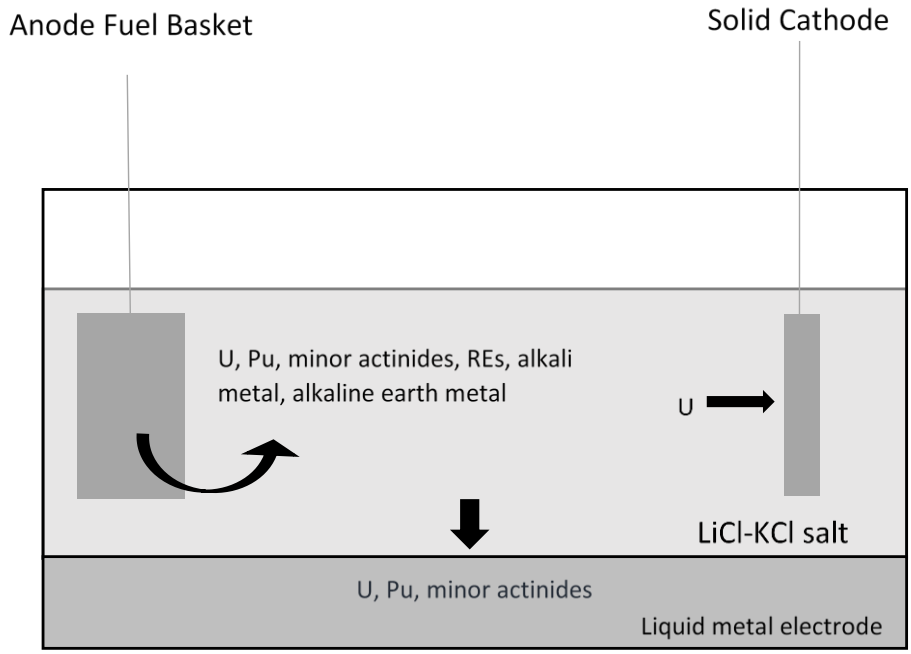

Figure 1-2: Schematic figure of one type of electrorefiner design.

1.2. **Recycling of used salt**

While UNF is continually replenished into the anode fuel basket for U, Pu, and minor actinides separation, REs will accumulate inside the salt and their reduction potentials will approach the value of U and Pu potentials in LiCl-KCl salt. Eventually, it starts affecting the recovery efficiency and the salt has to be removed from electrorefiner [5]. To minimize the salt waste, a conceptual flow sheet for pyroprocessing is developed [15] including the recycle of LiCl-KCl salt. As shown in Figure 1-3, RE drawdown from molten salt is an important part in pyroprocessing and can be achieved by using electrolysis technique [10,15]. As shown in Figure 1-2, after the removal of U, Pu and minor actinides from the salt, RE including lanthanides are the noble elements left in the salt. Like the recovery of U, by applying a current between the anode and cathode in the elctrorefiner, RE ions can be reduced and electro-deposited as metals on the cathode. To perform RE drawdown with electrolysis, physical properties (e.g., activity coefficient and diffusion coefficient) of RE in LiCl-KCl salt at different concentration is essential to separate various REs and optimize the drawdown process.

However, most available data are measured in dilute solution (<1.5 wt%) and are assumed to be concentration independent. In reality, for molten salt recycle, depending on the fuel burn up rate and pyroprocessing operation time, the RE concentration may vary from dilute to 10 wt% where these properties are no longer independent of their concentration [16]. Moreover, little data has been reported for more complex molten salt systems

containing both REs and other active fission products such as cesium that is expected in a true, industrial-scale RE drawdown electrolysis process. Thus, detailed experiments and corresponding models must be conducted and developed, respectively, to provide the data required to predict the electrochemical behavior of the REs in such a molten salt mixture so that the technological feasibility of the RE drawdown by electrolysis to enable molten salt recycling can be evaluated.

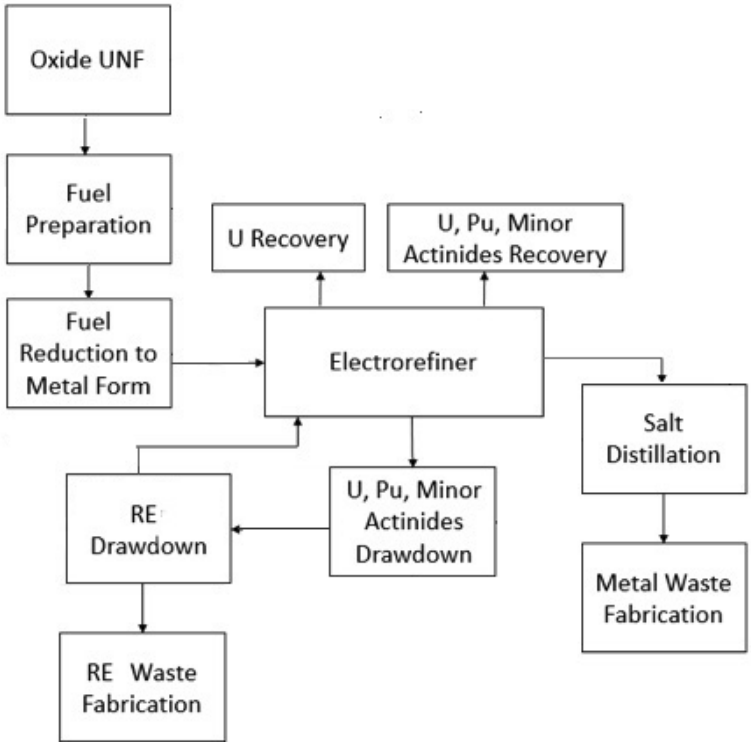

Figure 1-3: Conceptual flowsheet for the treatment of used LWR fuel.

1.3. **Literature data review**

In this section, the activity coefficient and diffusion coefficient of Res including La, Ce, Pr, Nd, Sm, Eu, Gd, Tb, Dy and Er in LiCl-KCl salt are reviewed. Correlations of the properties with temperature have been developed and summarized in PI's publication [17]. In this review, we attempt to organize these properties as a function of concentration to identify its effect on these properties.

1.3.1. Lanthanum

La^{3+} is reported to be the stable oxidation state of lanthanide in molten LiCl-KCl salt. The apparent standard potential of La^{3+}/La^{0} [18,19,20,21,22,23,24] along with the experiment concentration ranging from 10^{-3} to 10^{-5} molar fraction are summarized in Table A - 1 and Table A - 2. Given the definition of the apparent standard potential (E^{*}), the activity coefficient of RE can be calculated accordingly:

$$E^{*}_{M^{n+}/M} = E^{0}_{M^{n+}/M} + \frac{RT}{nF} ln \frac{\gamma_{M^{n+}}}{\gamma_{M}} \quad (1\text{-}2)$$

where $E^{0}_{M^{n+}/M}$ versus Cl_2/Cl^- equals $\Delta G^{0}_{f}(MCl_4)/nF$, ΔG^{0}_{f} represents Gibbs free energy at liquid or super cooled state [17], γ is activity coefficient and can be assumed 1 for pure metals.

By inserting equation (1-2) in equation (1-1), the following correlation can be derived based on which the redox potential can also be directly calculated from the apparent potential and molar fraction (X):

$$E_{M^{n+}/M} = E^{*}_{M^{n+}/M} + \frac{RT}{nF} ln \frac{X_{M^{n+}}}{X_{M}} \quad (1\text{-}3)$$

In Lantelme and Berghoute's paper [22], a series of experiments with different concentrations ranging from 10^{-3} to 10^{-2} in molar fraction were carried out and the results of which are given in Table A - 2, and the corresponding curves as functions of the temperature and concentration are shown in Figure 1-4. The figure shows that the apparent potential becomes more negative when the concentration of La in the molten salt decreases. This indicates that the concentration of La in the molten salt affects its apparent potential in the salt. In a more recent study conducted by Samin [25], it is demonstrated that the apparent potential of La is indeed affected by its concentration and the results are summarized in Table A - 3.

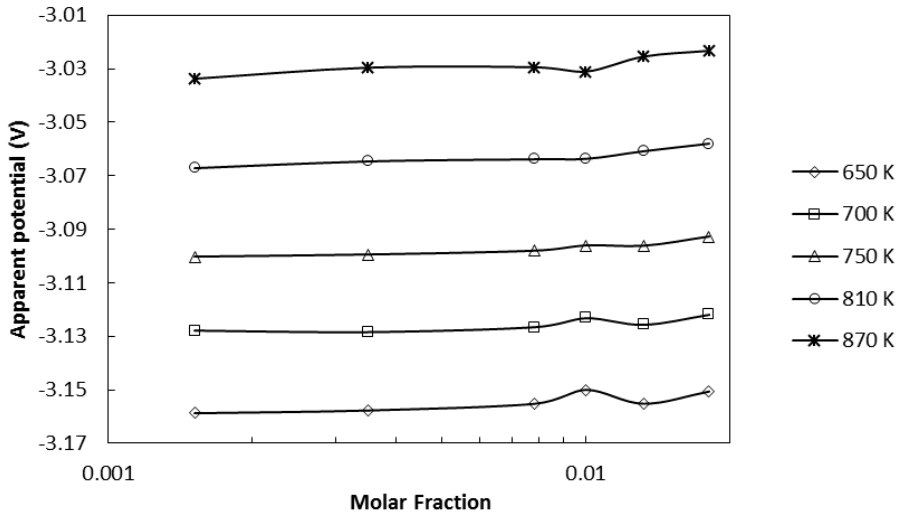

Figure 1-4: Apparent potential of La^{3+}/La^{0} at different concentration with different temperature [22].

The Gibbs free energy (kJ/mol) of $LaCl_3$ at super cooled state is -872.976 kJ/mol at 723 K and -836.764 kJ/mol at 823 K [21], the corresponding activity coefficient is calculated as

$log\gamma = -2.268$ at 723 K with rare earth working electrode by Castrillejo [21]. In more recent research, Tang and Pesic [24] reported activity coefficient of $LaCl_3$ from 693 K to 813 K in Table A - 9. The activity coefficient from Castrillejo [21] is four times higher than the value Tang [24] reported at 723 K. Based on Figure 1-4 and Eq. (1-2), the activity coefficient of La in the salt should also slightly depend on the concentration. However, similar to the apparent potential, a correlation expression can be obtained based on current available data.

The diffusion coefficients of La^{3+} in molten LiCl-KCl salt are summarized in Table A - 11. The diffusion coefficient obtained by interpolation from Tang's [24] data at 723 K shows good agreement with Masset [20] at around 1.27×10^{-5} cm^2s^{-1} at a mole fraction 0.00763. Lantelme [22] reported that diffusion coefficient equals to 0.8×10^{-5} cm^2s^{-1} at 723 K and a mole fraction of 0.00293. The two data points at 723 K show the trend of the decrease of the diffusion coefficient with the concentration. However, the experimental data is too scarce to draw a general conclusion or a correlation between the diffusion coefficient and the concentration of La in the molten salt.

1.3.2. Cerium

Ce^{3+} is the stable oxidation state of Ce in LiCl-KCl salt. The apparent potential of Ce^{3+}/Ce has been studied and summarized in Table A - 5 [19,21,26]. Apparent potential from the three references agree well among each other between 673 K and 723 K despite the three tests conducted at different concentrations. At 723 K, all three references reported a value around -3.098 V. No correlation is found in apparent potential based on available data.

The activity coefficient of $CeCl_3$ is summarized [26,27,28] in Table A - 9**.** Marsden [26] reported a series of activity coefficient (logγ) ranging from 673 K to 973 K. However, the activity coefficient reported showed different behavior when compared with other lanthanides. The activity coefficient decreases as temperature rises, while other lanthanide's activity coefficient increases when temperature increases. The activity coefficients at 723 K with different concentrations are plotted in Figure 1-5. As shown in the figure, the activity coefficient $CeCl_3$ increases as temperature increases, which also leads to the apparent potential becoming more positive with concentration.

The diffusion coefficients of $CeCl_3$ in molten LiCl-KCl salt are studied by cyclic voltammetry (CV) and chronopotentiometry (CP) method. The values at different temperature are summarized in Table A - 12. Diffusion coefficients measured by CP method from three references [26,28,29] are 1.96×10^{-5} cm^2s^{-1}, 1.71×10^{-5} cm^2s^{-1} and 1.53×10^{-5} cm^2s^{-1} at 773 K while CV method reports a smaller value of 0.99×10^{-5} cm^2s^{-1} at 773 K. At lower temperature 653 K, CV and CP method show similar result with 0.47×10^{-5} cm^2s^{-1} for CV and 0.53×10^{-5} cm^2s^{-1} for CP. Compared between the CP results at 773 K from different sources with different concentrations, the diffusion coefficient decreases from 1.96×10^{-5} cm^2s^{-1} at a mole fraction 0.011 to 1.53×10^{-5} cm^2s^{-1} at a mole fraction of 0.00189, which indicates that the diffusion coefficient decreases with the concentration.

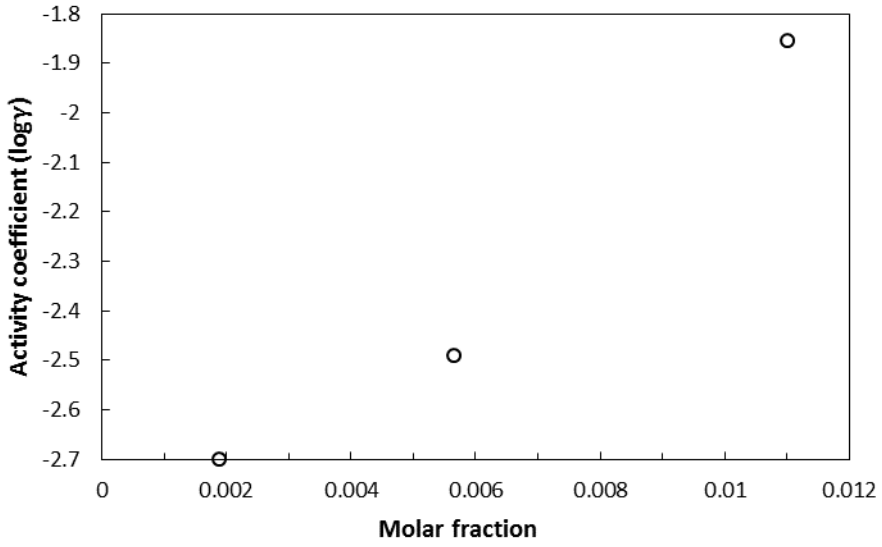

Figure 1-5: Activity coefficient of $CeCl_3$ at different concentration at 723 K [27].

1.3.3. Praseodymium

Pr^{3+} is the stable oxidation state in molten LiCl-KCl salt. The apparent potentials of Pr^{3+}/ Pr were studied and summarized [19, 21] in Table A - 5. The two references agree well between 673 K and 773 K. However, at the same temperature the potential from Fusselman [19] is always more negative than that from Castrillejo [21], which may be due to the different concentrations used in the two experiments. There is not enough data to conclude on the dependence of apparent potential on the concentration.

The activity coefficient of $PrCl_3$ was studied by Castrillejo [21] and summarized in Table A - 9. The activity coefficient (logγ) is reported to be -2.517 at 723 K and increases to -2.129 as temperature goes to 823 K. However, 723 K and 823 K are the only two temperatures that the activity coefficient is reported, and thus it is not sufficient to establish a correlation.

The diffusion coefficients of $PrCl_3$ in molten LiCl-KCl salt are studied by CP and convolution method [29] and are summarized in Table A - 11**.** Both CP and convolution method showed similar results between 653 K and 773 K and diffusion coefficient increases as temperature increases. All these measurements were conducted at the same concentration; therefore, it is impossible to get the concentration effects on the diffusion coefficients based on these data. Further experiments for different concentration are needed.

1.3.4. Neodymium

Nd^{3+} and Nd^{2+} are the two stable oxidation states in molten LiCl-KCl salt. The apparent potential of Nd^{3+}/Nd, Nd^{2+}/Nd and Nd^{3+}/Nd^{2+} are collected and summarized [20,21,30,31,32] in Table A - 4. The apparent potential shows no correlation with concentration of Nd in the molten salt based on different experiments at different

concentrations ranging from 10^{-3} to 10^{-2} in molar fraction. Apparent potential of Nd^{3+}/Nd at 723 K are reported as -3.093 V, -3.105 V and -3.127 V.

The activity coefficient of $NdCl_3$ is studied [20,21,30] and summarized in Table A - 8. In Vandarkuzhali's research, Nd was found to form intermetallic compound with aluminum and cadmium electrode and thus leads to a smaller activity coefficient with a value ($log\gamma$) of -11.5 and -8.8 for aluminum and cadmium electrode at 723 K. At the same time, Masset and Castrillejo reported much smaller value with -4.0969 at 733 K and -3.516 at 723 K.

The diffusion coefficient of Nd^{3+} and Nd^{2+} are summarized in Table A - 12. Masset reported the diffusion coefficient of Nd^{3+} to be 1.1×10^{-5} cm^2s^{-1} while the result from Vandarkuzhali's is only 0.28×10^{-5} cm^2s^{-1}. Vandarkuzhali also reported the diffusion coefficient of Nd^{2+} to be 0.98×10^{-5} cm^2s^{-1} at 723 K. All these tests were conducted at the same concentration.

1.3.5. Samarium

The electrochemical behavior of Samarium in LiCl-KCl salt has been studied, and it is reported that Sm^{3+} and Sm^{2+} are the two stable oxidation states. The apparent potential of Sm^{2+}/ Sm is too close to Li^+/Li and, as such, the measurement on Sm^{2+}/ Sm couple's apparent potential via CV and CP method is not reliable [33]. The collected Sm^{3+}/Sm^{2+} apparent potential is summarized in Table A - 6 [34,35]. The apparent potentials are reported as -2.04 V and -2.099 V at 723 K respectively.

The activity coefficient of $SmCl_3$ is summarized in Table A - 8 [34,35]. Cordoba reported the value to be -3.617 at 723 K and Castrillejo reported a more negative value of -4.35 at 723 K. The data is not sufficient to make comparison between the two. The activity coefficient (logγ) of $SmCl_3$ increases as temperature increases, but the concentration-dependent information is not available.

The diffusion coefficient of $SmCl_3$ in molten LiCl-KCl salt is studied by CV, CP, convolution and semi-integral methods [34,35]. The summarized results are shown in Table A - 13. Diffusion coefficients studied by CV, CP and convolution by Castrillejo shows good agreement with each other while results from Cordoba show larger discrepancies between each method. Overall, diffusion coefficients studied by different methods show positive linear relation with temperature and diffusion coefficient at 723 K ranges between 0.51×10^{-5} cm^2s^{-1} and 0.95×10^{-5} cm^2s^{-1}. Although the two references [34,35] used different concentrations (0.00225 and 0.00372) for their measurements, the measured diffusion coefficients at the same temperature are almost identical.

1.3.6. Europium

Eu^{3+} and Eu^{2+} are the two stable oxidation states in molten LiCl-KCl salt. Similar to Sm, only the Eu^{3+}/Eu^{2+} apparent potential data is reliable. The apparent standard potential of Eu^{3+}/Eu^{2+} is studied by Caravaca [31] and summarized in Table A - 6. At 723 K, apparent potential is found to be -0.848 V.

The activity coefficient of $EuCl_3$ is studied and summarized in Table A - 10**.** The activity coefficient ($log\gamma$) at 723 K is reported to be -2.977.

The diffusion coefficients of $EuCl_3$ in molten LiCl-KCl salt are studied by CV, CP and other methods [31,36,37]. The diffusion coefficient of Eu^{2+} is also studied and summarized in Table A - 14. At 773 K, data from Kim and Bermejo agrees well where Kim reported 0.92×10^{-5} cm^2s^{-1} and Bermejo reported the value between 0.889×10^{-5} cm^2s^{-1} and 0.93×10^{-5} cm^2s^{-1}. The diffusion coefficient of Eu^{2+} is found to have similar value with Eu^{3+} studied by Kim and Bermejo.

1.3.7. Gadolinium

Thermodynamic and electrochemical properties of Gd in molten LiCl-KCl is studied [19, 22,28,31,38]. Gd^{3+} is reported as the only stable oxidation state. The apparent standard potential of Gd^{3+} in LiCl-KCl with different $GdCl_3$ concentration is summarized in Table A - 7 and the corresponding curves are given in Figure 1-6. Figure 1-6 indicates that the apparent potential of Gd^{3+} from Lantelme [22] shows correlation with its concentration in the molten salt. Higher $GdCl_3$ concentration results in a higher apparent potential. This phenomenon is similar to the apparent potential of lanthanide in LiCl-KCl salt. La's and Gd's apparent potential are the only two lanthanides that were studied over a range of concentrations, and the results show a correlation between apparent potential and concentration. Further investigation will help to establish correlation between apparent potential and concentration.

The activity coefficient of Gd in LiCl-KCl is studied by Iizuka and Caravaca [28,31]. The summarized result is given below in Table A - 10. The activity coefficient ($log\gamma$) reported by Iizuka is only -3.769 while Caravaca reported a much higher value -2.586 at 723 K.

For the diffusion coefficient of $GdCl_3$ in molten LiCl-KCl salt. Iizuka [28] carried out the experiment with different concentration ranging from 3.9×10^{-4} to 2.3×10^{-3} molar fractions, while Caravaca [31] did it with CV, CP and convolution methods. The summarized results are shown in Table A - 15. In Caravaca's research, convolution method showed similar value with Iizuka's result at 723 K where the values are 0.88×10^{-5} cm^2s^{-1} for Convolution and 0.873×10^{-5} cm^2s^{-1} from Iizuka's data. At the same time, CV and CP method reported lower values at 0.31×10^{-5} cm^2s^{-1} and 0.64×10^{-5} cm^2s^{-1} respectively. No significant impact is found when concentration is changed.

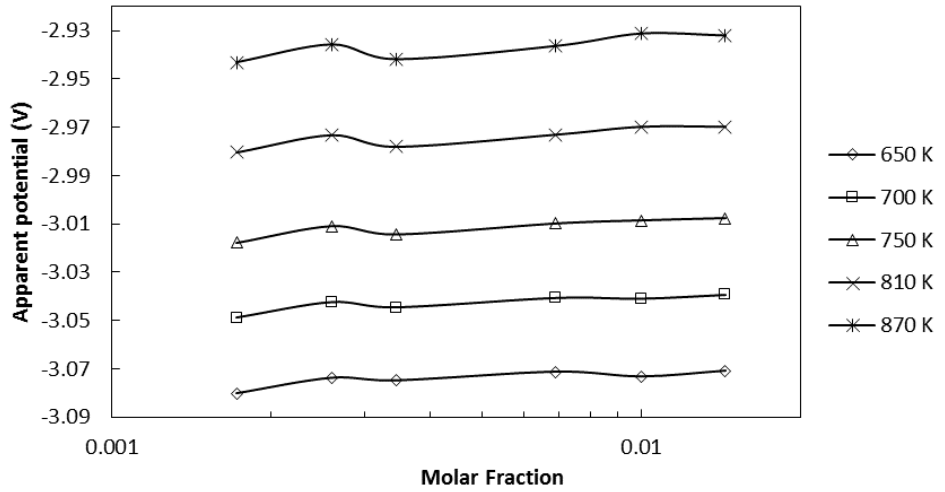

Figure 1-6: Apparent potential of Gd^{3+}/Gd at different concentration with different temperature [22].

1.3.8. Terbium

Tb^{3+} is the only stable oxidation state of Tb in LiCl-KCl salt. The apparent potential of Tb^{3+} has been studied and summarized [39,40] in Table A - 6. The apparent potential measured by Kim [40] agrees well with Bermejo's [39] if the apparent potential correlation given by Bermejo is extended to a higher temperature. The activity coefficient of $TbCl_3$ is also summarized in Table A - 10 [39].

The diffusion coefficient of $TbCl_3$ in molten LiCl-KCl salt is studied by CV and CP methods and is summarized in Table A - 16. The diffusion coefficient form Kim [40] is way higher than Bermejo's [39] value at 887 K. Possible reason for the difference is due to using different electroanalyitcal methods.

1.3.9. Dysprosium

Dy^{3+} and Dy^{2+} are the two stable oxidation states of Dy in molten LiCl-KCl salt. The apparent potential of Dy^{2+}/ Dy^{0} at 723 K is reported to be -3.254 V versus Cl_2/Cl^- for Dy^{3+}/ Dy^{2+}, the apparent potential at 723 K is reported to be -3.243 V versus Cl_2/Cl^- [41]. The experiment is taken with a concentration of 0.00465 molar fraction.

The diffusion coefficient of $DyCl_3$ in molten LiCl-KCl salt was studied by CP method and summarized in Table A - 16. The diffusion coefficient is reported to be $1.03\times10^{-5}\ cm^2s^{-1}$ at 723 K.

1.3.10. Erbium

Er^{3+} is the only stable oxidation state of Er in LiCl-KCl salt. The apparent potential of Er^{3+} has been studied and summarized [42,43,44] in Table A - 6 and the activity coefficient of $ErCl_3$ is summarized in Table A - 10. Both properties increase as temperature increases, which is similar to the behavior of other lanthanides.

The diffusion coefficient of $ErCl_3$ in molten LiCl-KCl salt is studied by CV and CP methods and is summarized in Table A - 16. The diffusion coefficient from Tang [42] and Castrillejo [43] corresponds well between 683 K and 813 K. Diffusion coefficient measured by Peng [44] also agrees well with Tang and Castrillejo's result when extending diffusion coefficient correlation to 873 K.

1.3.11. Summary

Available thermodynamics and electrochemical data of lanthanides including La, Ce, Pr, Nd, Sm, Eu, Gd, Tb, Dy, Er and Tm in molten LiCl-KCl salt are collected for pyroprocessing molten salt recycle. Apparent potential, activity coefficient and diffusion coefficient and exchange current density are the four properties that we reviewed. The data collection includes the concentration of lanthanide in molten LiCl-KCl salt as well as the measuring method reference used. The prime focus of the review is to figure out concentration effects on these properties. Unfortunately, no solid conclusions on the concentration effects were obtained because of the scarce of the data. However, some trends of the thermodynamic properties of some lanthanides in the molten salt as a function of their concentration were observed based on available data.

Lanthanum and gadolinium are two of the lanthanides that were studied extensively in the past and show correlation between apparent potential and lanthanide concentration in molten LiCl-KCl salt. As lanthanide concentration increases, the apparent potential also slightly increases. At the same time, the activity coefficient of Ce is also found to have a positive relation with concentration. Establishing correlation between potential/activity coefficient and concentration will help to predict the actual pyroprocessing behavior since the process takes place in concentrated molten salt, where most of the properties are concentration dependent. In general, the self-diffusion coefficient, which does not depend on the concentration, can represent the chemical diffusion coefficient for dilution cases for which it has been recognized that the activity coefficient is non-concentration dependent. If activity coefficient increases with concentration as it is found for La and Gd, the apparent potential should decrease with the concentration which was not found based on the available data for La and Gd. Therefore, we are interested in conducting the study of fundamental data measurements at different concentration to develop these property database.

2. Fundamental properties measurement and analysis

2.1. Experimental setup and methods

2.1.1. Materials and electrochemical cell

The sample preparation and electrochemical experiments are performed in customized argon-atmosphere glovebox (Figure 2-1(a)) with oxygen level lower than 1 ppm and H_2O level less than 4 ppm. Kerr Maxi Electro-Melt furnace with a customized lid that allows electrodes to pass through is used to control the temperature within ±1°C from the target temperature. Anhydrous LiCl-KCl eutectic (+99.99% purity) was purchased from Sigma-Aldrich, anhydrous $LaCl_3$, $NdCl_3$ and $GdCl_3$ (99.99% purity) was purchased from APL Engineered Materials and all are received in sealed glass ampoules with inert atmosphere. Silver chloride (99.999% purity, Aldrich) and 1mm diameter silver wire (99.999% purity, Alpha Aesar) were used for reference electrode. All materials are opened inside the argon-atmosphere glovebox and no further purification process is made. LiCl-KCl-$RECl_3$ salts were mixed inside alumina crucible purchased from SPI Supplies and heated up to the desired temperature.

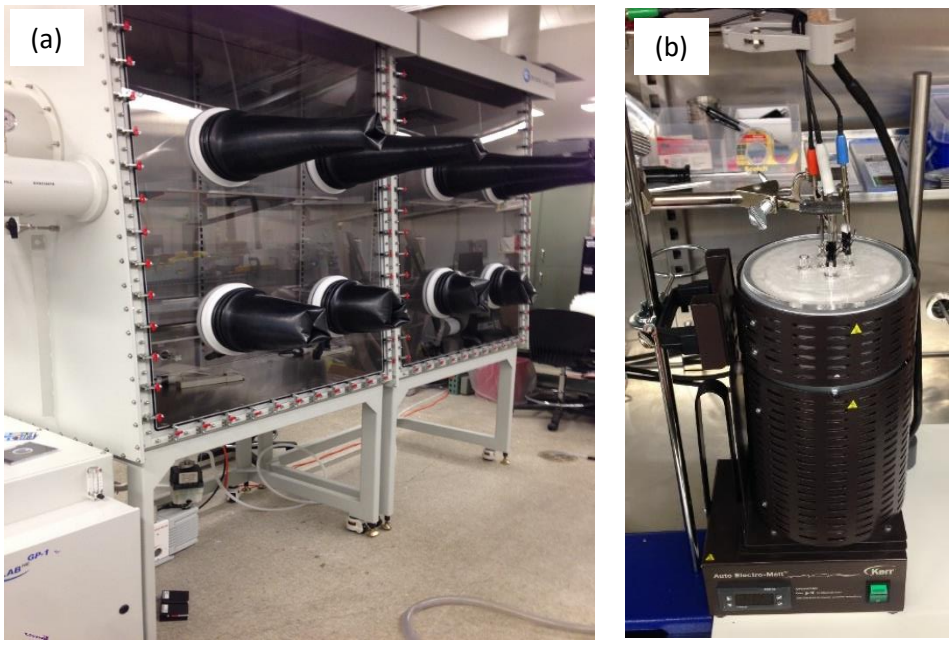

Figure 2-1: (a) Glove box system; (b) Electrochemical cell.

A working-counter-reference three electrode system was established to perform electrochemical tests. 1 mm to 3 mm diameter Tungsten electrode was purchased from Daimond Ground as working and counter electrode. The diameter of the counter electrode is greater than the working electrode to avoid counter electrode being the current limiting factor. As for reference electrode, silver-silver chloride (10 wt% / 0.0402 molar fraction, AgCl in LiCl-KCl) and 1 mm silver wire was placed into a 6 mm diameter pyrex tube

(Specialty Glass) and dipped into the salt. A photo of the electrochemical cell is given in Figure 2-1(b) and the schematic diagram is shown in Figure 2-2.

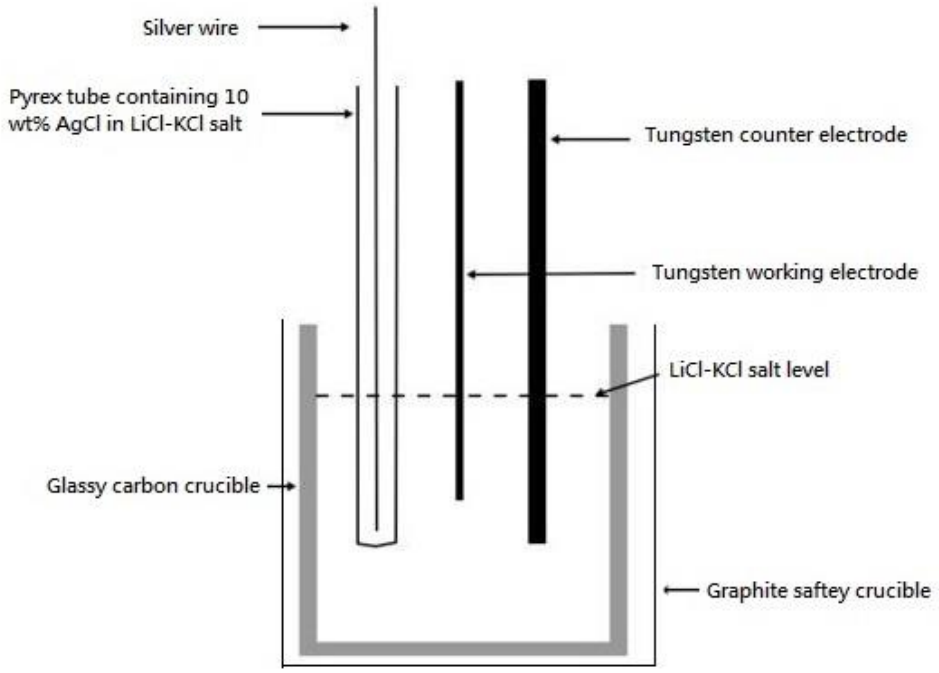

Figure 2-2: A sketch of the experimental setup inside the furnace.

To determine the apparent potential and compare with literature, the potential has to be reported relative to Cl_2/Cl^- couple instead of directly measured value relative to Ag/AgCl couple. The apparent potential obtained by the experiment can reference into Cl_2/Cl^- by the following equation:

$$E^*_{La/La^{3+}}(vs.\,Cl_2\,/\,Cl^-) = E^*_{La/La^{3+}}(vs.\,Ag/\,AgCl) + E^0_{AgCl} + \frac{RT}{F}\,ln\left(X_{AgCl}\right) \qquad (2\text{-}1)$$

where $E^*_{La/La^{3+}}(vs.\,Ag/\,AgCl)$ and $E^*_{La/La^{3+}}(vs.\,Cl_2\,/\,Cl^-)$ are the apparent potential versus different reference states, X_{AgCl} is the mole fraction of AgCl, and E^0_{AgCl} is the standard reduction potential of Ag/AgCl relative to Cl_2/Cl^-. According to Young and Hudson [45], the standard reduction potential of Ag/AgCl relative to Cl_2/Cl^- can be expressed as:

$$E^0_{AgCl} = -1.0910 + 0.0002924T \qquad (2\text{-}2)$$

Gamry Interface 1000 potentiostat and Gamry Electrochemistry Software are used to perform electrochemical measurement. After each electrochemical test, a stripping potential of 0.2 V versus Ag/AgCl reference electrode is applied for 20-60 seconds depending on $RECl_3$ concentration to remove RE metal from the electrode. This cleaning process was examined by 6 identical CV tests with $LaCl_3$ in LiCl-KCl salt with 10 cycles on each CV run. The relative standard deviation of cathodic peak current value between cycles is less than 0.1% and less than 1.2% between different CV tests. This shows that the working electrode is well restored to its initial condition. The active electrode area was

measured after each experiment by measuring the immersed depth of the electrode in molten salt with an accuracy of ±0.1 mm. The actual salt composition is analyzed using ICP-OES measurement after the experiment is finished.

2.1.2. Electrochemical measurements and analysis methods

In this part, we summarized all the electrochemical techniques that we used to determine apparent potential, activity coefficient, diffusion coefficient and exchange current density.

2.1.2.1. Square wave voltammetry (SWV)

The number of electron transfer for a redox reaction is used in every electrochemical analysis and needs to be determined first. For most of the RE, the number of electrons transferred are summarized by Zhang [17], but it is important to make sure this property remains unchanged in high concentration using SWV. When SWV is performed, a single peak will be observed for each redox reaction, and the peak shape can be approximated by Gaussian distribution for reversible reaction [30]. The width of the peak at half height is directly related to the number of electrons transferred as shown in the following equation:

$$W_{1/2} = \frac{3.52RT}{nF} \tag{2-3}$$

where $W_{1/2}$ is the width of the peak at half height, R is the universal gas constant ($JK^{-1}mol^{-1}$), F is the Faraday constant, T is the temperature (K) and n is the number of electrons transferred. By determining the number of electrons transfer during the reaction, we can safely step further to calculate RE apparent potential, Gibbs formation of energy, activity coefficient, diffusion coefficient and exchange current density based on the number of electrons transferred we measured.

2.1.2.2. Cyclic voltammetry (CV)

2.1.2.2.1. Conventional CV analysis

CV has been widely used to measure RE thermodynamics and transport properties in LiCl-KCl salt. In conventional CV analysis, the major focus is to determine the cathodic peak current and the corresponding potential. A typical cyclic voltammogram measured in our lab is shown in Figure 2-3 and the cathodic peak is marked.

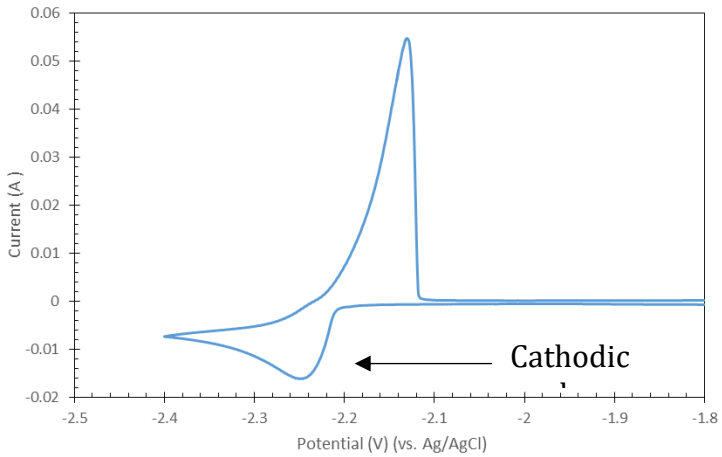

Figure 2-3: Cyclic voltammogram for 2.787 wt% ($1.872 \times 10^{-4}\ mol/cm^3$) $LaCl_3$ in LiCl-KCl salt at 723 K for three different scan rates. The electrode area is 0.905 cm^2.

It is important to know that most equations applied to CV are based on the assumption that the reaction during CV scan is reversible. There are two methods that are capable of determine the reversibility of the reaction at different scan rates. The first one is plotting the cathodic peak current versus square root of scan rate. If a linear relationship is established, the reaction is considered quasi-reversible or reversible. For a more precise way to determine the reversibility of the reaction, Matsuda and Ayabe criteria [46] is applied. However, this method requires more information of the reaction based on the assumption that the reaction is reversible or quasi-reversible. Hence, we will investigate the criteria after the analysis from other methods are completed.

After identifying the reversibility of the reaction at different scan rate, thermodynamic properties are calculated. Berzins and Delahay [47] have derived an equation for soluble-insoluble reversible system to determine the apparent potential of the system based on cyclic voltammogram cathodic potential peak location. This equation is then used in LiCl-KCl salt to determine uranium apparent potential even though the system is in quasi-reversible [20]. This method is widely used to determine REs apparent potential later on. The equation can be expressed as:

$$E_{p,c} = E^*_{\mathrm{Re^{n+}/Re}} + \frac{RT}{nF} lnX_{\mathrm{Re^{n+}}} - 0.854\frac{RT}{nF} \tag{2-4}$$

where $E_{p,c}$ is the cathodic current peak location. For a soluble-soluble case, the apparent potential can be expressed as [48]:

$$E^*_{\mathrm{Re^{n+}/Re^{m+}}} = E_{1/2} + \frac{RT}{(n-m)F} \ln\left(\sqrt{\frac{D_{RE^{n+}}}{D_{RE^{m+}}}}\right) \tag{2-5}$$

wherer $E_{1/2}$ is the half wave potential.

Once the apparent potential is obtained, the activity coefficient can also be calculated based on following equation:

$$\ln \gamma_{RE^{n+}} = \frac{nF}{RT}(E^* - E^0) \quad (2\text{-}6)$$

Diffusion coefficient characterizes the kinetic effect of REs in LiCl-KCl salt and is another important property to be measured. Berzins and Delahay [47] derived the equation for diffusion coefficient in soluble-insoluble reversible system as shown below:

$$i_p = 0.611nFC_0(nFvD/RT)^{1/2} \quad (2\text{-}7)$$

where i_p is the cathodic peak current density from the voltammogram (A/cm^2), C_0 is the concentration (mol cm^{-3}), v is the scan rate (V/s) of CV and D is the diffusion coefficient (cm^{2}s^{-1}). For irreversible case, charge transfer coefficient α is introduced and a new equation yields:

$$i_p = 0.496nFC_0(\alpha nFvD/RT)^{1/2} \quad (2\text{-}8)$$

For a soluble-soluble system, the diffusion coefficient can be expressed by Randle-Shevchik equation [48]:

$$i_p = 0.4663nFC_0(nFvD/RT)^{1/2} \quad (2\text{-}9)$$

2.1.2.2.2. Numerical simulation using BET model

Besides using the traditional CV analysis methods, we have also developed a BET model to determine formal potential, diffusion coefficient, transfer coefficient, and standard rate constant by fitting experimental CV data [25,49]. In the model, both oxidized (RE^{3+}) and reduced species (RE) concentration as a function of time and location is governed by diffusion equations:

$$\frac{\partial c_O}{\partial t} = D_O \frac{\partial^2 c_O}{\partial x^2} \quad (2\text{-}10)$$

$$\frac{\partial c_R}{\partial t} = D_R \frac{\partial^2 c_R}{\partial x^2} \quad (2\text{-}11)$$

where c_O and c_R are the concentrations of the oxidized and reduced species. The domain on which the equations are solved is $0 \le x \le L$, where we choose $L = 12\sqrt{DT_{max}}$ (T_{max} is the time needed for one full CV cycle). The diffusion coefficient of reduced specie on the electrode D_R is assumed with a low value of 10^{-20} cm^2/s since it is in solid state.

In the model, the adsorption of RE on the electrode is described by the BET isotherm originally proposed by Brunauer, Emmett and Teller [50]

$$\Gamma_R(t) = \frac{\Gamma_s K_1 c_R(0,t)}{\left(1 - K_d c_R(0,t)\right)\left(1 + K_1 c_R(0,t) - K_d c_R(0,t)\right)} \quad (2\text{-}12)$$

where Γ_s is the maximum surface concentration of the product species, and K_1 and K_d are adsorption equilibrium constants. The boundary conditions are obtained by:

$$D_O \left.\frac{\partial c_O}{\partial x}\right|_{x=0} = c_O(0,t)k_f^o e^{-\frac{\alpha nF}{RT}\left(E-E_f^0\right)} - c_R(0,t)\mathrm{k_b^o e}^{\frac{(1-\alpha)\mathrm{nF}}{\mathrm{RT}}(\mathrm{E}-\mathrm{E_f^0})} \quad (2\text{-}13)$$

$$\mathrm{D}_R \left.\frac{\partial c_R}{\partial x}\right|_{x=0} = \frac{d\Gamma_R}{dt} - c_O(0,t)k_f^o e^{-\frac{\alpha nF}{RT}\left(E-E_f^0\right)} + c_R(0,t)k_b^o e^{\frac{(1-\alpha)nF}{RT}(E-E_f^0)} \quad (2\text{-}14)$$

where k_f^o and k_b^o are forward and backward reaction rate constant. For initial condition, the surface concentration is considered the same as the bulk concentration, no absorption has happened yet and no reduced species exist in the system:

$$c_{\mathrm{O}}(\mathrm{x},\mathrm{t}=0) = c_{\mathrm{O}}(\mathrm{L},\mathrm{t}) = c_{\mathrm{bulk}} \quad (2\text{-}15)$$

$$c_{\mathrm{R}}(\mathrm{x},\mathrm{t}=0) = c_{\mathrm{R}}(\mathrm{L},\mathrm{t}) = 0 \quad (2\text{-}16)$$

$$\Gamma_P(t=0) = 0 \quad (2\text{-}17)$$

And the current flowing into the electrode surface is considered diffusion control:

$$I = -nFAD_O \left.\frac{\partial c_O}{\partial x}\right|_{x=0} \quad (2\text{-}18)$$

A software was then developed based on the BET model to fit the experiment signal using nonlinear least square procedure [51]. The software interface is shown in Figure 2-4. As shown in the figure, experiment condition and signal are entered into the software while initial guesses on the fitting properties are made in order to start the nonlinear least square fitting. All CV signals are run by the software and the formal potential and diffusion coefficients are being compared with results from traditional CV analysis.

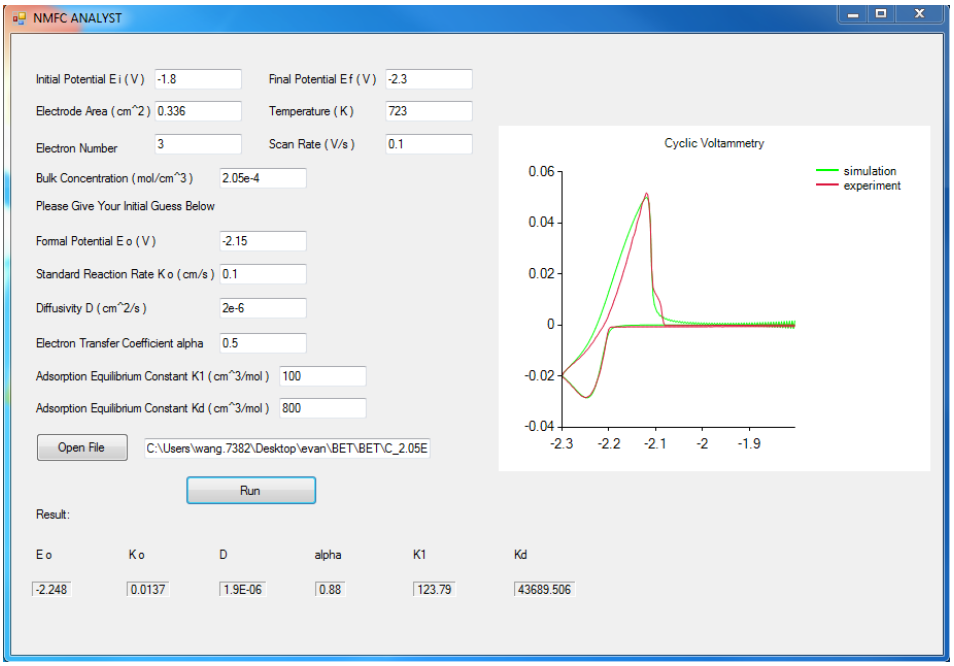

Figure 2-4: The interface of the developed BET model software. Inputs include experimental signal, condition of the experiment and initial guess on the value of formal potential, standard rate constant, diffusion coefficient, charge transfer coefficient, and adsorption equilibrium constants.

Figure 2-5 are two examples that show how the fitting results looks like. The fitting results agrees well with the experiment signal especially on the cathodic peak, which give us a reliable method to predict the crucial properties of REs in LiCl-KCl salt.

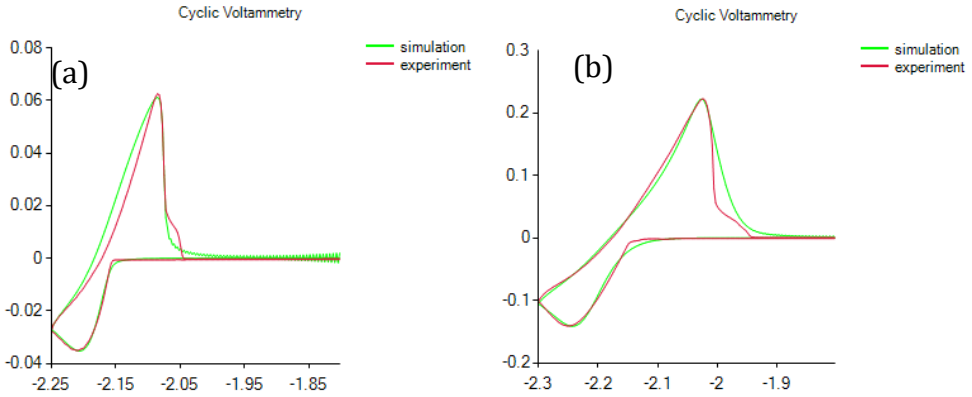

Figure 2-5: (a) Software fitting result for 3 wt% LaCl3 in LiCl-KCl salt at 823 K. (b) Software fitting result for 6 wt% LaCl3 in LiCl-KCl salt at 723 K.

2.1.2.3. Chronocoulometry (CC) and chronopotentiometry (CP)

In CC, a step potential change is applied and the corresponding accumulated charge is recorded. The measured charge behavior can be separated into two parts. The first part usually last about a couple milliseconds. During this period, charge due to electrolysis of RE from molten salt, double layer charging and charge due to electrode adsorption of RE can contribute to charge accumulation. After the short period of time, electrolysis of RE from molten salt is solely the contributor of charge accumulation and the charge to time behavior is governed by Anson equation [48] as shown below:

$$Q = 2\mathrm{nFA}C_0 D^{1/2}\pi^{-1/2}t^{1/2} + nFA\Gamma_0 + Q_{dl} \qquad (2\text{-}19)$$

where Γ_0 is the surface concentration of adsorbed RE (mol cm^{-2}) and Q_{dl} is the charge due to double layer charging. In Figure 2-6(a), CC data for 1 wt% $LaCl_3$ in LiCl-KCl salt is measured with a stepping down potential -2.16 V. It is demonstrated that the abrupt increase of charge initially results from double layer charging and electrode surface adsorption. The acuumulate charge curve flats out later as diffusion takes over the total charge accumulation. In Figure 2-6(b), the stepping down potential plays an important role in the diffusion coefficient measurement, with excess potential applied, the slope of the curve increase significantly which results in greater diffusion coefficient calculated.

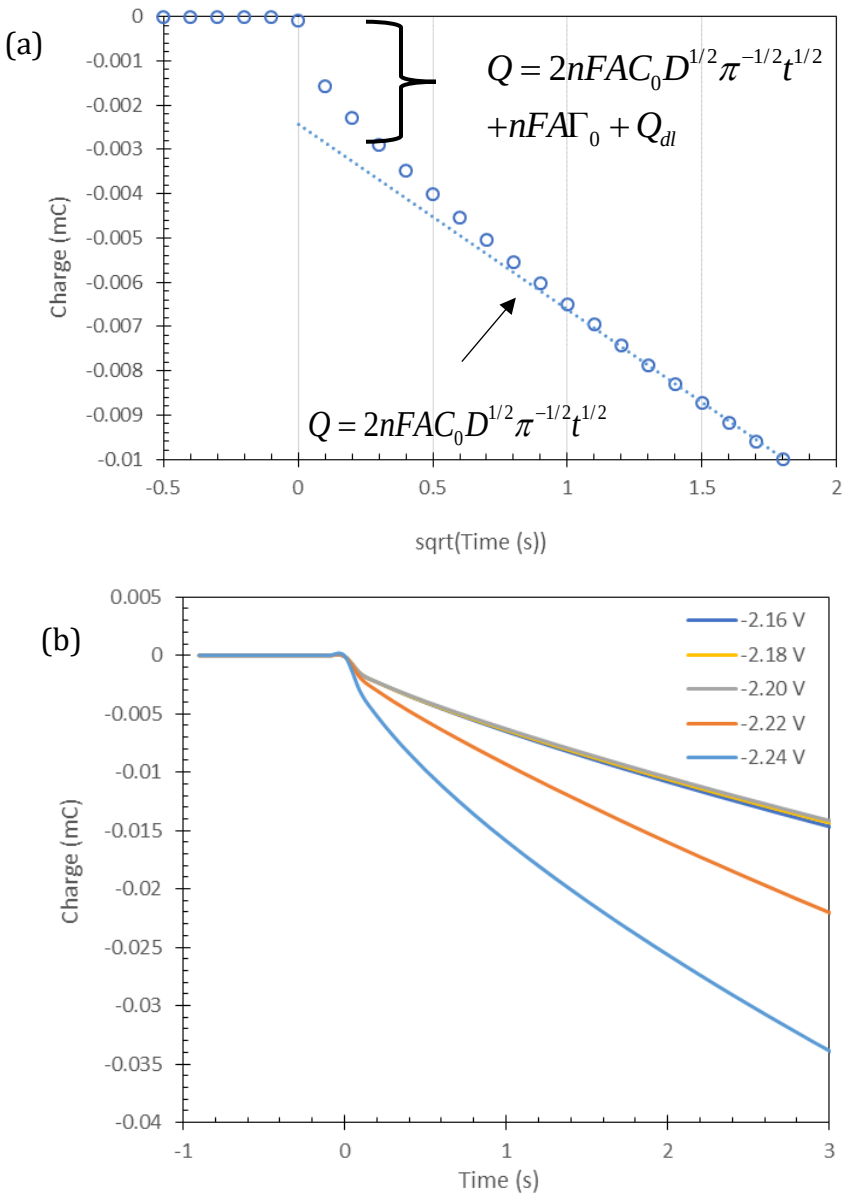

Figure 2-6: (a) Chronocoulummetry for 1 wt% LaCl3 in LiCl-KCl salt at 723 K with a stepping down potential -2.16 V. (b) Chronocoulummetry results for 1 wt% La with different stepping voltage at 723 K.

For CP, a constant current signal is applied and the voltage is monitored over time. The relation between the current and the diffusion coefficient follows Sand's law [52]:

$$i\sqrt{\tau} = 0.5\mathrm{nFC}_{\mathrm{RE^{n+}}}\mathrm{S}\sqrt{\pi \mathrm{D}_{\mathrm{RE^{n+}}}} \qquad (2\text{-}20)$$

in which τ is the transition time (when the concentration of electrolyzed species is equal to zero).

Figure 2-7 shows chronopotentiometry data for 3 wt% $LaCl_3$ in LiCl-KCl at 823 K with different magnitude of pulse current applied in the first 10 seconds. The method to determine the transition time from CP curves is indicated by the red dotted lines.

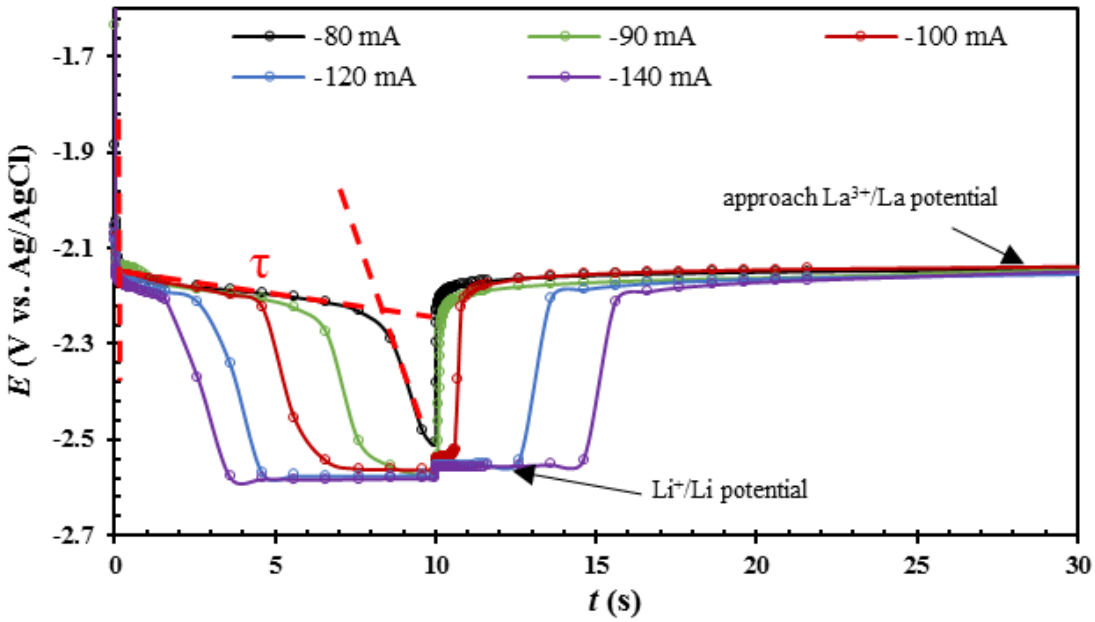

Figure 2-7: Chronopotentiometry for 3 wt% $LaCl_3$ in LiCl-KCl at 823 K with different magnitude of pulse current applied in the first 10 seconds.

2.1.2.4. Tafel method and liner polarization (LP) method

Exchange current density provides insight on the bonding and structure in REs and electrodes and are necessary for developing electrolysis model for molten salt recycle [53]. Under steady state, the current pass through the electrode surface is defined by Butler-Volmer equation based on the assumption of no mass-transfer effect [48]:

$$i = i_0\left\{\exp[\frac{(1-\alpha)nF}{RT}\eta] - \exp[\frac{-\alpha nF}{RT}\eta]\right\} \quad (2\text{-}21)$$

where i is current density (A cm^{-2}), α is charge transfer coefficient and η is overpotential $\eta = E - E^{eq}$. E is the potential applied and E^{eq} is the redox potential at equilibrium. For Tafel method, when η is sufficiently large, the second exponential term in Butler-Volmer equation can be ignored. The equation can then be simplified as:

$$\ln(i) = \ln(i_0) + \frac{\alpha nF}{RT}\eta \quad (2\text{-}22)$$

Hence, linear relation between η and $\ln(i)$ can be observed in Tafel plot when η is high. The exchange current density can be calculated by fitting linear Tafel region and calculating its intercept at zero overpotential. Figure 2-8(a) shows the linear Tafel region of 9 wt% $GdCl_3$ at 773 K. All Tafel plots in our experiment are swept from -300 mV relative to equilibrium potential to at least 120 mV relative to equilibrium potential. The scan rate is set to 5 mV and 10 mV to minimize the mass transfer effect while avoiding significant electrode area

growth during the process. As shown in Figure 2-8(a), by extending the linear Tafel region into 0 overpotential, the corresponding current is the exchange current density.

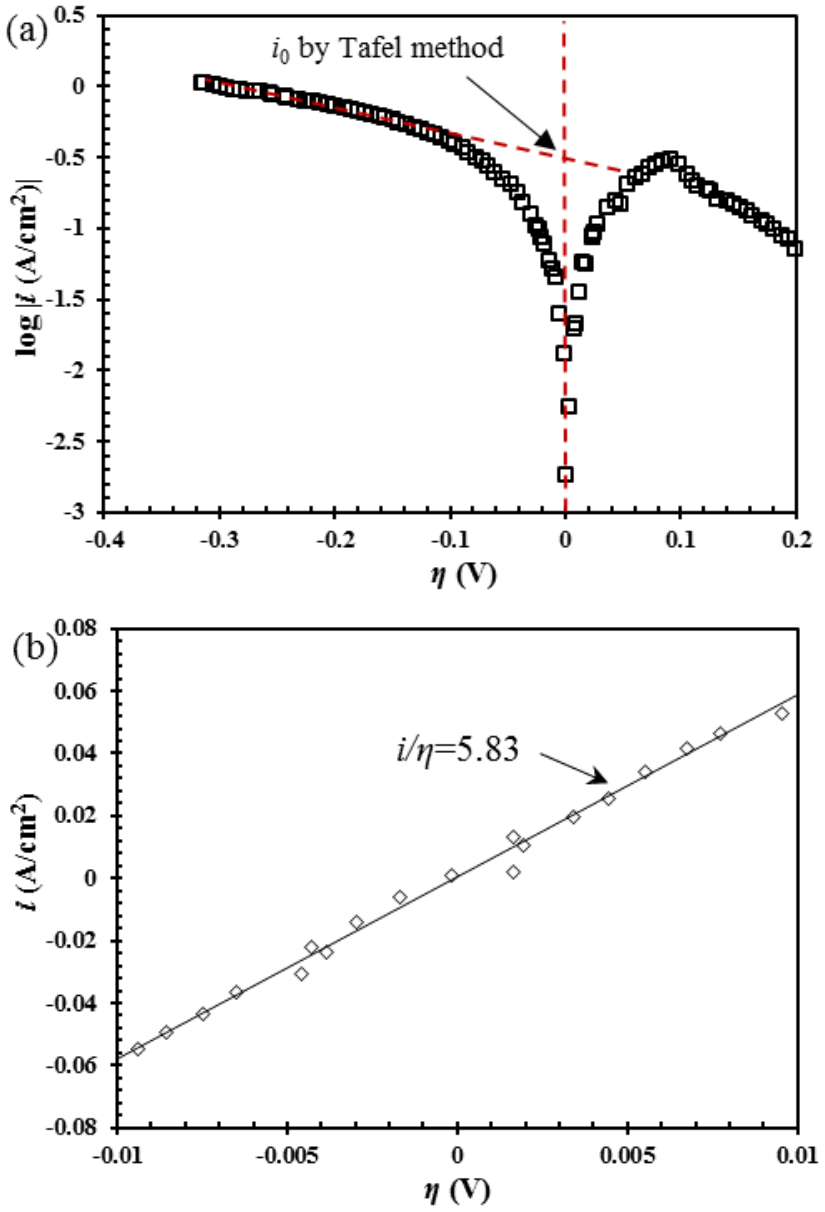

Figure 2-8: (a) Tafel Method and (b) LP method to determine exchange current density from polarization data measured at LiCl-KCl-9 wt% $GdCl_3$ at 773 K.

Linear polarization is another method that is derived from Butler-Volmer equation. By applying small overpotential, Butler-Volmer equation can be simplified by Tyler expansion:

$$i = i_0 \frac{nF}{RT}\eta \tag{2-23}$$

where η/i is defined as the charge transfer resistance R_{ct}.

With R_{ct} obtained through the slope of potential-current plot, the exchange current density can be determined quickly. In this work, potential-current data from CV and potentiodynamic polarization results at small overpotentials were analyzed by the linear polarization method. Figure 2-8(b) shows an example of using LP method to obtain charge transfer resistance from polarization data in LiCl-KCl containing 9 wt% $GdCl_3$ at 773 K.

2.1.2.5. Electrode kinetic simulation method

In conventional methods, both Tafel method and linear polarization assume no mass transfer effect during experiment. In fact, an electrode reaction involves the charge transfer process at the electrode-electrolyte interface and the mass transfer process of the reactant and product to/away from the electrode surface. In some cases, the electrode reaction rate can be significantly influenced by the mass transfer process, for example, the electrodeposit of RE from molten LiCl-KCl eutectic.

For the electrode reaction $\mathrm{RE} \leftrightarrow \mathrm{RE}^{3+} + 3\mathrm{e}^{-}$, the current density corresponding to the forward reaction rate and the backward reaction rate can be written as:

$$i_a = nFk_aC_{RE} \tag{2-24}$$

$$i_c = -nFk_cC^s_{RE^{3+}} \tag{2-25}$$

where i_a and i_c are the anodic current density and cathodic current density respectively; F is the Faraday constant, 96485 C/mol; k_a and k_c are the reaction rate constant respectively, cm/s; $C^s_{RE^{3+}}$ is the concentration of RE^{3+}at the electrode surface, mol/cm^3; C_{RE} can be set to unity for pure RE or W electrode with fully covered RE.

The reaction rates constant k_a and k_c are dependent on the electrode potential E [54]:

$$k_a = k^0 \exp\left[\frac{n(1-\alpha)F}{RT}(E - E^{0\prime})\right] \tag{2-26}$$

$$k_c = k^0 \exp\left[-\frac{n\alpha F}{RT}(E - E^{0\prime})\right] \tag{2-27}$$

where k^0 are the standard reaction constant that is independent of potential; α is the charge transfer coefficient; E and $E^{0\prime}$ are the electrode potential and the formal standard potential respectively, V;

Therefore, the relation of overall current density i with electrode potential E can be expressed as:

$$i = i_a + i_c = nFk^0\left\{\exp\left[\frac{(1-\alpha)nF}{RT}\left(E - E^{0\prime}\right)\right] - C^s_{RE^{n+}}\exp[\frac{-\alpha nF}{RT}(E - E^{0\prime})]\right\} \tag{2-28}$$

Given the definition of i_0:

$$i_0 = i_a^{eq} = i_c^{eq} = nFk_a^{eq} = nFk_c^{eq} C_{RE^{n+}}^b \quad (2\text{-}29)$$

where superscript 'eq' represents at equilibrium potential; $C_{RE^{3+}}^b$ is the concentration of Gd^{3+}in the bulk electrolyte, mol/cm^3.

Equation (2-28) can be rewritten in the form of Butler-Volmer equation:

$$i = i_0 \left\{ \exp[\frac{(1-\alpha)nF}{RT}\eta] - \frac{C_{RE^{n+}}^s}{C_{RE^{n+}}^b} \exp[\frac{-\alpha nF}{RT}\eta] \right\} \quad (2\text{-}30)$$

where overpotential $\eta = E - E^{eq}$

At any potential, the net current density i equals the diffusion current of RE^{3+} from bulk solution to the electrode surface. Hence, i can also be calculated by equation (2-31) based on the Nernst diffusion layer model, and the limiting current density i_L can be expressed by (2-32) [54].

$$i = -nFD \frac{C_{RE^{n+}}^b - C_{RE^{n+}}^s}{\delta} \quad (2\text{-}31)$$

$$i_L = -nFD \frac{C_{RE^{n+}}^b}{\delta} \quad (2\text{-}32)$$

where D is the diffusion coefficient of RE^{n+}, cm^2/s; δ is the diffusion layer thickness defined by the Nernst diffusion layer model, cm. Combination of equations (2-31)and (2-32) yields [54]:

$$\frac{C_{RE^{3+}}^s}{C_{RE^{3+}}^b} = 1 - \frac{i}{i_L} \quad (2\text{-}33)$$

Then (2-30) can be transformed by substitution of $C_{RE^{n+}}^s / C_{RE^{n+}}^b$ from (2-33):

$$i = \frac{i_0 \left\{ \exp[\frac{(1-\alpha)nF}{RT}\eta] - \exp[\frac{-\alpha nF}{RT}\eta] \right\}}{1 - \frac{i_0}{i_L} \exp[\frac{-\alpha nF}{RT}\eta]} \quad (2\text{-}34)$$

If the current density can be measured at various overpotential, the exchange current density i_0 can be obtained by fitting the measured current-overpotential curve using equation (2-34). In this study, the current-potential relation was measured by the potentiodynamic polarization in which the potential of the working electrode is varied at a certain scan rate and the external current is measured at each potential. However, the measured external current is composed of not only Faraday current but also the charging current. In a potentiodynamic polarization experiment, the continuous change of potential leads to the flow of the charging current. The charging current density is proportional to the production of the scan rate and the capacitance of the electrical double layer at the electrode surface. The charging current density can be estimated by the current plateau before the reduction peak. As shown in the zooming in plot, the charging current density increases with the scan rate, and the magnitude of the charging current density is less than 1 mA/cm^2 at scan rates up to 140 mV/s. Although the magnitude of charging current shows increasing tendency with decreasing potential (about 0.2 mA/cm^2 per 0.3V), the charging

current density is unlikely to be higher than 2 mA/cm^2 in the potential region where reduction of Gd^{3+} to Gd occurs.

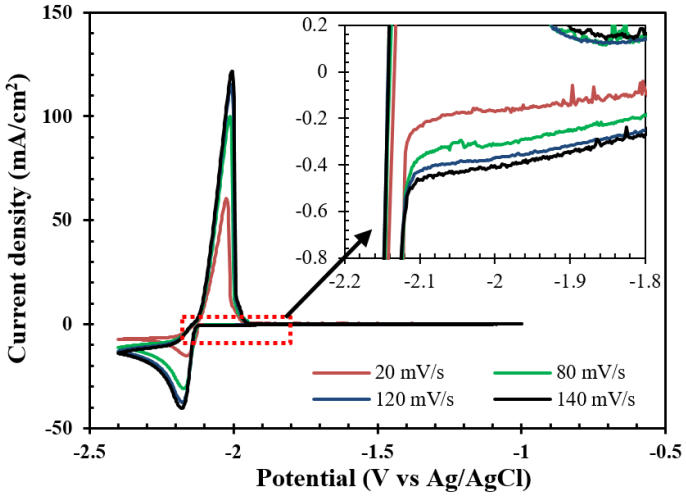

Figure 2-9: Cyclic voltammograms at tungsten electrode in LiCl-KCl eutectic containing 1 wt% $GdCl_3$ at 450°C [55].

2.1.2.6. Electrochemical impedance spectroscopy

EIS is shown to be one of the most promising technique to determine the charge transfer resistance and exchange current density of inner transition metals in LiCl-KCl salt [56,57]. One of the advantages of EIS is the ability to distinguish the impedance related to the charging and discharging process on the double layer, the charge transfer process, and the mass transfer process. During EIS measurements, the impedance of the cell is measured at a wide range of frequency. The measured impedance spectra provide insight on diffusion, kinetics, double layer and reactions at the electrode surface [58]. To perform EIS measurement with inert tungsten electrode, a method that applies minimum overpotential to the working electrode is proposed by previous research and has shown success on both Ce^{3+}/Ce and U^{3+}/U in LiCl-KCl salt [56,57]. The minimum overpotential for Gd^{3+}/Gd is determined by applying different potential along with a small alternative potential to the electrode as shown in Figure 2-10 (a).

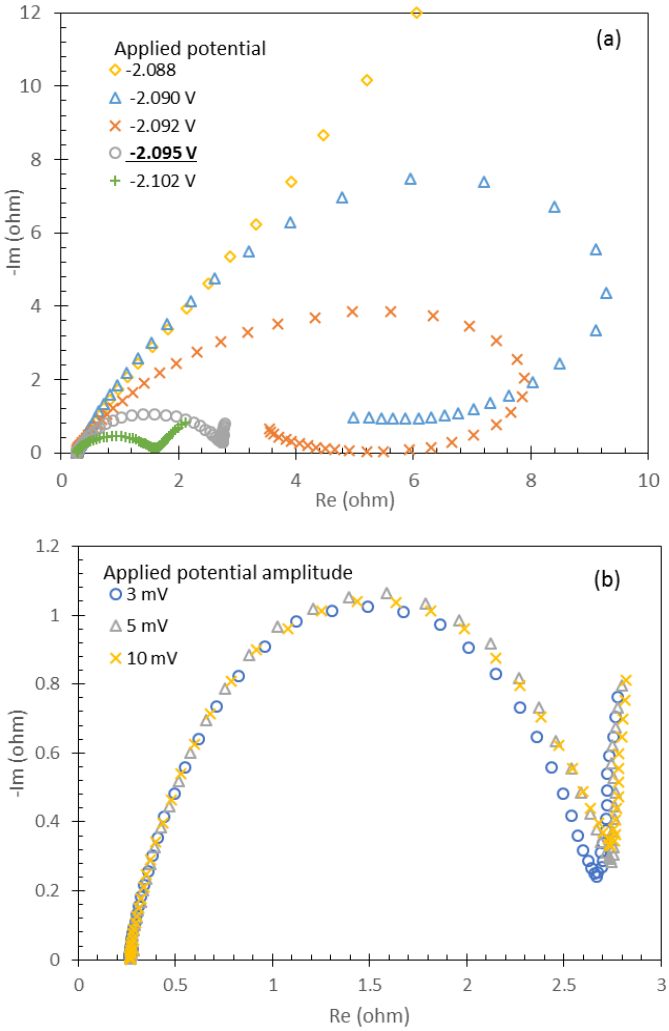

Figure 2-10: (a) Nyquist plots measured from 1 wt% $GdCl_3$ in LiCl-KCl salt at 773 K. Different potential ranging from -2.090 to -2.102 is applied to determine the minium overpotential. (b) Nyquist plots measured from 1 wt% $GdCl_3$ in LiCl-KCl salt at 773 K. Different potential amplitude is applied at the minimum over potential.

In Figure 2-10(a), before the potential reaches -2.095 V versus Ag/AgCl reference electrode, the impedance increases significantly at low frequency (right end of the impedance spectra) due to the difficulty of Gd^{3+} ions transfer to the electrode. As the applied potential decreases to -2.095 V, the energy of the electrons at the electrode surface gets high enough to occupy the Gd^{3+} ions vacant state in LiCl-KCl salt for reduction. This results in the presence of a steep Warburg diffusion impedance slope in low-frequency region on the impedance spectra. As the potential continues to decrease, the angle of the Warburg slope becomes smaller, indicating it's easier for Gd^{3+} to diffuse to the electrode. Applied potential at -2.095 is selected as the minimum overpotential to ensure the linear current response to applied potential. In Figure 2-10(b), different amplitude of alternative potential is applied for stable measurement verification purposes; the results show good agreement between each other.

All EIS measurements are carried out with the frequency from 50 kHz to 0.1 Hz. At each concentration and temperature combination, measurements are repeated two to four times to ensure reproducibility with the same experimental initial condition, and the standard deviation is reported in the figures as error bar. The impedance spectra is fitted to an equivalent circuit proposed by previous research as shown in Figure 2-11 [57] to determine the charge transfer resistance. In the circuit, R_s is the solution resistance and R_{ct} represents the charge transfer resistance. Constant phase element CPE_{dl} accounts for the double-layer capacitance which behaves as an imperfect capacitor. The diffusion related resistance is modeled by CPE_{diff} and Warburg impedance W in parallel.

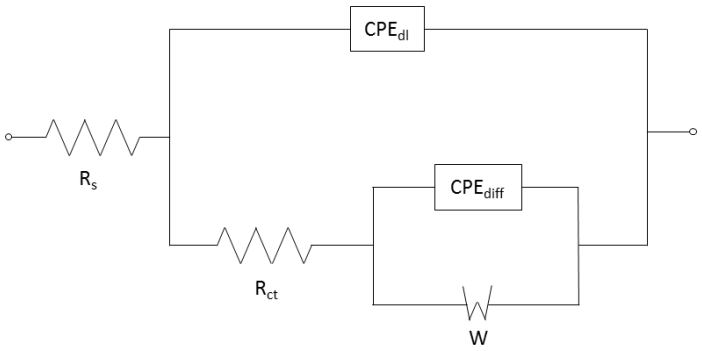

Figure 2-11: The equivalent circuit of the electrochemical cell. Including solution resistance, charge transfer resistance, CPE for double-layer capacitance and Warburg impedance for diffusion related resistance [57].

The fitting is carried out by Gamry Echem Analyst software with its auto fit feature using simplex method, the parameters obtained are then manually adjust to minimize relative error between each measurement. Based on the fitting results, the charge transfer resistance (Rct) is obtained and can be further used for exchange current density (i_0) calculation using the following equation [48]:

$$R_{ct} = \frac{RT}{nFi_0} \tag{2-35}$$

where R is the universal gas constant (J mol^{-1} K^{-1}), T is the absolute temperature (K), n is the number of electrons transferred, F is Faraday constant (C mol^{-1}). In Figure 2-12, it is showed that the impedance spectra of $GdCl_3$ can be fitted by the proposed equivalent circuit easily. However, it is found that the impedance spectra of $LaCl_3$ consistently behaves in a different way where neither a capacitor nor imperfect capacitor can fit the semi-circle part of the impedance spectra. Consequently, the impedance spectra is fitted with a 2^{nd} order polynomial equation to estimate the solution resistance and charge transfer resistance. Another useful information that can be obtained from EIS is the solution resistance which can be used for IR-drop compensation during other electrochemical measurements such as CV.

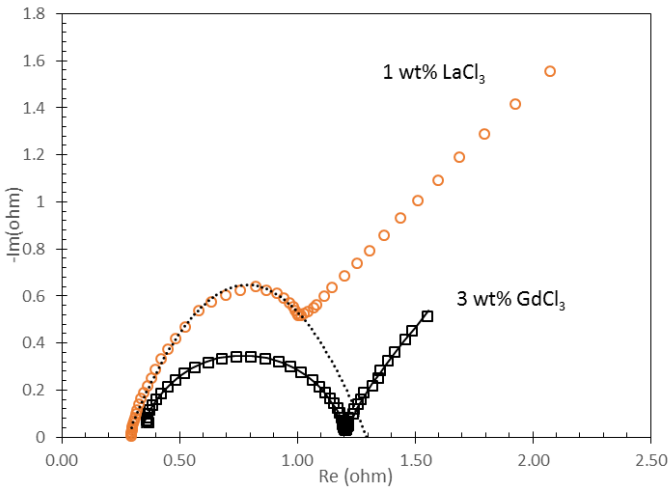

Figure 2-12: Impedance spectra of 1 wt% LaCl3 at 773 K and 3 wt% GdCl3 at 748 K.

2.2. Lanthanum property in LiCl-KCl eutectic salt

2.2.1. Thermodynamics and transport properties of $LaCl_3$ in LiCl-KCl

CV is selected as the primary method to determine the thermodynamics and transport properties of $LaCl_3$ in LiCl-KCl salt. Tests were performed at 723 K, 773 K, and 823 K at 3 wt% and 6 wt% and 9 wt% of $LaCl_3$. The concentrations of $LaCl_3$ in several salt samples were examined by ICP-MS.

Table 2-1: Electrolyte concentration of each sample.

Experiment	Prepared Concentration (wt%)	ICP-MS (wt%)	Mole cm^{-3}
1 wt% $LaCl_3$	1	1.108	7.491×10^{-5}
3 wt% $LaCl_3$	3	2.787	1.902×10^{-4}
6 wt% $LaCl_3$	6	5.862	4.075×10^{-4}

Before the experiment, a quick SWV is performed and the number of electron transfer in the reaction is calculated as 3.02, which agrees well with literature. For CV, the reversibility at different scan rate is tested and the current versus square root of scan rate at three different concentration is summarized in Figure 2-13, Figure 2-14, and Figure 2-15.

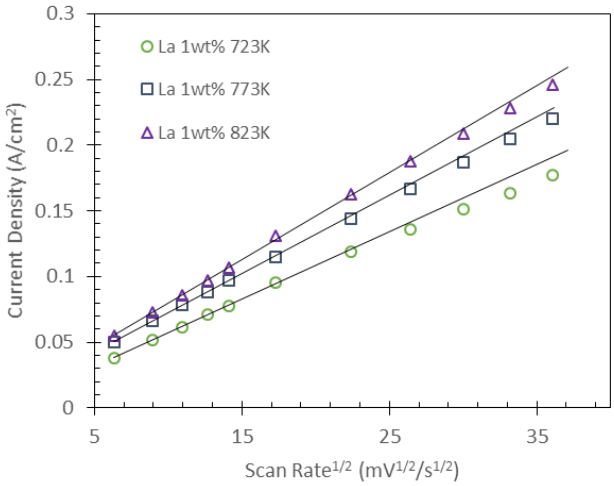

Figure 2-13: 1 wt% $LaCl_3$ in LiCl-KCl salt CV cathodic peak current density versus square root of scan rate.

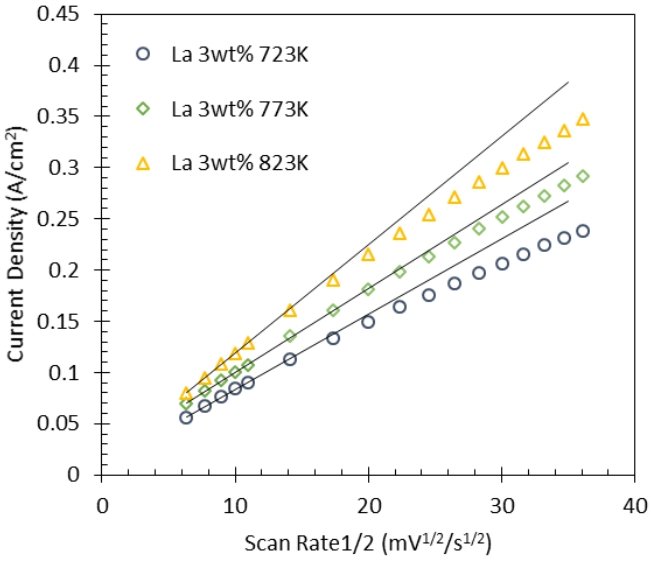

Figure 2-14: 3 wt% $LaCl_3$ in LiCl-KCl salt CV cathodic peak current density versus square root of scan rate.

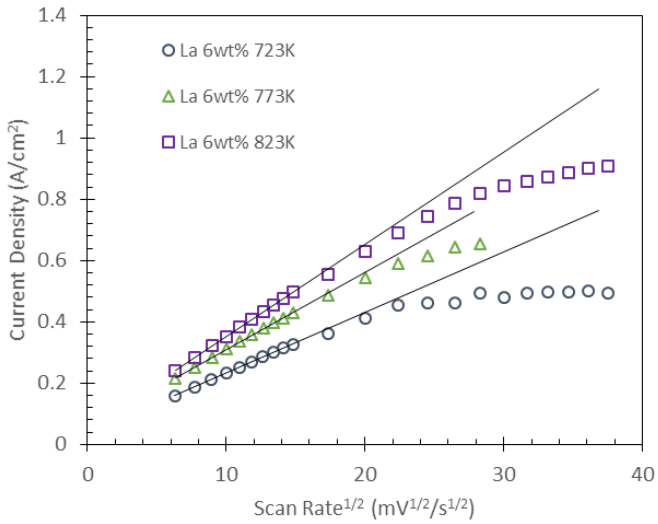

Figure 2-15: 6 wt% $LaCl_3$ in LiCl-KCl salt CV cathodic peak current density versus square root of scan rate.

The reversibility of the reaction can be observed from each of the curves. When scan rate is higher than 400 mV/s, the peak current density drops below the predicted dotted line, indicating that at a higher scan rate, the reaction shifted from quasi-reversible reaction to irreversible reaction. Another observation based on the three figures above is that the current density of higher concentration $LaCl_3$ shifts to the irreversible region at lower scan rates compare with low $LaCl_3$ concentration.

The reversibility of the reaction at different scan rate can also be checked by the Matsuda and Ayabe criteria [59]. It was shown that the reversibility of a reaction could be categorized into reversible, quasi-reversible and irreversible reaction depending on its reversibility parameter Λ where

Reversible $$\Lambda = \frac{k_0}{(DnvF/RT)^{1/2}} \geq 15 \quad (2\text{-}36)$$

Quasi-reversible $$10^{-2(1+\alpha)} < \Lambda = \frac{k_0}{(DnvF/RT)^{1/2}} \leq 15 \quad (2\text{-}37)$$

Irreversible $$\Lambda = \frac{k_0}{(DnvF/RT)^{1/2}} \leq 10^{-2(1+\alpha)} \quad (2\text{-}38)$$

The reversibility at different scan rate is calculated and the values are between 0.00756-0.02 for scan rates between 40 mV/s and 500 mV/s where the reversibility value Λ is considered quasi-reversible between 0.002 and 15. Apparent potential of La^{3+}/La can be obtained from CV. The calculated apparent potential of La^{3+}/La and activity coefficient are summarized in Table 2-2.

Table 2-2: Thermodynamics data of La in LiCl-KCl salt at different concentration and temperature.

Temperature (K)	Apparent potential	Activity coefficient
1 wt%		
723 K	-3.189±0.063	2.402×10^{-4}
773 K	-3.144±0.061	1.906×10^{-4}
823 K	-3.102±0.048	1.319×10^{-4}
3 wt%		
723 K	-3.200±0.075	1.414×10^{-4}
773 K	-3.151±0.053	1.391×10^{-4}
823 K	-3.112±0.047	8.642×10^{-5}
6 wt%		
723 K	-3.210±0.060	8.738×10^{-5}
773 K	-3.176±0.058	4.511×10^{-5}
823 K	-3.140±0.051	2.644×10^{-5}

In our results, apparent potential shows a linear relation with both concentration and temperature. As the concentration increases, the apparent potential decreases, resulting in lower activity coefficient. We are expecting ionic strength of the solution to change as more $LaCl_3$ is added into the salt and eventually the activity will approach 1 since in pure $LaCl_3$, the activity is always going to be 1. However, this is not the case at the concentration range of 1-6 wt%. The concentration dependence of the apparent potential is compared with reference and the overall trend agrees well as the apparent potential decreases with concentration in this concentration interval as shown in Figure 2-17.

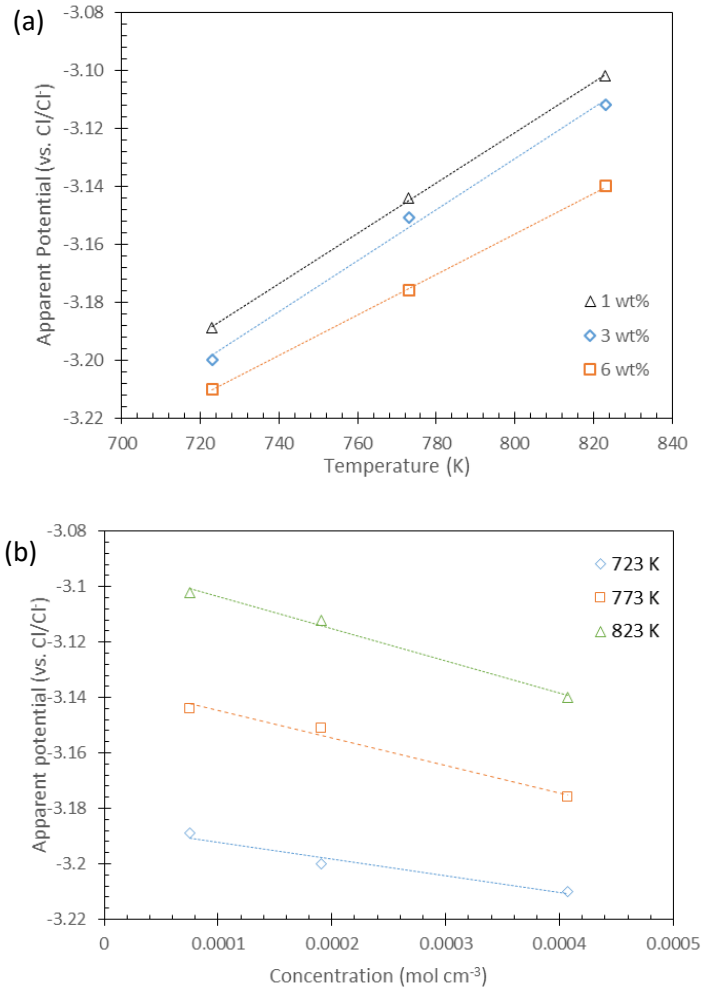

Figure 2-16. (a) Apparent potential of La^{3+}/La in LiCl-KCL salt as a function of temperature. (b) Apparent potential of La^{3+}/La in LiCl-KCL salt as a function of concentration.

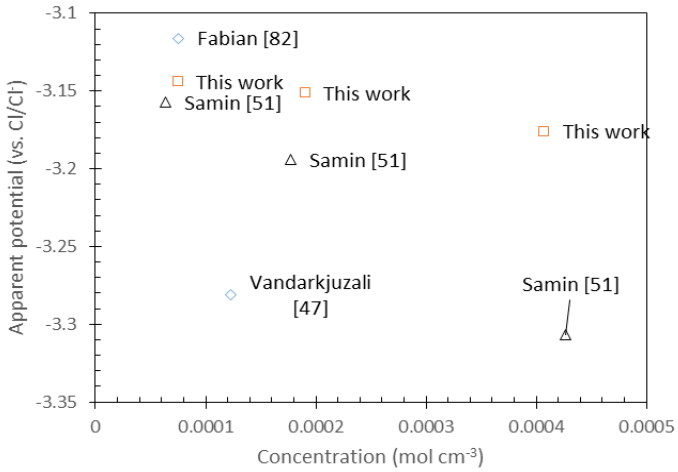

Figure 2-17: Apparent potential of La/La^{3+} at 773 K with different concentration.

Now we turn our attention to diffusion coefficient of La^{3+} in LiCl-KCl salt. Figure 2-18 and Table 2-3 show the diffusion coefficient obtained from CV quasi-reversible region using both Berzins-Delahay equation and BET model. In Figure 2-18, the biggest difference between traditional CV analysis and BET model at 1 and 3 wt% $LaCl_3$ where the 18.8% at 1 wt% and 37% at 3 wt%. At 6 wt% $LaCl_3$, up to 61% difference is found. In traditional CV analysis, it is assumed that the reaction is reversible. However, all experiments reversibility parameter is considered close to irreversible region. While in BET model, the analysis accounts the kinetic of the reaction and doesn't have to take the reversibility of the reaction into account. In later analysis on Gd, Gd is at the closer end to reversible reaction, hence, conventional analysis and BET model agrees well.

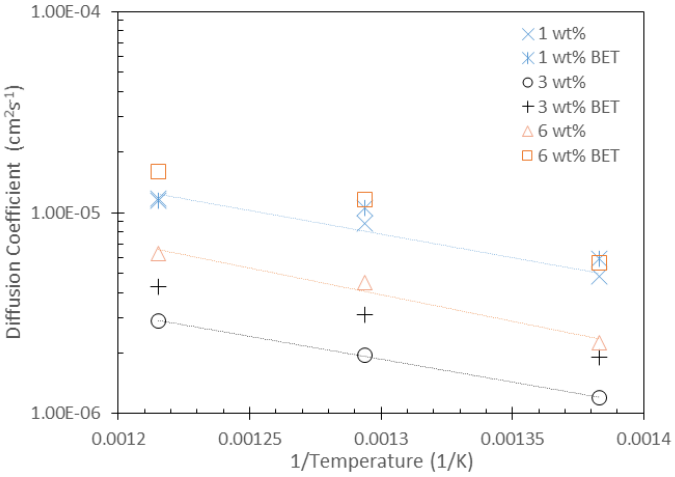

Figure 2-18: Diffusion coefficient of 1, 3, 6wt% $LaCl_3$ in LiCl-KCl salt at different temperature from both traditional analysis and BET model analysis.

Table 2-3: Diffusion coefficient of La^{3+} in LiCl-KCl salt at different concentration and temperature.

Temperature (K)	Diffusion Coefficient ($10^5 cm^2 s^{-1}$) from Berzins-Delahay	Diffusivity from BET model
1 wt%		
723 K	0.479±0.009	0.59±0.009
773 K	0.883±0.017	1.05±0.018
823 K	1.179±0.029	1.15±0.029
3 wt%		
723 K	0.12±0.002	0.19±0.003
773 K	0.195±0.002	0.31±0.004
823 K	0.289±0.007	0.43±0.008
6 wt%		
723 K	0.225±0.006	0.56±0.012
773 K	0.446±0.012	1.16±0.022
823 K	0.623±0.010	1.59±0.026

The diffusion coefficient is also examined by a series of CC experiments with different step voltage. The diffusion coefficients obtained are as shown in Figure 2-19. In Figure 2-19, a sudden drop of the diffusion coefficient is observed at the step down voltage of -2.2V. Considering the results obtained by CV, the step down voltage of CV tests cannot be above -2.2 V. In Figure 2-19, the cutting edge is found to be roughly equal to the cathodic peak potential location when CV is performed. This will serve as our diffusion coefficient selection criteria when looking for diffusion coefficient from CC. Diffusion coefficient calculated from CC is summarized in Table 2-4.

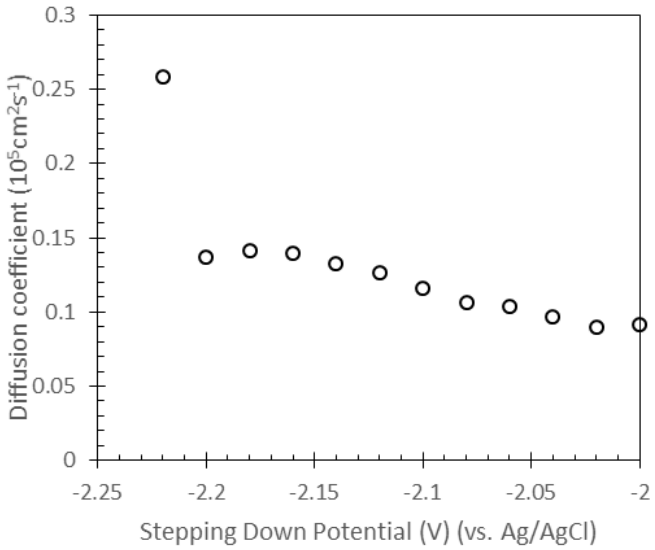

Figure 2-19: La Diffusion coefficient at 723 K obtained from Chronocoulumetry with different stepping down potential.

Table 2-4: Diffusion Coefficient of La in LiCl-KCl using chronocoulummetry.

Diffusion Coefficient (10^5 $cm^2 s^{-1}$)			
wt% \T (K)	**723**	**773**	**823**
1	0.805	1.69	2.58
3	0.070	0.131	0.097
6	0.107	0.151	0.267

Chronopotentiometry was also performed at 1 wt% and 3 wt% $LaCl_3$ at 723 K, 773 K, and 823 K. The transition time at various magnitude of current was determined and plotted against the current, as shown in Figure 2-20. Linear relationship of I versus $\tau^{-1/2}$ is observed and the diffusion coefficients can be calculated based on the slope using Sand's equation. The calculated diffusion coefficients are summarized in

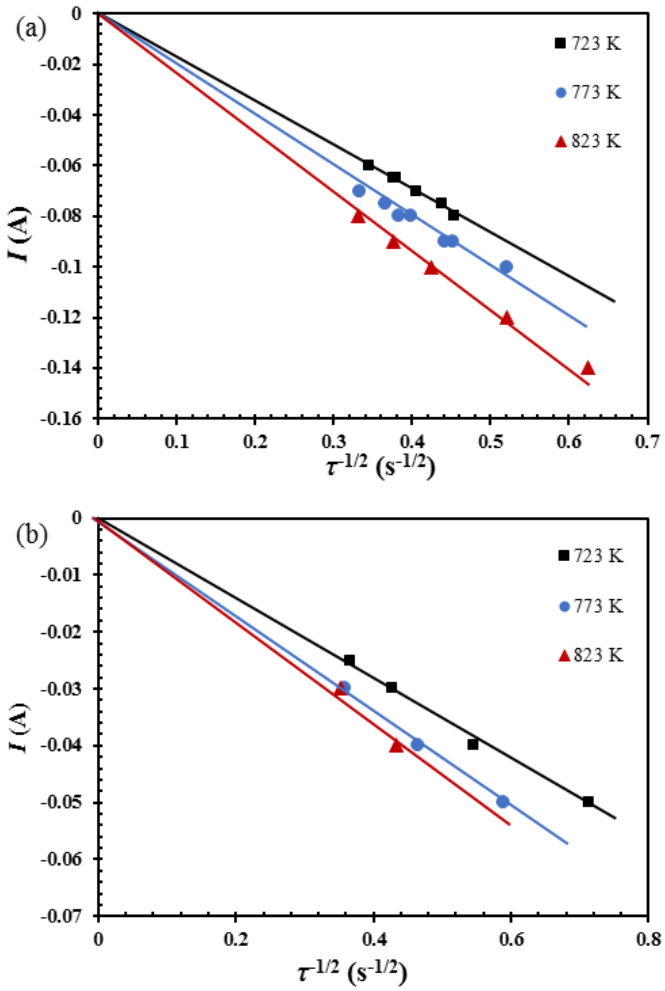

Figure 2-20: Linear relationship of I versus $\tau^{-1/2}$ for the chronopotentiometric data obtained at (a) 3 wt% $LaCl_3$ and (b) 1 wt% $LaCl_3$ in LiCl-KCl

Table 2-5: Diffusion Coefficient of La in LiCl-KCl using chronopotentiometry.

Diffusion Coefficient (10^5 cm^2s^{-1})			
wt% \T (K)	**723**	**773**	**823**
1	1.28	2.03	2.33
3	0.919	1.24	1.73

Based on CC and CP results, the trend of diffusion coefficient agrees with diffusion coefficient measured from CV where a local minimum diffusion coefficient exist between 1 and 6 wt% La, the diffusion coefficient of La at 723 K is shown in Figure 2-21 compares the diffusion coefficient at 723 K with previous research results [22,60,61] at different concentrations. In Figure 2-21, the overall trend is that the diffusion coefficient decreases as concentration increases. However, it is relatively hard to develop relation for concentration and diffusion coefficient.

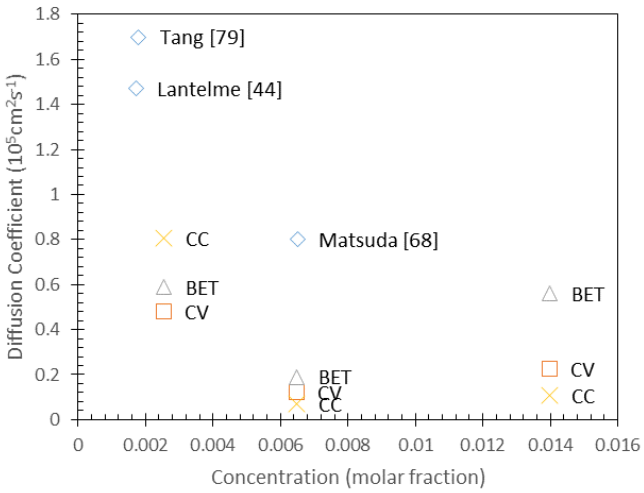

Figure 2-21: Diffusion coefficient of La in LiCl-KCl at 723 K with different methods. For diffusion coefficient obtained from CC, the step potentials are -3.327, -3.329 and -3.331 vs Cl_2/Cl^- low concentration to high concentration.

2.2.2. Exchange current density of La^{3+}/La in LiCl-KCl

2.2.2.1. EIS method

Due to the significant difference of impedance response to frequency, the proposed equivalent circuit did not fit well with the experiment especially on the double-layer capacitance part. As a consequence, the Nyquist plot is fitted by a second order polynomial equation to estimate both the solution resistance and the charge transfer resistance as shown in Figure 2-22. The exchange current density is summarized in Figure 2-23 with respect to temperature and concentration ($LaCl_3$ molar fraction). Overall, i_0 shows a positive linear relation with both temperature and concentration ranging from 0.0093 A cm^{-2} to 0.0789 A cm^{-2} with the highest relative standard deviation being 9.3%.

The solution resistance obtained from the fitting is also summarized in Table 2-6. The solution resistance is found to decrease as $LaCl_3$ concentration increases.

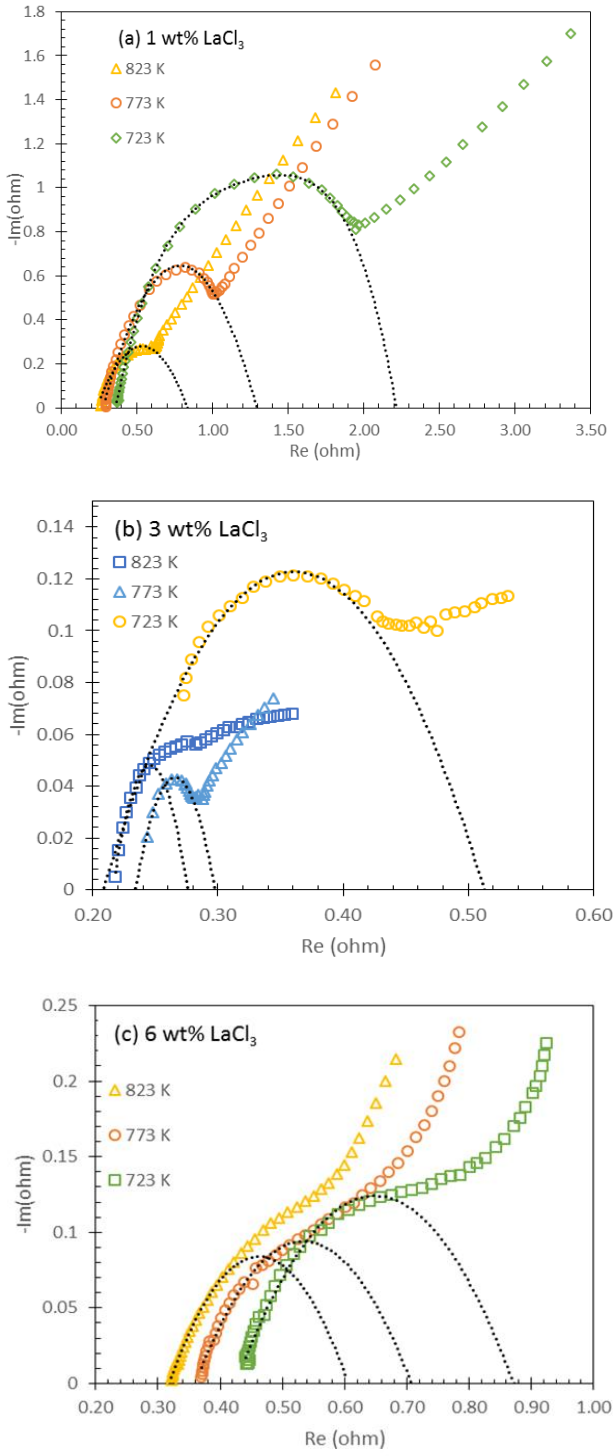

Figure 2-22: (a) Impedance spectra and the fitting results for 1 wt% $LaCl_3$ in LiCl-KCl salt. Electrode area is 1.056 cm^2. (b) Impedance spectra and the fitting results for 3 wt% $LaCl_3$ in LiCl-KCl salt. Electrode area is 1.734 cm^2 (c) Impedance spectra and the fitting results for 6 wt% $LaCl_3$ in LiCl-KCl salt. Electrode area is 0.503 cm^2.

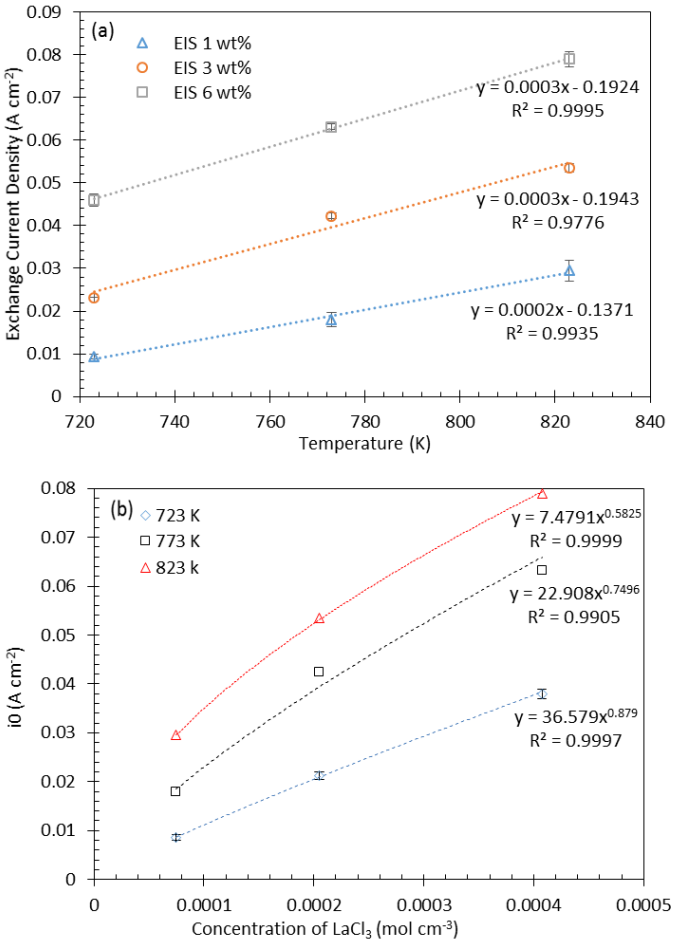

Figure 2-23: (a)Exchange current density (i_0) of La/$LaCl_3$ against temperature at different concentration. (b)Exchange current density (i_0) of La/$LaCl_3$ against concentration at 723, 773 and 823 K. The data are obtained from EIS.

Table 2-6: Solution resistance at different temperature and concentration.

Solution Resistance (ohm cm²)			
	1 wt%	**3 wt%**	**6 wt%**
723 K	0.3990	0.3676	0.2221
773 K	0.3113	0.3832	0.1869
823 K	0.2786	0.4248	0.1618

2.2.2.2. Tafel method

Figure 2-24 shows the linear Tafel region of 1 wt% $LaCl_3$ at different temperature. All Tafel plots are swept from -300 mV relative to equilibrium potential to at least 120 mV relative to equilibrium potential and the scan rate is set to 1 mV and 5 mV to minimize the mass

transfer effect while avoiding significant electrode area growth during the process. However, as the concentration of $LaCl_3$ increases, it becomes relatively hard to determine the linear region due to large amount of La deposition on to the electrode. Only measurements on 1 wt% $LaCl_3$ can yield consistent results as shown in Figure 2-25. The relative standard deviation are 11.9% at 723 K, 4.2% at 773 K and 6.0% at 823 K.

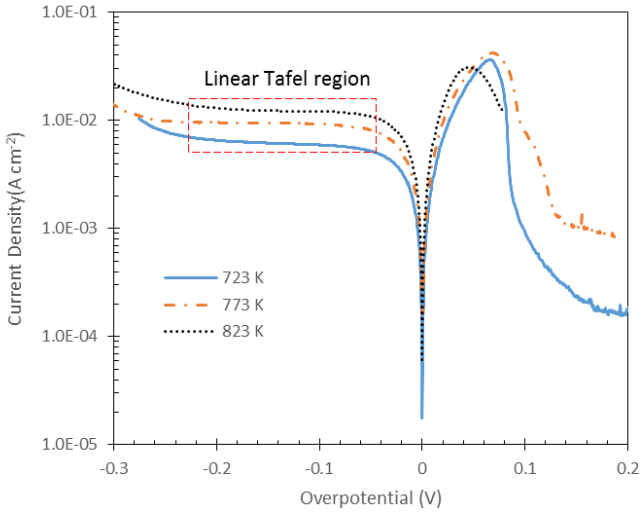

Figure 2-24: Tafel plot for 1 wt% LaCl3 at different temperature, scan rates: 5 mV/s.

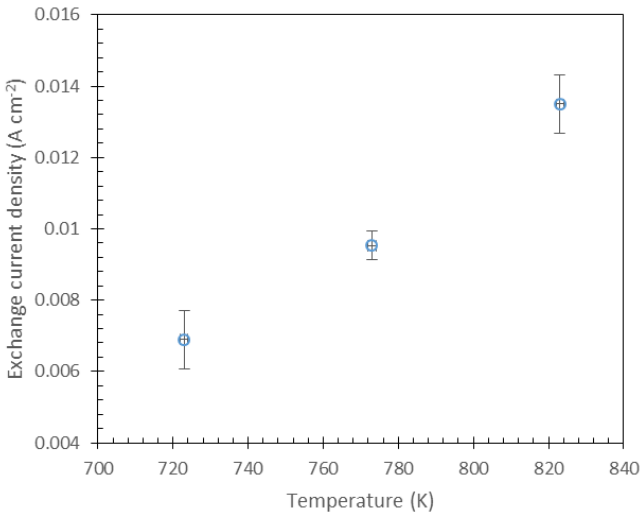

Figure 2-25: Exchange current density of 1 wt% $LaCl_3$ measured by Tafel method.

2.2.2.3. LP method using CV data

We then examine the exchange current density using LP method, and CV data at small overpotentials were used. Figure 2-26 shows how scan rate affects i_0 at different concentration. At all concentrations, no significant effect on i_0 is observed when scan rate is smaller than 100 mV/s. However, at higher scan rate, the increase in scan rate results in

higher i_0. The largest relative standard deviation of i_0 at different scan rate is observed at 1 wt% $LaCl_3$ with a value of 19.4% while the majority of errors are less than 4%.

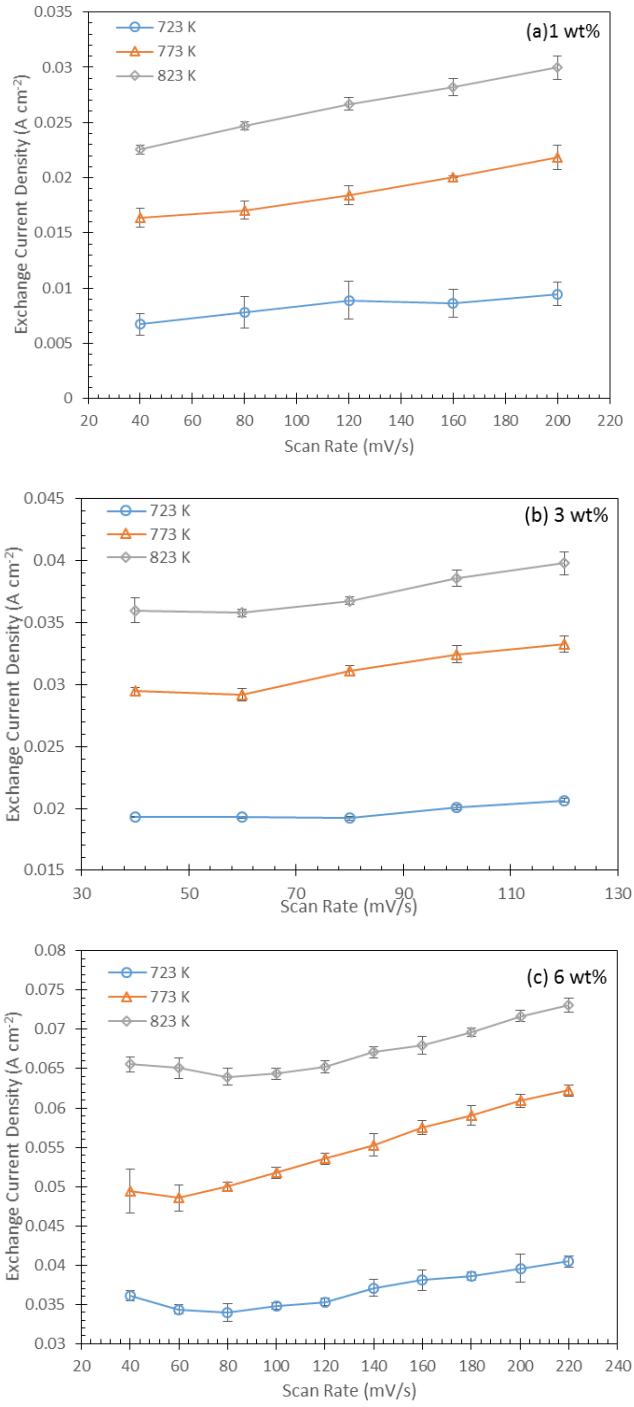

Figure 2-26: Analysis results of CV data using LP method. (a)Exchange current density (i_0) of 1 wt% $LaCl_3$ at different scan rate and temperature. (b)Exchange current density (i_0) of 3 wt% $LaCl_3$ at different scan rate and temperature. (c)Exchange current density (i_0) of 6 wt% $LaCl_3$ at different scan rate and temperature.

As stated in the previous part, the derivation of Butler-Volmer equation is based on no mass transfer effect. In the CV measurements, the scan rate is operated in the range that mass transfer cannot be ignored. As a consequence, in the later analysis, the exchange current density at lowest scan rate is selected. At lower concentration, i_0 shows linear relation with temperature and agrees well with i_0 measured from EIS method. Figure 2-27 summarized i_0 measured by LP method in terms of concentration. The results from this work is compared with i_0 reported by Tang el al. [62] at 2 wt% $LaCl_3$. Their LP analysis results were 0.023 A cm^{-2} (723 K), 0.034 A cm^{-2} (773 K), and 0.040 A cm^{-2} (823 K) on a Mo electrode. At the same concentration, our i_0 values as calculated from the correlations in Table 2-7 are 0.011 A cm^{-2} (723 K), 0.021 A cm^{-2} (773 K) and 0.028 A cm^{-2} (823 K) which are relatively low compared to results from Tang el al. [63]. This might result from the difference in electrode selection where tungsten electrode was used in this research instead of Mo.

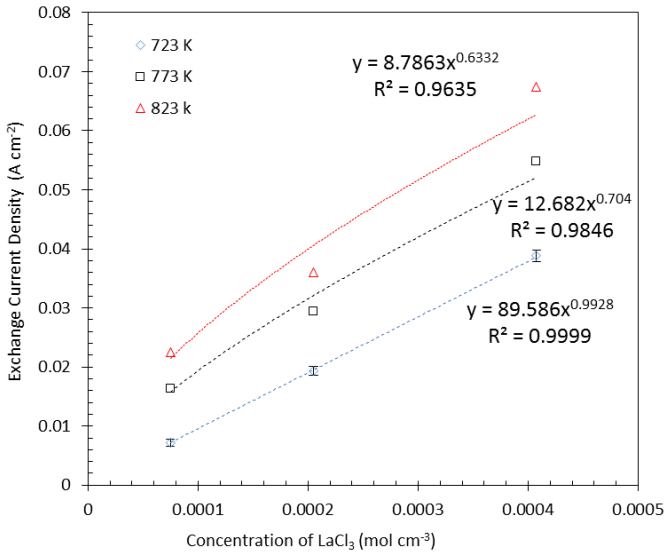

Figure 2-27: i_0 versus concentration (mol cm^{-3}) obtained by LP method at different temperature.

Table 2-7: Concentration and temperatue dependency obtained from LP method.

		Equation	R2
Temperature Dependence of i_0	1 wt% $LaCl_3$	1.40E-04 T – 9.37E-02	1
	3 wt% $LaCl_3$	2.35E-04 T - 1.47E-01	0.9800
	6 wt% $LaCl_3$	3.08E-04 T – 1.80E-01	0.9980
Concentration Dependence of i_0	723 K	39.77 $[C]^{0.8807}$	0.9953
	773 K	37.96 $[C]^{0.8284}$	0.9885
	823 K	19.93 $[C]^{0.7159}$	0.9975

*C is in mol cm^{-3}

2.2.2.4. Electrode kinetic simulation method

CV data are used for electrode kinetic model fitting. The data was selected in the range of -0.05 V to 0.08 V of ovepotential to fit for i_0 using (2-34). The optimization fitting was performed by iteration of the values of $\alpha, i_0,$ and i_L in the ranges of $0.01 \leq \alpha \leq 0.99$, $0.02i_{min} \leq i_0 \leq 10i_{min}$, and $i_{min} \leq i_L \leq 100i_{min}$, respectively. The curves calculated by the optimized parameters are shown in Figure 2-28, which shows good agreement with experimental data. If we evaluate the performance of the fitting using the average deviation $\frac{\sum_j^N |i_{exp} - i_{fit}/i_{fit}|}{N}$ where N is the number of fitted experimental data, the percent deviations for all tests are in the range of 2-8%. The values of i_0, α, and i_L obtained from the optimization fitting are listed in Table 2-8. For the tests with replicates, the average value and the corresponding standard deviation are reported. The optimization fitting for all test have a value of α ranging from 0.64 to 0.75, which is consistent.

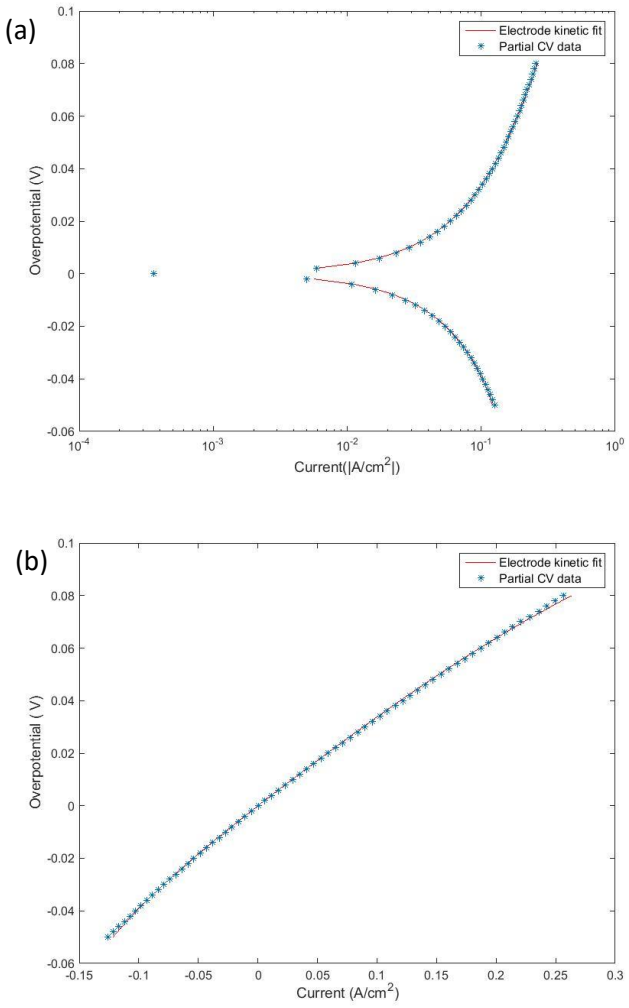

Figure 2-28: Electrode kinetic model fit on CV data, 823 K, 6 wt% $LaCl_3$.

Table 2-8: Parameters determined from optimization fitting of the CV curves.

Condition	i_0 (A/cm²)	α	i_L (A/cm²)	$\lvert i_L \rvert / i_0$
1 wt%, 723 K	0.0294 ± 0.00089	0.68 ± 0.021	-0.009 ± 0.0003	0.31
1 wt%, 773 K	0.0573 ± 0.00191	0.69 ± 0.023	-0.0193 ± 0.0006	0.34
1 wt%, 823 K	0.0705 ± 0.00312	0.64 ± 0.022	-0.0226 ± 0.0007	0.32
3 wt%, 723 K	0.0382 ± 0.00115	0.66 ± 0.021	-0.0341 ± 0.0010	0.89
3 wt%, 773 K	0.0671 ± 0.00185	0.73 ± 0.024	-0.0425 ± 0.0135	0.67
3 wt%, 823 K	0.0941 ± 0.00311	0.74 ±0.025	-0.0583 ± 0.0018	0.61
6 wt%, 723 K	0.0500 ± 0.00150	0.63 ±0.022	-0.1080 ± 0.0043	2.16
6 wt%, 773 K	0.0728 ± 0.00312	0.67 ± 0.021	-0.1217 ± 0.0061	1.67
6 wt%, 823 K	0.0996 ± 0.00299	0.69 ± 0.024	-0.2047 ± 0.0073	2.05

To validate the fitting results, it is necessary to consider the therotical correlation for the concentration dependence of i_0. As the exchange current density equals in magnitude to either the anodic or cathodic current density at equilibrium and $C^{\mathrm{s}}_{\mathrm{Re}^{n+}} = C^{\mathrm{b}}_{\mathrm{Re}^{n+}}$ at equilibrium potential, the exchange current density for RE^{n+}/Re can be expressed as $i_0 = nFk^0 C^{\mathrm{b}}_{\mathrm{Re}^{n+}} \exp[\frac{-\alpha nF}{RT}(E^{\mathrm{eq}} - E^*)]$ [54]. This combines with the Nernest equation $E^{\mathrm{eq}} = E^* + \frac{RT}{nF} \ln C^{\mathrm{b}}_{\mathrm{Re}^{n+}}$, yielding to the following correlation:

$$i_0 = nFk^0 C^{(1-\alpha)}_{\mathrm{Re}^{n+}} \tag{2-39}$$

where C is the concentration at the electrode surface in mol cm^{-3}.

The values of i_0 from Table 2-8 are plotted against concentration of $LaCl_3$ in mol/cm^3 at each temperature as shown in Figure 2-29. Instead of fitting the data with equation (2-39), we plotted the trend-line using average α value 0.68. As shown in Figure 2-29. The trend-line with $\alpha = 0.68$ agrees well with the experiment data at all temperature. The value of i_0 from experimental results is very sensitive to the coverage area of deposited La on the W electrode especially the experiment data is captured from CV with a scan rate of 40 mV/s. Although a full coverage of La is expected, the variety of the surface roughness of the deposited La layer and the accuracy of the W surface area measurement may still cause the deviation of current density from replicate tests. The value of k^0 in equation (2-39) can be calculated from the equations of the trend lines in Figure 2-29. The calculated k^0 are 1.89 × 10^{-6} cm/s at 723 K, 2.45 × 10^{-6} cm/s at 773 K, and 3.25 × 10^{-6} cm/s at 823 K. k^0 is showed to follow Arrhenius law as shown in Figure 2-30.

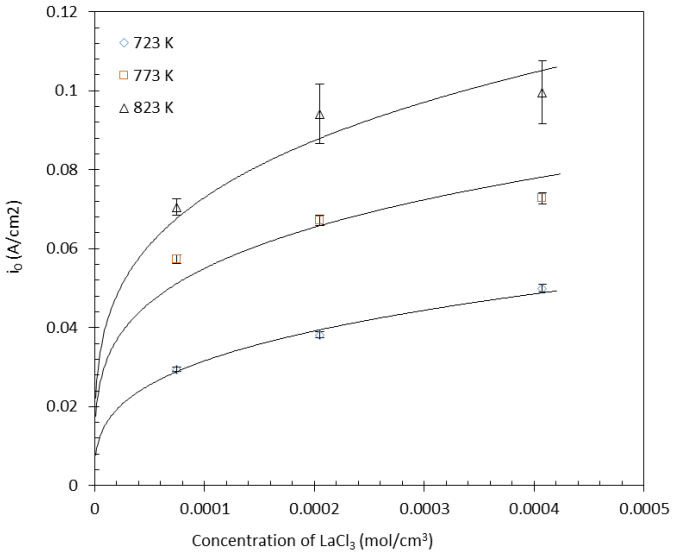

Figure 2-29: La exchange current density calculated from electrode kinetic model, the trend-line is plotted with $\alpha = 0.68$.

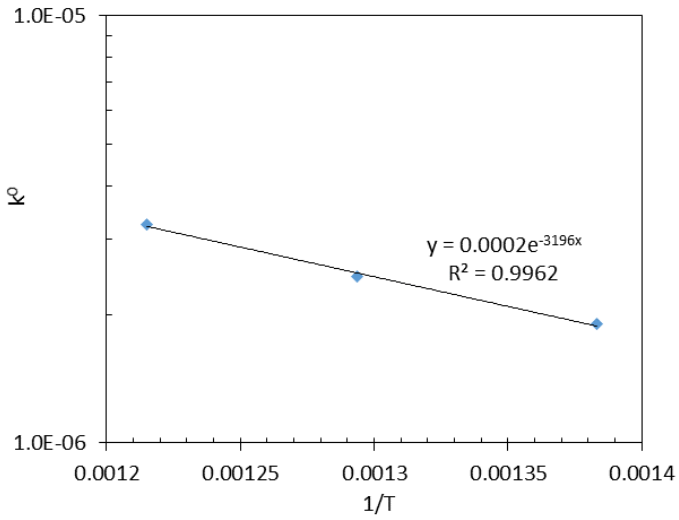

Figure 2-30: Temperature dependence of k^0 for La.

2.2.2.5. Comparison of results from different methods and discussion

The exchange current density of La/La^{3+} in LiCl-KCl were studied by EIS, Tafel, LP and electrode kinetic model at different temperature between 723 K to 823 K and concentration ranging from 1 wt% $LaCl_3$ to 6 wt% $LaCl_3$. The results at 723 K at different concentration is summarized in Figure 2-31. The i_0 measured by traditional methods agrees well within 25% relative difference from their average value. However, the concentration dependence observed from the traditional methods is inconsistent at various temperature. As indicated by the fitted power law equations in Figure 2-23 (b) and Figure

2-27, the corresponding α at 723 K, 773 K, and 823 K are 0.12, 0.25 and 0.42 for EIS and 0.01, 0.30, 0.37 for LP. In comparison, the results obtained from electrode kinetic simulation method show consistent α value at three temperatures and the concentration dependence agrees well with the theoretical equation (2-39).

It is also seen from Figure 2-31, the three traditional methods underestimate the exchange current density compared to the electrode kinetic model. It is important to know that in traditional methods, it is assumed that there is no mass transfer effect, indicating that the relation between limiting current and exchange current $|i_L|/i_0$ should approach infinite $|i_L|/i_0 \to \infty$. Figure 2-32 shows the $i-\eta$ curve becomes indistinguishable at $|i_L|/i_0$ above 100. Hence, at the ratios below 100, traditional method underestimates i_0. As seen in Table 2-8, the ratio of $|i_L|/i_0$ ranges from ~0.33 to ~ 2 with the increase in $LaCl_3$ concentration, which is all considered small. That is why the EIS and CV determined 'i_0' getting closer to the value of i_0 obtained from optimization fitting at higher concentration, as shown in Figure 2-31.

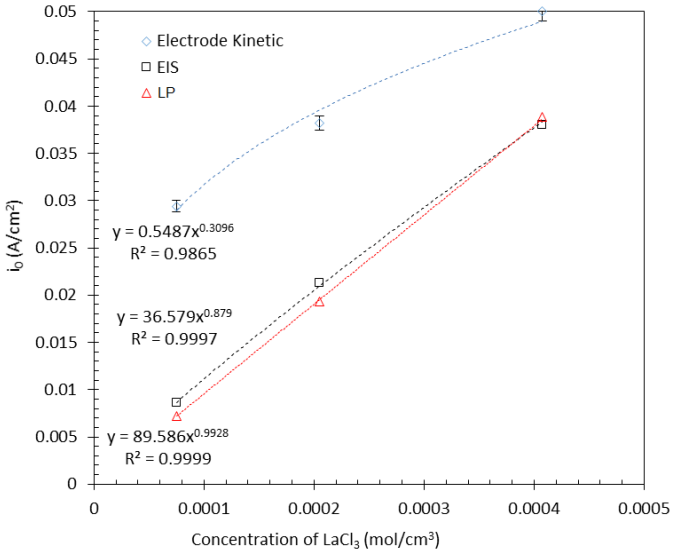

Figure 2-31: Exchange current density measured by different method at 723 K.

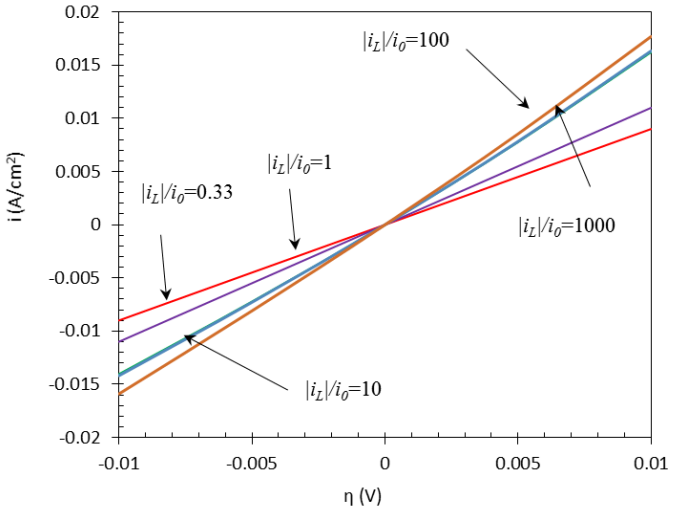

Figure 2-32: Errors of using LP method at different ratios of $|i_L|/i_0$. i_0 = 0.0573 A/cm², α = 0.68, T = 723 K.

2.3. Gadolinium property in LiCl-KCl eutectic salt

2.3.1. Thermodynamics and transport properties of $GdCl_3$ in LiCl-KCl

CV is selected as the primary method to determine the thermodynamics and transport properties of $GdCl_3$ in LiCl-KCl salt. Tests were taken at 723 K, 773 K, and 823 K at 1 wt%, 3 wt%, 6 wt%, and 9 wt% $GdCl_3$. The concentrations of $GdCl_3$ in several salt samples were examined by ICP-MS.

Table 2-9: Electrolyte concentration of each sample.

Experiment	Prepared Concentration (wt%)	ICP-MS (wt%)	Mole cm^{-3}
1 wt% $GdCl_3$	1	1.02	6.372×10^{-5}
3 wt% $GdCl_3$	3	3.01	1.912×10^{-4}
6 wt% $GdCl_3$	6	6.03	3.899×10^{-4}
9 wt% $GdCl_3$	9	9.02	5.967×10^{-4}

A quick SWV is performed and the number of electron transfer in the reaction is calculated as 2.97, which agrees well with literature. For CV, the reversibility at different scan rate is tested and the current versus square root of scan rate at three different concentration is summarized in Figures 2-33, 2-34, and 2-35.

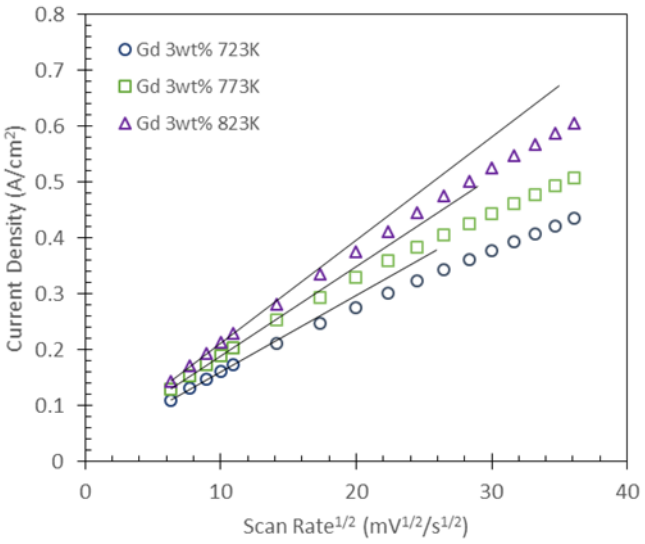

Figure 2-33: 3 wt% $GdCl_3$ in LiCl-KCl salt CV cathodic peak current density versus square root of scan rate.

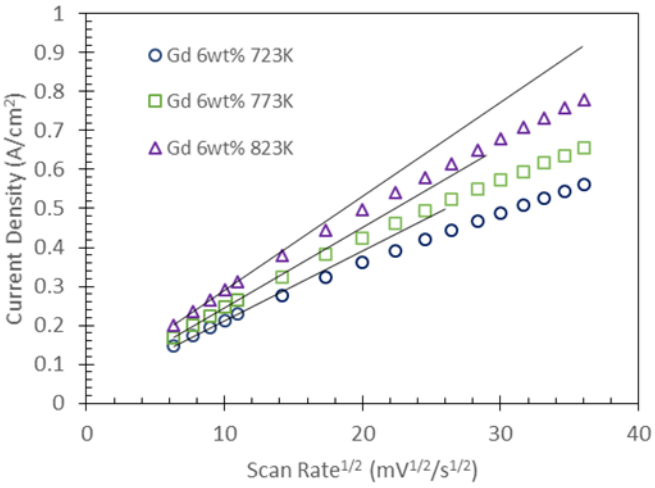

Figure 2-34: 6 wt% $GdCl_3$ in LiCl-KCl salt CV cathodic peak current density versus square root of scan rate.

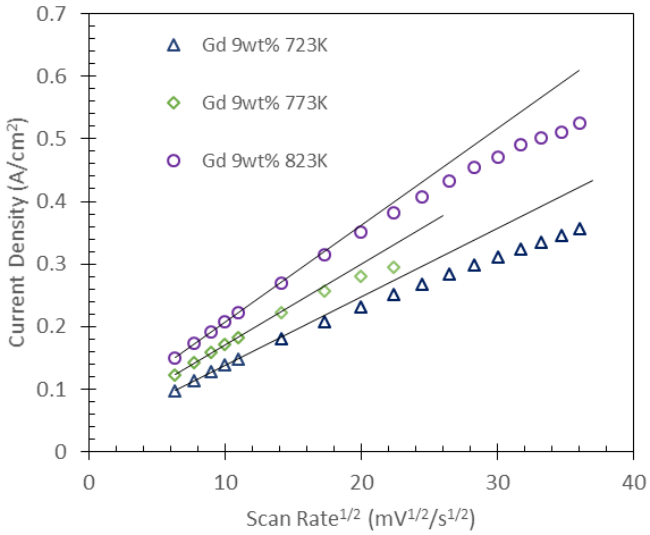

Figure 2-35: 9 wt% $GdCl_3$ in LiCl-KCl salt CV cathodic peak current density versus square root of scan rate.

The reversibility of the reaction can be observed from the current versus square root of scan rate plot. As scan rate goes higher than 250~300 mV/s, the peak current density starts to drop below the fitted straight line, indicating the reaction starts shifting from quasi-reversible reaction to irreversible reaction. The reversibility of the reaction at different scan rate is also examined by the Matsuda and Ayabe criteria [46] and the reversibility value Λ is between 0.033-0.120 for scan rates between 40 mV/s and 500 mV/s.

Thermodynamics data of $GdCl_3$ in LiCl-KCl are by evaluated by conventional CV method. The apparent potential and activity coefficients are summarized in Figure 2-36 and Table 2-10. Similar with what we found in La system, apparent potential shows positive linear relation with temperature. However, the concentration effect doesn't seem to have a linear relation with apparent potential. In the concentration interval 3-9 wt% $GdCl_3$, the activity coefficient also decreases as concentration increases. Activity coefficient is expected to increase as more $GdCl_3$ is added. The concentration dependence of apparent potential is compared with reference and the overall trend agrees well as apparent potential decreases with concentration in this concentration interval.

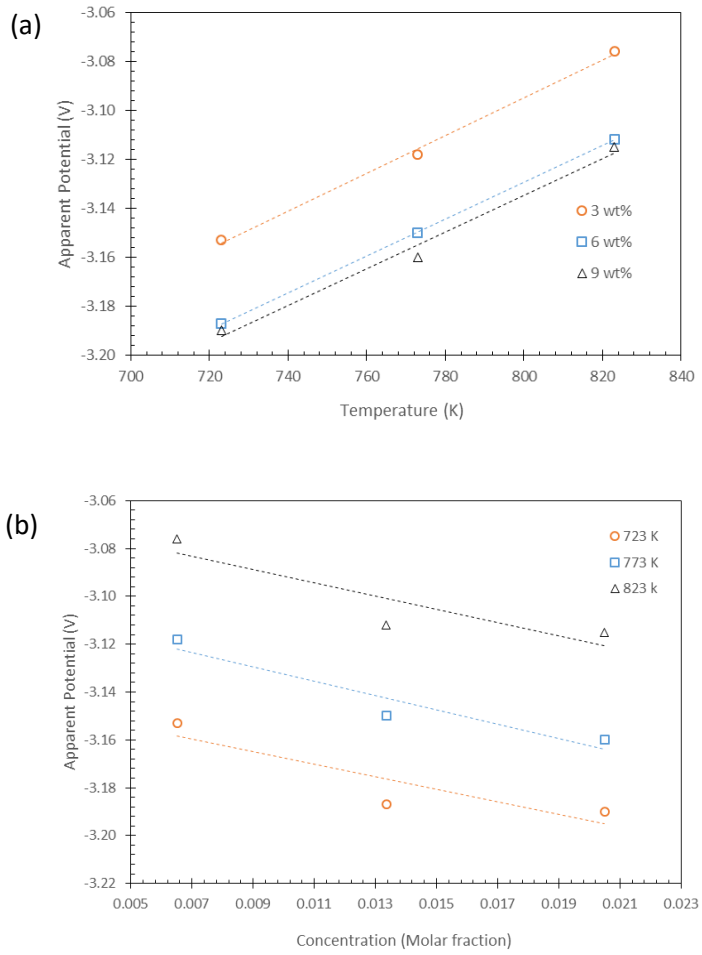

Figure 2-36: (a) Apparent potential of Gd^{3+}/Gd in LiCl-KCl salt at different temperature. (b) Apparent potential of Gd^{3+}/Gd in LiCl-KCl salt at different concentration.

Table 2-10: Apparent potentials of Gd in LiCl-KCl salt at different concentrations and temperatures.

Temperature (K)	Conventional CV analysis	Activity coefficient
3 wt%		
723 K	-3.153±0.021	1.0645×10^{-6}
773 K	-3.118±0.014	2.0644×10^{-6}
823 K	-3.076±0.043	5.0322×10^{-6}
6 wt%		
723 K	-3.187±0.017	2.0706×10^{-7}
773 K	-3.15±0.025	4.8849×10^{-7}
823 K	-3.112±0.036	1.0974×10^{-6}

9 wt%		
723 K	-3.19±0.025	1.7921×10^{-7}
773 K	-3.16±0.018	3.1135×10^{-7}
823 K	-3.115±0.051	9.6660×10^{-7}

The diffusion coefficient of Gd^{3+} in LiCl-KCl salt are calculated using both Berzins-Delahay equation and BET model and the results are shown in Figure 2-37 and Table 2-11. The diffusion coefficient at different concentration are being compared with previous research and the results are shown in Figure 2-38 [28,64].

As shown in Figure 2-37, both Berzins-Delahay equation and BET model yields similar results with 18% difference being observed at 3 wt%, 28% difference in 6 wt% and 35% difference in 9 wt%. The difference between the two methods is significantly lower than the difference from La. This is mainly a result from La reaction being more close to irreversible and Gd being closer to reversible. The diffusion coefficient and temperature follows the Arrhenius' equation and the results will be summarized in subsection 2.5. In Figure 2-38, the results are being compared with previous reference. A linear relation between concentration and diffusion coefficient can be observed at 773 K.

A series of CC is performed from high stepping down voltage to low stepping down voltage for 3, 6, and 9wt% of $GdCl_3$ in 723 K, 773 K, and 823 K. The diffusion coefficient calculated from CC and summarized in Table 2-12. Based on CC results, the trend of diffusion coefficient agrees with diffusion coefficient measured from CV where diffusion coefficient decrease as Gd concentration goes up, the diffusion coefficients of Gd at 773 K are show in Figure 2-39 and is being compared with CV method in Figure 2-39.

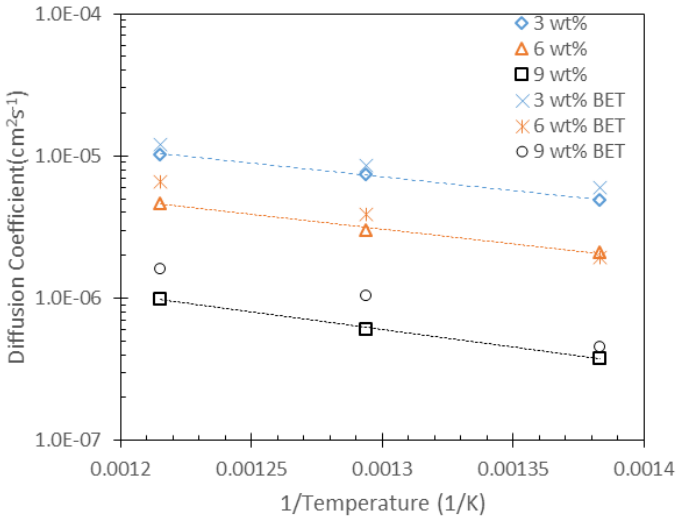

Figure 2-37: Diffusion coefficient of 3, 6, 9 wt% $GdCl_3$ in LiCl-KCl salt at different temperature.

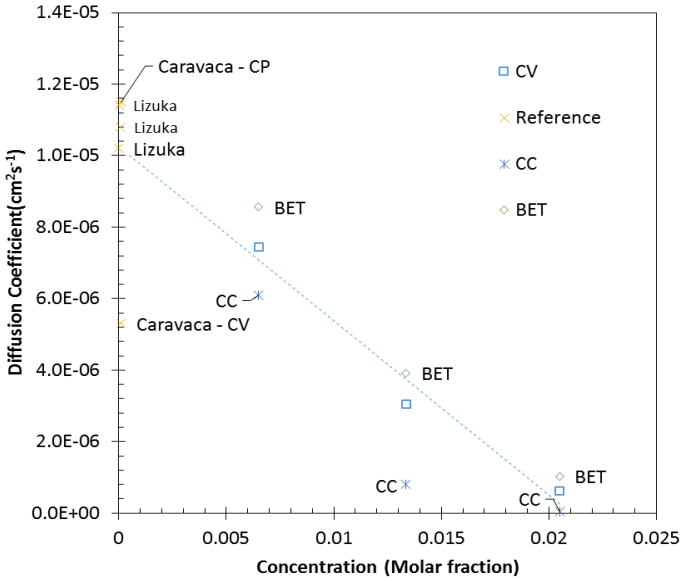

Figure 2-38: Gd Diffusion coefficient at 773 K.

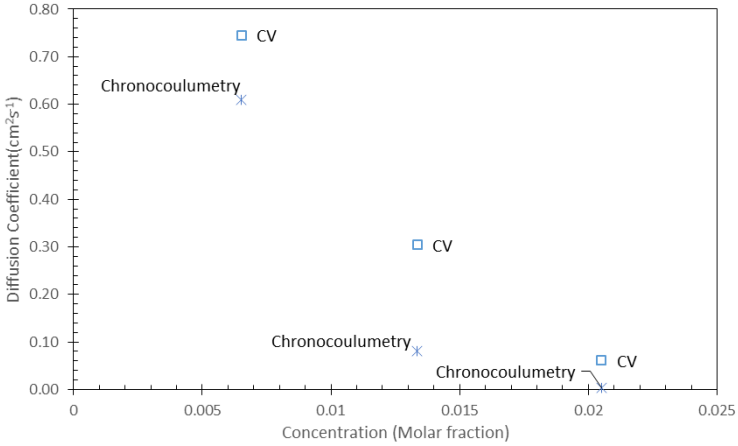

Figure 2-39: Diffusion coefficient of Gd in LiCl-KCl at 773 K with different methods.

Table 2-11: Diffusion coefficient of Gd in LiCl-KCl salt at different concentration and temperature.

Temperature (K)	Diffusion Coefficient ($10^5 cm^2 s^{-1}$) from Berzins-Delahay equation	Diffusivity from BET model
3 wt%		
723 K	0.489±0.0098	0.603±0.0099
773 K	0.745±0.0149	0.856±0.0152
823 K	1.031±0.0257	1.21±0.0261
6 wt%		
723 K	0.209±0.0046	0.194±0.0050
773 K	0.304±0.0030	0.392±0.0032
823 K	0.468±0.0072	0.656±0.0074
9 wt%		
723 K	0.038±0.0009	0.045±0.0011
773 K	0.061±0.0012	0.103±0.0015
823 K	0.099±0.0019	0.161±0.0021

Table 2-12: Diffusion Coefficient of Gd in LiCl-KCl using Chronocoulummetry.

Diffusion Coefficient ($10^5 cm^2 s^{-1}$)			
wt% \T (K)	**723**	**773**	**823**
3	0.221	0.61	1.23
6	0.048	0.0812	0.223
9	0.0022	0.0039	0.0092

2.3.2. Exchange current density of Gd^{3+}/Gd in LiCl-KCl

2.3.2.1. Electrode kinetic simulation method

The potentiodynamic polarization curves obtained at various $GdCl_3$ concentration are shown in Figure 2-40. The current density increases with the increase of $GdCl_3$ concentration. Considering the magnitude of the cathodic current density in Figure 2-40, the Gd layer with a thickness of $\times 10^0 \sim \times 10^2$ μm thick will be deposited in 60 s by assuming a uniform deposition of Gd on W electrode. Thus, a full coverage of Gd is expected shortly after the initiation of the polarization scan. Figure 2-40 shows the anodic polarization curves are greatly distorted above the potentials (typically between 0.05 – 0.1 V) where current density suddenly dropped. Considering the coverage area of Gd might already start to slightly decrease before the sudden drop, conservatively, the data in the overpotentials below 0.01 V excluding the distortion area at the most negative overpotential were selected for the fit of i_0 using equation (2-34). In fact, selection of data below 0.01 V and 0.05 V

resulted in less than 2% difference on the fitted results for most case. The optimization fitting was performed by iterations of the values of α, i_0, and i_L in the ranges of $0.01 \le \alpha \le 0.99$, $0.02\,|i_{min}| \le i_0 \le 5\,|i_{min}|$, and $i_{min} \le i_L \le 100\,i_{min}$ where i_{min} is the most negative measured current density. In this work, the values of α, i_0, and i_L were iterated by α + 0.005, $i_0 \times 1.05$, and $i_L \times 1.05$, respectively. Three iteration loops were set to calculate the polarization curve at all combinations of α, i_0, and i_L values. The difference between each calculated polarization curve and the experimental curve was compared. The difference was defined by the average deviation $\frac{\sum_j^N |(i_{exp} - i_{cal})/i_{exp}|}{N}$ where N is the number of experimental polarization data that used for fitting. For $GdCl_3$ concentrations of 3 – 9 wt% at all temperatures, the values of α, i_0, and i_L that resulted in the minimum average deviation (typically in the range of 5 – 10%) were considered as the optimized values and listed in Table 2-13. It should be mentioned, if the allowable average deviation is increased to 5% higher than the minimum deviation at the optimized fitting, multiple solutions in the ranges of $\alpha^{opt} \pm \sim 0.1$ and $(1 \pm \sim 0.2)\, i_0^{opt}$ exist where subscript 'opt' represents the optimized value. This is the natural truth for all fitting methods. Although the fitting of these values seemed also acceptable, the optimized values for $GdCl_3$ concentrations of 3 – 9 wt% were chose. This is not only because the optimized values have the best fitting, but also, more importantly, the optimized values of α are quite consistent from test to test at various test conditions. The optimized values of i_0 also show reasonable correlation with $GdCl_3$ concentrations which will be discussed later.

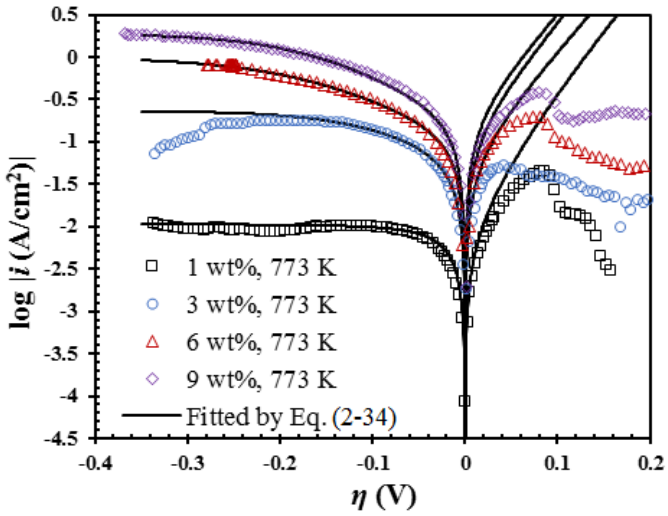

Figure 2-40: Potentiodynamic polarization curves obtained in the LiCl-KCl-$GdCl_3$ melt at 773 K and scan rate of 5 mV/s. Data are fitted by the electrode kinetic model (solid lines).

The fitting for polarization curve at 1 wt% $GdCl_3$ becomes a harder task as the lack of useful data at larger overpotentials. As shown in Figure 2-40, the cathodic current densities at η < -0.05 V are almost independent of potential at 1 wt% $GdCl_3$. This potential-independent current density corresponds to the i_L. Thus, only the small portion of data near the equilibrium potential are useful which shows good agreement (< 12% deviation) with the prediction of couples of combination of α and i_0 in a wide range. The optimization fitting

results for the tests with 1 wt% $GdCl_3$ showed values of α ranging from 0.54 to 0.68 which largely deviates from the typical α value of 0.31 - 0.43 from all other concentrations. Considering the consistence of the α value at various concentrations, the average α value 0.35 from all other concentrations was used for the fitting of experimental data at 1 wt% $GdCl_3$. The optimized i_0 values at α of 0.35 are given in Table 2-13. The fitting goodness by setting α = 0.35 is only 1% less than the results from the optimized value of α.

Table 2-13: Parameters determined from electrode kinetic simulation method.

Condition	i_0 (A/cm²)	α	i_L (A/cm²)	$\lvert i_L \rvert / i_0$
1 wt%, 723 K	0.023	0.35	-0.0072	0.32
1 wt%, 773 K	0.031	0.35	-0.011	0.34
1 wt%, 823 K	0.043	0.35	-0.013	0.29
3 wt%, 723 K	0.054	0.33	-0.19	3.4
3 wt%, 773 K	0.067 ± 0.003	0.33 ± 0.03	-0.21 ± 0.02	3.1
3 wt%, 823 K	0.098 ± 0.012	0.38 ± 0.01	-0.29 ± 0.01	2.9
6 wt%, 723 K	0.039	0.40	-0.20	5.5
6 wt%, 773 K	0.12 ± 0.02	0.31 ± 0.01	-0.95 ± 0.05	8.2
6 wt%, 823 K	0.18	0.33	-0.17	9.8
9 wt%, 723 K	0.099 ± 0.014	0.34 ± 0.01	-1.0 ± 0.1	10
9 wt%, 773 K	0.17 ± 0.01	0.36 ± 0.01	-1.8 ± 0.1	11
9 wt%, 823 K	0.22 ± 0.02	0.43 ± 0.01	-2.1 ± 0.1	9.7

As the power law indicated by equation (2-39), the values of i_0 from Table 2-13 are plotted against concentration of $GdCl_3$ in mol/cm³ to validate the optimization fitting results. As shown in Figure 2-41(a), all values from the electrode kinetic simulation method excluding one data point at 6 wt% $GdCl_3$ and 723 K show good agreement with the power law trend lines. The values of α indicated by the trend line equations are 0.35 at 723 K, 0.25 at 773 K, and 0.21 at 823 K, respectively. These numbers are close to the values of α obtained from the optimization fitting of individual test results (see Table 2-13). It must be stressed that the reliability of α value obtained from the concentration profile in Figure 2-41(a) strongly depends on the accuracy of the i_0 values from a series of experimental results at different concentrations while the value of α fitted from individual test does not. According to equation (2-39), the values of k^0 were calculated by i_0 which are 4.93×10^{-5} cm/s at 723 K, 7.21×10^{-5} cm/s at 773 K, and 9.13×10^{-5} cm/s at 823 K, respectively. In comparison, Tang and Pesic [65] reported the value of k^0 at 723 K is 6.15×10^{-5} cm/s which is estimated from the convolutive voltammetry performed in LiCl-KCl eutectic containing 2 wt% $GdCl_3$. The temperature dependence of i_0 and k^0 obey the Arrhenius law. The activation energy E_a for i_0 are in the range of 25.4 – 44.5 kJ/mol, varying at different concentrations of $GdCl_3$. The

natural logarithm of k^0 against the inverse temperature is shown in Figure 2-41 (b), and the corresponding E_a for k^0 is 30.5 kJ/mol which agree well with the values of E_a for i_0.

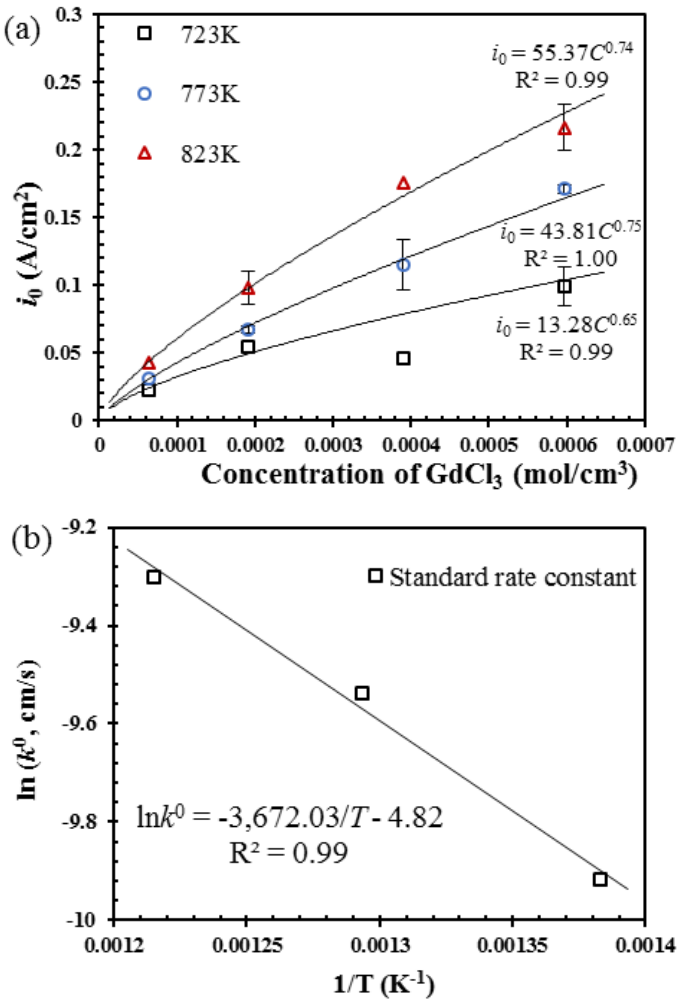

Figure 2-41: (a) The plot of i_0 from Table 2-13 versus $GdCl_3$ concentration; (b) Temperature dependence of k^0.

2.3.2.2. Tafel method

An example of determining the i_0 for Gd^{3+}/Gd using Tafel method is given in Figure 2-8(a). As the anodic polarization curve was greatly distorted by the dissolution of the deposited Gd on the W electrode, the cathodic polarization curve in the range of η < -0.1 V was extrapolated back to the equilibrium potential. The value of -0.1 V was selected as the anodic current density contributes less than 1% of the overall current below -0.1 V at the test temperatures. The charge-transfer coefficient α can be determined by the slope of the linear $\lg(|i|) - \eta$ curve in the cathodic Tafel region. The determined α values are around 0.012 – 0.021 at 1 wt% $GdCl_3$, 0.072 – 0.12 at 3 wt% $GdCl_3$, 0.061 – 0.15 at 6 wt% $GdCl_3$, and 0.12 – 0.17 at 9 wt% $GdCl_3$, respectively. In practice, an α value of 0.01 is not likely and

mostly implies the distortion of polarization curve by the limiting diffusion current. Nevertheless, the i_0 determined by Tafel method are listed in Table 2-14.

Table 2-14: Values of i_0 determined by Tafel, LP, and EIS methods.

Condition	Tafel	LP	EIS
1 wt%, 723K	0.0072	0.0037	0.0055
1 wt%, 748K	-	-	0.0063
1 wt%, 773K	0.0091	0.0060	0.0070 ± 0.0009
1 wt%, 798K	-	-	0.0092 ± 0.0010
1 wt%, 823K	0.013	0.0078	0.011 ± 0.001
3 wt%, 723K	0.081	0.034	0.013 ± 0.001
3 wt%, 748K	-	-	0.019 ± 0.001
3 wt%, 773K	0.071 ± 0.001	0.040 ± 0.003	0.021 ± 0.001
3 wt%, 798K	-	-	0.028 ± 0.003
3 wt%, 823K	0.12 ± 0.02	0.062 ± 0.018	0.041 ± 0.002
6 wt%, 723K	0.11	0.026	0.021 ± 0.001
6 wt%, 773K	0.21 ± 0.05	0.075 ± 0.014	0.046 ± 0.004
6 wt%, 823K	0.40	0.13	0.078 ± 0.005
9 wt%, 723K	0.22 ± 0.06	0.069 ± 0.008	0.050 ± 0.001
9 wt%, 773K	0.40 ± 0.02	0.14 ± 0.01	0.081 ± 0.001
9 wt%, 823K	0.49 ± 0.03	0.20 ± 0.03	0.11 ± 0.01

2.3.2.3. LP method

LP method is based on equation (2-23) which indicates i is linearly related to η in small overpotentials. Hence, the value of i_0 can be determined by the slope of the $i-\eta$ curve in the narrow potential range near the equilibrium potential. Figure 2-42 shows the linear relation of current-overpotential in the range of -10 mV < η < 10 mV. The values of i_0 calculated by the slopes of i/η at various temperatures and $GdCl_3$ concentrations are listed in Table 2-14. Tang and Pesic [65] determined the i_0 of Gd(III)/Gd using LP method in LiCl-KCl eutectic containing 2 wt% $GdCl_3$. The values are 0.00775 A/cm^2 at 723 K, 0.0165 A/cm^2 at 773 K, and 0.0257 A/cm^2 at 823 K. These numbers fall between the LP method determined i_0 values in 1 wt% and 3 wt% $GdCl_3$ in this study.

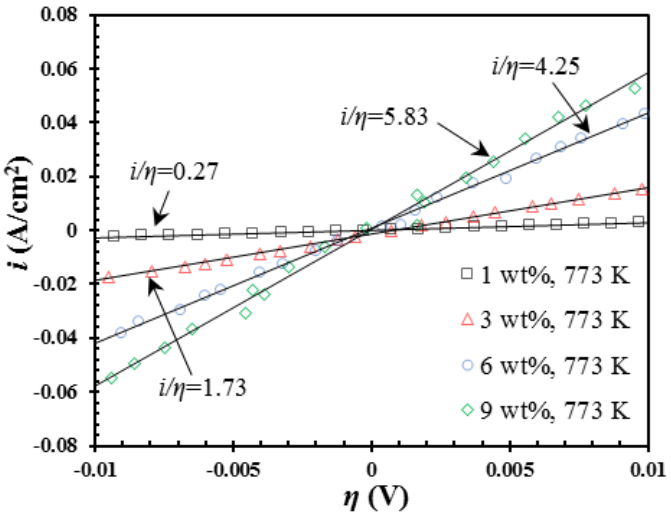

Figure 2-42: The plot of i versus η at small overpotentials.

2.3.2.4. EIS method

Figure 2-43 shows the EIS data at five temperatures for LiCl-KCl melt containing 1 wt% and 3 wt% $GdCl_3$ and three temperatures at 6 wt% and 9wt% $GdCl_3$, as shown in. The Randles cell equivalent circuit given in Figure 2-11 was adopted to fit the experimental EIS data. The fitting process was carried out by Gamry Echem Analyst software with its auto fit feature using simplex method, the parameters obtained was then manually adjust to minimize relative error between each measurement. The fitted curves are in good agreement with the experimental EIS data, as shown in Figure 2-43. The charge transfer resistance in Ω was obtained from the fitting results. The coverage ratio of Gd on W electrode at the minimum overpotential is assumed to be 1, and then the surface area of W electrode in the molten salt is used to convert the charge transfer resistance in $\Omega \cdot cm^2$. Finally, the exchange current density is calculated according to equation (2-35). The values of i_0 obtained from EIS method at all concentrations and temperatures are listed in Table 2-14.

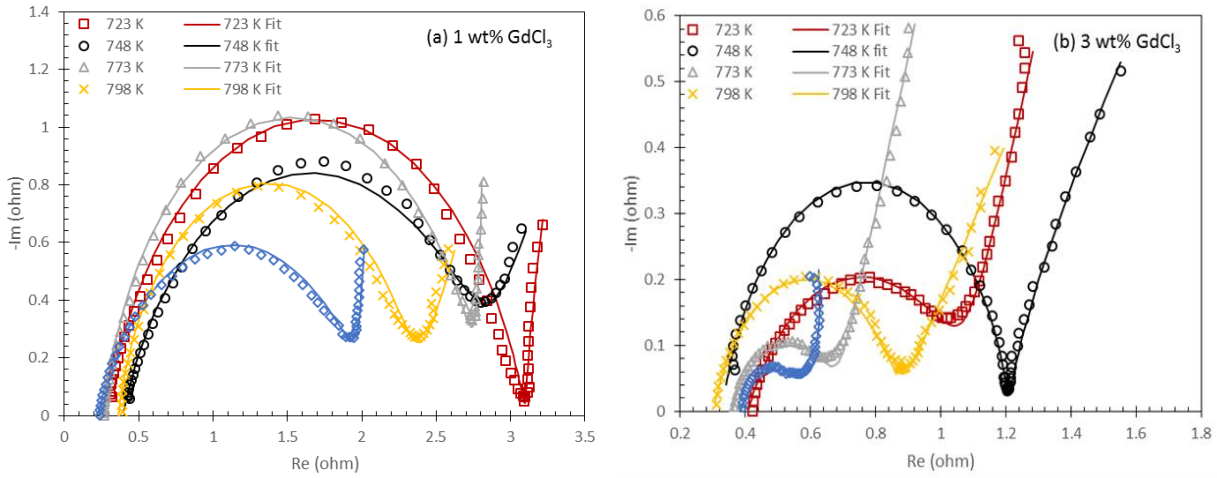

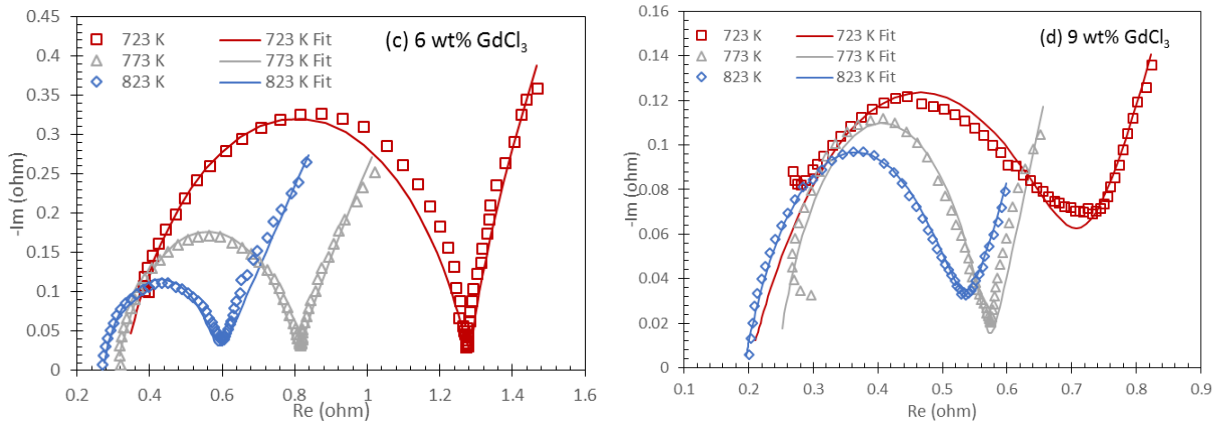

Figure 2-43: (a) Impedance spectra and the fitting results for 1 wt% $GdCl_3$ in LiCl-KCl salt. Electrode area is 1.256 cm^2. (b) Impedance spectra and the fitting results for 3 wt% $GdCl_3$ in LiCl-KCl salt. Electrode area is 1.570 cm^2 for 723, 773, 823 K and 1.0053 cm^2 for 748 and 798 K. (c) Impedance spectra and the fitting results for 6 wt% $GdCl_3$ in LiCl-KCl salt. Electrode area is 1.056 cm^2. (d) Impedance spectra and the fitting results for 9 wt% $GdCl_3$ in LiCl-KCl salt. Electrode area is 0.553 cm^2.

2.3.2.5. Comparison of results from different methods and discussion

Comparison of results in Table 2-13 and Table 2-14 reveals the difference of the values of i_0 determined by different methods. Figure 2-44 shows the profiles of i_0 with $GdCl_3$ concentration using different methods. Only the results from electrode kinetic simulation method shows reasonable power number close to the value of 1-α. Other methods indicate a α value of negative or zero which is invalid or unrealistic. The errors of the Tafel, LP, and EIS methods in this investigated system is simply due to the nonnegligible mass transfer effect, and the details are discussed below.

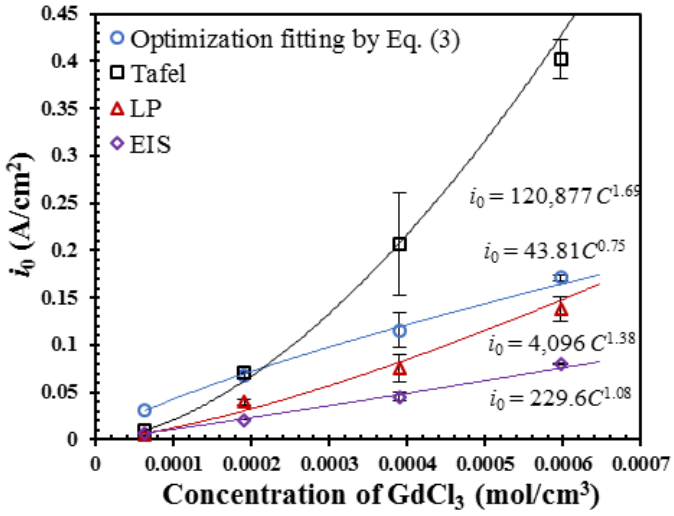

Figure 2-44: Comparison of i_0 determined by different methods.

Tafel method overestimates the i_0 at $GdCl_3$ concentrations above 3 wt% and underestimates the i_0 at 1 wt% $GdCl_3$. From Table 2-13, it is noticed that i_0 is smaller than the $|i_L|$ at concentrations above 3 wt%, but lower than $|i_L|$ at 1 wt% $GdCl_3$. As shown in Figure 2-40, the $\lg(|i|) - \eta$ curve in the cathodic section at 1 wt% $GdCl_3$ is nearly horizontal. Hence, the extrapolation of the horizontal curve using Tafel method results in a value of $i_0 \approx |i_L|$. Thus, in the case of $i_0 > |i_L|$, the 'i_0' determined by the Tafel method is actually a measuring of $|i_L|$, which for sure is lower than the real i_0. When $i_0 < |i_L|$ and $|i_L|/i_0$ is not sufficiently large, the denominator in equation (2-34) is larger than 1. This means the cathodic current will be retarded, as illustrated by Figure 2-45. In Figure 2-45, curve 2 (green double-line) is predicted by the no mass-transfer effect based Butler-Volmer equation (2-21) using the values of i_0 and α from electrode kinetic simulation method. It can be seen, the measured cathodic curves at larger overpotential is highly deviated from curve 1 which indicates the limiting of reduction rate of Gd^{3+} by its maximum diffusion rate. Hence, the 'i_0' determined by Tafel method falls in somewhere in middle of the real i_0 and $|i_L|$. Figure 2-45 also shows the curve 1 predicted by equation (2-21) using the values of i_0 and α determined by Tafel method. Although fairly good fitting is achieved in the cathodic Tafel region, large discrepancy exists in the small overpotential region. This means the application of equation (2-21) can only get a decent fitting either in the small potential region or the Tafel region (η < -0.1 V) but not for the entire cathodic curve, as indicated by the two predicted curves in Figure 2-45. If we consider the mass transfer limiting effect, the curves predicted the electrode kinetic model agree very well with the measured cathodic curves as shown in Figure 2-40. Therefore, it is believed the mass transfer effect was involved which fully or partially limited the reduction rate of Cd^{3+}.

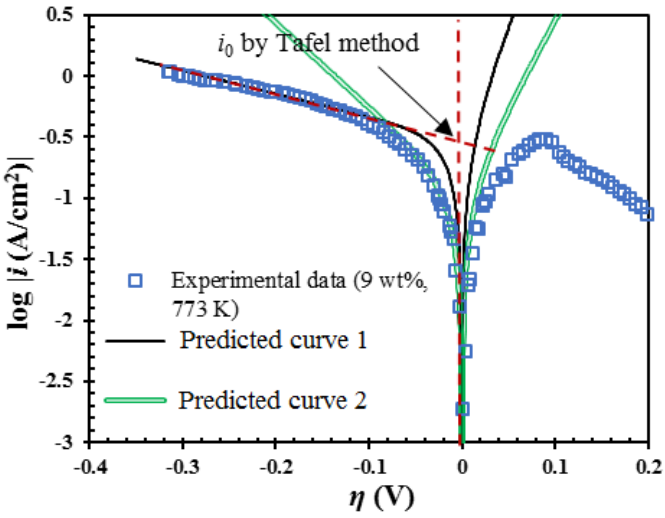

Figure 2-45: Errors of using Tafel method in the situation where mass transfer affects. Experiment data obtained at LiCl-KCl-9 wt% $GdCl_3$ at 773 K. Curve 1 and curve 2 are predicted by equation (2-21) using values of i_0 and α determined by Tafel method and electrode kinetic simulation method, respectively.

LP method underestimates the i_0 for all concentrations. As mentioned before, LP method is based on two assumptions: small overpotential and no mass transfer influence (i.e., small

ratio of i/i_L). Normally, 10 mV of overpotential is small enough to observe a fairly linear correlation, as shown in Figure 2-42 and Figure 2-46. Thus, the error should be from the assumption of $i/|i_L|$. For a given overpotential and a certain value of α, the magnitude of i is directly reflected by the magnitude of i_0. Hence, the magnitudes of errors that are introduced by LP method can be illustrated at different ratios of $|i_L|/i_0$, as shown in Figure 2-46. The curves in Figure 2-46 are predicted by electrode kinetic model using the same variables excluding i_L. It is seen, the slope of i/η increases with the increase of $|i_L|/i_0$. According to the assumption of LP method, the determined 'i_0' infinitely approaches to real i_0 when $|i_L|/i_0 \to \infty$. Figure 2-46 shows the $i-\eta$ curves become indistinguishable at $|i_L|/i_0$ above 100. Hence, at the ratios below 100, LP method underestimates the i_0. As seen in Table 2-13, the ratio of $|i_L|/i_0$ increased from ~0.33 to ~10 with the increase in $GdCl_3$ concentration. In fact, the error at $|i_L|/i_0$ of 10 is quite small. That is why the LP determined 'i_0' getting closer to the value of i_0 obtained from the optimization fitting method at 9 wt% $GdCl_3$, as shown in Figure 2-44.

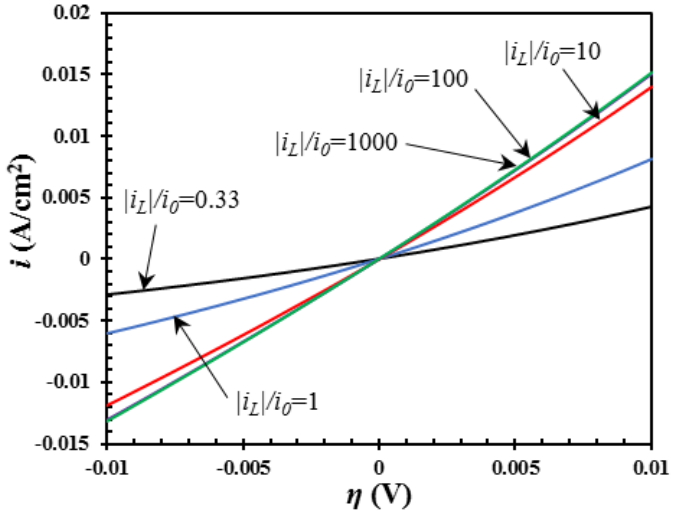

Figure 2-46: Errors of using LP method at different ratios of $|i_L|/i_0$. i_0 = 0.031 A/cm², α = 0.35, T = 773 K.

EIS method underestimates the i_0 for all concentrations. In fact, EIS method is based on the same two assumptions for LP method. The origin of $R_{ct} = \frac{RT}{nFi_0}$ for EIS method is derived from the following equation for Re^{n+}/Re reaction involving mass transfer effect [66]:

$$R_{\mathrm{ct}} = \frac{RT}{nFi_0\left\{\exp[\frac{(1-\alpha)nF}{RT}\eta] - \frac{C^{\mathrm{s}}_{\mathrm{RE^{n+}}}}{C^{\mathrm{b}}_{\mathrm{RE^{n+}}}}\exp[\frac{-\alpha nF}{RT}\eta]\right\}} \qquad (2\text{-}40)$$

To estimate the value of i_0 from the R_{ct} characterized by EIS measurement, the variables α and $C^{\mathrm{s}}_{\mathrm{Gd(III)}}$ in equation (2-40) must be eliminated. The simplification of equation (2-40) to $R_{ct} = \frac{RT}{nFi_0}$ is based on two assumptions: 1) the overpotential is sufficiently small that the exponential terms $e^{f(\eta)}$ can be approximated as $1 + f(\eta)$; 2) the net current i is negligible

compared to i_L, thus the ratio of $C^s_{Gd(III)}/C^b_{Gd(III)} \approx 1$. Since mass transfer effect is involved as we know from the electrode kinetic simulation results, $C^s_{Gd(III)}/C^b_{Gd(III)}$ deviates from 1 at smaller ratio of $|i_L|/i_0$. Like LP method, the conversion of i_0 from R_{ct} using EIS method will also cause underestimations at smaller values of $|i_L|/i_0$.

Although the errors of using Tafel, LP, and EIS methods were found in the studied molten salt system, these methods are convenient and reliable when the mass transfer effect is not considerable. When the mass transfer effect is involved, electrode kinetic simulation method is recommended especially for the case of distorted anodic polarization curve (e.g., using an inert electrode to measure the exchange current density of a deposited metal) as the rest cathodic polarization curve can be largely influenced by the limiting diffusion current. Despite the advantages of the electrode kinetic model, its limitations should also be acknowledged. As the non-simplified kinetics equation (2-34) contains three variables (α, i_0, and i_L), a wide variety of fitted values with acceptable fitting goodness with the experimental data are possible. In some cases such as the nearly potential-independent cathodic current at 1 wt% $GdCl_3$, the optimized values from the fitting can be far away from the actual values due to the lack of useful current-potential data points. In that case, it is almost impossible to get the accurate and valid solutions. Therefore, knowledge of the valid range of the parameters should be considered to give more constrains to the fitting. One way to check the validity of the fitted values is to take the consistence of α and the theoretical correlation (Eq. (2-39)) of i_0 with concentration and α into account.

2.4. Neodymium property in LiCl-KCl eutectic salt

2.4.1. Thermodynamics and transport properties of $NdCl_3$ and $NdCl_2$

CV and SWV are two of the primary methods used for Nd property study in LiCl-KCl salt. Salt sample used are summarized in Table 2-15. Tests were taken at 723 K, 773 K and 823 K with an initial $NdCl_3$ concentration of 3 wt%, 6 wt% and 9 wt%. Square wave voltammetry is used to determine number of charge transfer during the experiment and follow by CV which provides insight on exchange current density, diffusion coefficient and thermodynamics properties.

Table 2-15: Electrolyte concentration of each sample.

Experiment	Prepared Concentration (wt%)	ICP-MS (wt%)	Mole cm^{-3}
3 wt% $NdCl_3$	3	3.01	2.091×10^{-4}
6 wt% $NdCl_3$	6	5.98	4.182×10^{-4}
9 wt% $NdCl_3$	9	9.02	6.273×10^{-4}

As stated in the literature review section, the reduction process of $NdCl_3$ involves two step process:

$$Nd^{3+} + e^- \rightarrow Nd^{2+} \quad (2\text{-}41)$$

$$Nd^{2+} + 2e^- \rightarrow Nd^0 \quad (2\text{-}42)$$

SWV is performed to determine the number of electron transferred during redox reaction. It is also showed to be a good method to identify the location of Nd^{3+}/Nd^{2+} and Nd^{2+}/Nd redox reaction. As shown in Figure 2-47, SWV is performed at different square wave frequency. The increase in frequency results in higher peak current at Nd^{2+}/Nd^0 but lower peak current at Nd^{3+}/Nd^{2+} but the change is considered small. SWV data are fit by bi-Gaussian distribution as shown in Figure 2-47 and the number of electron transferred is showed in Table 2-16, at all concentration, the number of charge transfer is always around 1 at the smaller peak and 2 at the major peak.

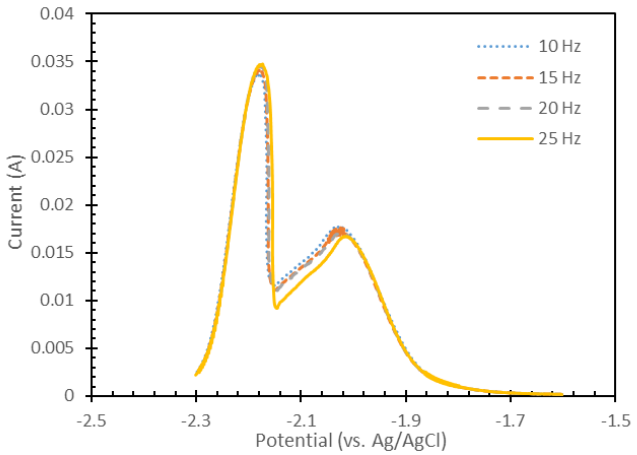

Figure 2-47: SWV results for 3wt% $NdCl_3$ in LiCl-CKl salt.

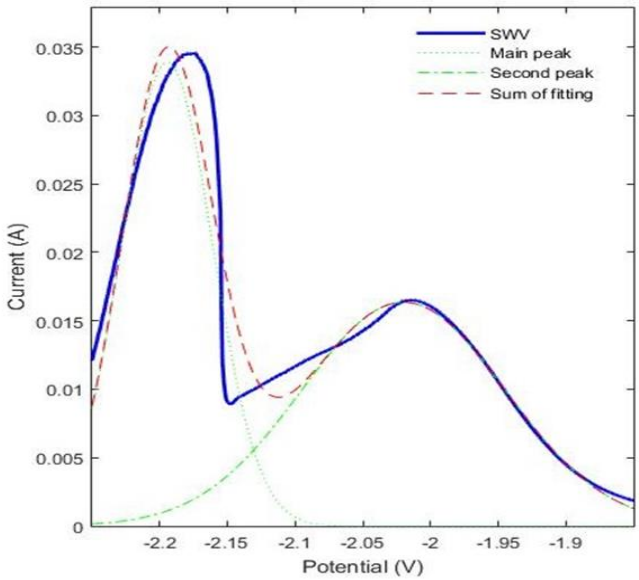

Figure 2-48: Bi-Gaussian fitting for SWV results at 3wt% $NdCl_3$ in LiCl-CKl, 723 K.

Table 2-16: Number of electron transferred for Nd in LiCl-KCl.

	3 wt%	6 wt%	9 wt%
Nd^{3+}/Nd^{2+}	0.83	1.17	1.08
Nd^{2+}/Nd	2.47	2.16	2.32

Unlike La and Gd, the CV curve of Nd system involves 4 peaks as shown in Figure 2-49. The main peak Nd^{2+}/Nd^{0} can be easily distinguished while Nd^{3+}/Nd^{2+} peak can barely be seen on CV curve. In order to figure out the peak potential and peak current of Nd^{3+}/Nd^{2+} couple, 4th order Savitzky-Golay filter using nearby 16 points is applied to the CV data. The filtering process is performed by Gamry software and the results is shown in Figure 2-50.

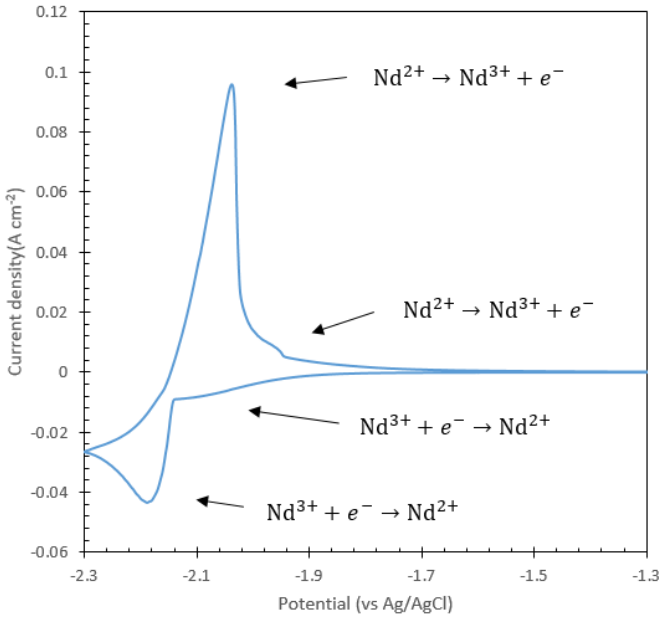

Figure 2-49: CV and SWV of 3 wt% $NdCl_3$ in LiCl-KCl salt at 723 K.

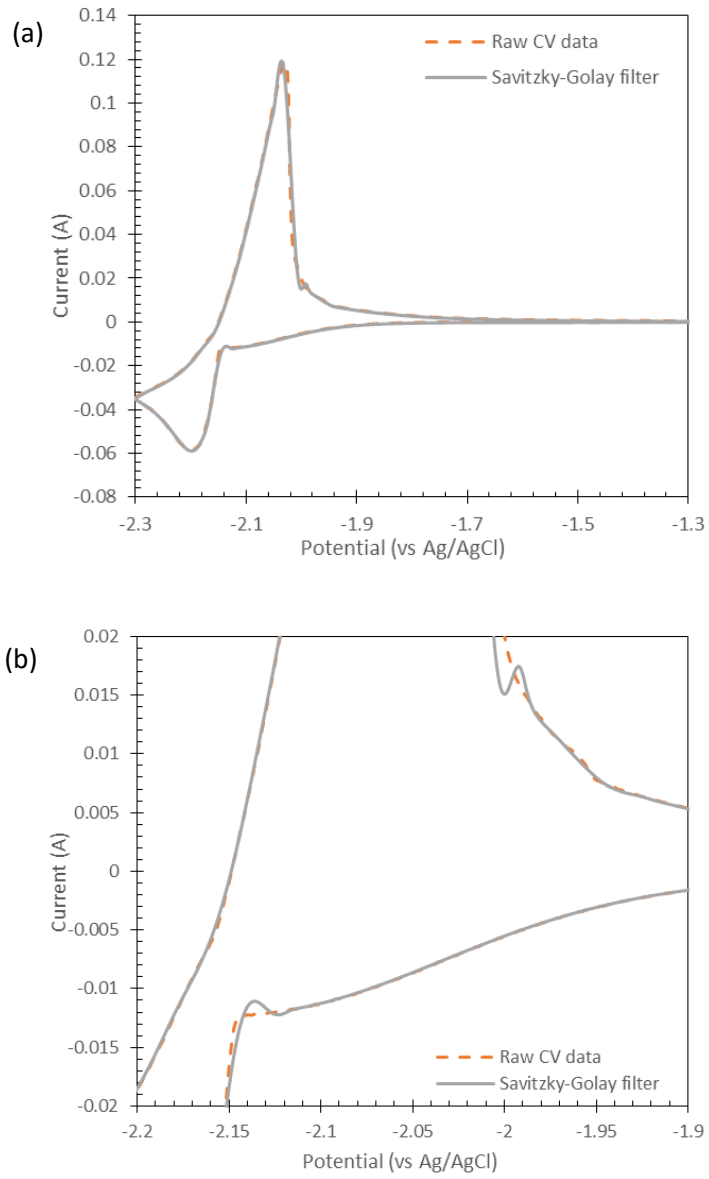

Figure 2-50: (a) Result for Savitzky-Golay filter, Cyclic voltammogram taken at 3wt% $NdCl_3$ in LiCl-KCl at 723 K, scan rate is 80 mV/s, electrode area is 0.247 cm^2. (b) Zoom in view of CV curve.

As shown in Figure 2-50(b), the Nd^{3+}/Nd^{2+} peak can now be easily identified. The peak current density of both Nd^{3+}/Nd^{2+} and Nd^{2+}/Nd^{0} cathodic peak is plotted against each scan rate to determine when the reaction starts to become irreversible. For Nd^{2+}/Nd^{0} couple, it is found that the peak current starts usually shift away from quasi-reversible to irreversible after scan rate exceeds 250 mV/s.

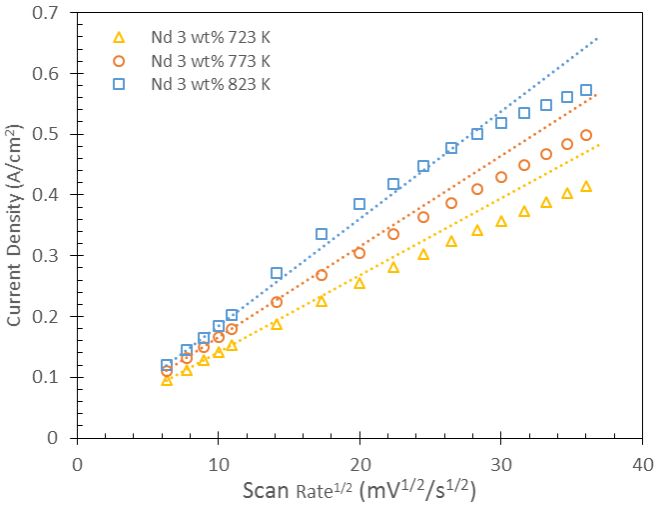

Figure 2-51: Cathodic peak current density versus square root of scan rate, 3 wt% $NdCl_3$.

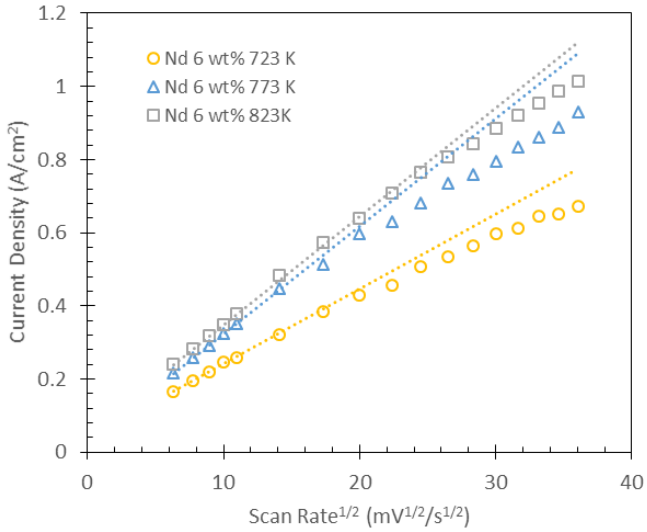

Figure 2-52: Cathodic peak current density versus square root of scan rate, 6 wt% $NdCl_3$.

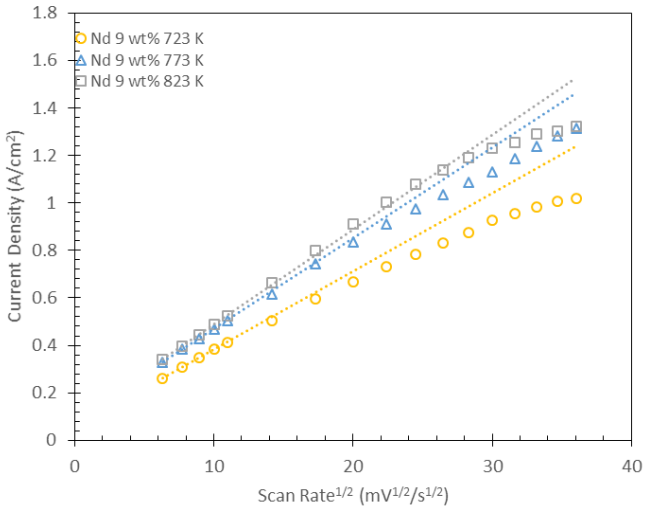

Figure 2-53: Cathodic peak current density versus square root of scan rate, 9 wt% $NdCl_3$.

Again, the reversibility of the reaction at different scan rate is determined by Matsuda and Ayabe criteria [46]. The reversibility at different scan rate is calculated and the values are between 0.00253-0.00899 for scan rates between 40 mV/s and 500 mV/s which is still considered quasi-reversible with the lower end of irreversible threshold is 0.00158-0.002512 depending on the concentration. The reversibility of Nd^{3+}/Nd^{2+} couple is also examined at different scan rate as shown in Figure 2-54.

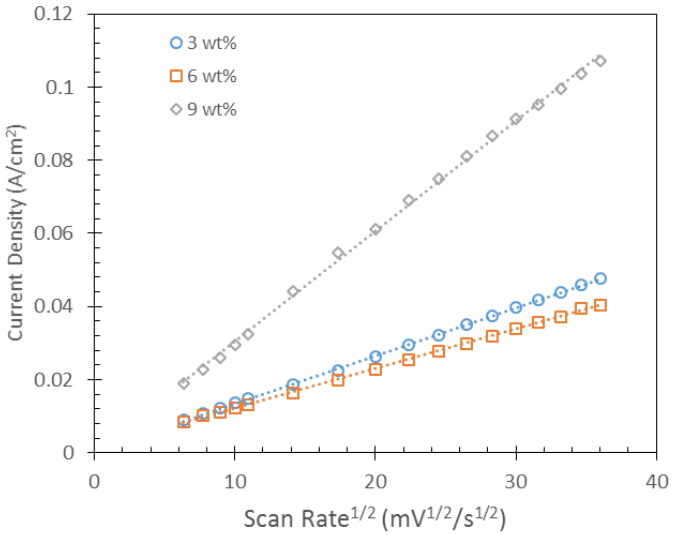

Figure 2-54: Cathodic peak current density versus square root of scan rate for Nd^{3+}/Nd^{2+} couple at 723 K.

As shown in Figure 2-54, for Nd^{3+}/Nd^{2+} soluble-soluble couple, the reaction is reversible/ quasi-reversible at all scan rate since the peak current maintain linear relation with square root of scan rate all the time. After the reversibility of both reaction is determined, we then

focus on the calculation of diffusion coefficient for both Nd^{3+} and Nd^{2+}. The most important assumption we made here is we treat the concentration of Nd^{3+} and Nd^{2+} the same since no reliable method is able to measure the Nd^{2+} and Nd^{3+} ratio in salt at the working temperature as of today. This assumption was originally made by Delahay [67] and later on being adopted in other research when measuring Nd properties in LiCl-KCl salt [20,21,30,31].

The diffusion coefficient of Nd^{2+} and Nd^{3+} are calculated and summarized in Table 2-17 and Figure 2-55. Diffusion coefficient of Nd^{2+} and Nd^{3+} is found to be relatively close to each other and increase as temperature increase. At the same time, the increase in concentration tends to lower the diffusion coefficient for both Nd^{2+} and Nd^{3+}.

Table 2-17: Diffusion coefficient and apparent potential of Nd^{2+} in LiCl-KCl.

Temperature (K)	Diffusion Coefficient ($10^5 cm^2 s^{-1}$) of Nd^{2+}	Diffusion Coefficient ($10^5 cm^2 s^{-1}$) of Nd^{3+}
3 wt%		
723 K	1.09±0.012	0.69±0.008
773 K	1.65±0.025	1.03±0.024
823 K	2.36±0.041	1.46±0.032
6 wt%		
723 K	0.81±0.008	0.62±0.007
773 K	1.45±0.015	1.19±0.022
823 K	1.95±0.028	1.71±0.029
9 wt%		
723 K	0.74±0.014	0.52±0.007
773 K	1.36±0.021	0.97±0.023
823 K	1.59±0.023	1.07±0.025

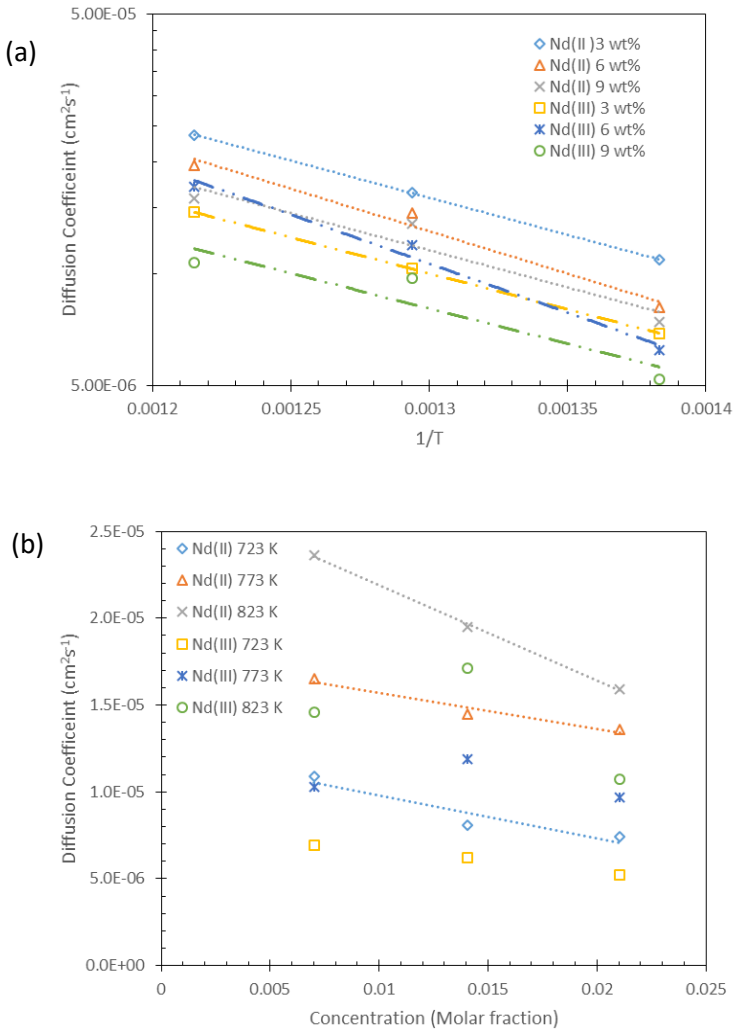

Figure 2-55: (a) Diffusion coefficient of Nd^{2+} and Nd^{3+} in LiCl-KCl salt at different temperature. (b) Diffusion coefficient of Nd^{2+} and Nd^{3+} in LiCl-KCl salt at different concentration.

As shown in Figure 2-55 (a), Nd^{2+} diffusion coefficient is slightly greater than Nd^{3+} diffusion coefficient. The temperature dependence of both Nd^{2+} and Nd^{3+} diffusion coefficients follow Arrhenius' equation. In Figure 2-55(b), it can be discovered that diffusion coefficient of Nd^{2+} shows linear relation with concentration while no correlation with concentration is found for Nd^{3+}. With both diffusion coefficients known, the apparent potential of Nd^{3+}/Nd^{2+} can be calculated. Nd^{3+}/Nd can be calculated by combining $Nd^{3+}/Nd^{2+}$and Nd^{2+}/Nd apparent potential together [68]:

$$E^*_{Nd(III)/Nd(0)} = \frac{E^*_{Nd(III)/\mathrm{Nd(II)}} + 2E^*_{Nd(II)/Nd(0)}}{3} \qquad (2\text{-}43)$$

The apparent potentials are summarized in Figure 2-56 and Table 2-18.

Table 2-18: Apparent potential of Nd^{3+}/Nd^{2+}, Nd^{2+}/Nd^{0} and Nd^{3+}/Nd^{0} in LiCl-KCl.

Temperature (K)	Apparent potential of Nd^{3+}/Nd^{2+} (vs. Cl_2/Cl^-)	Apparent potential of Nd^{2+}/Nd^{0} (vs. Cl_2/Cl^-)	Apparent potential of Nd^{3+}/Nd^{0} (vs. Cl_2/Cl^-)
3 wt%			
723 K	-3.139±0.05	-3.094±0.05	-3.124±0.05
773 K	-3.109±0.06	-3.053±0.05	-3.090±0.05
823 K	-3.087±0.04	-3.029±0.06	-3.067±0.05
6 wt%			
723 K	-3.123±0.04	-3.115±0.03	-3.120±0.03
773 K	-3.096±0.05	-3.074±0.06	-3.088±0.06
823 K	-3.053±0.03	-3.041±0.04	-3.049±0.04
9 wt%			
723 K	-3.083±0.03	-3.149±0.05	-3.105±0.04
773 K	-3.055±0.04	-3.106±0.04	-3.072±0.04
823 K	-3.017±0.04	-3.079±0.03	-3.037±0.03

As shown Figure 2-56 (a), both Nd^{2+} and Nd^{3+} increase linearly as temperature increase. However, Nd^{2+} and Nd^{3+} have a very different response as concentration increase where the apparent potential of Nd^{3+} increase and Nd^{2+} apparent potential decrease.

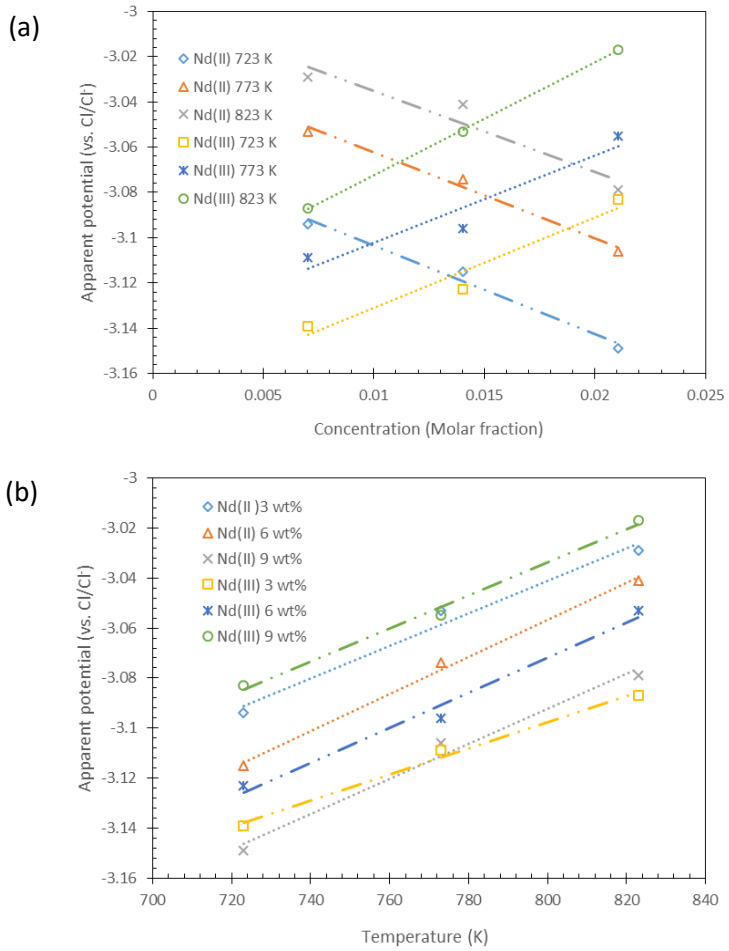

Figure 2-56: (a) Apparent potential of Nd^{2+} and Nd^{3+} in LiCl-KCl salt at different temperature. (b) Apparent potential of Nd^{2+} and Nd^{3+} in LiCl-KCl salt at different concentration.

2.4.2. Exchange current density of Nd^{2+}/Nd in LiCl-KCl

Several attempts have been made to analyze the exchange current density of Nd^{2+}/Nd using Tafel method, LP method, and the electrode kinetic model. However, due to the co-existence of Nd^{3+}/Nd^{2+} reaction in the system, the Nd^{2+}/Nd reaction current is overlapped with the Nd^{3+}/Nd^{2+} reaction current. The influence is complicated, as indicated by the electrode kinetic model. If we extend the electrode kinetic model to two reactions, the fitting of the experimental data will be performed with 6 unknown parameters, i.e., two sets of (i_0, α, *and* i_L). These two sets of parameters are not correlated to each other. It is expected that tons of solutions with large variety will fit well with the relatively simple experimental polarization curves. It is hard to distinguish the actual Nd^{2+}/Nd signal from Nd^{3+}/Nd^{2+} and background current. If we assume the Nd^{3+}/Nd^{2+} around the equilibrium potential region of Nd^{2+}/Nd is fully limited by the diffusion, LP method may be applied as the slope of η/i will remain the same in such case. Thus, the exchange current density of Nd^{2+}/Nd is determined by LP method but the deviation is unknown and should be mentioned.

CV data in small overpotentials were used to determine the exchange current density i_0 of Nd^{2+}/Nd reaction using LP method. All CV measurements are taken with the scan rate from 40 mV/s to 120 mV/s to identify scan rate dependence of i_0. Figure 2-57 shows how scan rate affects i_0 at different concentration. At all concentration, arbitrary effect on i_0 is observed with different scan rate with the biggest relative standard deviation between scan rate being observed at 9 wt% $GdCl_3$ with a value of 9.28%. Figure 2-58 summarized i_0 measured by CV regarding concentration and temperature.

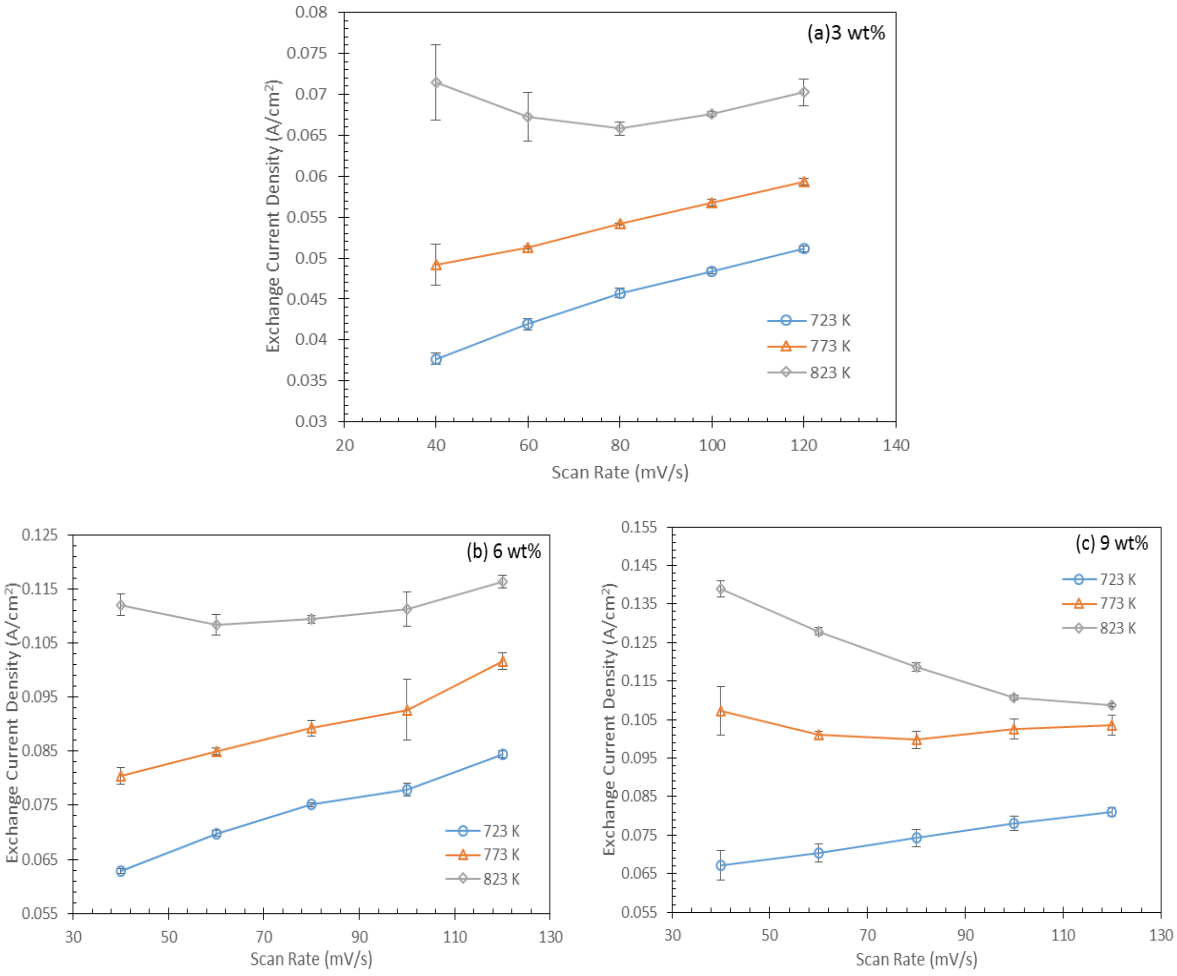

Figure 2-57. (a)Exchange current density (i_0) of 3 wt% Nd^{2+}/Nd at different scan rate and temperature. (b)Exchange current density (i_0) of 6 wt% Nd^{2+}/Nd at different scan rate and temperature. (c)Exchange current density (i_0) of 9 wt% Nd^{2+}/Nd at different scan rate and temperature.

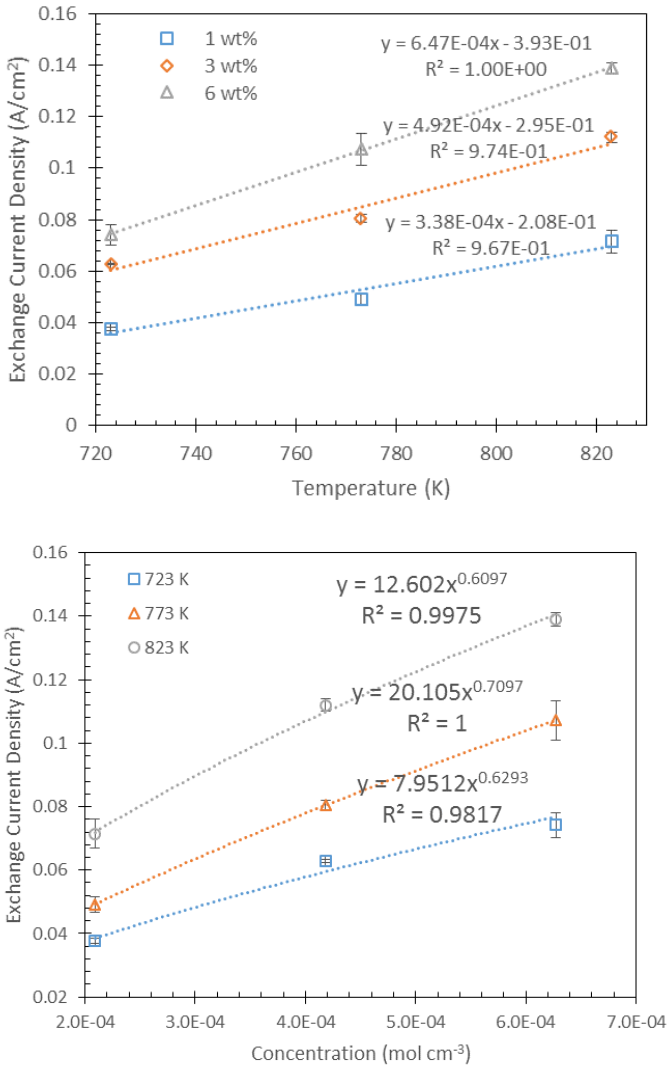

Figure 2-58. (a)Exchange current density (i_0) of Nd^{2+}/Nd against concentration at different temperature. (b) Exchange current density (i_0) of Nd^{2+}/Nd against temperature at different concentration.

A power equation model is developed to characterize the behavior of Nd^{2+}/Nd i_0 response to temperature and concentration and the results are summarized in Table 2-21. Figure 2-58(b) shows i_0 versus concentration obtained by CV and the results are fitted by a power equation. The corresponding α for 3 wt%, 6 wt% and 9 wt% $NdCl_3$ are 0.371, 0.293 and 0.391. Meanwhile, k^0 can also be obtained from the fitting and the result is summarized in Table 2-20.

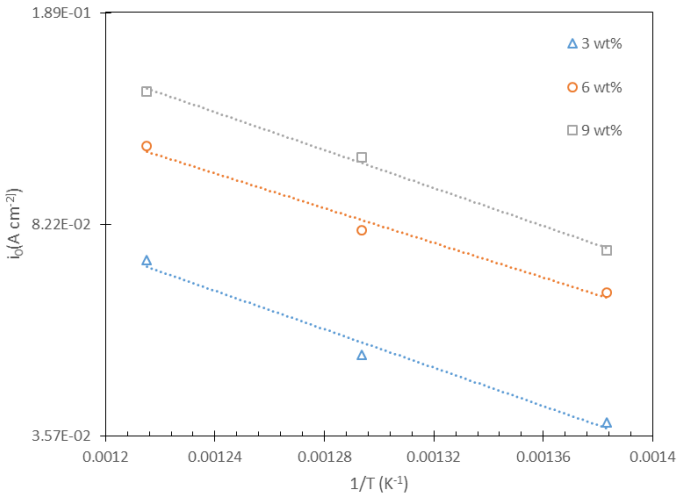

Figure 2-59. Logarithm of i_0 versus inverse temperature.

Table 2-19. Linear model for concentration and temperatue dependency.

		Equation	R2
Temperature Dependence of i_0	3 wt% $NdCl_3$	3.38E-04 T – 2.08E-01	9.670
	6 wt% $NdCl_3$	4.92E-04 T – 2.94E-01	0.9739
	9 wt% $NdCl_3$	6.47E-04 T – 3.93E-01	0.9998
Concentration Dependence of i_0	723 K	$7.9512\ [C]^{0.629}$	0.9970
	773 K	$20.105\ [C]^{0.709}$	0.9771
	823 K	$12.602\ [C]^{0.609}$	0.9872

*C is in mol cm^{-3}

Table 2-20. k^0 for Nd/Nd^{2+} reaction at different temperature.

Temperature (K)	K^0 (cm s^{-1})	R^2 from Error! Reference s ource not found.
723	4.119×10^{-5}	0.9975
773	1.041×10^{-4}	1.0000
823	6.530×10^{-5}	0.9817

2.5. Correlations for temperature and concentration dependence

The goal of this research is to develop the fundamental database for REs properties in LiCl-KCl salt. Exchange current density, apparent potential, activity coefficient, diffusion coefficient, reaction rate constant, charge transfer coefficient for La, Gd and Nd in LiCl-KCl

salt are measured and the correlation with temperature and concentration is evaluated. Exchange current density, apparent potential and diffusion coefficient are three of the most important properties to estimate molten salt recycle efficiency where apparent potential provides insight on when the extraction of REs will happen, exchange current density governs how fast the reaction can happen and diffusion coefficient determines how fast REs ions travel in the molten salt.

In general, apparent potential has a linear relationship with temperature and concentration. Exchange current density has a linear relation with temperature and can be fitted by a power equation with concentration. Diffusion coefficient has an Arrhenius relation with temperature but no consistent correlation can be found with concentration. Table 2-21, Table 2-22, and Table 2-23 summarized all correlations we found in this research.

Table 2-21: Linear model for concentration and temperatue dependency of La properties.

		Equation	R2
Temperature Dependence of E^*			
	1 wt% $LaCl_3$	$7.00\times10^{-4}\,T - 3.72$	0.9997
	3 wt% $LaCl_3$	$8.80\times10^{-4}\,T - 3.83$	0.9957
	6 wt% $LaCl_3$	$8.70\times10^{-4}\,T - 3.82$	0.9996
Concentration Dependence of E^*			
	723 K	-60.937 [C]-3.186	0.9596
	773 K	-98.667 [C]-3.134	0.9808
	823 K	-116.16 [C]-3.092	0.9916
Temperature Dependence of $D_{La^{3+}}$			
	1 wt% $LaCl_3$	$0.0087\exp(\frac{-5393}{T})$	0.9725
	3 wt% $LaCl_3$	$0.0108\exp(\frac{-6096}{T})$	0.9751
	6 wt% $LaCl_3$	$0.0017\exp(\frac{-5234}{T})$	0.9995
Temperature Dependence of i_0			
	1 wt% $LaCl_3$	$1.40\times10^{-4}\,T - 9.37\times10^{-2}$	1
	3 wt% $LaCl_3$	$2.35\times10^{-4}\,T - 1.47\times10^{-1}$	0.9800
	6 wt% $LaCl_3$	$3.08\times10^{-4}\,T - 1.80\times10^{-1}$	0.9980
Concentration Dependence of i_0			
	723 K	$39.77\,[C]^{0.8807}$	0.9953
	773 K	$37.96\,[C]^{0.8284}$	0.9885
	823 K	$19.93\,[C]^{0.7159}$	0.9975
Temperature Dependence of k_0		$0.0002\exp(\frac{-3196}{T})$	0.9962

Table 2-22: Linear model for concentration and temperatue dependency of Gd properties.

		Equation	R2
Temperature Dependence of E^*			
	3 wt% $GdCl_3$	$7.70\times10^{-4}\,T - 3.710$	0.9972
	6 wt% $GdCl_3$	$7.50\times10^{-4}\,T - 3.729$	0.9999
	9 wt% $GdCl_3$	$7.50\times10^{-4}\,T - 3.734$	0.9868
Concentration Dependence of E^*			
	723 K	-89.597 [C]-3.186	0.8003
	773 K	-102.44 [C]-3.134	0.909
	823 K	-95.201 [C]-3.092	0.7972
Temperature Dependence of $D_{Gd^{3+}}$			
	3 wt% $GdCl_3$	$0.0023\exp(\frac{-4445}{T})$	0.9986
	6 wt% $GdCl_3$	$0.0015\exp(\frac{-4783}{T})$	0.9939
	9 wt% $GdCl_3$	$0.0010\exp(\frac{-5688}{T})$	0.9981
Concentration Dependence of $D_{Gd^{3+}}$			
	723 K	-1.11×10^{-2} [C] + 6.81×10^{-6}	0.9781
	773 K	-1.68×10^{-2} [C] + 1.03×10^{-5}	0.9692
	823 K	-2.29×10^{-2} [C] + 1.43×10^{-5}	0.9835
Temperature Dependence of i_0			
	1 wt% $GdCl_3$	$5.686\times10^{-5}\,T - 0.0036$	0.9681
	3 wt% $GdCl_3$	$2.623\times10^{-4}\,T - 0.1787$	0.9144
	6 wt% $GdCl_3$	$5.679\times10^{-4}\,T - 0.3911$	0.9951
	9 wt% $GdCl_3$	$6.946\times10^{-4}\,T - 0.4576$	0.9992
Concentration Dependence of i_0			
	723 K	$13.284\,[C]^{0.653}$	0.9890
	773 K	$43.807\,[C]^{0.753}$	0.9970
	823 K	$81.648\,[C]^{0.790}$	0.9940
Temperature Dependence of k_0		$0.1447\exp(\frac{-5869}{T})$	0.9779

*C is in mol cm^{-3}

Table 2-23: Linear model for concentration and temperatue dependency of Nd properties.

		Equation	R2
Temperature Dependence of E^*			
for Nd^{3+}/Nd^{2+}	3 wt% $NdCl_3$	5.20×10^{-4} T – 3.511	0.9925
	6 wt% $NdCl_3$	7.00×10^{-4} T – 3.631	0.9829
	9 wt% $NaCl_3$	6.60×10^{-4} T – 3.563	0.9923
Concentration Dependence of E^* for Nd^{3+}/Nd^{2+}			
	723 K	133.91 [C] – 3.1710	0.9423
	773 K	129.13 [C] – 3.1407	0.9178
	823 K	167.39 [C] – 3.1233	0.9997
Temperature Dependence of E^*			
for Nd^{2+}/Nd^{0}	3 wt% $NdCl_3$	7.00×10^{-4} T – 3.652	0.9829
	6 wt% $NdCl_3$	7.40×10^{-4} T – 3.649	0.9961
	9 wt% $NaCl_3$	6.50×10^{-4} T – 3.561	0.9777
Concentration Dependence of E^* for Nd^{2+}/Nd^{0}			
	723 K	-131.52 [C] – 3.0643	0.9817
	773 K	-126.74 [C] – 3.0247	0.9858
	823 K	-119.57 [C] – 2.9997	0.9173
Temperature Dependence of $D_{Nd^{3+}}$			
	3 wt% $NdCl_3$	$0.0033\exp(\frac{-4460}{T})$	1
	6 wt% $NdCl_3$	$0.0282\ \exp(\frac{-6065}{T})$	0.9842
	9 wt% $NaCl_3$	$0.0033\ \exp(\frac{-4355}{T})$	0.8755
Temperature Dependence of $D_{Nd^{2+}}$			
	3 wt% $NdCl_3$	$0.0063\exp(\frac{-4597}{T})$	1
	6 wt% $NdCl_3$	$0.0121\ \exp(\frac{-5257}{T})$	0.9781
	9 wt% $NaCl_3$	$0.0046\ \exp(\frac{-4203}{T})$	0.9173
Concentration Dependence of $D_{Nd^{2+}}$			
	723 K	-8.369×10^{-3} [C] + 1.23×10^{-5}	0.8928
	773 K	-6.934×10^{-3} [C] + 1.78×10^{-5}	0.9542
	823 K	-1.841×10^{-2} [C] + 2.73×10^{-5}	0.9986

*C is in mol cm^{-3}

2.6. Calculation of RE properties using molecular dynamics simulation

In the present study, activity coefficient, apparent potential, and diffusion coefficient of lanthanum, yttrium, scandium, and terbium in the molten salt (58 at% LiCl and 42 at% KCl) were calculated by the method of molecular dynamics simulation up to a concentration around 3 at% at temperatures of 723 K and 773 K.

2.6.1. Methodology

The system of LiCl-KCl-$RECl_3$ (RE=La, Y, Sc, Tb) can be treated as a homogeneous binary solution because the composition of LiCl-KCl does not change for all the calculations. Therefore, the total Gibbs free energy can be expressed by

$$G_{real} = n_1({\mu_1}^0 + RTlnx_1 + RTln\gamma_1) + n_2({\mu_2}^0 + RTlnx_2 + RTln\gamma_2) \quad (2\text{-}44)$$

where ${\mu_1}^0$ and ${\mu_2}^0$ are the chemical potentials of the pure component 1 and 2, R is the gas constant, n is mole number, x is mole fraction, γ is activity coefficient.

For the ideal solution, the activity coefficient of every component is unit, so the total Gibbs free energy is simplified into

$$G_{ideal} = n_1({\mu_1}^0 + RTlnx_1) + n_2({\mu_2}^0 + RTlnx_2) \quad (2\text{-}45)$$

Thus, the excess Gibbs free energy is

$$G_{excess} = G_{real} - G_{ideal} = n_1RTln\gamma_1 + n_2RTln\gamma_2 \quad (2\text{-}46)$$

With respect to the mole number n_1, the partial derivative should be

$$\left(\frac{\partial G_{excess}}{\partial n_1}\right)_{n_2,p,T} = RTln\gamma_1 + n_1RT\frac{\partial ln\gamma_1}{\partial n_1} + n_2RT\frac{\partial ln\gamma_2}{\partial n_1} = RTln\gamma_1 \quad (2\text{-}47)$$

Hence, the activity coefficient γ_1 can be calculated by excess Gibbs free energy.

For the calculation of self-diffusion coefficient, it is related to the mean squared displacement (MSD) by [69,70]

$$D_s = \frac{1}{6}\lim_{t\to\infty}\frac{d}{dt}(MSD) \quad (2\text{-}48)$$

where D_s is the self-diffusion coefficient, t is time. *MSD* is determined by [70]

$$MSD = \langle(p(t) - p_0)^2\rangle = \frac{1}{N}\frac{1}{n_t}\sum_{j=0}^{n_t}\sum_{i=0}^{N}(p_i\left(t_{0j} + t\right) - p_i(t_{0j}))^2 \quad (2\text{-}49)$$

where $p(t)$ is the positon at the time of t and p_0 is the initial position, N is the atom number, n_t is the time origins number, t_{0j} is the initial timestep at time j. However, what we need is the chemical diffusion coefficient, also called diffusivity, it can be expressed by [71]

$$D_c = D_s(1 + \frac{dln\gamma}{dlnx}) \quad (2\text{-}50)$$

where D_c is the chemical diffusion coefficient, γ is activity coefficient and x is mole fraction.

As for the simulation details, molecular dynamics simulation and thermodynamic integration [72] were used in this research. All of our simulations were run with molecular dynamics software LAMMPS [73,74] using the Born-Mayer-Huggins potential. The parameters used are given in Ref. [75].

2.6.2. Results

Figure 2-60 shows the calculated activity coefficients of $LaCl_3$, YCl_3, $ScCl_3$, and $TbCl_3$ in LiCl-KCl from the simulation. In general, the activity coefficients increase with the increase in species concentration which is consistent with our experimental findings. However, it should be mentioned that, compared to the experimental activity coefficient of $LaCl_3$, the model overestimates the value in 1-2 order of magnitude.

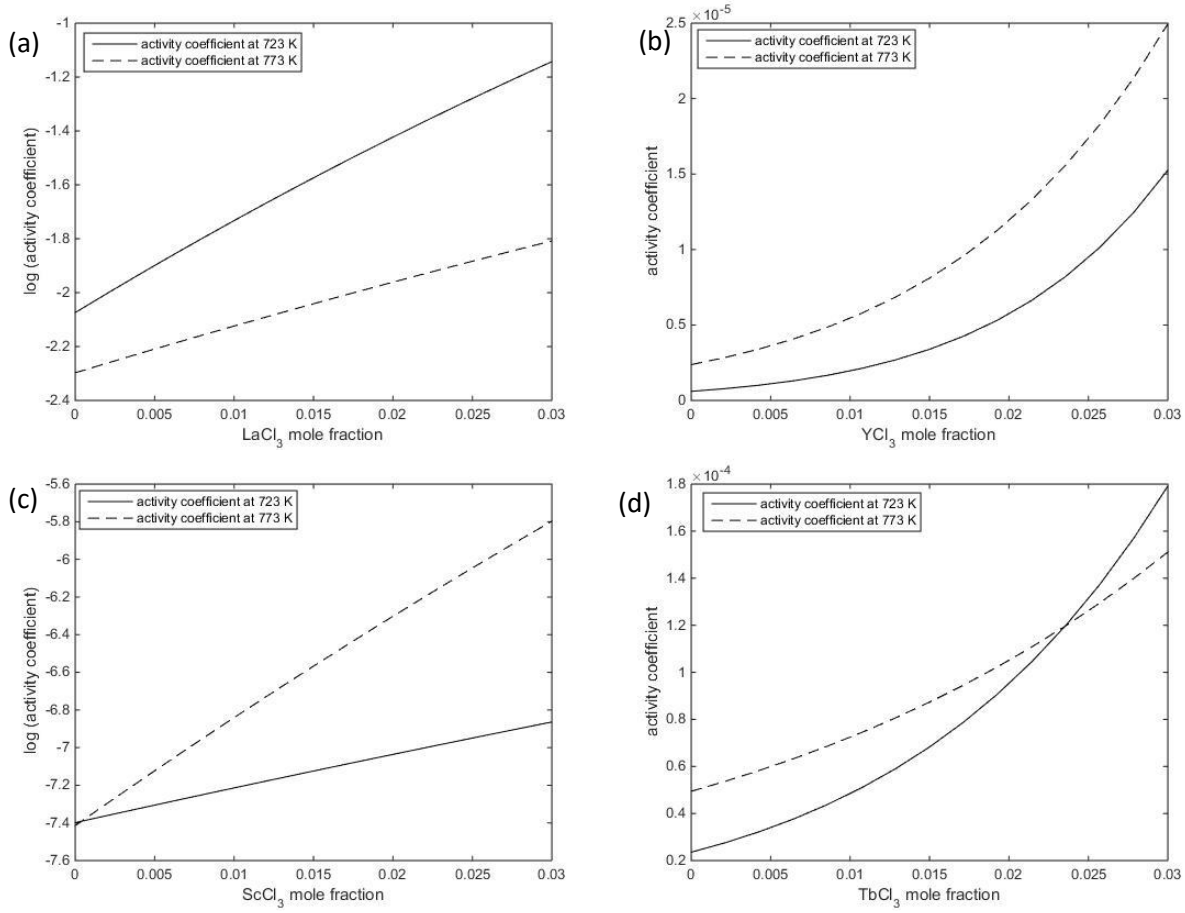

Figure 2-60: Calculated activity coefficient of (a) $LaCl_3$ (b) YCl_3 (c)$ScCl_3$ (d) $TbCl_3$ in LiCl-KCl eutectic.

Figure 2-61 shows the calculated self diffusion coefficient and chemical diffusion coefficient of $LaCl_3$, YCl_3, $ScCl_3$, and $TbCl_3$ in LiCl-KCl from the simulation. It seems that the chemical diffusion coefficients are slightly depend on the concentrations although it increases for lower concentrations and then decreases slightly when the concentration of $RECl_3$ in eutectic molten salt is high enough. The interesting result is that there is no big change in the self-diffusion coefficient with the increase of concentration and it almost keeps stable. The simulated $LaCl_3$ diffusion coefficients agree well with the experimental values at lower concentrations.

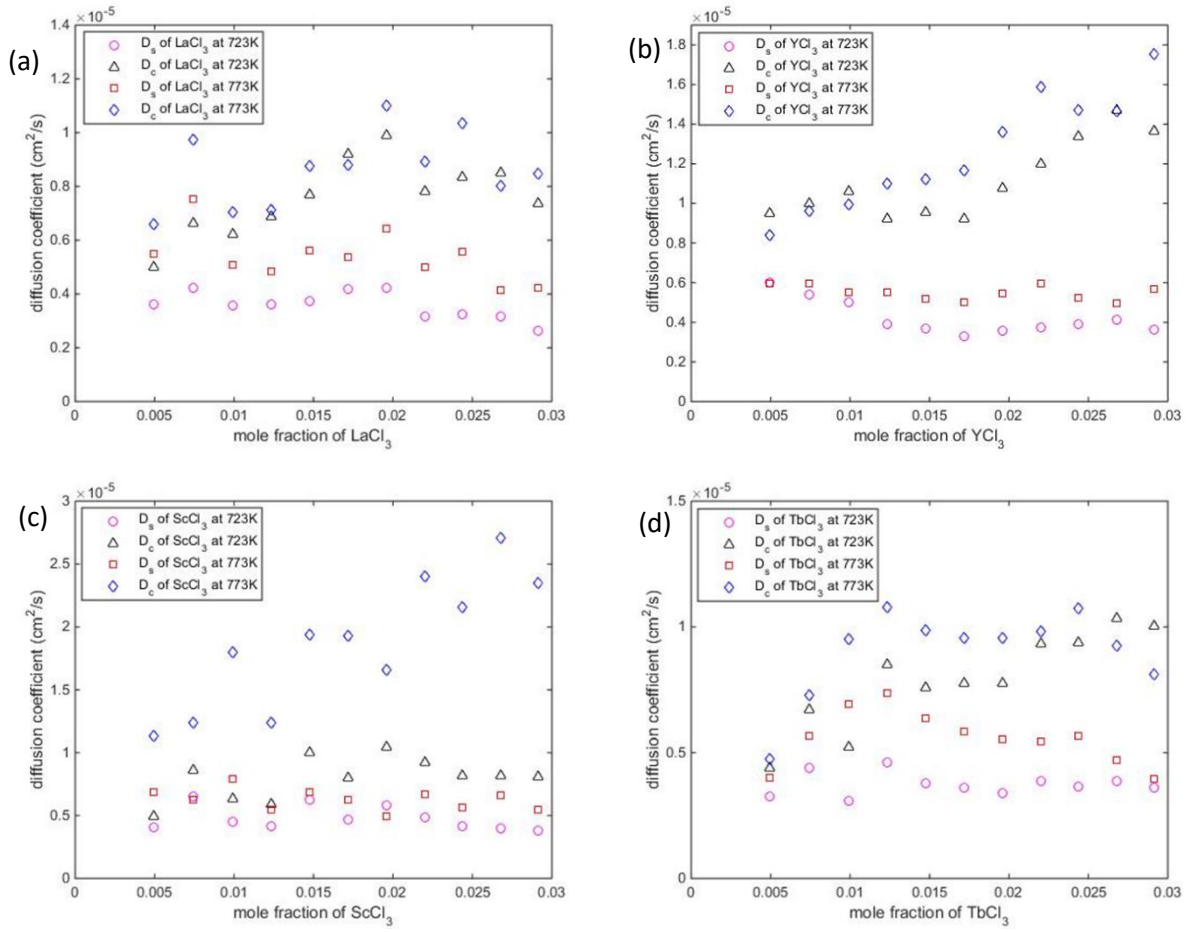

Figure 2-61: Self diffusion coefficient and chemical diffusion coefficient of (a) $LaCl_3$ (b) YCl_3 (c)$ScCl_3$ (d) $TbCl_3$ in LiCl-KCl eutectic.

3. Effects of CsCl on fundamental properties

3.1. Experimental system and methods

3.1.1. Salt preparation and handling

Because of the extremely hygroscopic nature of these salts, they must be handled, mixed, and sampled in a dry atmosphere. Two argon atmosphere glove boxes have been installed in the University of Utah's Nuclear PyroMetallurgy Laboratory (NPML) to support these tests in addition to other studies. A photograph of NPML Glovebox #2 is shown in Figure 3-1. Both glovebox atmospheres are maintained at <1 ppm for both water and oxygen gas. These gloveboxes were purchased by the University of Utah using startup funding for Prof. Simpson's research and were acquired from Innovative Technologies. They feature heat exchangers and chillers to maintain a safe operating temperature inside of the glove box while as many as two furnaces are simultaneously operating.

Figure 3-1: Argon atmosphere glove box and high temperature electrochemistry furnace.

To efficiently collect both electrochemical and thermophysical data from each experiment, the process flow shown in Figure 3-2 was adopted. A key aspect of our experiments is the study of concentration effects. Development of an efficient method for changing the salt composition was, thus, an important achievement for the first year of the project. This methodology will be described later but is represented in Figure 3-2 in the "change salt composition" box.

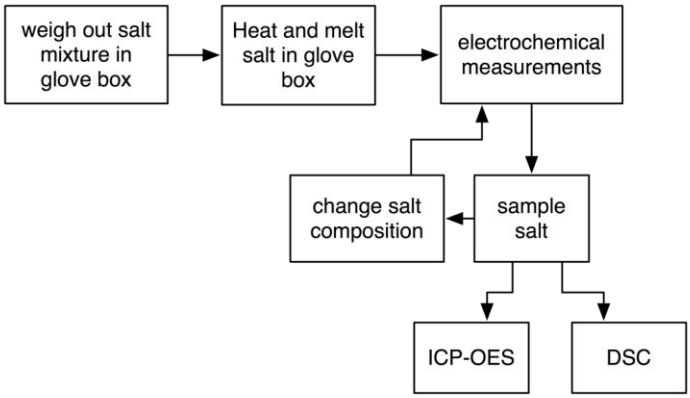

Figure 3-2: Process flow for experimental measurements in section 3.

Within the glove boxes, salts are weighed and mixed in alumina crucibles, and heated in Kerr electromelt furnaces. The only time that salts are exposed to outside air atmosphere is when they are being quickly loaded into the DSC (described in more detail later). A photograph of a Kerr furnace being used for an electrochemical measurement of molten salts is shown in Figure 3-3. These furnaces can be heated up to 1120°C and have a heated zone with a diameter of 5.5 cm and a depth of 10 cm. Salt mixtures contained in alumina crucibles are heated nominally to 500°C or an alternative temperature as desired to ensure formation of a homogenous fused salt solution.

Figure 3-3: Kerr electromelt furnace used for melting salts in the NPML gloveboxes.

3.1.2. Electrochemical measurements

The primary electrochemical measurement made under this task was an open circuit potential measurement of a La, Gd, Ce, or Nd metal rod versus a reference electrode. This yields an equilibrium potential for rare earth ion reduction that can be used to calculate apparent standard potential and activity coefficient using the Nernst Equation. Configuration for the test cell is shown in Figure 3-4. Options for the reference electrodes (RE) included a variety of different redox pairs enclosed in a closed-ended tube make of Pyrex or mullite. NMR tubes were used for the Pyrex option, while the mullite tubes were purchased from Ceramic Solutions (5 mm OD, 3 mm ID). Three various redox pairs used for the reference electrodes are described as follows.

- For $GdCl_3$ experiments, the reference electrode used in these experiments was a 70 mol% Gd|$GdCl_3$-LiCl-KCl electrode. It was determined that 70 mol%, the $GdCl_3$ is super saturated in LiCl-KCl at 500 °C. Hence, a 70 mol% reference electrode has excess solid $GdCl_3$ present in the reference electrode. The presence of this solid is critical to the experimental set-up. The reference electrode was conditioned at 650 °C for a few hours to make a homogenous mixture in the reference electrode. This conditioned electrode was now used for the experiments.
- For $CeCl_3$ experiments, the reference electrode used in these experiments was a 70.3 mol% Ce|$CeCl_3$-LiCl-KCl electrode. Previous tests conducted by us showed that at 70 mol%, the $CeCl_3$ is super saturated in LiCl-KCl at 500°C. Hence, a 70 mol% reference electrode has excess sold $CeCl_3$ present in the reference electrode. The presence of this solid is critical to the experimental set-up. The reference electrode was conditioned at 500°C for 24 hours to make a homogenous mixture in the reference electrode. This conditioned electrode was now used for the experiments.
- Ag wire in 5 mol% AgCl in LiCl-KCl contained in either a Pyrex or mullite closed-ended tube. The other electrode is the working electrode (WE) which consisted of a stainless steel basket loaded with a La metal rod. The mass of salt in the crucible was normally 49 grams of LiCl-KCl eutectic. The potential difference between the RE and WE was measured using an Autolab 302N potentiostat.

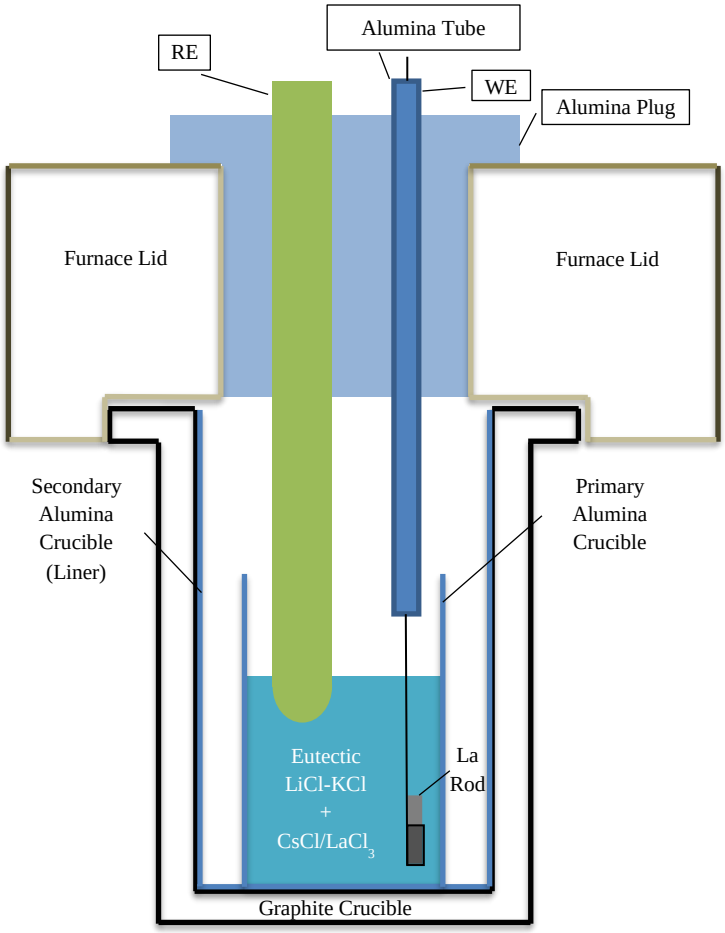

Figure 3-4: Electrochemical test cell configuration.

3.1.3. Salt sampling/addition

The method for sampling the salt is key in order to ensure that a representative composition is obtained. In our view, allowing the salt to refreeze in the crucible followed by chipping away solid samples is unacceptable. The slow cooling of the salt can result in zone refining, as has been previously demonstrated by researchers at KAERI and University of Idaho. The method used in these tests is to insert an alumina tube into the salt, hold a finger on the end of the tube protruding from the furnace, extract the tube, and remove the finger while holding the tube over an aluminum sample pan. This results in the collection of small droplets of salt that can then be crushed and loaded into a differential scanning calorimeter (DSC) pan or dissolved in acid for ICP-OES analysis. After running an initial set of experiments in which the salt was allowed to cool down before adding more $LaCl_3$, a procedure was adopted for making incremental additions of $LaCl_3$ during the experiment to allow for multiple OCP measurements and samplings in a single day. We believe this improved the accuracy of the measurements, since a single RE could be used for a wide range of salt concentrations. The salt addition procedure was as follows: The desired quantity of salt was calculated and weighed out an analytical balance inside the glove box.

The salt was then added using a custom glass funnel with a large stem diameter. The large stem diameter ensured that none of the salt got stuck to the wall of the funnel stem. After the addition, the molten salt was stirred to with a thermocouple. Subsequently, the salt was allowed to stand to ensure that the newly added salt melted and dissolved. It was generally observed that after about 30 minutes of equilibration time, the La metal electrode was re-inserted into the molten salt. The system was again allowed to equilibrate for about 15 minutes. Thereafter, the OPC measurements were made.

3.1.4. Differential scanning calorimetry

The key instrument for developing phase diagrams for this task is the differential scanning calorimeter (DSC). In the NPML, a Q600 TGA/DSC unit from TA Instruments has been installed and made operational. The Q600 operates simultaneously as a DSC and a thermogravimetric analyzer (TGA). DSC's measure heat flow in a sample, while TGA's measure change in mass—all while the sample is subjected to a particular temperature program. This unit is shown in the photograph in Figure 3-5. Initially, the plan was to install and operate this instrument inside one of the gloveboxes. But it was found that the power supply repeatedly failed in an inert, dry atmosphere. It is assumed that the issue is that the electronics are incompatible with the dry atmosphere. Thus, the instrument was kept outside of the glovebox. The modified procedure is to prepare the samples and load the DSC pans inside of the glovebox and carefully transfer the samples in sealed vials out of the box and then load them into the Q600. The Q600 uses an ultra high purity (UHP) Ar gas as the carrier at nominally 100 ml/min. The samples are only exposed to the laboratory atmosphere for a few seconds while loading the instrument. This should be sufficiently short to ensure that there is no pickup of water into the samples. It was shown previously by researchers at University of Wisconsin that this approach could be reliably used [76].

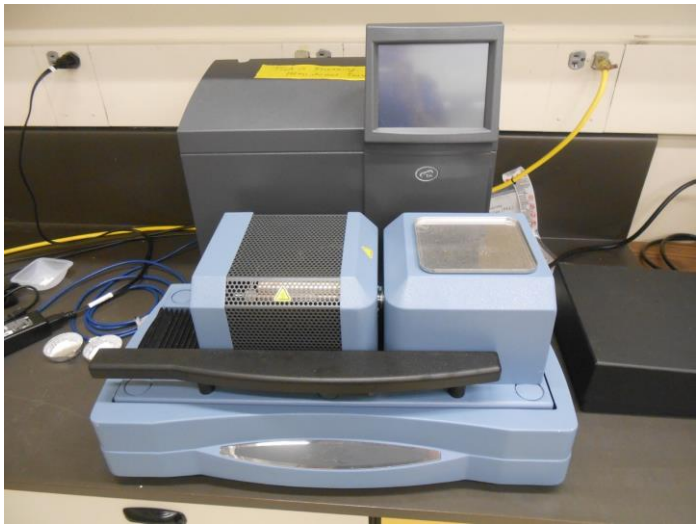

Figure 3-5: Q600 Simultaneous Thermal Analyzer by TA Instruments

The samples were heated in disposable aluminum pans. Each test was performed with about 10 mg of sample. The sample was heated at 10°C/min to 500°C for each run. For salts, the heating curve should be used to determine the liquidus and solidus temperatures due to the effect of super cooling [77]. Using such a heating cycle, endothermic peaks represent transitions from solid to liquid phases. Peak temperatures were determined to represent the various solid/liquid transitions occurring, and the peaks were integrated to determine heat of fusion. Instructions provided by TA Instruments were followed for temperature and heat flow calibrations prior to starting these experiments.

3.1.5. Galvanic drawdown of UCl_3 and $MgCl_2$ from LiCl-KCl

All of the drawdown experiments were performed inside a glove box (Innovative Technologies) with an argon atmosphere (<0.1 ppm O_2 and <0.1 ppm H_2O). Reagents used for this work included eutectic LiCl-KCl (ultra-dry 99.99 %, SAFC Hitech), UCl_3 (anhydrous, synthesized in house), $MgCl_2$ (99.99% anhydrous, Alfa Aesar), gadolinium metal rod (6.35 mm OD x 100 mm; 99.9 % ESPI Metals), $LaCl_3$ (99.99% anhydrous, ultra-dry, Alfa Aesar), $NdCl_3$ (99.99% anhydrous, ultra-dry, Alfa Aesar), and $CeCl_3$ (99.99% anhydrous, ultra-dry, Sigma Aldrich) Two distinct experimental set-ups were used for this study. The schematic of Experimental Setup 1 is shown in Figure 3-6. In this experimental setup, a Gd metal rod (6.35 mm OD x 25 mm) was placed inside a perforated stainless steel basket (12 mm OD, 35 mm height). The stainless steel basket was lined on the inside with a 450 micron stainless steel mesh screen. The stem of the basket was inserted into a rotating disk electrode rotator (Autolab). This allowed the Gd/basket assembly to be rotated at a specified rate.

The Experimental Setup 2 that was also used for this study is shown in Figure 3-7. In this configuration, a Gd rod (6.35 mm OD x 75 mm) was attached to a stainless steel coupler using a setscrew mechanism. This coupler/Gd assembly was then short circuited (outside the molten salt) to a stainless steel basket identical to the one used for Experimental Setup 1. Further, the stem of the stainless steel basket was inserted into an Autolab rotating disk electrode rotator (Metrohm). This allowed the stainless steel basket to be rotated at a desired RPM. In both of the experimental configurations, the rotator was mounted on a stand and clamp assembly atop the furnace (Kerr Electro-melt). The design for Experimental Setup 2 allowed for a reference electrode to be incorporated into the experimental setup giving access to data on potential of the rod and basket.

For these studies, a mixture of LiCl-KCl was prepared in a stainless steel crucible (57 mm OD x 86 mm, Lee Valley Tools). In the working electrolyte, the desired analyte species (UCl_3 with optional inclusion of $MgCl_2$, $LaCl_3$, $NdCl_3$, and $CeCl_3$) were introduced. $MgCl_2$ can be used as an electrochemical surrogate for other actinide chlorides, since its standard reduction potential is relatively close to that of the minor actinides. It is not a perfect surrogate, however, since it reduces by a 2-electron transfer rather than a 3-electron transfer. Thus, its inclusion in this study was intended to demonstrate possible behavior of the transuranic actinides during galvanic reduction. Testing with actual transuranic chlorides is needed to truly elucidate their behavior in this system. Such testing cannot be performed in our laboratory because of the radiological properties of the transuranics. $LaCl_3$, $NdCl_3$, and $CeCl_3$ were used to represent rare earth fission product impurities in the salt. Table 1 lists the conditions for all experiments. Rather than using as weighed concentrations, the initial concentrations of the salts and subsequent concentrations at

different sampling times were measured via ICP-MS (Agilent Technologies). This salt mixture was heated to 773±5 K in a Kerr electro-melt furnace. The temperature of the molten salt was confirmed by direct measurement of the salt using RTD thermocouples (Omega). No external current/potential was applied to drive the electrochemical reactions.

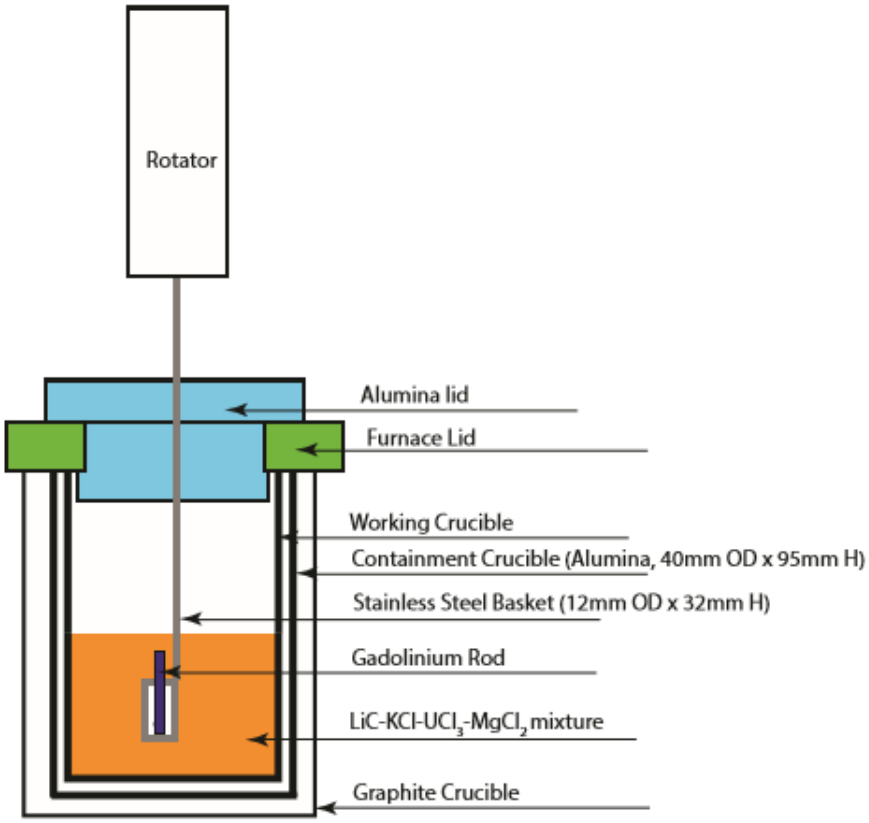

Figure 3-6: Schematic of the experimental set-ups used for this study (Setup 1)

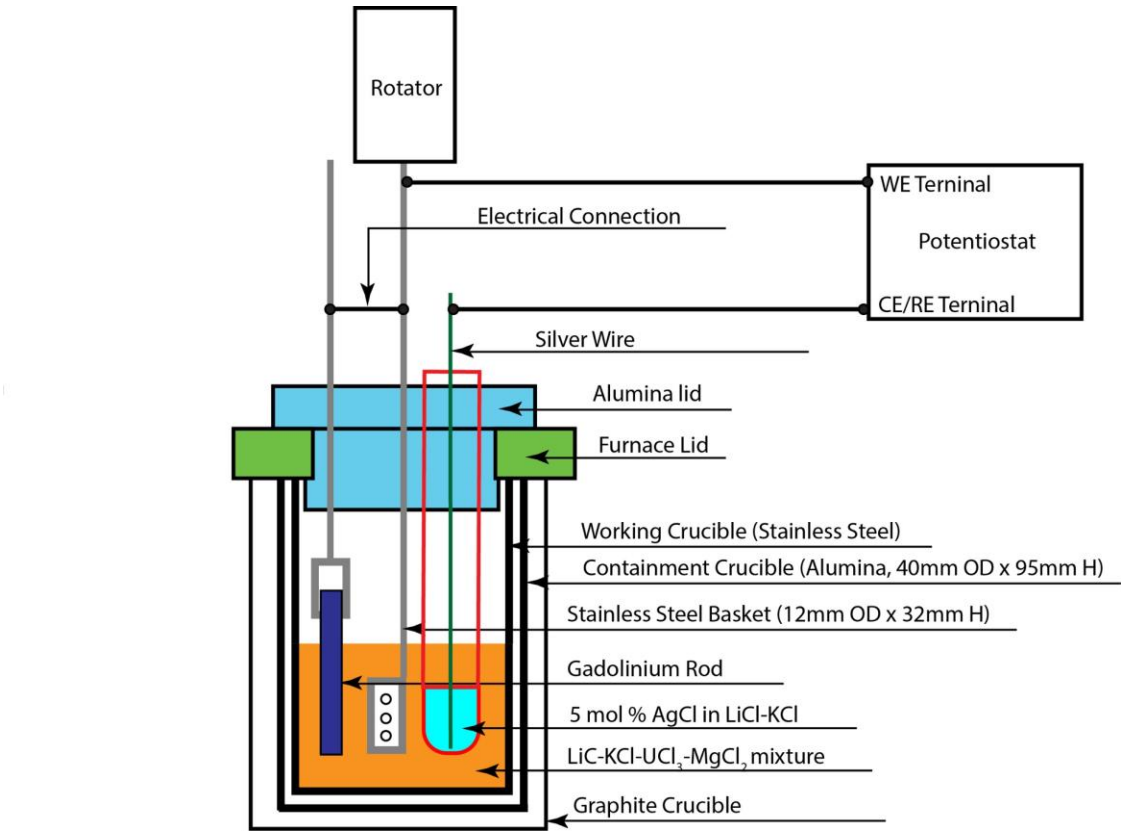

Figure 3-7: Schematic of the experimental set-ups used for this study (Setup 2)

Table 3-1: Summary of galvanic reduction experiments performed for this study

Test ID	Salt Mixture	Experimental Set-up	Rotation (RPM)	Temperature (K)
G1	LiCl-KCl-UCl_3	Setup 1	100	758
G2	LiCl-KCl-UCl_3	Setup 1	0	758
G5	LiCl-KCl-UCl_3	Setup 2	100	788
G6	LiCl-KCl-$MgCl_2$	Setup 2	100	788
G7	LiCl-KCl-UCl_3-$MgCl_2$	Setup 2	100	788
G8	LiCl-KCl-UCl_3-$MgCl_2$-$LaCl_3$-$NdCl_3$-$CeCl_3$	Setup 2	100	788

3.1.6. ICP-OES

ICP-OES was performed on the samples taken from the molten salt system. The samples were taken using a metal all-thread. When the all-thread is inserted into the molten salt mixture, the salt freezes on it. Upon withdrawal, this frozen salt can be easily separated from the all-thread using pliers, giving us salt flakes with a random size distribution. To

avoid errors associated with sampling and the inevitable segregation during solidification, all of the sample taken for a particular test was weighed and dissolved in an acidic solution having the same matrix as the standards used from calibration. After dissolution, the samples were diluted to make a concentration range of 0-100 ppm for the La concentration. Standards were prepared to generate a calibration curve for La within the 0-100 ppm concentration range. The dilution was performed using set of Eppendorf Pipettes (Research Plus). The accuracy of the pipettes was always checked before commencing dilutions using an analytical balance and ultra-pure water (18.2 M-Ohm). The ICP was performed on a Spectro Genesis ICP-OES instrument available at the university. The instrument available is equipped with an auto sampler, which helped with expedited analysis of the samples. No special treatment for the ICP-OES data was required.

3.2. Effects of CsCl on the electrochemical properties of $LaCl_3$, $NdCl_3$, $GdCl_3$, and $CeCl_3$ in LiCl-KCl

3.2.1. Theory

3.2.1.1. Calculation of activity coefficients

Electrochemical measurements can supplement thermal analysis data for developing phase diagrams for LiCl-KCl-$LaCl_3$-CsCl solutions. Specifically, the calculation of activity coefficients can be made on the basis of the Nernst equation given below specifically for the La^{3+}/La redox couple in this salt.

Electrochemical measurements can supplement thermal analysis data for developing phase diagrams for LiCl-KCl-$LaCl_3$-CsCl solutions. Specifically, the calculation of activity coefficients can be made on the basis of the Nernst equation given below specifically for the La^{3+}/La redox couple in this salt.

$$E_{eq,La3+/La} = E^{o}_{La3+/La} + \frac{RT}{nF}\ln\left(\frac{a_{La3+}}{a_{La}}\right) \quad (3\text{-}1)$$

Activity coefficient (γ_{LaCl3}) is defined as follows:

$$a_{La3+} = \gamma_{La3+} x_{La3+} \quad (3\text{-}2)$$

Standard reduction potential ($E^{0}_{La3+/La}$) can be calculated from the standard free energy of formation of super-cooled $LaCl_3$.

$$E^{o}_{La3+/La} = \frac{\Delta G^{o}_{f,LaCl3}}{3F} \quad (3\text{-}3)$$

Note that this standard potential is defined relative to the standard chlorine reference. Since our experiments use either AgCl/Ag, $CeCl_3$/Ce, or $GdCl_3$/Gd reference electrodes, it is necessary to convert potentials to the Cl^-/Cl_2 reference. For the use of AgCl/Ag, conversions were made using correlations reported by Shirai et. al. [78]. The standard free energy of

formation values were calculated using HSC Chemistry v7. The results of these calculations are given in Table 3-2.

Table 3-2: Calculated Standard Free Energy of Formation and Standard Reduction Potential for $LaCl_3$ Calculated Using HSC Chemistry v7. Standard potentials are relative to the Cl^-/Cl_2 electrode.

T (°C)	$\Delta G^o_{f,LaCl3}$ (kJ/mole)	$E^o_{La3+/La}$ (V)
400	-904.1	-3.123
425	-898.2	-3.103
450	-892.4	-3.083
500	-880.9	-3.043

For electrochemistry measurements of $CeCl_3$ and $GdCl_3$ in LiCl-KCl, special saturated reference electrodes were used. By using this approach, it is simpler to calculate activity based on an OCP measurement. Consider the following equation for OCP for $GdCl_3$, which can easily be re-written for $CeCl_3$.

$$E = \left(E^0_{GdCl3} + \frac{RT}{nF}\ln(activity)_{GdCl3}\right)_{WE} - \left(E^0_{GdCl3} + \frac{RT}{nF}\ln(activity)_{GdCl3}\right)_{RE} \quad (3\text{-}4)$$

In the reference electrode, since solid $GdCl_3$ is in equilibrium with liquid $GdCl_3$, their chemical potentials are equal. Hence, in the above equation, for the reference electrode term, E^0_{GdCl3} is equal to the standard potential of the solid $GdCl_3$ present. Now we can *choose* the standard state in the WE term to be the solid $GdCl_3$. Additionally, the $(activity)_{GdCl3}$ term in the RE is equal to 1 (since it is measured versus a solid). Hence, re-writing the above equation, we get equation (3-5).

$$E = \left(\frac{RT}{nF}\ln(activity)_{GdCl3}\right)_{WE} \quad (3\text{-}5)$$

Hence, using our experimental set-up we are able to measure the activity of the $GdCl_3$ in the working electrode. However, the standard state relative to which the activity is measured is the solid $GdCl_3$ standard state. To have a meaningful determination of the activity coefficient, we need to convert from the solid standard state to liquid standard state using Gibbs free energy of fusion of $GdCl_3$. Hence the final governing equation for our experimental set-up is as follows:

$$E = \left(\frac{RT}{nF}\ln(activity)_{GdCl3}\right)_{WE} + \frac{\Delta G_{Fusion}}{nF} \quad (3\text{-}6)$$

Equation (3-6) is the equation used to calculate the activity coefficient of the $GdCl_3$ present in the molten LiCl-KCl salt. We measure the E in our experiments as the OCP. This can be directly related back to the activity and activity coefficient. The Gibbs free energy of fusion of the $GdCl_3$ (at 773 K) was calculated to be 4.532 kJ/mole. This translated into 0.0156 V. For $CeCl_3$ (at 773 K), the Gibb's free energy of fusion is 13.478 kJ/mole.

3.2.1.2. Galvanic drawdown of actinides

As presented elsewhere in this report, equilibrium potentials were measured for $LaCl_3$/La, $CeCl_3$/Ce, $NdCl_3$/Nd, and $GdCl_3$/Gd in eutectic LiCl-KCl. The measured equilibrium potentials of the metals relative to a reference electrode were used to calculate apparent potentials (E^*) versus a standard Cl^-/Cl_2 potential, activity, and activity coefficient at concentrations ranging up to 4 mol % in eutectic LiCl-KCl [79,80]. The data indicated that the equilibrium potentials were more negative than those of the actinide chlorides over a wide range of rare earth chloride concentrations. The implication is that the natural potentials formed by rare earth metals in contact with molten LiCl-KCl contaminated with fission products and actinides could be used to reduce the actinides to metals and separate them from the salt. This could form the basis for a useful process to cleanup electrorefiner salt before it is disposed. Actinides could be recycled to the electrorefiner, and the waste salt could be rid of long-lived actinide isotopes that pose both radiological hard and proliferation risk. Hypothetically, a galvanic coupling of a rare earth metal with an electrochemically noble metal such as stainless steel could be used to drive reduction of the actinides onto the noble metal. A mixed potential effect occurs as shown in the diagram in Figure 3-8.

The Gd rod and stainless steel basket are at the corrosion potential (E_{corr}), which is more cathodic than the equilibrium U^{3+}/U potential and more anodic than the Gd^{3+}/Gd potential. This should drive reduction of UCl_3 to U on the stainless steel basket and oxidation of Gd metal to form $GdCl_3$ in the molten salt. The overpotentials cause the corresponding half cell reactions as per the Butler-Volmer equation. Gd metal is an ideal choice for reducing metal, since its equilibrium potential is more positive than that of the other rare earth chlorides ($NdCl_3$, $LaCl_3$, and $CeCl_3$) over the range of concentrations tested [81]. This should minimize or eliminate co-reduction of other rare earth metals during the process. Other rare earths should be considered in future expanded studies, including Y which has been demonstrated to also be effective at reducing UCl_3[82].

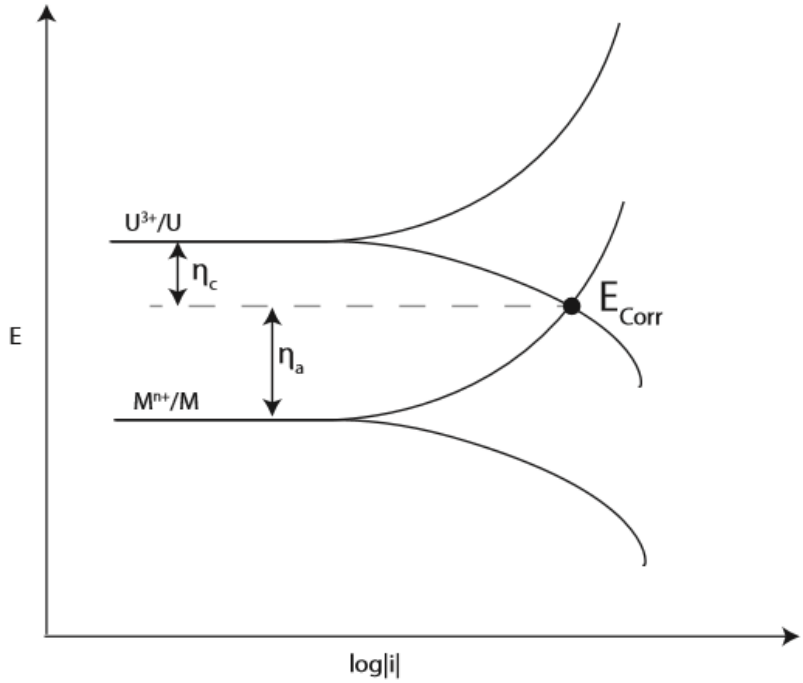

Figure 3-8: Schematic of the Butler-Volmer reactions for the U/Gd galvanic couple

The Gd rod and stainless steel basket are at the corrosion potential (E_{corr}), which is more cathodic than the equilibrium U^{3+}/U potential and more anodic than the Gd^{3+}/Gd potential. This should drive reduction of UCl_3 to U on the stainless steel basket and oxidation of Gd metal to form $GdCl_3$ in the molten salt. The overpotentials cause the corresponding half cell reactions as per the Butler-Volmer equation. Gd metal is an ideal choice for reducing metal, since its equilibrium potential is more positive than that of the other rare earth chlorides ($NdCl_3$, $LaCl_3$, and $CeCl_3$) over the range of concentrations tested [81]. This should minimize or eliminate co-reduction of other rare earth metals during the process. Other rare earths should be considered in future expanded studies, including Y which has been demonstrated to also be effective at reducing UCl_3 [82].

3.2.2. Electrochemistry of LiCl-KCl-$LaCl_3$ and LiCl-KCl-$LaCl_3$-CsCl

The first set of electrochemical measurements with LiCl-KCl-$LaCl_3$ (Test 2-7) were performed without any added CsCl. For each test, the $LaCl_3$ concentration was constant, while OCP measurements were made at four temperatures ranging from 400 to 500°C. The OCP values are equivalent to the equilibrium potential, E_{eq}, as defined above via the Nernst Equation. The E_{eq} values are tabulated in Table 3-3 in addition to an apparent standard potential, $E^*_{La3+/La}$, that is defined via the following modification to the Nernst Equation.

$$E_{eq} = E^*_{La3+/La} + \frac{RT}{3F}\ln\left(x_{LaCl3}\right) \qquad (3\text{-}7)$$

Table 3-3: Measured equilibrium reduction potential data for La^{3+}/La in LiCl-KCl relative to the Cl^-/Cl_2 reference potential. There was no CsCl added to the salt for these tests.

Test	Wt % $LaCl_3$	T=400ºC		T=425ºC		T=450ºC		T=500ºC	
		E_{eq}	E*	E_{eq}	E*	E_{eq}	E*	E_{eq}	E*
2	1.60	-3.250	-3.142	-3.237	-3.125	-3.223	-3.107	-3.195	-3.071
3	3.51	-3.236	-3.143	-3.222	-3.126	-3.212	-3.112	-3.181	-3.075
4	5.62	-3.219	-3.135	-3.208	-3.121	-3.191	-3.101	-3.158	-3.062
5	6.70	-3.217	-3.138	-3.201	-3.119	-3.190	-3.105	-3.158	-3.067
7	10.07	-3.215	-3.144	-3.202	-3.128	-3.186	-3.109	-3.158	-3.076
Zhang [17]			-3.164		-3.149		-3.134		-3.103

*All Potentials vs. Cl^-/Cl_2 electrode.

The apparent standard potentials listed in the bottom row were calculated from the following correlation reported in a paper by Zhang [17].

$$E^*_{La3+/La}(V) = -3.575 + 6.1 \times 10^{-4} T(K) \quad (3\text{-}8)$$

The calculation of activity coefficients from EMF cell measurements is an exponential mathematical relationship. Even a small error in the measurements of the open circuit potentials will not only propagate through the calculations but gets magnified as we go through our calculations. Hence we decided to curve fit (smooth) the open circuit measurements at this initial stage using a suitable mathematical model to prevent the further propagation and magnification of these errors. This data was modeled in Matlab. The open circuit potential measurements were fitted to a model of the form shown in equation below.

$$y = ae^{bx} + ce^{dx} \quad (3\text{-}9)$$

OCP data collected using LiCl-KCl with varying concentrations of $LaCl_3$ is tabulated in Table 3-4, and the OCP data is plotted in

Figure 3-9 with a fit based on the above equation.

Table 3-4: Results of open circuit potential measurements for La metal in contact with LiCl-KCl-$LaCl_3$ at T=500°C. Potentials have been corrected to be versus the Cl^-/Cl_2 reference electrode. Concentrations are based on concentration as determined by ICP-OES

Test ID	Wt. % $LaCl_3$	Mole % $LaCl_3$	OCP Values (model)	Apparent Standard Potential*	Activity Coefficient(γ)
MX-8-2	0.17%	0.04%	-3.301	-3.127	0.0029
MX-8-3	0.27%	0.06%	-3.293	-3.128	0.00275
MX-8-4	0.41%	0.09%	-3.281	-3.127	0.00298
MX-8-5	0.84%	0.19%	-3.257	-3.118	0.00442
MX-8-6	1.20%	0.27%	-3.243	-3.112	0.0057
MX-8-7	1.85%	0.43%	-3.228	-3.107	0.00712
MX-8-8	2.48%	0.57%	-3.221	-3.106	0.00738
MX-8-9	3.11%	0.72%	-3.217	-3.107	0.00705
MX-8-10	5.48%	1.30%	-3.210	-3.114	0.0053
MX-8-11	8.97%	2.19%	-3.204	-3.119	0.00418
MX-8-12	9.82%	2.42%	-3.202	-3.120	0.00407
MX-8-13	10.64%	2.64%	-3.201	-3.120	0.00399

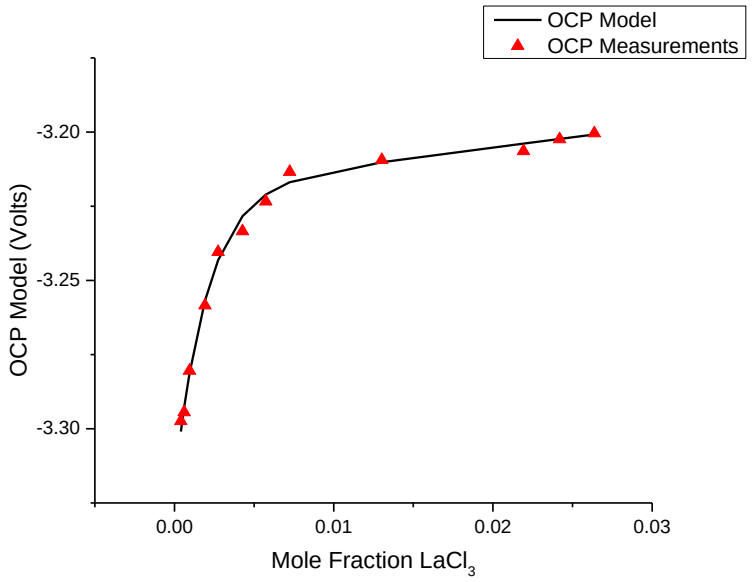

Figure 3-9: The Matlab fit for the OCP data.

A comparison between the measured values and modeled values showed that the average divergence between the model and experimental values was observed to be about 2 mV with a standard deviation of 1.4 mV. Such small errors are well within the realm of experimental error associated with physical measurements.

Figure 3-9 shows the experimental values of OCP plotted along with the model fit. The goodness of fit for the model and the actual data was greater than R^2=0.99. For all further calculations, the values obtained from the model were used.

Using the values obtained, we can calculate the apparent reduction potential and activity coefficients of dissolved La(III) in the molten salt. Figure 3-10 shows a plot of the apparent reduction potential plotted as a function of concentration. It can be observed that the value of the reduction potential is not a constant value as previously assumed and is indeed a function of concentration. The value of E^* initially increases (becomes more positive) reaching its most positive value at about 0.55 mole % La. It then proceeds to decrease (becomes more negative) and beginning to taper off at higher concentrations to a constant value. Within the concentration range tested, it is observed that the electrochemical potential for the reduction of La(III) to La(0) varies by about 25 mV.

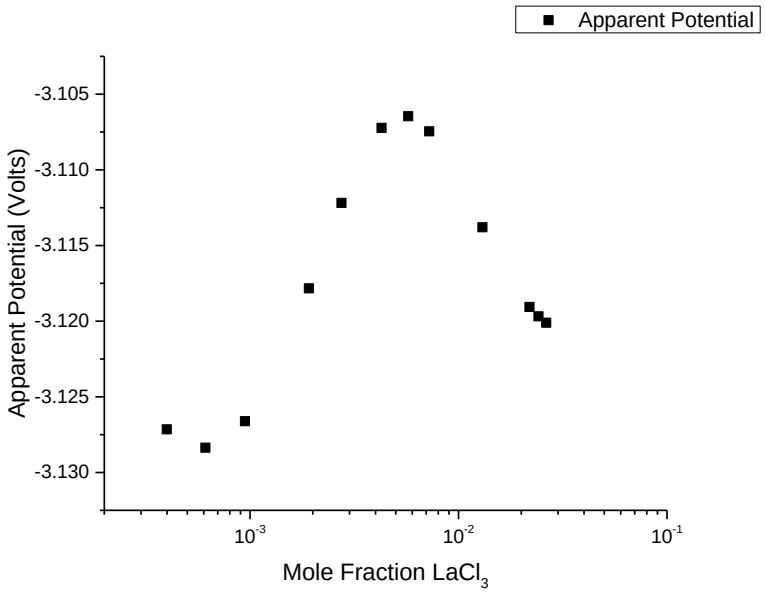

Figure 3-10: Apparent Reduction Potential of La(III)/La(0) plotted as a function of $LaCl_3$ concentration.

The activity coefficient of La(III), $\gamma_{La^{3+}}$ can now be calculated for each $LaCl_3$ concentration at which the open circuit measurement was performed. The standard state used for such calculations was the "Pure Supercooled Liquid Standard State." Figure 3-11 shows the plot of $\gamma_{La^{3+}}$ as a function of $LaCl_3$ concentration. We can see that the activity coefficient ($\gamma_{La^{3+}}$) of La(III) varies with concentration, initially increasing and subsequently decreasing, a function that is similar to the variation of apparent potential. Previously in literature, the value of $\gamma_{La^{3+}}$ is assumed to be independent of concentration. This data clearly show that the activity coefficient is a function of concentration of $LaCl_3$. The free energy of the pure supercooled liquid standard state used for our calculations is 867.628 kJ/mole. This corresponds to a E^o value of -2.997 V. This value is for 773 K only.

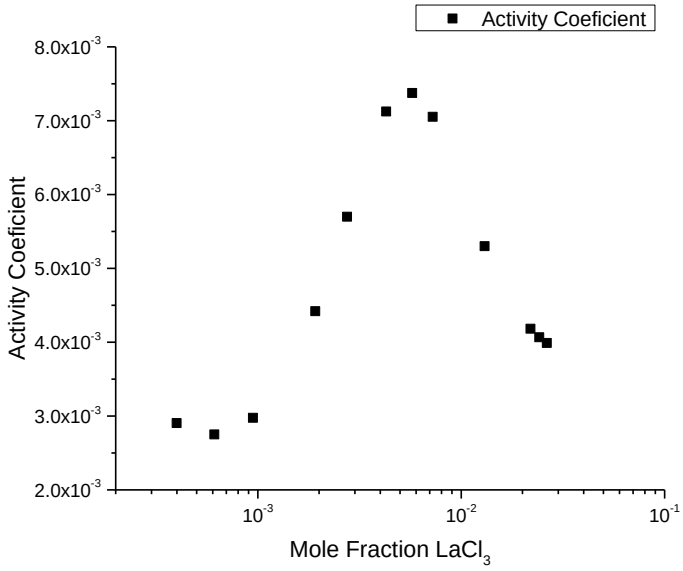

Figure 3-11: Activity Coefficient of La(III) plotted as a function of $LaCl_3$ concentration.

The effect of CsCl was studied at two concentrations. The two tests had an average concentration of CsCl of 0.69 mole % (Standard Deviation: 0.04 mole %) and 1.40 mole % (Standard Deviation: 0.04 mole %) CsCl. We followed the same methodology for analysis as was used in the analysis of the previous section. Initially the OCP values were fitted to a model. The average difference between the experimentally measured values and modeled values was again found to be less than 2 mV. The actual data for the two tests is presented in Tables 3-5 and 3-6.

Table 3-5: Results of open circuit potential measurements for La metal in contact with LiCl-KCl-$LaCl_3$ at T=500°C. Potentials have been corrected to be versus the Cl^-/Cl_2 reference electrode. Concentrations are based on concentration as determined by ICP-OES. Average CsCl concentration for this test is 0.69 mole % CsCl

Test ID	Wt. % $LaCl_3$	Mole % $LaCl_3$	OCP Values (model)	Apparent Standard Potential*	Activity Coefficient(γ)
Test 11-03	0.14%	0.03%	-3.297	-3.118	0.00441
Test 11-04	0.22%	0.05%	-3.291	-3.122	0.00369
Test 11-05	0.39%	0.09%	-3.279	-3.123	0.00348
Test 11-06	0.58%	0.13%	-3.268	-3.122	0.00374
Test 11-07	0.80%	0.19%	-3.259	-3.119	0.0042
Test 11-08	1.26%	0.29%	-3.245	-3.115	0.00499
Test 11-09	2.17%	0.51%	-3.230	-3.113	0.00543
Test 11-10	3.76%	0.89%	-3.220	-3.116	0.0049
Test 11-11	5.47%	1.32%	-3.213	-3.117	0.00454
Test 11-12	7.88%	1.94%	-3.204	-3.117	0.00469
Test 11-13	8.45%	2.09%	-3.202	-3.116	0.00481
Test 11-14	10.82%	2.73%	-3.192	-3.112	0.00564

Table 3-6: Results of open circuit potential measurements for La metal in contact with LiCl-KCl-$LaCl_3$ at T=500°C. Potentials have been corrected to be versus the Cl^-/Cl_2 reference electrode. Concentrations are based on concentration as determined by ICP-MS. Average CsCl concentration for this test is 1.40 mole % CsCl

Test ID	Wt. % $LaCl_3$	Mole % $LaCl_3$	OCP Values (model)	Apparent Standard Potential*	Activity Coefficient(γ)
MX 14-01	0.75%	0.18%	-3.257	-3.116	0.00476
MX 14-02	1.06%	0.25%	-3.251	-3.118	0.00443
MX 14-03	1.03%	0.24%	-3.251	-3.118	0.00444
MX 14-04	1.37%	0.32%	-3.245	-3.118	0.00443
MX 14-05	1.77%	0.42%	-3.238	-3.117	0.00468
MX 14-06	2.82%	0.67%	-3.222	-3.111	0.00593
MX 14-07	4.92%	1.20%	-3.200	-3.102	0.00922
MX 14-08	6.42%	1.58%	-3.190	-3.098	0.01096
MX 14-09	7.56%	1.88%	-3.185	-3.097	0.0115
MX 14-10	9.57%	2.42%	-3.181	-3.098	0.01072
MX 14-11	11.91%	3.07%	-3.182	-3.104	0.00807

Figure 3-12 shows a plot of the values of open circuit potential values for tests with three concentrations of CsCl; 0, 0.69 and 1.40 mole % CsCl as a function of $LaCl_3$ concentration. It can be observed that there is not much difference between the open circuit potentials for La/La(III) for the tests with the two lowest concentrations of CsCl i.e., 0 and 0.69 mole %. However, the equilibrium potentials for the species of interest (i.e., La/La(III)) shows a notable positive deviation in the presence of 1.40 mole % CsCl. This is only true at higher concentrations of $LaCl_3$. At low concentrations of $LaCl_3$, the equilibrium potentials for all of the three tests seem to be fairly similar. An additional key observation that can be made here is that, for the test with 0.69 % CsCl, we do see the OCP become more positive than the test with no CsCl present at higher $LaCl_3$ concentrations.

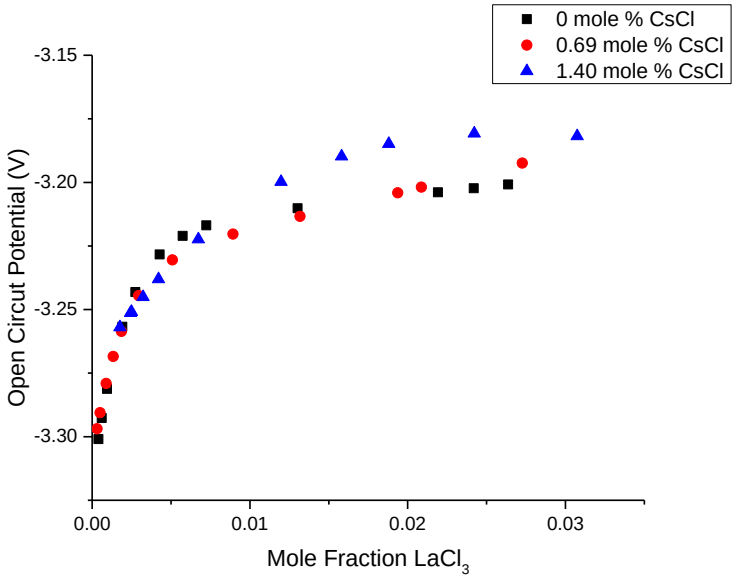

Figure 3-12: OCP (model) values plotted as a function of $LaCl_3$ concentration at three concentrations of CsCl; 0, 0.69 and 1.40 mole % CsCl.

Figure 3-13 shows the plot of apparent reduction potential as a function of $LaCl_3$ concentrations, for three distinct concentrations of 0, 0.69 and 1.40 mole %. CsCl. From the figure, we can observe that the nature of the graphs for all of the three tests are similar. All the three tests demonstrate that the apparent potential does indeed follow function pseudo Gaussian function, with a maximum at some concentration followed by a decline. The presence of the CsCl does indeed seem to have an effect on the apparent reduction potential of La(III). However 0.69 mole % Cs does not seem to have a substantial impact on the apparent potential. However, the presence of 1.40 mole % Cs does seem to move the curve to the right and make the apparent reduction potential of the La(III) more positive. An additional observation is that, both without any CsCl and with the presence of 0.69 mole % CsCl, the apparent reduction potential for La(III) reaches its most positive value at about

0.55 mole % $LaCl_3$. Similar behavior is observed for the activity coefficients of La(III) as shown in Figure 3-14.

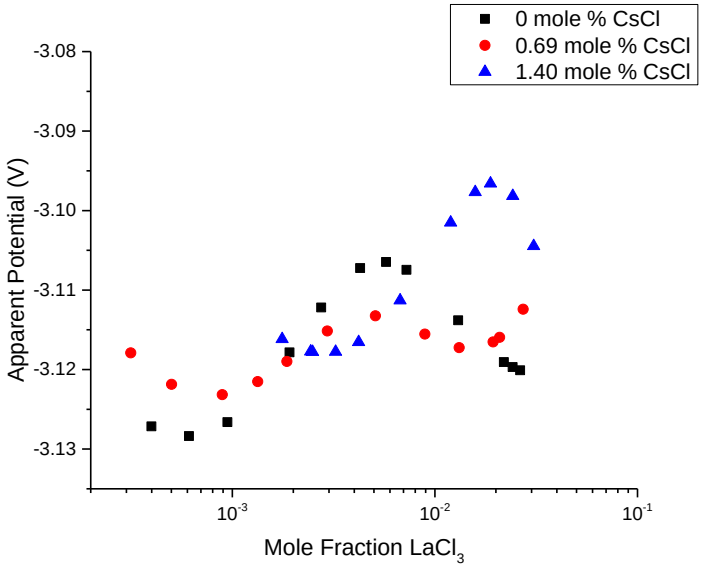

Figure 3-13: Apparent reduction potential for La(III)/La(0) plotted as a function of $LaCl_3$ concentration at three concentrations of CsCl; 0, 0.69 and 1.40 mole % CsCl.

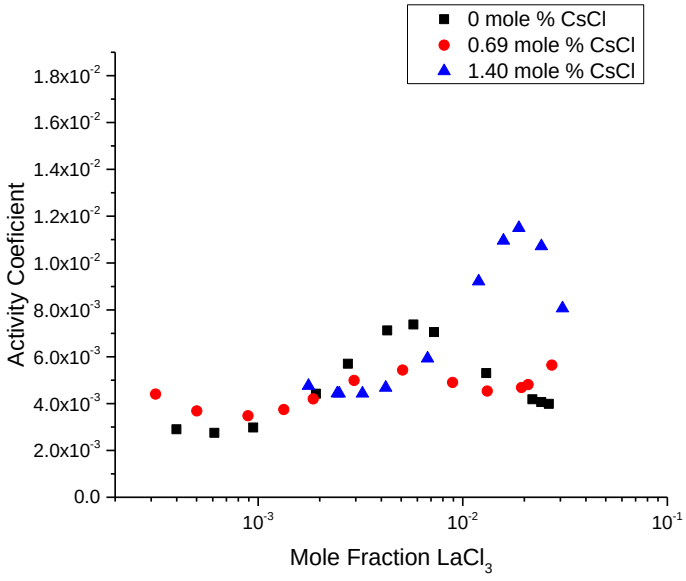

Figure 3-14: Activity Coefficient of La(III) plotted as a function of $LaCl_3$ concentration at three concentrations of CsCl; 0, 0.69 and 1.40 mole % CsCl.

3.2.3. Electrochemistry of LiCl-KCl-$NdCl_3$

Testing with the $NdCl_3$ system proved to be very challenging. We initially tried to use a saturated $NdCl_3$/Nd reference electrode. However, it was impossible to obtain stable and reproducible potentials during any of these tests. In some cases, midway during the attempted testing, the reference electrode casing of either mulite or pyrex broke, bringing a premature end to the tests. A literature survey reported that the Nd(II) species present is very unstable and has a propensity to corrode SiO_2 (which is present in both pyrex and mulite) to form NdOCl species. The redox equilibrium reaction of Nd(III) + Nd = Nd(II) is likely shifted to the right, since there is an excess amount of Nd metal present in the reference electrode. Hence, it is possible that the reference does not reach equilibrium. This may be the reason for the potentials being continuously unstable during testing.

After repeated failed attempts were made to use the Nd-$NdCl_3$-LiCl-KCl reference electrode, tests were conducted using a 5 mole % Ag/AgCl reference electrode encased in a mullite tube. During this test, the potentials observed were extremely stable.

The challenge of knowing the relative amounts of species in the two oxidation states (+2 and +3) still remains. After $NdCl_3$ is dissolved into the molten salt mixture, it can undergo redox reactions to form a mixture of Nd(II) and Nd(III) species. Hence, it cannot be assumed that all of the added $NdCl_3$ is present as Nd(III). Since a piece of Nd metal is in the salt, there is a pathway to forming Nd(II). Determining the oxidation state in the molten salt can be done with only a few techniques (UV-Vis, Raman Spectroscopy), but they are rarely available in systems that feature high temperature, inert atmosphere cells. It is thus impossible to determine exact mole fraction of the $NdCl_3$ species in the molten salt mixture. Without availability of such information, it is at this point only possible to determine the activity and not activity coefficient of $NdCl_3$ in the molten salt, as activity can be inferred from equilibrium potential using the Nernst equation as follows.

$$a = exp\left(\frac{nF}{RT}\left(E_{eq} - E^{o}\right)\right) \tag{3-10}$$

Figure 3-15 shows the results OCP vs. log of the mole fraction of $NdCl_3$ added into the molten salt mixture measured versus a 5 mole % Ag/AgCl reference electrode. Using these measurements, the activity of the $NdCl_3$ in the molten salt species can be determined and is shown in Figure 3-16. The Raoultian standard reduction potential for Nd(III)/Nd reduction was calculated to be -2.909 vs. Cl^-/Cl_2 electrode. Figure 3-16 shows the comparison for the ideal and real activity of $NdCl_3$ in the molten salts. It can be observed that the real activity deviates significantly for ideal behavior. The raw data for the experiments is presented in Table 3-7.

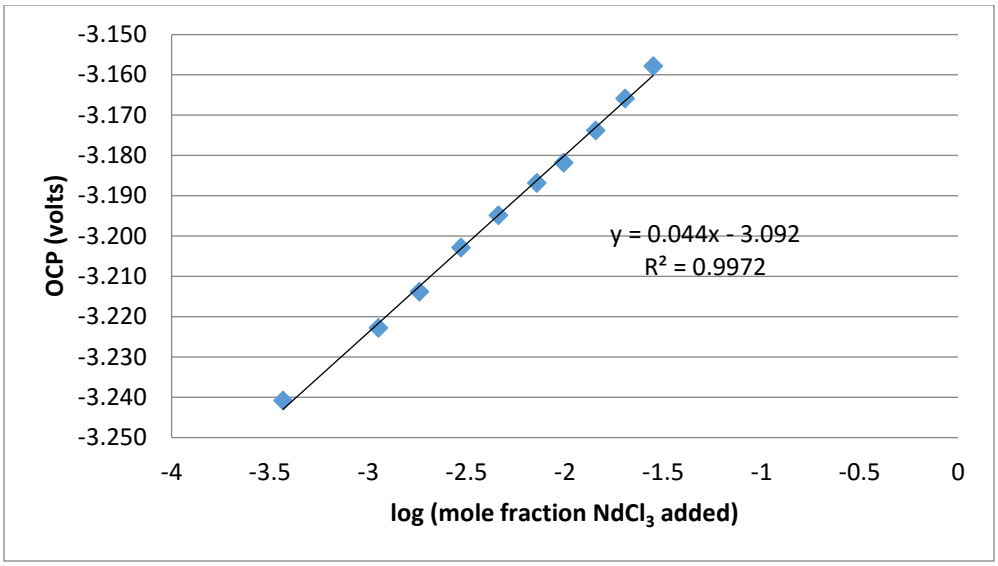

Figure 3-15: OCP plotted as a function of log($NdCl_3$) added to the eutectic LiCl-KCl at 773 K.

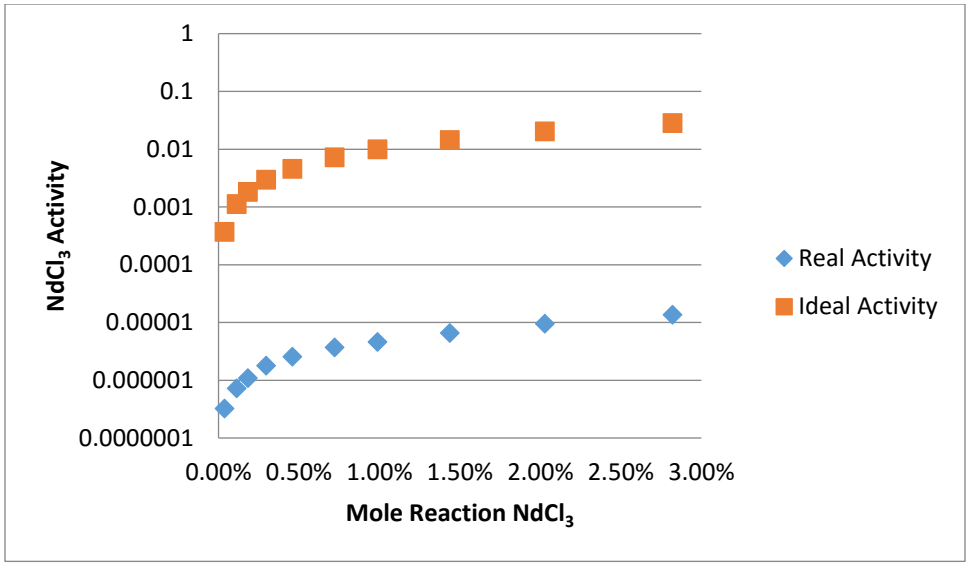

Figure 3-16: Activity plotted as a function of mole fraction $NdCl_3$ added to the eutectic LiCl-KCl at 773 K.

Table 3-7: Results from Electrochemical Testing. Concentrations are based on concentration as-weighed.

Test ID	Wt. % $LaCl_3$	Mole % $LaCl_3$	OCP Values	Real Activity
18-Nd-01	0.17%	0.04%	-3.241	$3.24x10^{-7}$
18-Nd-02	0.51%	0.11%	-3.223	$7.28 x10^{-7}$
18-Nd-03	0.82%	0.18%	-3.214	$1.09 x10^{-6}$
18-Nd-04	1.33%	0.30%	-3.203	$1.79 x10^{-6}$
18-Nd-05	2.07%	0.46%	-3.195	$2.57 x10^{-6}$
18-Nd-06	3.26%	0.72%	-3.187	$3.68 x10^{-6}$
18-Nd-07	4.48%	0.99%	-3.182	$4.61 x10^{-6}$
18-Nd-08	6.55%	1.44%	-3.174	$6.61 x10^{-6}$
18-Nd-09	9.30%	2.03%	-3.166	$9.48 x10^{-6}$

3.2.4. Electrochemistry of LiCl-KCl-$CeCl_3$ and LiCl-KCl-$CeCl_3$-CsCl

Figure 3-17 shows a graph of OCP versus mole fraction of CeCl3 in LiCl-KCl. In Figure 3-17, OCP(LSS) =(measured E + ΔG_F). It can be seen that the OCP shows a pseudo – logarithmic relationship. From the OCP, the activity can be calculated as shown in equation (3-6). This has been shown in Figure 18. As it can be seen from Figure 3-18, the activity of the $CeCl_3$ deviates significantly from the ideal behavior. Finally, knowing the activity and the mole fraction, the activity coefficient can be calculated. This has been plotted as a function mole % $CeCl_3$ and shown in Figure 3-19. It can be observed from Figure 3-19 that the activity coefficient increases almost linearly with concentration. Table 3-8 gives all of the results for OCP testing with LiCl-KCl-$CeCl_3$.

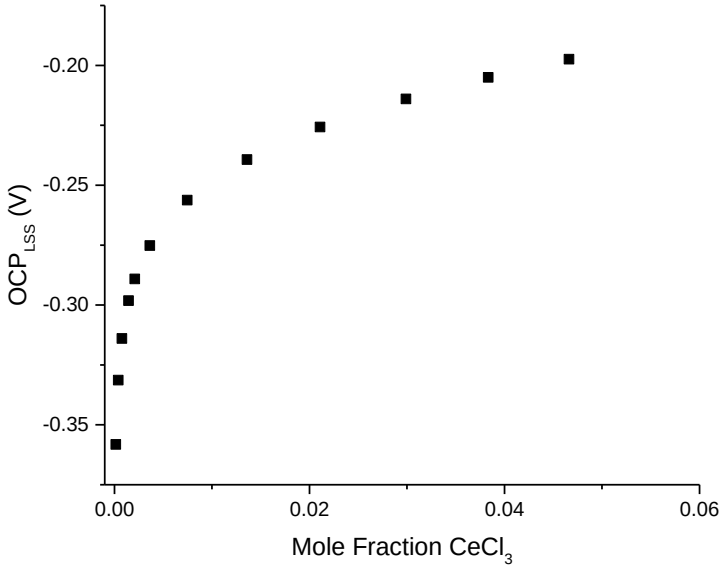

Figure 3-17: OCP vs. mole fraction of $CeCl_3$.

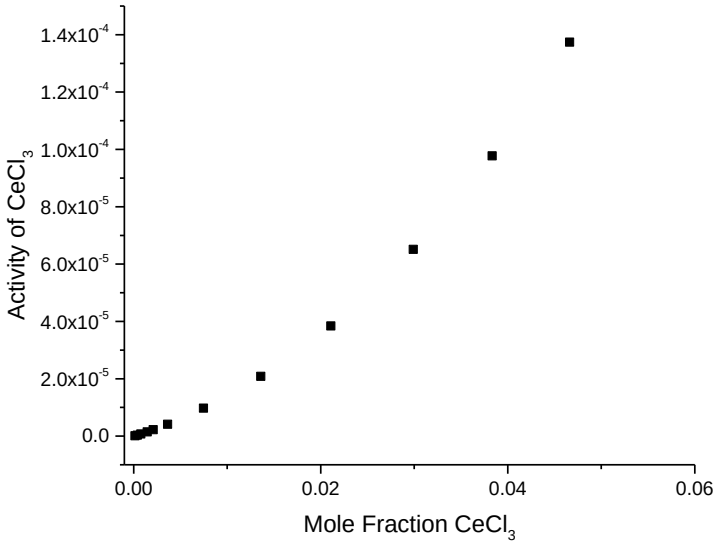

Figure 3-18: Activity of $CeCl_3$ as a function of mole percent $CeCl_3$

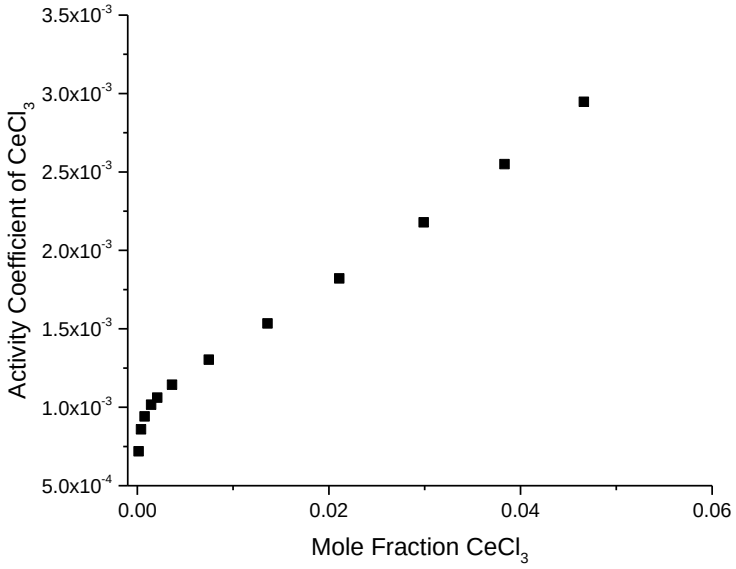

Figure 3-19: Activity coefficient of $CeCl_3$ as a function of mole percent $CeCl_3$

Table 3-8: Results from Electrochemical Testing with LiCl-KCl-$CeCl_3$. Concentrations are based on concentration as-weighed.

Test ID	Mole % $CeCl_3$	OCP (LSS)	Real Activity	Activity Coefficient
25-Ce-1	0.01%	-0.358	$9.86x10^{-8}$	$7.19x10^{-4}$
25-Ce-2	0.04%	-0.331	$3.30x10^{-7}$	$8.59\ x10^{-4}$
25-Ce-3	0.08%	-0.314	$7.21x10^{-7}$	$9.42\ x10^{-4}$
25-Ce-4	0.14%	-0.298	$1.47x10^{-6}$	0.00102
25-Ce-5	0.21%	-0.289	$2.21x10^{-6}$	0.00106
25-Ce-6	0.36%	-0.275	$4.14x10^{-6}$	0.00114
25-Ce-7	0.75%	-0.256	$9.73x10^{-6}$	0.0013
25-Ce-8	1.36%	-0.239	$2.08x10^{-5}$	0.00153
25-Ce-9	2.11%	-0.225	$3.84x10^{-5}$	0.00182
25-Ce-10	2.99%	-0.214	$6.51x10^{-5}$	0.00218
25-Ce-11	3.83%	-0.205	$9.77x10^{-5}$	0.00255
25-Ce-12	4.66%	-0.197	$1.37x10^{-4}$	0.00295

To evaluate the effect of CsCl on the activity of $CeCl_3$, a similar approach to the $GdCl_3$ mixture was adopted. The concentration of $CeCl_3$ was kept constant at 4.66 mol % $CeCl_3$,

and CsCl was progressively added to a concentration of 1.92 mol % while the OCP was measured. It is observed as shown in Figure 3-20 that the OCP remains unchanged, which means that the activity/activity coefficient is also almost unchanged as well.

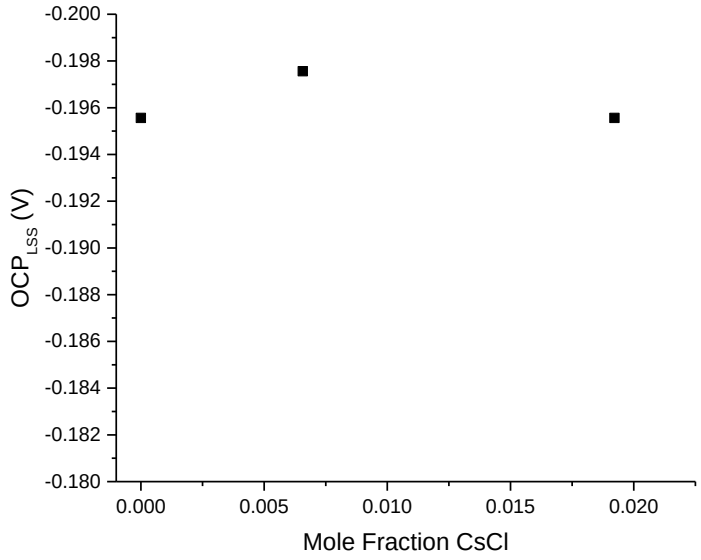

Figure 3-20: OCP of Ce/$CeCl_3$ for as a function of CsCl concentrations at a fixed concentration of 4.66 mol % $CeCl_3$.

3.2.5. Electrochemistry of LiCl-KCl-$GdCl_3$ and LiCl-KCl-$GdCl_3$-CsCl

Results of OCP measurements in LiCl-KCl-$GdCl_3$ are tabulated in Table 3-9. Figure 3-21 shows a graph of OCP versus mole fraction of $GdCl_3$ in LiCl-KCl. In Figure 3-21, OCP(LSS) =(measured E + ΔG_F). It can be seen that the OCP shows a pseudo – logarithmic relationship. From the OCP, the activity can be calculated as shown in equation (3-6). This has been shown in Figure 3-22. As it can be seen from Figure 3-22, the activity of the $GdCl_3$ deviates significantly from the ideal behavior. Finally, knowing the activity and the mole fraction, the activity coefficient can be calculated. This has been plotted as a function mole % $GdCl_3$ and shown in Figure 3-23. It can be observed from Figure 3-23 that initially, the activity coefficient decreases with concentration, reaching an almost constant value of 5 x 10^{-5}. Around 2 mol % $GdCl_3$, the activity coefficient again begins increasing. This graph demonstrates concentration dependence for the activity coefficient over a range of concentrations of 0 to 4.5 mol%. In the range of 0.5 to 2.5 mol%, the activity coefficient is constant. These results show why other researchers have mistakenly assumed dilute solution activity coefficients to be constant. If the standard state is defined as the pure solute, there is no fixed relationship between concentration and activity coefficient near the infinite dilution condition.

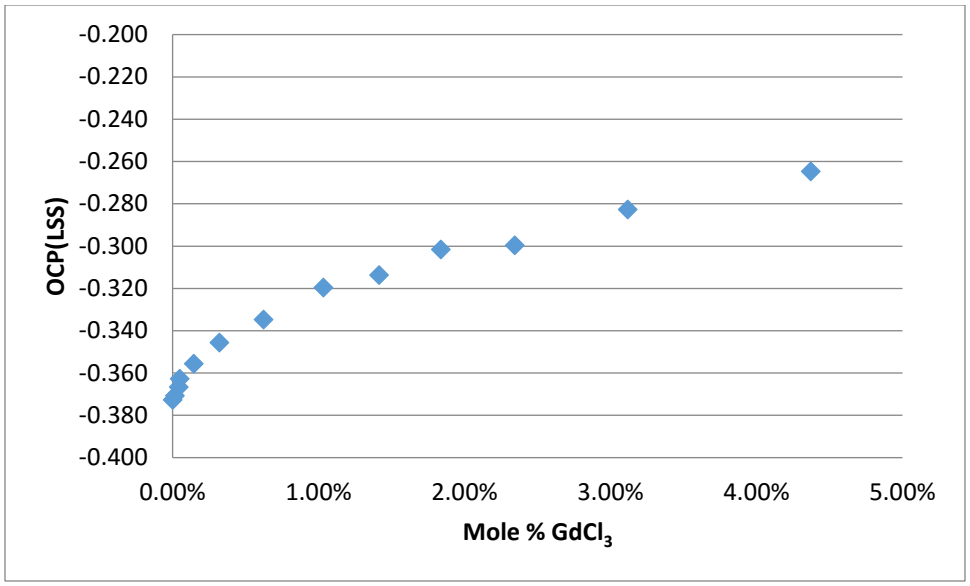

Figure 3-21: OCP vs. mole fraction of $GdCl_3$.

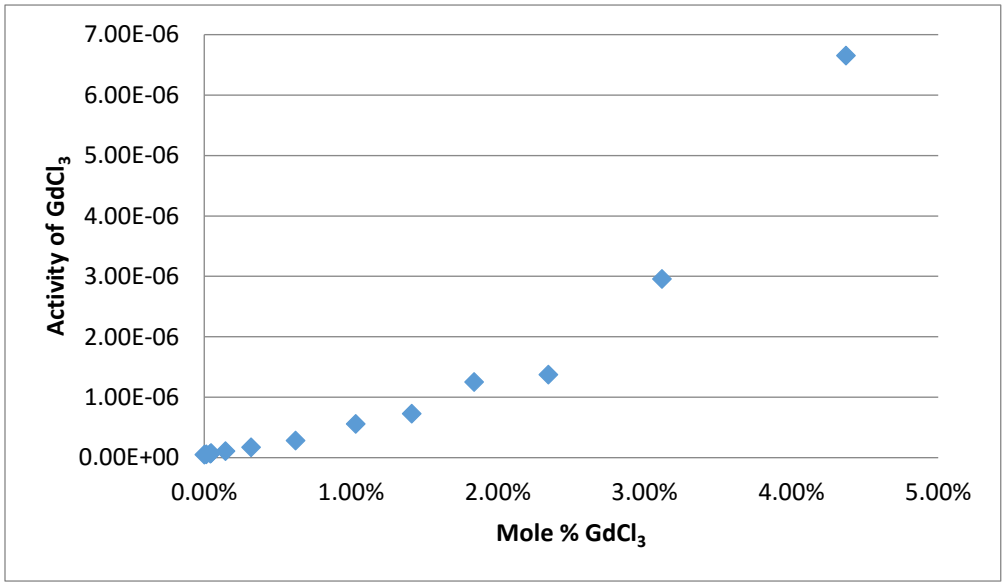

Figure 3-22: Activity of $GdCl_3$ as a function of mole percent $GdCl_3$

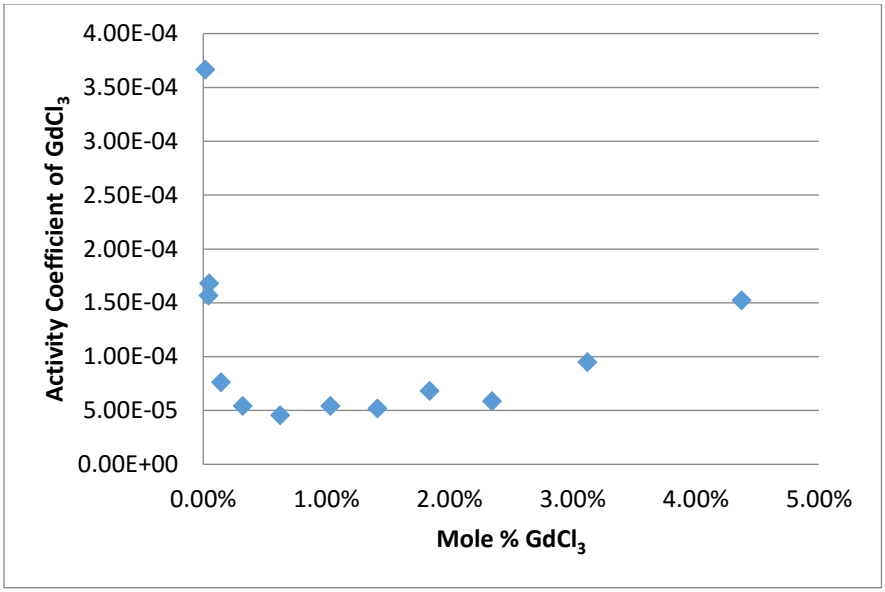

Figure 3-23: Activity coefficient of $GdCl_3$ as a function of mole percent $GdCl_3$ in LiCl-KCl at 773 K

The sensitivity of the activity coefficient calculation to the selection of standard state is shown in Figure 3-24. While Figure 3-23 uses the liquid standard state only, Figure 3-24 shows the activity coefficient versus concentration for both the liquid and solid standard state assumptions.

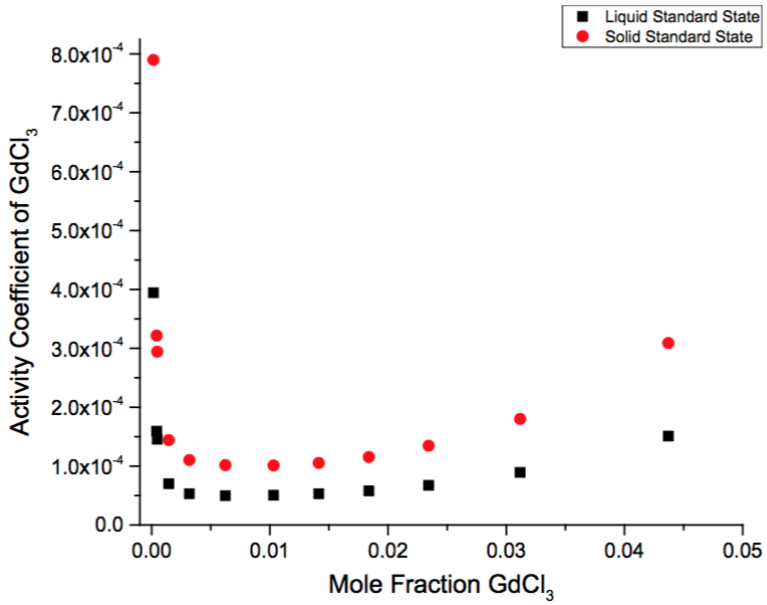

Figure 3-24: Activity coefficient of $GdCl_3$ as a function of mole percent $GdCl_3$ in LiCl-KCl at 773 K using two different standard states.

Table 3-9: Results from Electrochemical Testing of LiCl-KCl-$GdCl_3$ at 773 K. Concentrations are based on concentration as-weighed.

Test ID	Mole % $GdCl_3$	OCP (LSS)	Real Activity	Activity Coefficient
18-Gd-1	0.00%	-0.373	5.14E-08	1.22E-02
18-Gd-2	0.02%	-0.371	5.62E-08	3.66E-04
18-Gd-3	0.04%	-0.367	6.73E-08	1.57E-04
18-Gd-4	0.05%	-0.363	8.06E-08	1.68E-04
18-Gd-5	0.14%	-0.356	1.10E-07	7.62E-05
18-Gd-6	0.32%	-0.346	1.73E-07	5.42E-05
18-Gd-7	0.62%	-0.335	2.84E-07	4.56E-05
18-Gd-8	1.03%	-0.320	5.59E-07	5.42E-05
18-Gd-9	1.41%	-0.314	7.32E-07	5.18E-05
18-Gd-10	1.84%	-0.302	1.26E-06	6.84E-05
18-Gd-11	2.34%	-0.300	1.38E-06	5.87E-05
18-Gd-12	3.12%	-0.283	2.96E-06	9.49E-05
18-Gd-13	4.37%	-0.265	6.66E-06	1.52E-04

Additional tests were conducted to evaluate the effect of presence of CsCl on the activity of $GdCl_3$. Two series of tests were run. In one set, the CsCl concentration was fixed at 0.7 mol%, and the $GdCl_3$ concentration varied up to 5 mol%. A plot comparing the OCP with 0 versus 0.7 mol% CsCl is shown in Figure 3-25 below. This appears to show no effect of CsCl at this concentration level on the measured OCP. In the other set of tests, the concentration of $GdCl_3$ was maintained constant at 4.29 mole % and the CsCl was treated as an independent variable and increased from 0.7 to 3.5 mol%. It does appear that increasing CsCl concentration above 0.7 mol% decreases the activity coefficient of $GdCl_3$. The OCP effect is shown in Figure 26, and the activity coefficient effect is shown in Figure 3-27. All of the data collected in mixtures containing CsCl are included in Table 3-10.

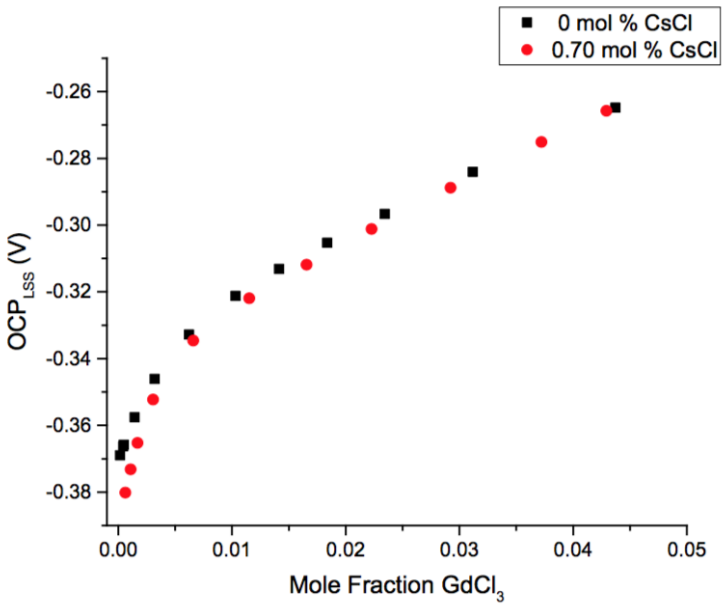

Figure 3-25: Open circuit potential for the Gd/GdCl$_3$ system in LiCl-KCl as a function of mole fraction for two concentrations of CsCl at 773 K.

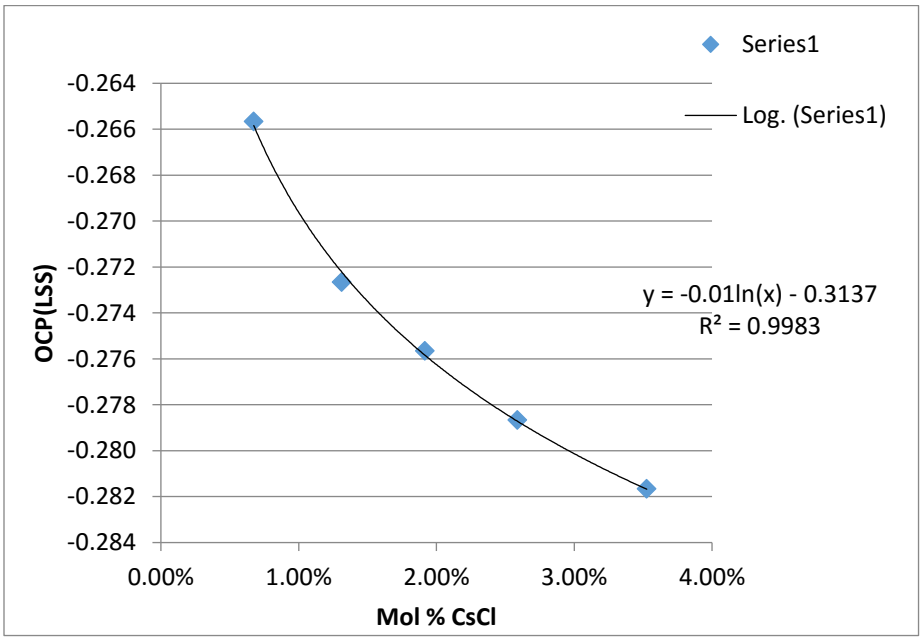

Figure 3-26: OCP of Gd/GdCl$_3$ for as a function of CsCl concentrations at a fixed concentration of 4.29 mol % GdCl$_3$ at 773 K.

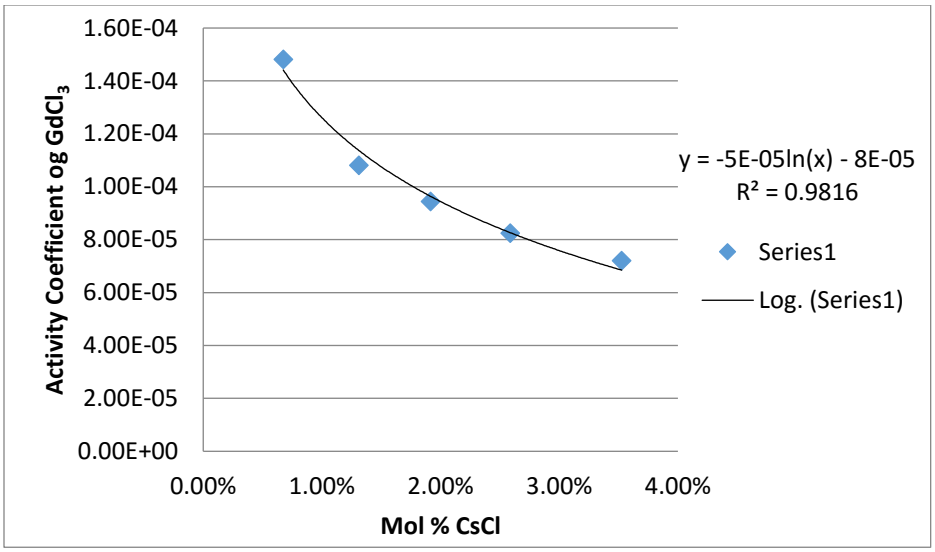

Figure 3-27: Activity coefficient of $GdCl_3$ for as a function of CsCl concentrations at a fixed concentration of 4.29 mol % $GdCl_3$.

Table 3-10: Results from Electrochemical Testing with LiCl-KCl-$GdCl_3$-CsCl. Concentrations are based on concentration as-weighed.

Test ID	Mole % $GdCl_3$	Mole % CsCl	OCP (LSS)	Real Activity	Activity Coefficient
20Gd-02	0.03%	0.70%	-0.392	2.18×10^{-8}	7.25×10^{-5}
20Gd-03	0.06%	0.70%	-0.377	4.29×10^{-8}	6.82×10^{-5}
20Gd-04	0.11%	0.70%	-0.371	5.62×10^{-8}	5.19×10^{-5}
20Gd-05	0.17%	0.70%	-0.363	8.06×10^{-8}	4.75×10^{-5}
20Gd-06	0.31%	0.70%	-0.355	1.16×10^{-7}	3.76×10^{-5}
20Gd-07	0.66%	0.70%	-0.339	2.38×10^{-7}	3.60×10^{-5}
20Gd-08	1.15%	0.70%	-0.319	5.85×10^{-7}	5.07×10^{-5}
20Gd-09	1.66%	0.69%	-0.310	8.77×10^{-7}	5.30×10^{-5}
20Gd-10	2.23%	0.69%	-0.302	1.26×10^{-6}	5.64×10^{-5}
20Gd-11	2.92%	0.68%	-0.287	2.47×10^{-6}	8.46×10^{-5}
20Gd-12	3.72%	0.68%	-0.277	3.88×10^{-6}	1.04×10^{-4}
20Gd-13	4.29%	0.67%	-0.266	6.36×10^{-6}	1.48×10^{-4}
20Gd-14	4.29%	1.31%	-0.273	4.64×10^{-6}	1.08×10^{-4}
20Gd-15	4.29%	1.92%	-0.276	4.06×10^{-6}	9.45×10^{-4}
20Gd-16	4.30%	2.59%	-0.279	3.54×10^{-6}	8.25×10^{-5}
20Gd-17	4.29%	3.53%	-0.282	3.10×10^{-6}	7.21×10^{-5}

3.2.6. Mixed potential testing

This test was performed to examine the influence of using a stainless steel basket to hold the rare earth metal during open circuit potential measurements. It was originally assumed that the presence of the stainless steel basket would not influence the open circuit potential measurement value. This is based on that fact that stainless steel is more noble than cerium in LiCl-KCl. An experiment was conducted to verify this assumption. For this test, a two electrode electrochemical cell was set-up where the working electrode was a Ce metal rod inserted in a stainless steel basket identical to the one used for this whole project. The counter electrode was a Ce metal wire directly inserted in the molten salt bath which was a mixture of LiCl-KCl-$CeCl_3$. If the stainless steel basket, indeed, causes no mixed potential, the potential difference between Ce/stainless steel and Ce should be zero. The measured potential difference was 2 mV. This value represents less than 1 percent error of the actual measured OCP values for the Ce study presented in this paper and is well within the acceptable realm of errors associated with experimental measurements.

3.2.7. Galvanic drawdown of UCl_3 and $MgCl_2$

In the preliminary short communication [83], data was presented that demonstrated the use of a galvanic couple of stainless steel with Gd metal to reduce or "drawdown" UCl_3 and $MgCl_2$ from eutectic LiCl-KCl. In the reported test, the salt composition changed from 1.39 mol % UCl_3 and 0.83 mol % $MgCl_2$ to 0.12 mol% UCl_3 (at 1 hour) and 0.09 mol % $MgCl_2$ at the end of three hours. Using an experimental setup identical to the one used in the previous study, the primary motivation of additional experiments was to demonstrate that this separation process could further reduce UCl_3 concentrations below 0.01 mol % (100 ppm on molar basis). This objective could be accomplished using a two-step process in which the majority of the U is reduced onto a first basket, and then a second basket acts as a polishing step to clean the salt to the desired level of purity. Hence in the first test for this study (Test G1), the starting composition was 0.19 mol % UCl_3 (no $MgCl_2$ present).

The results of this test are shown in Figure 3-28. It can be observed from Figure 28 that the concentration of UCl_3 decreased to 0.0193 mol % (193 ppm on molar basis) in about 20 minutes, subsequently oscillating. During oscillation in concentration, the low value of UCl_3 concentration in the salt was 0.0074 mol % (74 ppm on molar basis), which does meet the target concentration in the molten salt. The reason for the oscillation in UCl_3 concentration is not currently understood. It may be a result of the Gd metal becoming covered by U metal, leading to U metal corrosion, followed by further galvanic reduction. But the Gd concentration in the salt did not oscillate, possibly implicating that the variation of U concentration is entirely due to analysis error. Measurements of the potential of the galvanic couple would have been useful to better understand the cause of the oscillating concentration, but the Experimental Setup 1 did not allow for inclusion of a reference electrode. This effect was the motivation to develop an alternative cell configuration in which the Gd metal was physically separated from the stainless steel basket but still in electric contact. In the previous publication [83], it was verified that the metal deposited on

the basket was indeed U metal using both XRD analysis and using a Geiger Counter (since U was the only radioactive substance in the set-up). For the tests reported in this study, presence of U metal on the basket was verified using only a Geiger Counter.

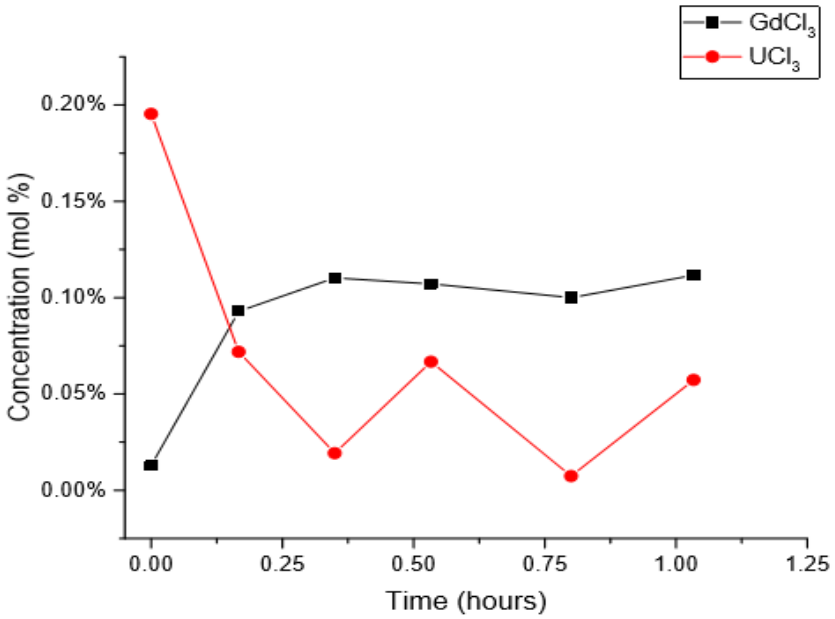

Figure 3-28: Test G1: mole fraction of UCl_3 and $GdCl_3$ plotted as a function of time. Experimental Conditions: T = 758 K, Rotation = 100 rpm

A second test (G2) was performed using Experimental Setup 1 to investigate the importance of rotation in this process. In Test G2, the basket was held stationery (RPM = 0). It was observed that though the extraction process did occur, the process was extremely slow. At the end of 150 minutes, there was found to be a significant concentration of UCl_3 present based on the light purple color of the salt. Pure LiCl-KCl is white, while UCl_3 is a dark purple. As a comparison, at the end of 30 minutes in Test G1, the molten salt sample was completely white.

To prevent blockage of access to the Gd metal, the experimental configuration was redesigned as shown in Figure 3-7. Experimental Setup 2 uses the Gd as an anode and the stainless steel basket as a cathode. In theory, separating the two metals physically should prevent passivation or blockage of access to the Gd metal. In this new set-up, the Gd metal was held stationery (RPM = 0), while the stainless steel basket was rotated. Additionally, in this new experimental setup, a 5 mol % Ag/AgCl reference electrode was also incorporated. This facilitated measurement of the potential of the Gd and stainless steel basket (which were electrically shorted to each other) during each experiment.

Using this new setup (Experimental Setup 2), Test G5 was performed with a LiCl-KCl-UCl_3 mixture. In this test, the open circuit potential (OCP) of the Gd and basket versus the reference electrode was also recorded. The results of Test G5 are shown in Figure 3-29. It can be observed from Figure 3-29 that as soon as the rotation is commenced at t = 0, there is a precipitous decline in the UCl_3 concentration. Within 30 minutes of the test starting, the

concentration of the UCl_3 in the molten salt reaches 25 ppm (molar basis). At 45 minutes, the concentration of UCl_3 is below 1 ppm (molar basis). Beyond that, the UCl_3 concentration continues to trend downwards.

In the last two samples, the uranium concentration was below the detection limit of the ICP-MS instrument of 0.002 mg/L uranium. That translates into an UCl_3 concentration of <0.4 ppm (molar basis) in the molten salt. The $GdCl_3$ concentration also tracks well with the UCl_3 data. Most of the $GdCl_3$ is introduced into the molten salt solution during the initial 30-45 minutes. After that, the $GdCl_3$ concentration changes very little, similar to the UCl_3 concentration. It does seem that the final $GdCl_3$ concentration is slightly higher than the starting UCl_3 concentration. The reason for that is not clear. From the reaction, it is anticipated that one mole of $GdCl_3$ will be generated for one mole of UCl_3 reduction. This asymmetry in the $GdCl_3$ and UCl_3 concentrations may be a result of some non-stoichiometry reactions and/or presence of some impurities.

The open circuit potential data tracks well with the UCl_3 concentration data. The OCP starts of at a fairly positive value of about -2.6 V vs. Cl^-/Cl_2 and becomes more negative as the uranium is removed from the salt. In fact, in the region where most of the U metal is removed, the OCP drops rapidly. As the U concentration tapers off, the OCP also flat lines. This indicates that OCP measurements can be used to determine when the reaction has gone to completion. They can also be used to monitor the actinide content of the salt for process control or safeguards purposes. The kinetics of the U deposition reaction is extremely fast, as observed from this data. 98.5 % of the UCl_3 is removed from the salt in 30 minutes, and 99.94 % of the uranium is removed in 45 minutes as seen in Table 3-11. From the results of Test G5, it is clear that the Experimental Setup 2 is more efficient at removing UCl_3 from the molten salts than the original setup. Physically separating the reducing metal from the basket improves the maximum extent of reduction.

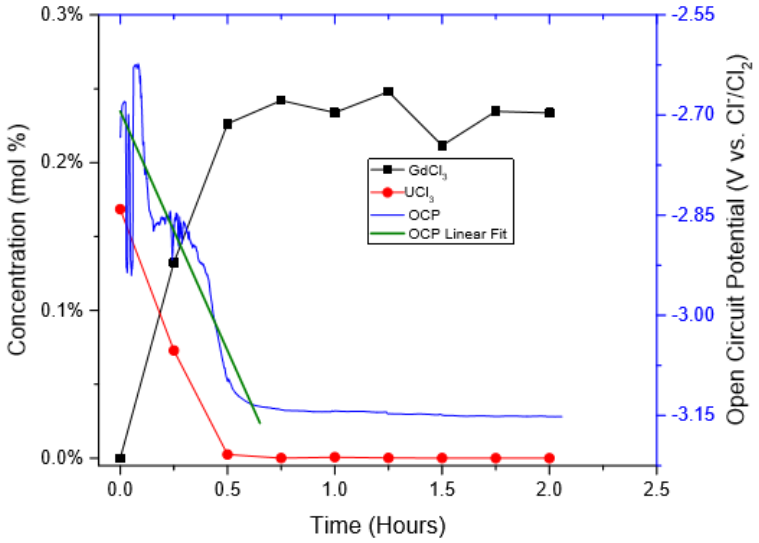

Figure 3-29: Test G5: mole fraction of UCl_3 and $GdCl_3$ plotted as a function of time (Y1). Open circuit potential (vs. Cl^-/Cl_2) plotted as a function of time (Y2). Experimental Conditions: T = 788 K, Rotation = 100 rpm

Table 3-11: Concentration of UCl_3 in LiCl-KCl Eutectic Salt for Test G5

Time Elapsed (minutes)	UCl_3 Concentration (molar ppm)	% Removed
0	1685.08	0%
15	728.86	56.74%
30	25.19	98.50%
45	0.93	99.94%
60	7.25	99.56%
75	1.53	99.90%
90	1.27	99.92%
105	<0.4	<99.97%
120	<0.4	<99.97%

The next test (Test G6) that was performed was with the LiCl-KCl-$MgCl_2$ system with no UCl_3 present. $MgCl_2$ has been shown to be an effective electrochemical surrogate for $PuCl_3$ in LiCl-KCl eutectic salt. The results for Test G6 are shown in Figure 3-30. This test was run for about 160 minutes. At the end of that time, 137 ppm (molar basis) of $MgCl_2$ remained in the salt. This represented a removal of 96.81 % $MgCl_2$. It appears that the extraction process for $MgCl_2$ is much slower than that for UCl_3 extraction, which is probably an electrode reaction kinetics effect. Mass transfer is fast due to the rotation of the basket, so electrode reaction kinetics may be dominating. The lower reduction potential for $MgCl_2$ compared to UCl_3 translates to a lower overpotential for reduction. In Test G6 again, the correlation between OCP and concentration of $MgCl_2$ is excellent. The $GdCl_3$ concentration does not increase as sharply as observed in Test G5. In the latter part of the test, the $GdCl_3$ concentration is trending upwards at a slow rate similar to the slow downward trend in the $MgCl_2$ concentration. In this test, the significant difference between the final $MgCl_2$ and $GdCl_3$ concentrations can be mainly attributed to the reaction stoichiometry. Due to the difference in the oxidation states of the two species, 0.66 moles of $GdCl_3$ is generated for every mole of $MgCl_2$ reduced to Mg.

The next test (Test G7) used a mixture of LiCl-KCl-UCl_3-$MgCl_2$. In this test, the reference electrode seemed to have malfunctioned. The OCP data was very noisy, making interpretation challenging. Hence, for this test, the OCP data was not reported. The concentrations of the three species of interest: UCl_3, $MgCl_2$, and $GdCl_3$ for Test G7 are shown in Figure 3-31. Consistent with the results from Test G6, the kinetics for the uranium extraction is faster than that for $MgCl_2$ extraction from the salt.

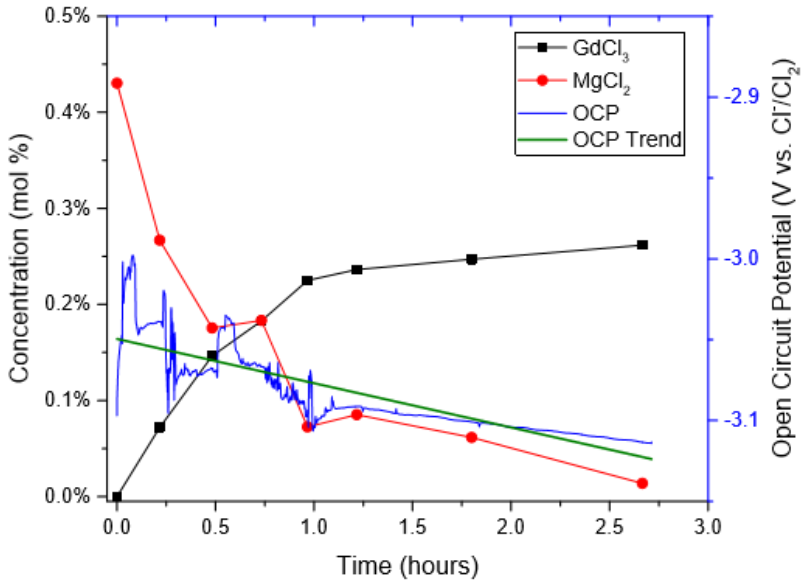

Figure 3-30: Test G6: mole fraction of $MgCl_2$ and $GdCl_3$ plotted as a function of time (Y1). Open circuit potential (vs. Cl^-/Cl_2) plotted as a function of time (Y2). Experimental Conditions: T = 788 K, Rotation = 100 rpm

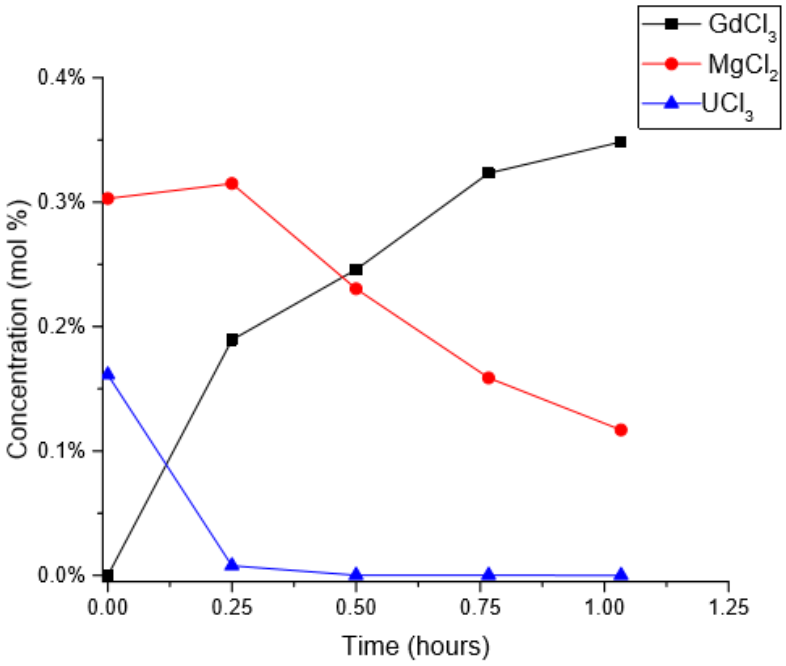

Figure 3-31: Test G7: mole fraction of $MgCl_2$, UCl_3, and $GdCl_3$ plotted as a function of time. Experimental Conditions: T = 788 K, Rotation = 100 rpm

The final test (Test G8) that was performed was with a mixture of LiCl-KCl-UCl_3-$MgCl_2$-$LaCl_3$-$NdCl_3$-$CeCl_3$. The rare earth chlorides were introduced into the mixture to examine

the selectivity of the extraction process and verify the suitability of Gd as the sacrificial anode. For Test G8, the starting concentration of the rare earth chlorides ($LaCl_3$, $NdCl_3$, and $CeCl_3$) was about 0.5 mol % which was intentionally designed to be significantly higher than the 0.25-0.30 mol % for $MgCl_2$ and UCl_3 concentrations. The results from Test G8 are is shown in Figure 3-32. The rare earth concentration of $CeCl_3$ and $LaCl_3$ are observed to increase for the first 0.25 hours. The initial increase in rare earth chloride concentration is likely due to their incomplete dissolution in the molten LiCl-KCl. The experiment may have started prematurely with those concentrations still rising. As soon as the rotation was commenced at t = 0 hrs, these undissolved rare earth salts dissolved in an accelerated fashion due to enhanced kinetics. The peak rare earth salt concentrations are in-line with the expected concentrations based on the weights of the salts added into the mixture at the start of the experiment. At t = 0 hours, the rotation is commenced and immediately it can be observed that the UCl_3 concentration plummets as expected. UCl_3 concentration continues to decline with time for the remaining life of the test. The $MgCl_2$ concentration remains unchanged for the first 0.25 hrs. Similar to the behavior in Test G7, the $MgCl_2$ concentration begins to decline after the majority of the UCl_3 has been removed from the salt.

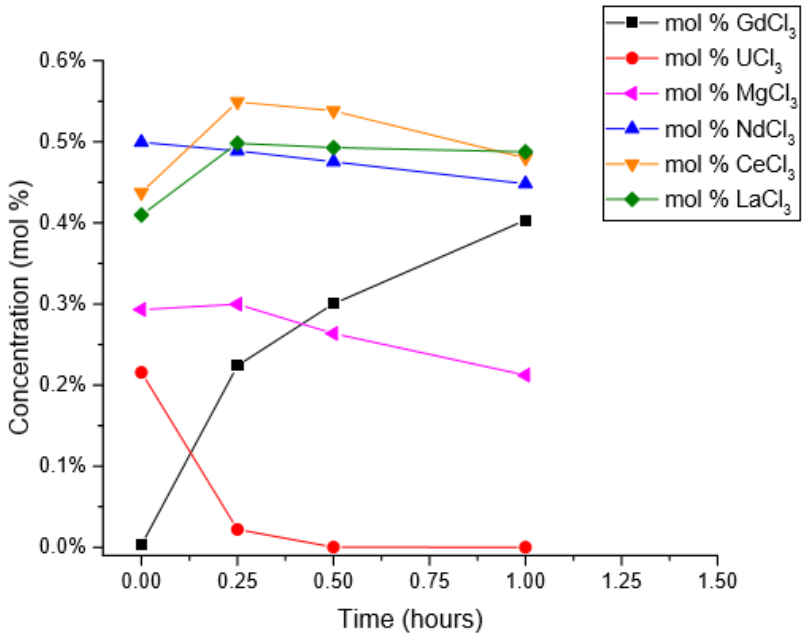

Figure 3-32: Test G8: mole fraction of $MgCl_2$, UCl_3, $CeCl_3$, $NdCl_3$, $LaCl_3$, and $GdCl_3$ plotted as a function of time. Experimental Conditions: T = 788 K, Rotation = 100 rpm.

The initial concentrations of the rare earth chlorides ($LaCl_3$, $NdCl_3$, and $CeCl_3$) did not significantly reduce during the time span of the test. $MgCl_2$ was still in the process of being reduced at the end of the test, which may have prevented any rare earths from being reduced. But it still may be concluded that this process yields excellent selectivity for reduction of actinides in the absence of fission products. The OCP profile for Test G8 was follows a trend similar to the OCP for Test G5 as can be seen in Figure 3-33. However, the

open circuit potential for the Test G8 plateaus at a level that is more positive than G5 or G6. There is a correlation between residual concentration of $MgCl_2$ in the salt and OCP. In Test G5, there is no $MgCl_2$ in the salt, which resulted in the lowest (most negative) OCP. In Test G6, the $MgCl_2$ concentration drops to 137 ppm, which yields an intermediate OCP. In Test G8, the $MgCl_2$ concentration is 0.23 mol % at the end of the test, which results in the highest OCP.

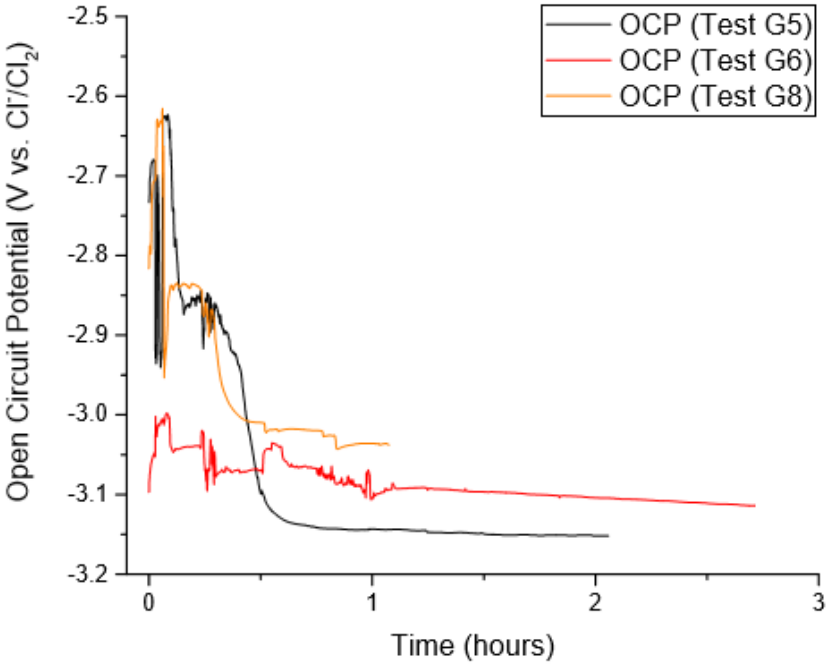

Figure 3-33: Open Circuit Potential of Tests G5, G6, and G8. Experimental Conditions: T = 788 K, Rotation = 100 rpm.

3.2.8. Discussion of electrochemical testing results

From Figure 3-34, it can be observed that activity of all of the rare earth chlorides studied here departs significantly from ideal solution behaviors. The degree to which the species depart from ideal solution behavior seems to be dependent on atomic number. Lanthanum(Z = 57) departs the least from ideal solution behavior followed by cerium (Z = 58), neodymium (Z = 60), and gadolinium (Z = 64) respectively. It is important to note that for the elements in the lanthanide series, there is a phenomenon known as lanthanide contraction. This means that as the atomic weights of the elements increase, their ionic sizes decrease. In Table 12, the ionic radii of the four rare earths studied in this work have been summarized. This data was obtained from an online database hosted by the Imperial College, London. The ionic radius naturally changes with the coordination number and charge. In Table 3-12, the ionic radius has been reported for the +3 charge and coordination number of 6, which is the most commonly encountered oxidation state and coordination number for rare earths in molten salts. Table 3-12 shows that as the atomic number increases, both the crystal radius and ionic radius decrease, as expected. A similar

trend was observed for the other coordination numbers and oxidation states from the data hosted at Imperial College.

From Figure 3-35 and Table 3-12, one can draw the conclusion that as the ionic radius of the underlying element becomes smaller, a larger deviation from ideal solution behavior for the corresponding rare earth chloride is observed. In Figure 35, the activity of all of the four rare earth chlorides at four concentrations of 1 mol %, 1.5 mol %, 2 mol %, and 2.5 mol % is plotted versus the ionic radius listed in Table 3-12. Figure 3-35 has the activity plotted on a logarithmic scale which demonstrates a linear relationship with ionic radii of species involved with an excellent fit for all four concentrations studied. Though factors other than ionic size are likely important, the evidence from Figure 3-35 leads to the conclusion that the ionic size is the essential condition in predicting the activity of rare earth chlorides in molten salts.

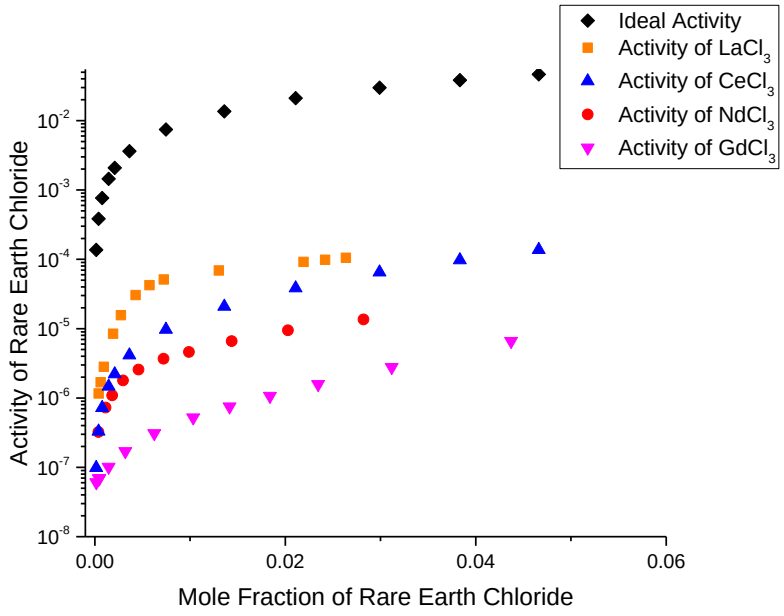

Figure 3-34: The activity data for four rare earth chlorides as a function of mole fraction.

Table 3-12: Results from TGA Testing. Concentrations are based on ICP-OES measurements.

Element	Atomic Number	Charge	Coordination Number	Ionic Size (A)
Lanthanum	57	+3	VI	1.032
Cerium	58	+3	VI	1.01
Neodymium	60	+3	VI	0.983
Gadolinium	64	+3	VI	0.938

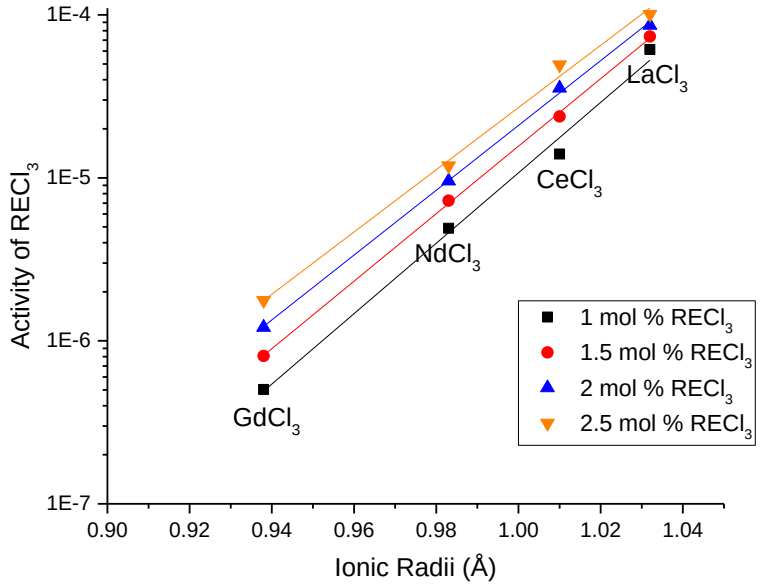

Figure 3-35: The activity data for four rare earth chlorides as a function of ionic size.

The correlations generated from Figure 3-35 have been listed in Table 3-13. The log *a* values calculated using the correlations in Table 3-5 and those from experimental measurements were in excellent agreement with about 1% errors.

Table 3-13: Ionic size dependent, predictive correlation for the activity of rare earth chlorides for four concentrations from 1 mol % to 2.5 mol % $RECl_3$. Valid from Z = 57 to 64 at T = 773 K (r = ionic radii in angstrom)

Concentration	Predictive Correlation	Average Error
1 mol % $RECl_3$	log *a* = -26.623 + 21.648*r	1.44%
1.5 mol % $RECl_3$	log *a* = -25.517 + 20.711*r	0.60%
2 mol % $RECl_3$	log *a* = -24.564 + 19.886*r	0.61%
2.5 mol % $RECl_3$	log *a* = -23.660 + 19.091*r	0.79%

Using the correlations presented in Table 3-13, it is possible to easily calculate the values of the activity of any rare earth chlorides between lanthanum (Z= 57) to gadolinium (Z = 64) for a concentration range of 1 to 2.5 mol % $RECl_3$. This correlation should prove very useful for future research, engineering, and design studies.

3.2.9. Conclusions regarding drawdown

A novel process to drawdown actinide chlorides from LiCl- KCl has been investigated in detail. Tests have been performed with UCl_3 and $MgCl_2$ to simulate electrorefiner salt containing UCl_3 and transuranic chlorides. Using a galvanic couple between a cathode basket made of stainless steel and a Gd rod, rapid reduction of UCl_3 to U and $MgCl_2$ to Mg was observed from the LiCl-KCl eutectic molten salt mixtures. Physical separation of the Gd rod from the stainless steel basket was very effective at increasing the efficiency of the drawdown. UCl_3 concentration of less than 0.4 ppm (molar basis) was achieved starting with 1 wt %. $MgCl_2$ removal is much slower than the UCl_3 removal process, due to the difference in electrode kinetics for the two reactions. However, after about 3 hours, greater than 96% of the $MgCl_2$ can removed from the molten salt. Higher degrees of removal are expected if longer times are allowed for the reduction process. The selectivity of actinide reduction in the presence of rare earths was demonstrated. UCl_3 removal was accomplished from the salt without any co-reduction of $LaCl_3$, $NdCl_3$, or $CeCl_3$. Open circuit potential (OCP) measurements were found to correlate with degree of drawdown. OCP decreased during drawdown and reached a plateau when the UCl_3 or $MgCl_2$ concentration reached a lower level plateau. Benefits of this process include passive operation, short processing times, removal of actinides as metals, and high selectivity for actinides relative to rare earths. The resulting actinide-free salt can either be subjected to subsequent treatment to separate the rare earth fission products or can be processed into waste forms and disposed in a geologic nuclear waste repository. Removal of actinides will greatly reduce the long term generation of heat and radiological dose from the waste.

3.3. Phase diagram measurement

Electrolysis of the molten salt results in a perturbation of the composition, which in turn can affect the equilibrium phase behavior—notably including liquidus temperature of the molten salt. While phase behavior data has been collected for a limited number of rare earth chlorides in LiCl-KCl [76], more complex salt mixtures as will be encountered in real electrorefiner salt drawdown have not been studied. Constructing phase diagrams is an important approach for evaluation of such phase behavior. Phase diagrams relate the solubility of RE ionic compounds (e.g. RE chlorides) in molten salts to composition and temperature. Conversely, liquidus temperatures can be determined as a function of composition. This is important for determining concentration limits for the molten salts during electrolysis and other pyroprocessing steps. Thus, this portion of the project involved analyzing several series of differential scanning calorimetry (DSC) experiments with LiCl-KCl-$RECl_3$-CsCl mixtures. For consistency with the electrochemical property measurements, CsCl was used as a representative active metal chloride. While LiCl-KCl has a DSC thermal transition peak at about 350^{o}C, the mixtures containing rare earth chlorides are expected to have higher temperature peaks. These peaks can be directly related to the liquidus temperature of the salt solution. The rare earth chlorides studied in this project include $LaCl_3$, $GdCl_3$, $CeCl_3$, and $NdCl_3$ at concentrations comparable to salt used in electrorefiners. Note that phase diagrams for LiCl-KCl-$LaCl_3$ and LiCl-KCl-$NdCl_3$ were constructed by Sridharan et. al. during a previous NEUP funded project [76]. Accordingly,

only a limited number of tests with those salt mixtures were performed to verify the experimental procedure and ensure consistency with that study. Sets of salts were prepared with LiCl-KCl-CsCl mixed with the rare earth chlorides. Of particular interest will be how the presence of CsCl changes the liquidus temperature (if at all) of the rare earth chloride mixtures. Liquidus curves on x-T phase diagrams can be used to directly infer the solubility of the rare earth chlorides as a function of temperature. The highest temperature peak on a DSC scan for a given composition represents a solubility limit at that temperature. And these curves can be extrapolated to higher concentrations via employing thermodynamics models such as the regular solution model.

3.3.1. Phase diagram measurement for LiCl-KCl-LaCl3-CsCl System

The phase diagram previously developed for LiCl-KCl-$LaCl_3$ under a previous NEUP project is shown in Figure 3-36 below.

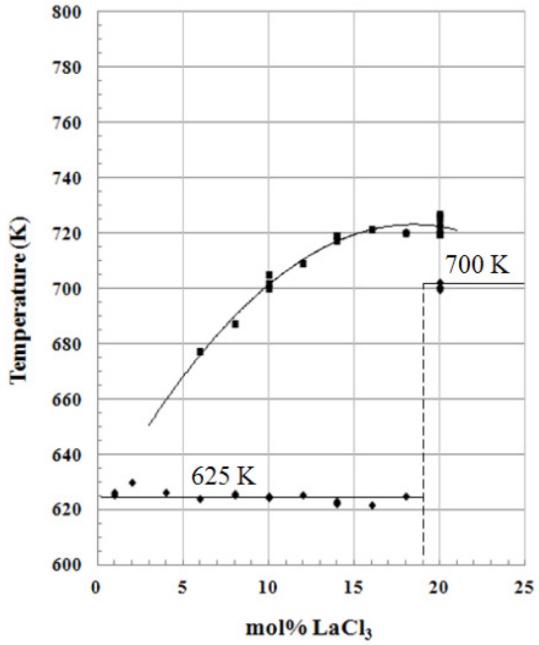

Figure 3-36: Partial pseudo-binary phase diagram of the LiCl-KCl-$LaCl_3$ system constructed by DSC scans by Sridharan et. al. [76].

There are two important aspects of this phase diagram that are important to mention—much of the data was taken at concentrations much higher than expected in the drawdown process, and there are no fission products present in the mixture other than $LaCl_3$. Our rationale for revisiting this phase diagram is that lower $LaCl_3$ concentrations are of higher interest (<5 mol%), and we need to understand the affect of other fission products such as CsCl on the phase behavior.

Thus, samples of LiCl-KCl-$LaCl_3$ and LiCl-KCl-CsCl-$LaCl_3$ mixtures prepared for the electrochemical measurements were analyzed using the TGA/DSC instrument described in

the experimental methods section. Initially, the DSC was programmed to both ramp the temperature up and down. Endothermic peaks on the heating curve represent melting transitions, while exothermic peaks on the cooling curve represent melting transitions. A series of DSC runs performed on LiCl-KCl with varying concentrations of $LaCl_3$ is shown in Figure 3-37.

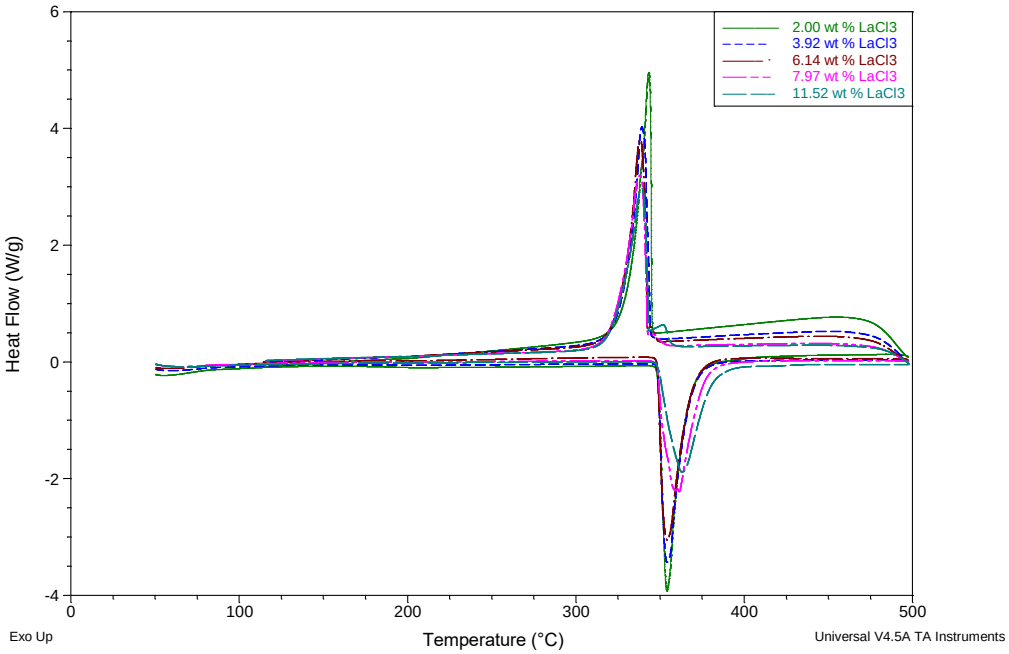

Figure 3-37: DSC curves for LiCl-KCl-$LaCl_3$ mixtures with $LaCl_3$ concentration ranging from 2 to 11.5 wt%.

Then for a series of salts containing 1 wt% CsCl in addition to the other salts, the scans are shown in Figure 3-38. Note in this figure that some higher temperature peaks are observed for the cooling portion of the cycle.

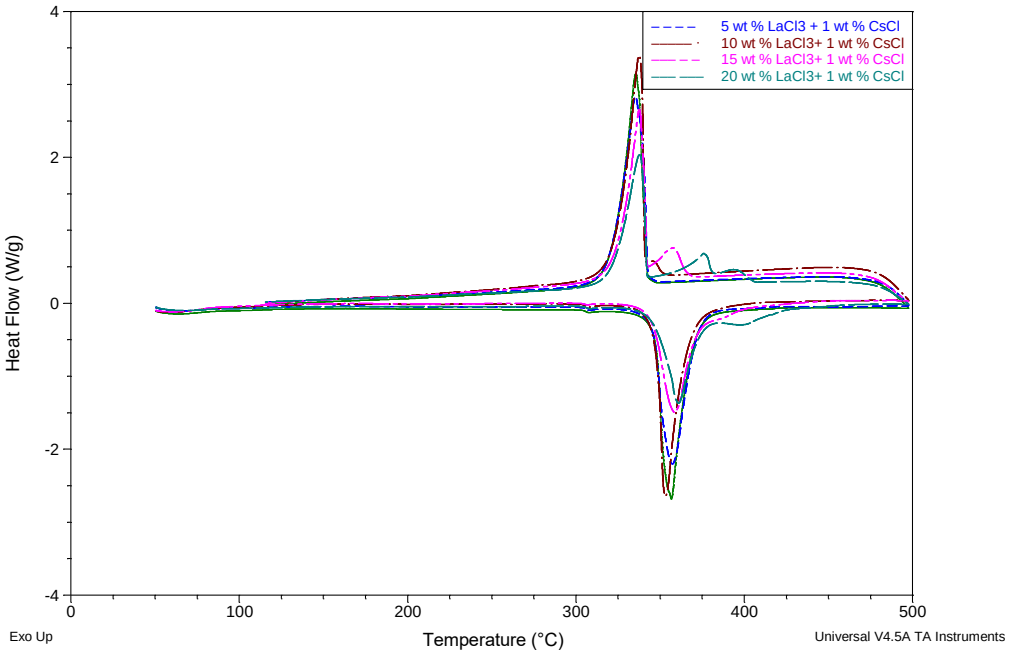

Figure 3-38: DSC curves for LiCl-KCl-$LaCl_3$–CsCl mixtures with $LaCl_3$ concentration ranging from 5 to 20 wt% and CsCl concentration set at 1 wt%.

In these plots, we generally only consider the main peak, which occurs at 335 to 365°C, to be of interest. Referring back to Figure 3-36, this transition appears to coincide with the solidus line, which may also be a liquidus line at these low concentrations. It is assumed that higher concentrations of $LaCl_3$ are required to cause higher temperature peaks to form similar to what is seen in Figure 3-36. To understand whether that line is affected by the presence of CsCl, peak temperatures from Figures 3-37 and 3-38 were plotted versus concentration of $LaCl_3$ and overlaid for Figure 3-39. The transition temperatures appear to be close for the 0 and 1 wt% CsCl mixtures, but more experiments with a wider range of CsCl concentrations is needed to better evaluate the effect.

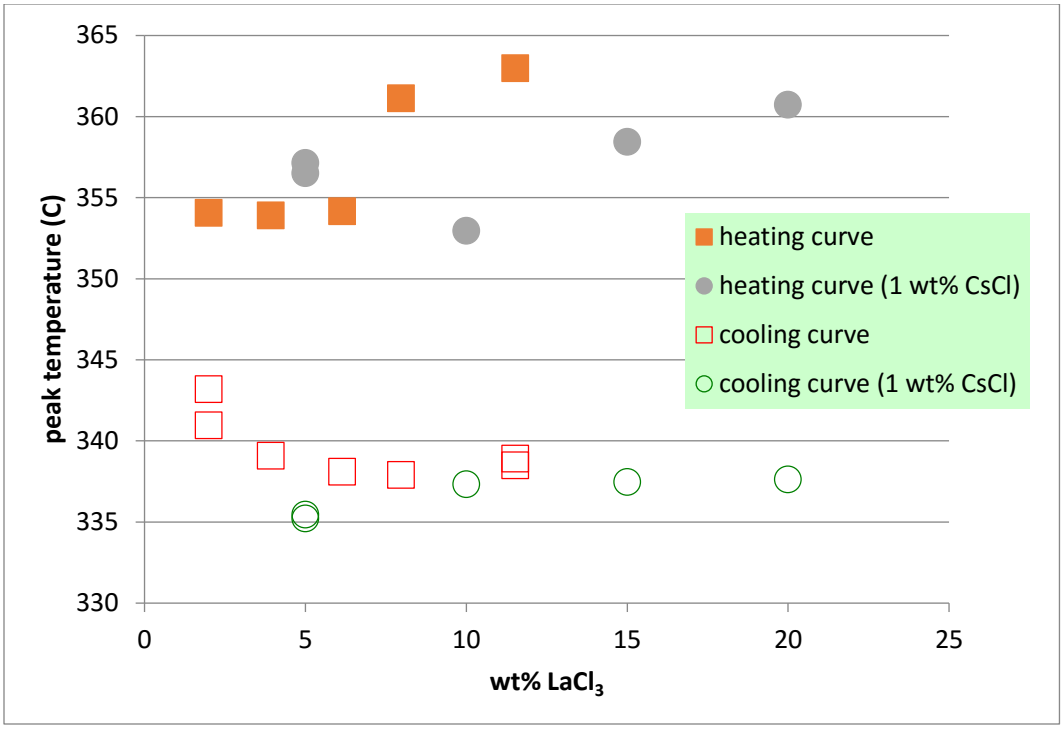

Figure 3-39: Peak temperatures from DSC runs of LiCl-KCl-$LaCl_3$ and LiCl-KCl-$LaCl_3$-CsCl

Even though it appears to be less sensitive to secondary peaks, the heating curve should preferentially be used to determine the liquidus and solidus temperatures for salts due to the effect of super cooling [77]. Thus, in subsequent runs, the temperature was ramped up but not down.

In one such set of runs, samples from Test 11 with 2 wt% CsCl were analyzed. Four of the DSC scans were overlaid and are plotted in Figure 3-40. From this plot, it appears that increasing the CsCl still does not result in any noticeable change in the phase behavior. There is still only a single transition peak.

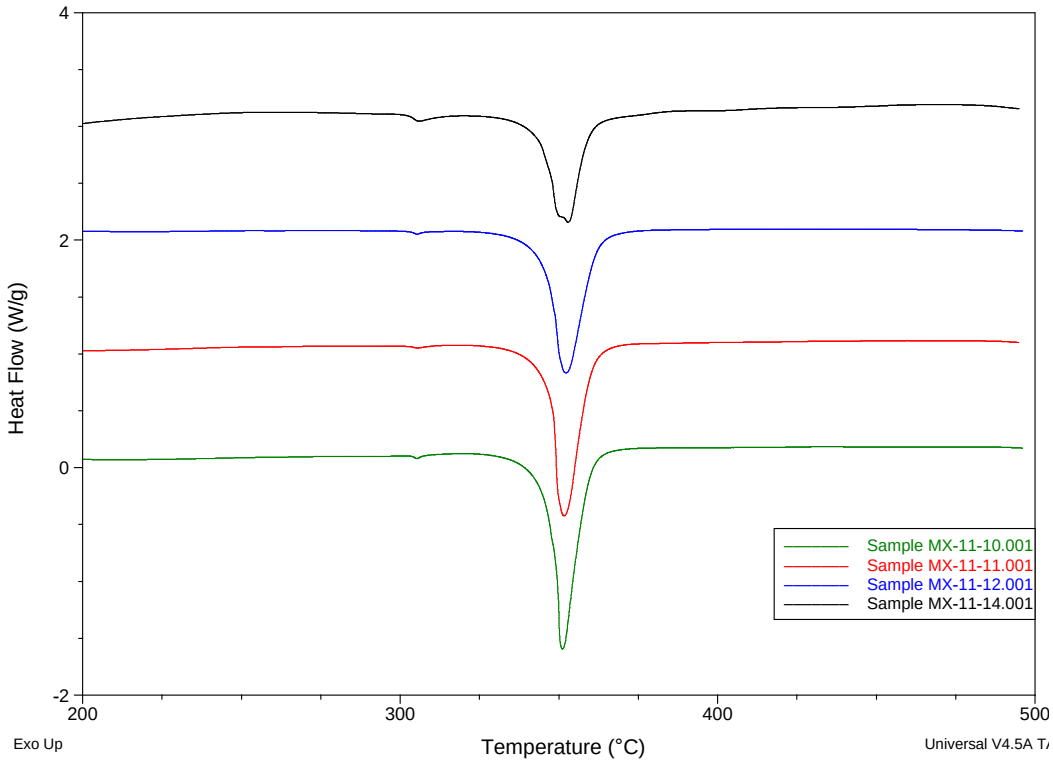

Figure 3-40: DSC heating curves for Test 11 samples with LiCl-KCl-CsCl (2 wt%). 11-10 (3.8% $LaCl_3$), 11-11 (5.6 wt% $LaCl_3$), 11-12 (7.2 wt% $LaCl_3$), 11-14 (11.0 wt% $LaCl_3$)

When the CsCl concentration was raised to 4 wt%, however, the shape of the DSC curves changed. An example is shown in Figure 3-41. A very noticeable lower temperature peak has appeared at about 300°C, and a very small peak has appeared just slightly higher in temperature than the main one. Recall from the discussion of the electrochemical measurement results that the salt is noticed to have turned orange at higher concentrations of CsCl. This could be due to a new phase, which corresponds to one of these two new peaks. Further investigation is needed, as there currently is insufficient evidence to make any conclusions. In Table 3-14, the peak temperatures are presented along with the salt compositions. Note that the DSC had been recently re-calibrated, and T2 values before and after calibration are included in this table. This was intended to evaluate the relative importance of frequent calibrations. Some of the DSC data collected in the first year had questionable pedigree with respect to calibration of the instrument. The comparison of T2's in Table 3-14 appears to indicate a minor difference, but perhaps not one that is so significant to motivate the discarding of data. Thus, peak temperature data was included in this report with and without pre-calibration.

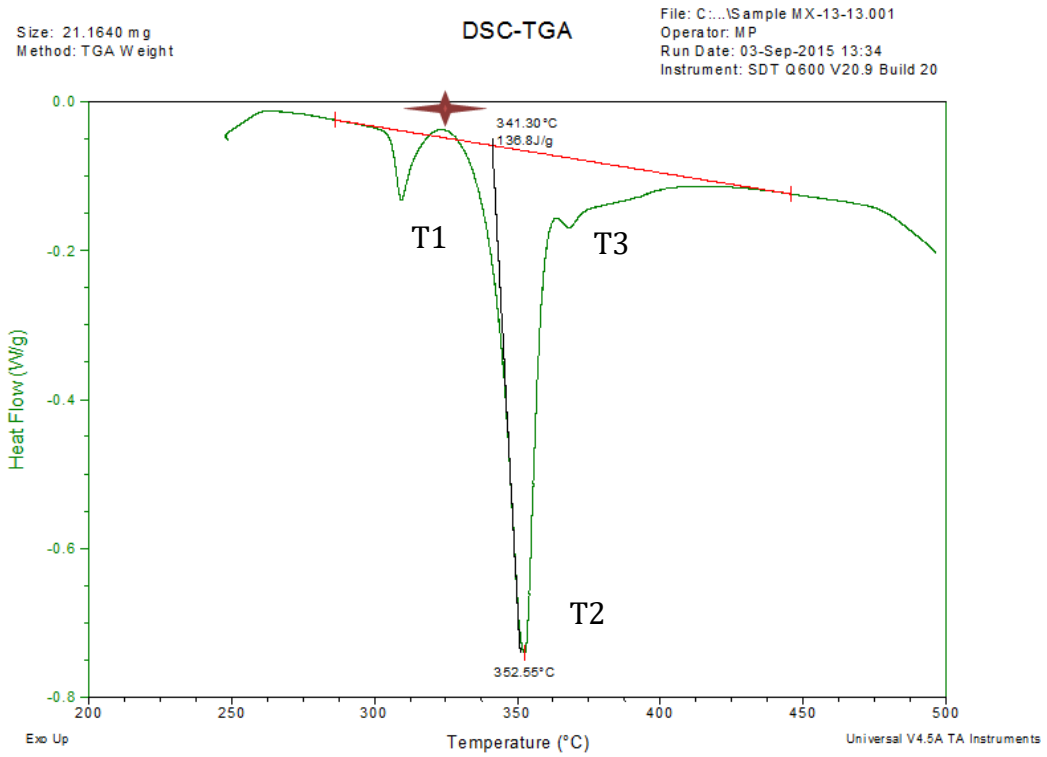

Figure 3-41: TGA/DSC scan for the MX-13-13 sample (8.5 wt% $LaCl_3$, 4.0 wt% CsCl)

*Table 3-14: Results of TGA/DSC for Series 13 experiments. Temperature calibration run prior to this series of measurements. *indicates concentration values that need to be verified via ICP-OES.*

Sample ID	Composition		Peaks (°C)			
	Wt. % $LaCl_3$*	Wt. % CsCl*	T1	T2	T2 (uncal)	T3
MX 13-07	0.703	4.023	318.4	352.2	350.3	No Peak
MX 13-08	1.260	4.000	310.6	351.0	348.3	No Peak
MX 13-09	2.369	4.094	309.8	350.5	348.9	No Peak
MX 13-10	3.933	4.029	309.5	349.7	346.8	No Peak
MX 13-11	5.461	3.964	309.3	349.4	348.3	No Peak
MX 13-12	7.057	4.031	309.2	349.9	350.5	366.0~365
MX 13-13	8.497	3.969	309.5	352.6	349.1	~365
MX 13-14	10.907	4.030	309.0	349.2	347.9	Very Broad

A full comparison of T2 values with a wide range of concentrations is shown in Table 3-15 with CsCl levels of 0, 1, 2, and 4 wt%. Overlay plots of T2 versus wt% $LaCl_3$ are shown in

Figure 3-42. In this figure, it is apparent that CsCl does actually lower the transition temperature. From the standpoint of designing a drawdown process, this should be considered a positive outcome. Accumulation of other fission products may actually help the salt mixture stay in the liquid state.

Table 3-15: Results of DSC testing for LiCl-KCl-$LaCl_3$-CsCl mixtures (presenting only liquidus temperatures). All reported concentrations are as-weighed and not verified with ICP-OES.

Composition of Sample		T2 (C)
Wt. % $LaCl_3$	**Wt. % CsCl**	
1.6	0	354.05
3.51	0	353.9
5.62	0	354.15
6.70	0	361.12
10.07	0	362.97
5.0	1.0	356.5
5.0	1.0	357.14
10	1.0	352.95
15	1.0	358.43
3.8	2.0	351.1
5.6	2.0	351.7
7.2	2.0	352.3
11.0	2.0	352.9
0.703	4.02	352.2
1.260	4.00	351.0
2.369	4.09	350.5
3.933	4.03	349.7
5.461	3.96	349.4
7.057	4.03	349.9
8.497	3.97	352.6
10.907	4.03	349.2

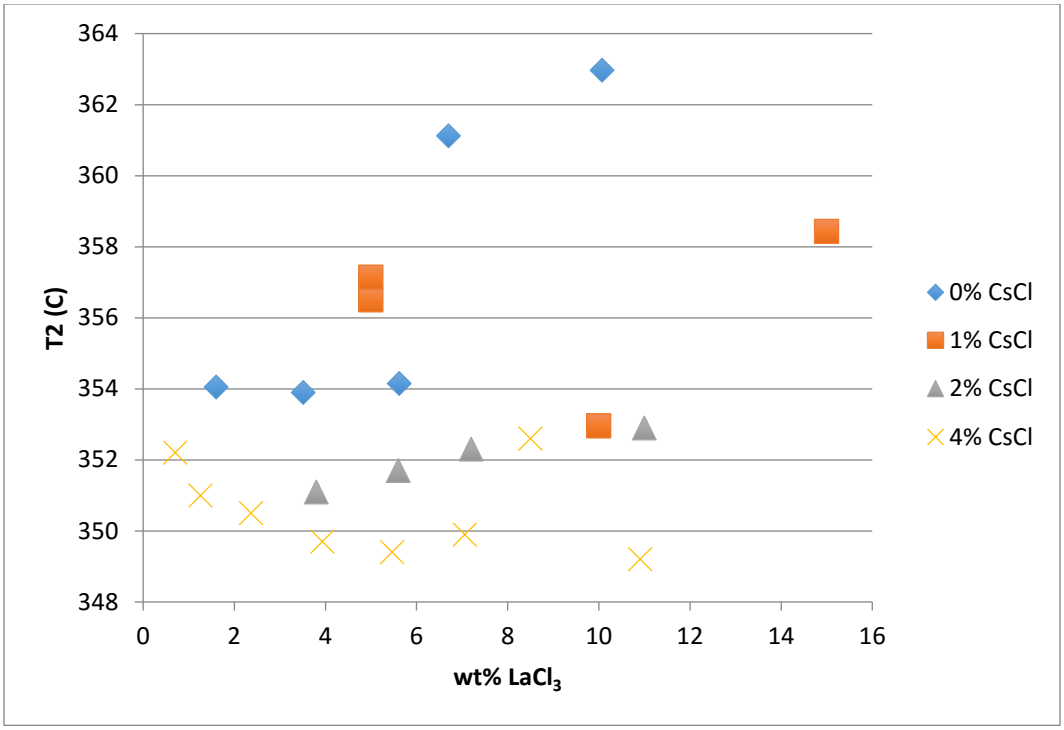

Figure 3-42: Overlay plot of T2 transition temperatures for LiCl-KCl-$LaCl_3$-CsCl at various concentrations. Concentrations based on nominal as-weighed amounts for the LiCl-KCl-$LaCl_3$-CsCl data set.

Heats of fusion values were also measured by integrating the endothermic peak T2 on the heating curves. To utilize the heat of fusion data for determination of phase behavior, a binary mixture model was developed in which LiCl-KCl-CsCl is assumed to be one component and $LaCl_3$ is assumed to be the other component. The heat of fusion of the mixture can be expressed by the following equation (A=$LaCl_3$, B=LiCl-KCl-CsCl).

$$\Delta H_{m,mix} = x_A \Delta H_{m,A} + x_B \Delta H_{m,B} + \Omega x_A x_B \qquad (3\text{-}11)$$

This assumes that the components form a regular solution. From the literature, values of 54.4 and 13.3 kJ/mole were found for heat of fusion of $LaCl_3$ and eutectic LiCl-KCl, respectively. The importance of the Ω parameter is in how it can be used to construct phase diagrams. This is through the excess Gibb's Free Energy, which is calculated via the following equation.

$$G^{XS} = \Omega x_A x_B \qquad (3\text{-}12)$$

That can then lead to the calculation of the Gibb's free energy of mixing via the following equation. This function must be less than zero for a mixture to form a stable phase.

$$\Delta G_{mix} = RT\left(x_A \ln x_A + x_B \ln x_B\right) + G^{XS} \qquad (3\text{-}13)$$

The heats of fusion are measured by the DSC in units of kJ/gram but were converted to units of kJ/mole and plotted in Figure 3-43. Test 13 samples (4 wt%) were not included in this plot, because it was difficult to establish the baseline as shown in Figure 3-41. This plot

seems to confirm that CsCl has a measurable impact on the phase behavior of the LiCl-KCl-$LaCl_3$ system. Attempts to fit equation (13) to determine values of Ω were unsuccessful. Additional mixing models should be considered and connections between these models and activity coefficients sought. Ideally, activity coefficients measured electrochemically should be consistent with those measured via thermal analysis.

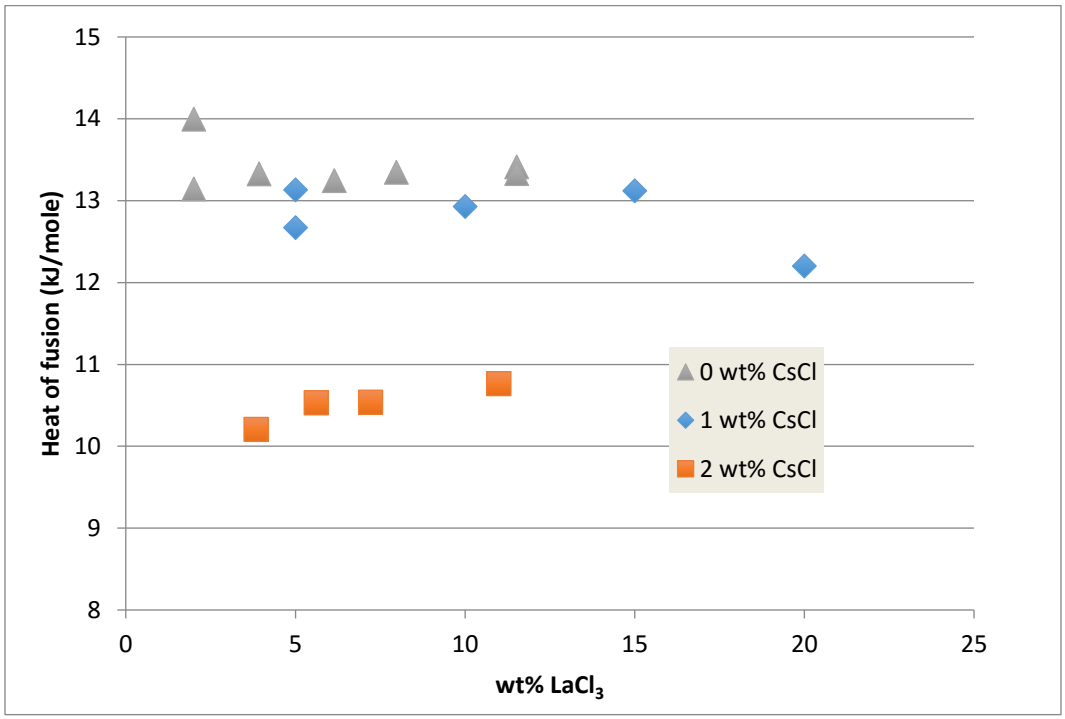

Figure 3-43: Heat of fusion for LiCl-KCl-$LaCl_3$-CsCl as function of $LaCl_3$ concentration at different levels of CsCl contamination.

Elementary phase diagrams for the $LaCl_3$-CsCl-LiCl-KCl system are given in Figures 3-44 and 3-45. All of the temperatures plotted here are the defined as the temperature of the onset of the endothermic event during heat-up.

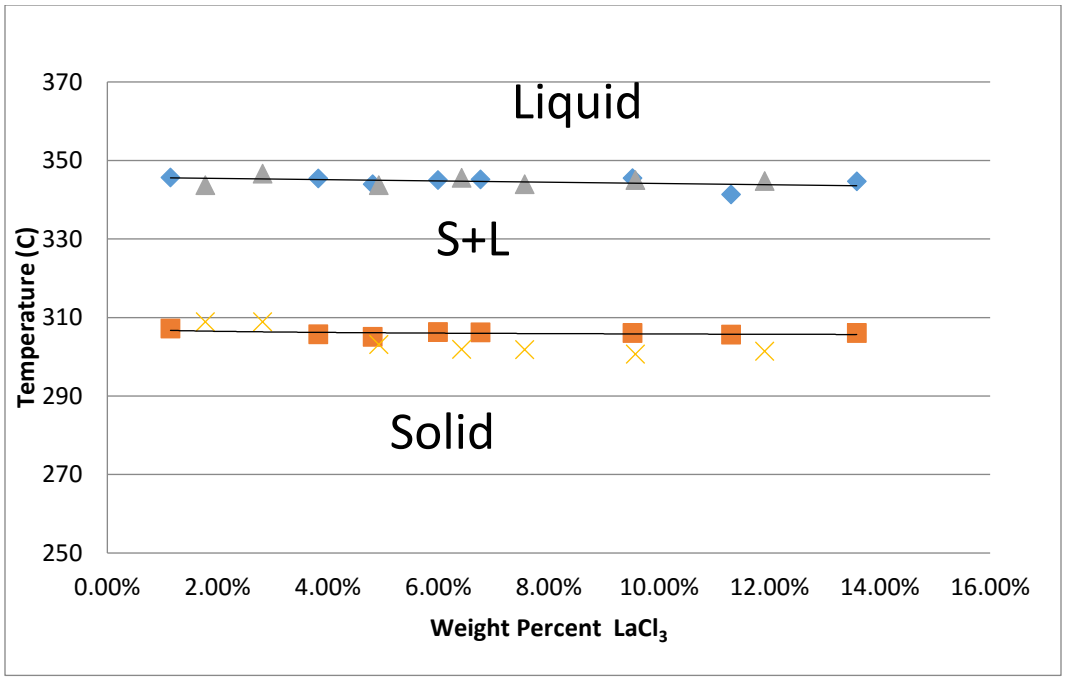

Figure 3-44: Phase diagram for xLaCl₃-LiCl-KCl-4 wt. % CsCl system.

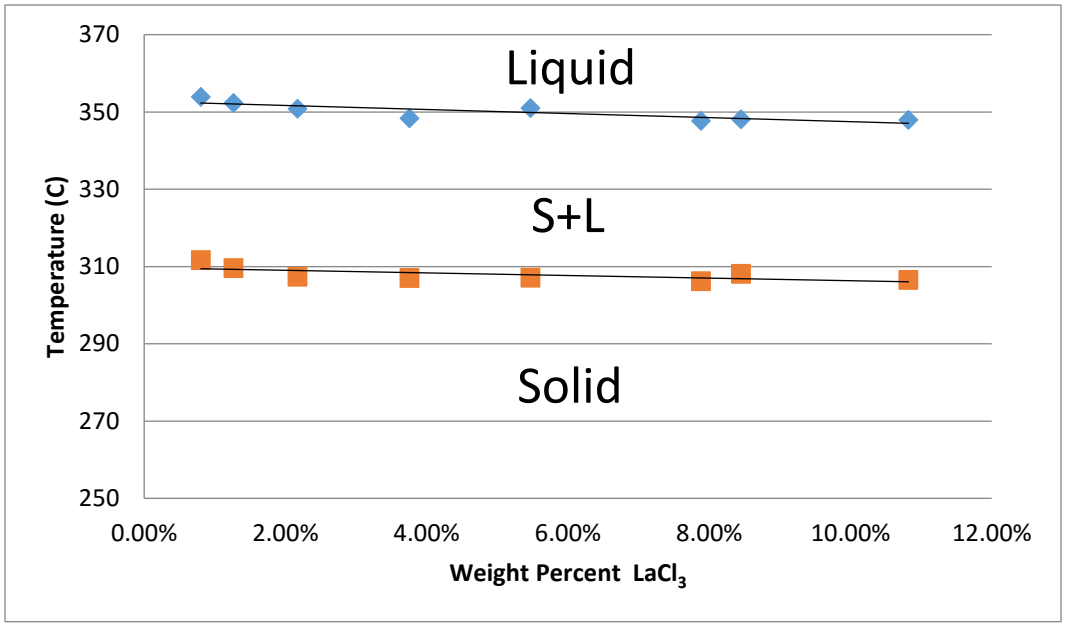

Figure 3-45: Phase diagram for xLaCl₃-LiCl-KCl-2 wt. % CsCl system.

We can see from that, with the presence of CsCl, there is a definite formation of the S+L region in the diagrams. In the presence of the only $LaCl_3$, there is only a single liquidus line. A comparison of the liquidus temperatures for the three concentrations of CsCl is shown in Figure 3-46. It can be observed that the presence of 2 wt. % CsCl does not really influence the melting temperature of the salt substantially. However, there is a definite depression in

the melting temperature of the salt in the presence of 4 wt. % CsCl. The data used for these plots are shown in Table 3-16.

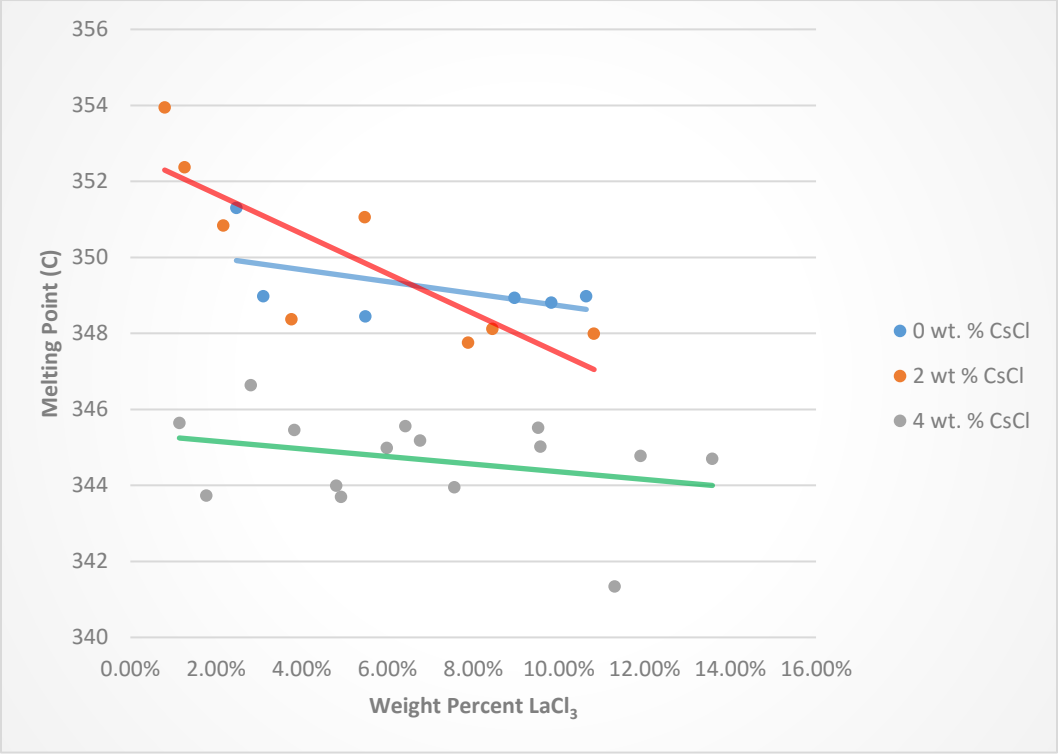

Figure 3-46: Liquidus lines for three concentrations of CsCl.

Table 3-16: Results of DSC testing of LiCl-KCl-$LaCl_3$-CsCl. Concentrations are based on concentration as determined by ICP-MS/OES.

Sample ID	Composition		Melting Point (°C)		
	Wt. % $LaCl_3$	Wt. % CsCl	T1	T2	T3
MX 8-8	2.48%	0	NA	351.3	
MX 8-9	3.11%	0	NA	348.98	
MX 8-10	5.48%	0	NA	348.45	
MX 8-11	8.97%	0	NA	348.94	
MX 8-12	9.82%	0	NA	348.81	
MX 8-13	10.64%	0	NA	348.98	
MX 11-07	0.80%		311.67	353.95	
MX 11-08	1.26%	2.02%	309.63	352.37	
MX 11-09	2.17%		307.42	350.84	
Mx 11-10	3.76%	2.04%	307.08	348.37	

MX 11-11	5.47%		307.12	351.06
MX 11-12	7.88%	2.06%	306.2	347.76
MX 11-13	8.45%		308.13	348.12
MX 11-14	10.82%	2.05%	306.57	347.99
MX 13-07	1.14%	4.02%	307.22	345.64
MX 13-08 After OCP	3.83%	4.14%	305.69	345.46
MX-13-09	4.81%	4.01%	305.09	343.99
MX-13-10	5.99%		306.29	344.99
MX 13-11	6.76%	3.96%	306.24	345.18
MX 13-12	9.52%		306.04	345.52
MX 13-13	11.30%	4.20%	305.6	341.34
MX 13-14	13.58%	4.33%	306.08	344.7
MX 14-05	1.77%	3.96%	308.93**	343.73
MX 14-06	2.82%	3.90%	308.94**	346.64
MX 14-07	4.92%	4.07%	303.11	343.7
MX 14-08	6.42%	4.00%	301.87	345.56
MX 14-09	7.56%	3.95%	301.83	343.95
MX 14-10	9.57%	4.06%	300.66	345.02
MX 14-11	11.91%	3.97%	301.4	344.78

**Peak not well defined

3.3.2. Phase diagram measurement for LiCl-KCl-$NdCl_3$-CsCl system

Mixtures of LiCl-KCl-$NdCl_3$-CsCl were also tested using the DSC via heat-up cycles to determine temperatures of endothermic phase transitions. The data for samples that did not contain CsCl are shown in Table 3-17 and plotted in Figure 3-47. Notice that only single transitions were detected, which have been assigned to the liquidus line on the phase diagram.

Table 3-17: Results of DSC testing of LiCl-KCl-$NdCl_3$. Concentrations are based on concentration as-weighed.

Sample ID	Composition		Melting Point (°C)		Heat of Fusion (J/g)
	Wt. % $NdCl_3$	Wt. % CsCl	T1	T2	
18-Nd-01	0.17%	0	356.20	NA	222.1
18-Nd-02	0.51%	0	357.23	NA	212.6
18-Nd-03	0.82%	0	357.01	NA	183.1
18-Nd-04	1.33%	0	354.18	NA	194.2
18-Nd-05	2.07%	0	353.59	NA	149.6
18-Nd-06	3.26%	0	355.05	NA	111.4
18-Nd-07	4.48%	0	354.08	NA	127.3
18-Nd-08	6.55%	0	352.39	NA	138.0
18-Nd-09	9.30%	0	353.68	NA	108.0

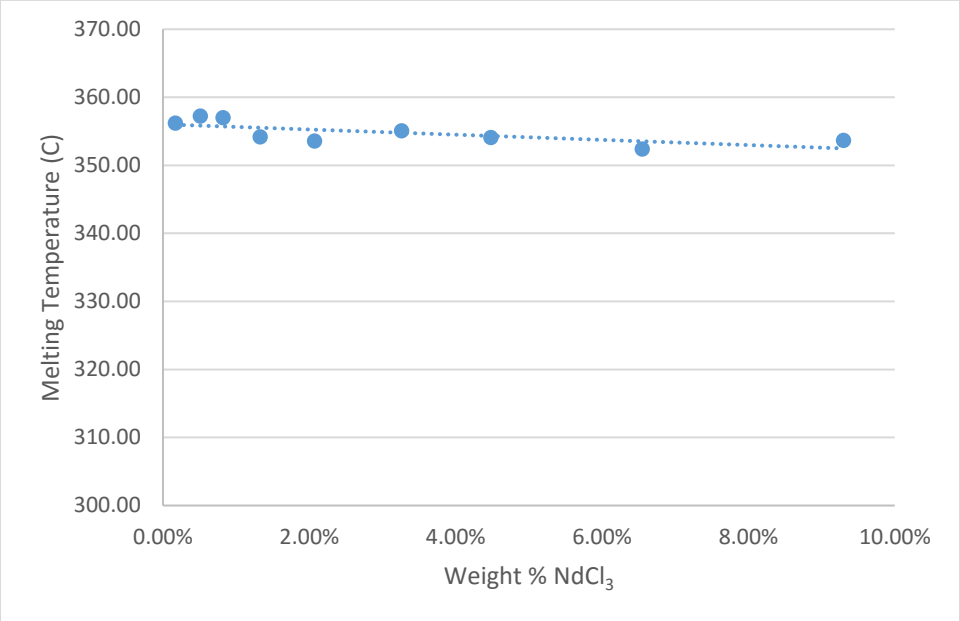

Figure 3-47: Liquidus curve for LiCl-KCl-$NdCl_3$.

In Figure 3-48 and Table 3-18, the liquidus temperatures are presented for mixtures that included CsCl. For the $NdCl_3$ system, no departure from eutectic behavior was observed in the concentration range tested, meaning that there was no detected two phase (solid + liquid) region. However, it did appear that additions of CsCl lowered the liquidus temperature of the mixture.

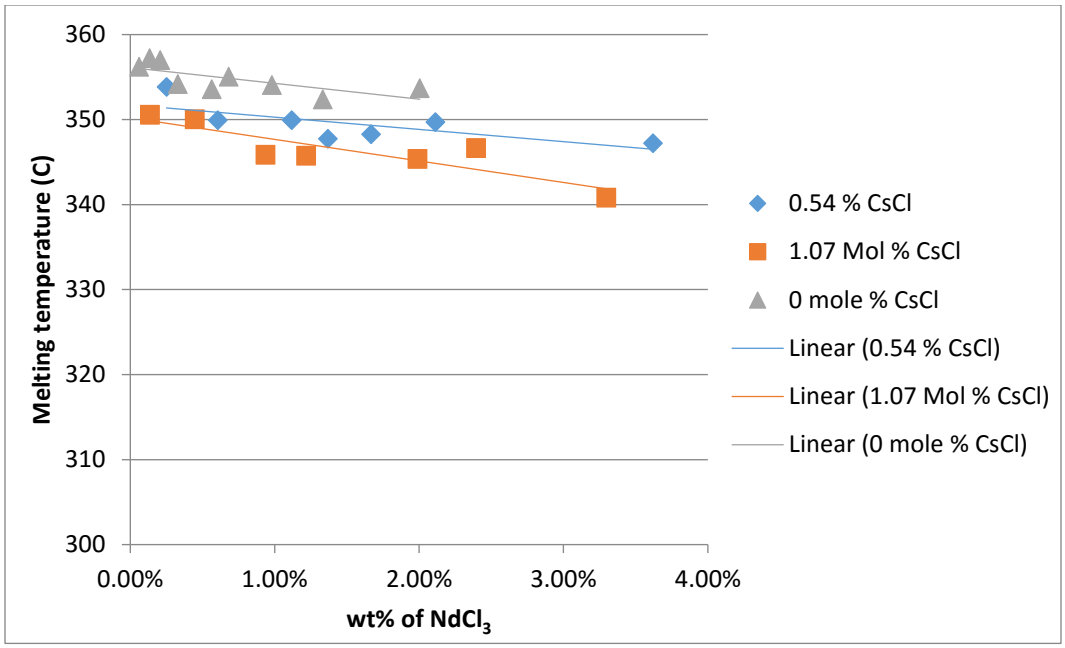

Figure 3-48: Phase diagram for LiCl-KCl-NdCl3-CsCl.

Table 3-18: Results from DSC Testing of LiCl-KCl-NdCl3-CsCl. Concentrations are based on ICP-MS results.

Sample ID	Composition		Melting Point (°C)		
	Mol % $NdCl_3$	Mol % CsCl	T1	T2	T3
18-Nd-01	6.05E-04	0		355.13	
18-Nd-02	0.13%	0		353.64	
18-Nd-03	0.21%	0		353.24	
18-Nd-04	0.33%	0		354.08	
18-Nd-05	0.56%	0		354.08	
18-Nd-06	0.68%	0		353.98	
18-Nd-07	0.98%	0		355.78	
18-Nd-08	1.33%	0		356.45	
18-Nd-09	2.01%	0		353.05	
TGA-Nd1-1	0.25%	0.35%		353.85	
TGA-Nd1-2	0.61%	0.46%		349.94	
TGA-Nd1-3	1.12%	0.59%		349.93	
TGA-Nd1-4	1.37%	0.57%		347.73	
TGA-Nd1-5	1.67%	0.59%		348.26	
TGA-Nd1-6	2.11%	0.61%		349.69	
TGA-Nd1-7	3.62%	0.64%		347.22	
TGA-Nd2-1	0.14%	0.53%		350.57	
TGA-Nd2-2	0.45%	0.95%		350.03	
TGA-Nd2-3	0.94%	1.06%		345.85	
TGA-Nd2-4	1.22%	1.23%		345.75	
TGA-Nd2-5	1.99%	1.37%		345.39	
TGA-Nd2-6	2.40%	1.17%		346.64	
TGA-Nd2-7	3.30%	1.22%		340.81	

3.3.3. Phase diagram measurement for LiCl-KCl-$CeCl_3$-CsCl system

As expected, for the LiCl-KCl-$CeCl_3$ system with no CsCl present, a single sharp endothermic event was observed in the DSC data. This corresponded to the melting of the mixture close to the eutectic melting temperature of the LiCl-KCl mixture (Figure 3-49).

In the mixtures with 0.70 mol % CsCl, a small shoulder peak is observed with at around 328°C. This probably represents the melting of some phase at a lower temperature (Figure

3-50). This small peak is not present at low concentrations of $CeCl_3$, but becomes more prominent as the concentration of $CeCl_3$ increases in the presence of CsCl.

Finally, in samples with 1.40 mol % CsCl a small endothermic peak is observed at about 267°C, this is followed by a small shoulder at around 330°C, then the main endothermic peak at around 350°C. At the higher concentrations of $CeCl_3$, some endothermic peaks are also observed at around 400°C (Figure 3-51). This system is at this point deemed too complex to accurately determine the solidus and liquidus temperatures using only TGA/DSC data.

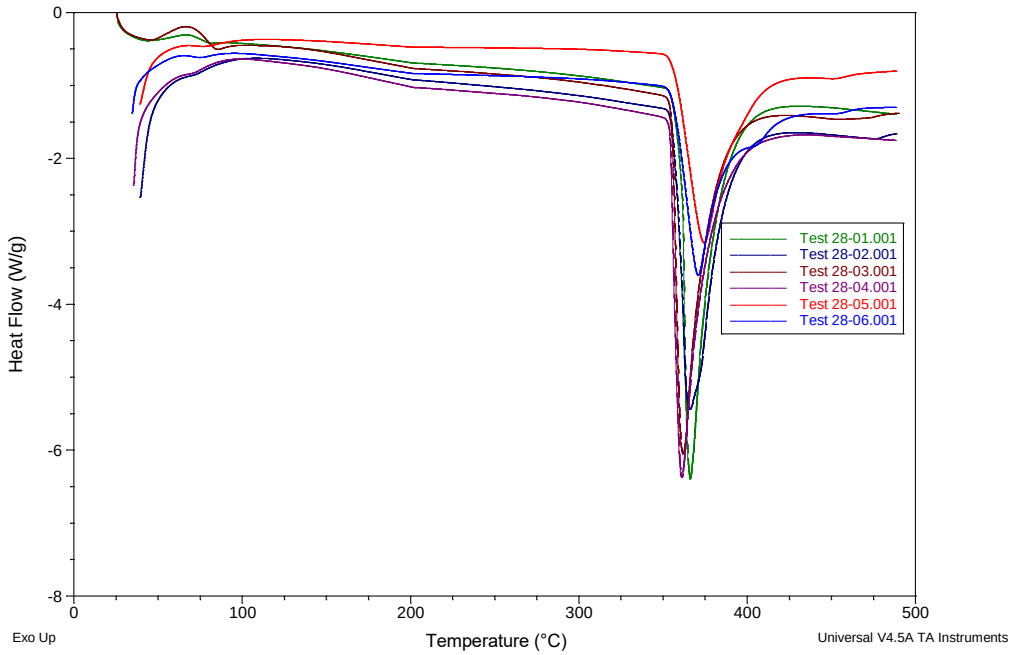

Table 3-19: DSC curves for the LiCl-KCl-$CeCl_3$ system

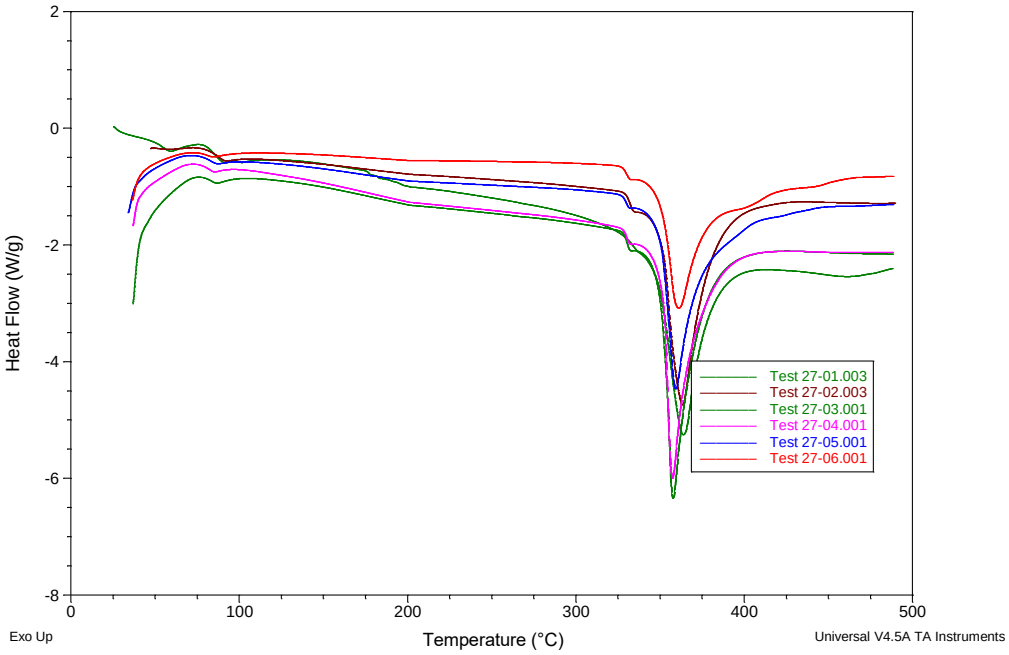

Figure 3-49: DSC curves for the LiCl-KCl-CsCl-$CeCl_3$ system with presence of 0.70 mol % CsCl.

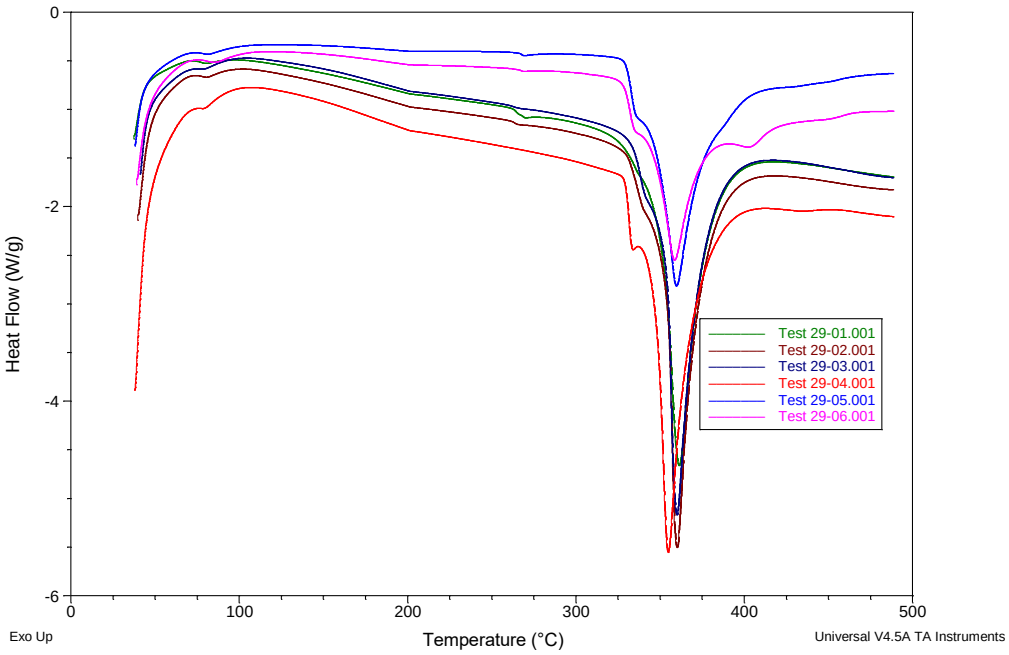

Figure 3-50: DSC curves for the LiCl-KCl-CsCl-$CeCl_3$ system with presence of 1.40 mol % CsCl.

The phase transition data obtained from DSC for LiCl-KCl-$CeCl_3$-CsCl are shown in Table 3-19. Figure 3-52 contains a plot of the liquidus temperatures for all of the tests for this series. A slight depression in the liquidus temperature is observed in the presence of 0.7

and 1.4 mol % CsCl. This depression seems to be identical for both of these CsCl concentrations.

Table 3-20: Results from DSC Testing with LiCl-KCl-$CeCl_3$-CsCl. Concentrations are based on ICP-OES measurements.

Sample ID	Composition		Melting Point (°C)		
	Mol % $CeCl_3$	Mol % CsCl	T1	T2	T3
27Ce-01	0.09%	0.70%		NA	346.16
27Ce -02	0.57%	0.69%		328	349.49
27Ce -03	1.02%	0.69%		328	351.01
27Ce -04	2.18%	0.68%		328	351.48
27Ce -05	3.79%	0.67%		328	349.15
27Ce -06	5.13%	0.66%		328	349.92
28Ce-01	0.20%	0.00%			361.02
28Ce -02	0.47%	0.00%			357.71
28Ce -03	0.83%	0.00%			355.39
28Ce -04	2.03%	0.00%			354.15
28Ce -05	2.81%	0.00%			356.22
28Ce -06	3.48%	0.00%			356.43
29Ce-01	0.09%	1.44%	269.67	NA	349.95
29Ce -02	0.28%	1.43%	266.00	340	353.25
29Ce -03	0.99%	1.42%	266	341	352.86
29Ce -04	2.12%	1.41%	NA	333.19	345.73
29Ce -05	3.92%	1.39%	266.14	335	341.7
29Ce -06	4.06%	1.37%	268.75	335.62	343.97

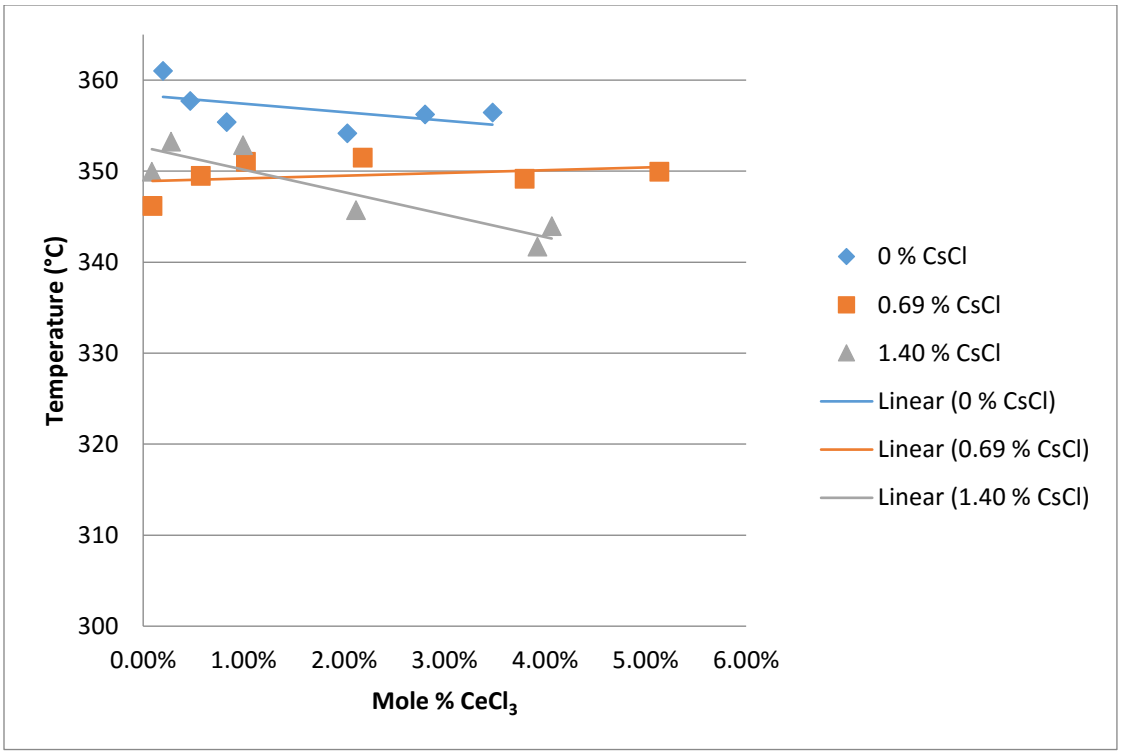

Figure 3-51: The liquidus temperatures for the LiCl-KCl-CsCl-$CeCl_3$ quaternary system.

3.3.4. Phase diagram measurement for LiCl-KCl-$GdCl_3$-CsCl system

Figure 3-53 shows a plot of the liquidus temperatures for the LiCl-KCl-$GdCl_3$-CsCl system. A slight reduction of the liquidus temperature appears to have been achieved from adding both 0.7 and 1.4 mol % CsCl. Both concentrations of added CsCl yield the same liquidus temperatures. At the highest concentration of CsCl tested (1.40 mol %), a solidus peak is observed at about 260°C. These peaks were not observed for 0 or 0.7 mol% CsCl. The solidus peak also disappears at high concentrations of $GdCl_3$. This results in a phase diagram as shown in Figure 3-54. All of the DSC results are summarized for LiCl-KCl-$GdCl_3$-CsCl in Table 3-20.

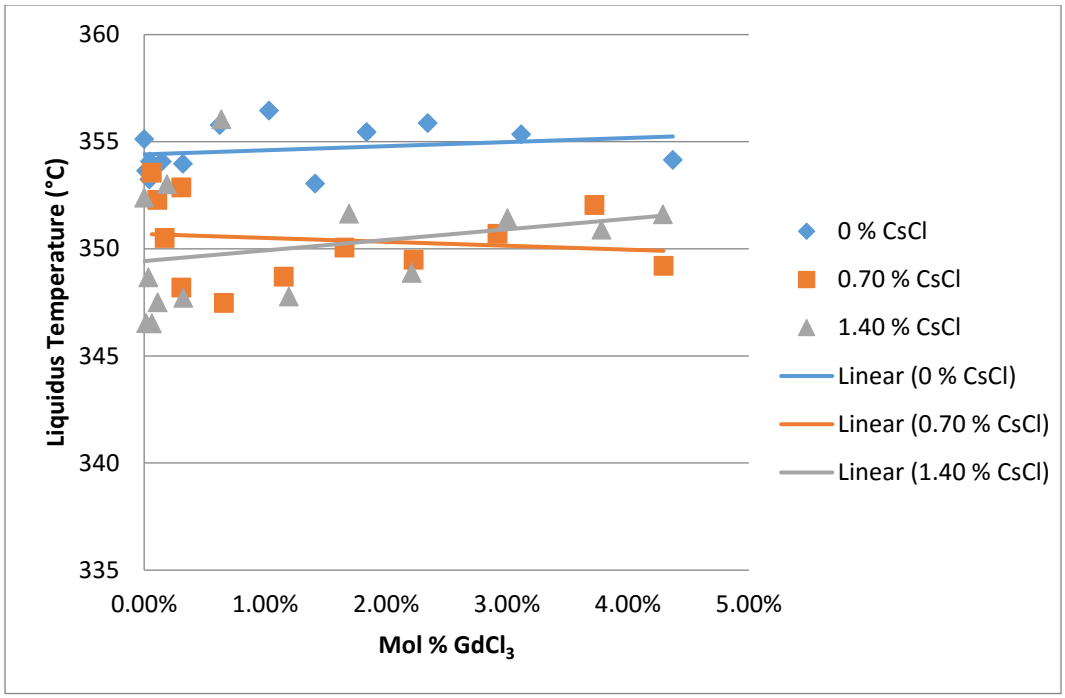

Figure 3-52: Liquids temperatures for LiCl-KCl-$GdCl_3$-CsCl at the three concentrations of CsCl tested.

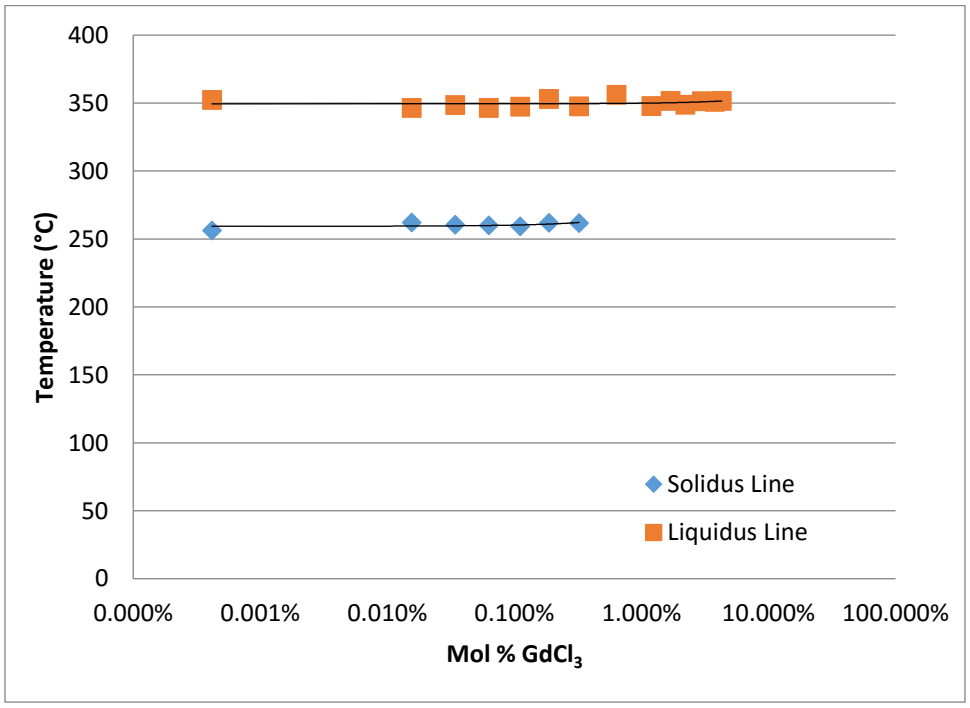

Figure 3-53: Phase diagram for LiCl-KCl-$GdCl_3$-CsCl with 1.40 mol % CsCl present.

Table 3-21: Results of DSC testing of LiCl-KCl-$GdCl_3$-CsCl. Concentrations are as-weighed.

Sample ID	Composition		Melting Point (°C)		
	Mol % $GdCl_3$	Mol % CsCl	T1	T2	T3
18Gd-01	0.00%	0.00%		355.13	
18Gd-02	0.02%	0.00%		353.64	
18Gd-03	0.04%	0.00%		353.24	
18Gd-04	0.05%	0.00%		354.08	
18Gd-05	0.14%	0.00%		354.08	
18Gd-06	0.32%	0.00%		353.98	
18Gd-07	0.62%	0.00%		355.78	
18Gd-08	1.03%	0.00%		356.45	
18Gd-09	1.41%	0.00%		353.05	
18Gd-10	1.84%	0.00%		355.45	
18Gd-11	2.34%	0.00%		355.87	
18Gd-12	3.12%	0.00%		355.34	
18Gd-13	4.37%	0.00%		354.15	
20Gd-02	0.03%	0.70%			
20Gd-03	0.06%	0.70%		353.55	
20Gd-04	0.11%	0.70%		352.28	
20Gd-05	0.17%	0.70%		350.51	
20Gd-06 AD	0.31%	0.70%		352.87	
20Gd-06 FD	0.31%	0.70%		348.19	
20Gd-07	0.66%	0.70%		347.48	
20Gd-08	1.15%	0.70%		348.7	
20Gd-09	1.66%	0.69%		350.06	
20Gd-10	2.23%	0.69%		349.49	
20Gd-11	2.92%	0.68%		350.7	
20Gd-12	3.72%	0.68%		352.04	
20Gd-13	4.29%	0.67%		349.21	
23Gd-01	0.00%	1.43%	256.22	352.39	
23Gd-02	0.02%	1.43%	262.12	346.54	
23Gd-03	0.03%	1.43%	260.48	348.67	
23Gd-04	0.06%	1.43%	260.17	346.52	
23Gd-05	0.11%	1.43%	259.38	347.51	

23Gd-06	0.19%	1.43%	261.89	353.02
23Gd-07	0.32%	1.43%	261.67	347.71
23Gd-08	0.64%	1.42%	NA	356.05
23Gd-09	1.20%	1.42%	NA	347.78
23Gd-10	1.69%	1.43%	NA	351.65
23Gd-11	2.21%	1.42%	NA	348.88
23Gd-12	3.00%	1.44%	NA	351.44
23Gd-13	3.78%	1.43%	NA	350.9
23Gd-14	4.29%	1.42%	NA	351.61

3.3.5. Discussion of phase diagram studies

In the ensuing discussion, an attempt will be made to explain the reasons for the observed effects. Two pathways will be discussed.

From the phase diagram data reported above, it can be concluded that the presence of CsCl depresses the liquidus temperature for all four systems studied here. In three of the systems, $LaCl_3$, $CeCl_3$, and $GdCl_3$ a low temperature peak observed is additionally observed. The consistency of the depression in the liquidus temperatures with the addition of CsCl points to a common underlying phenomenon that may be contributing to the lowering of liquidus temperatures. This phenomenon is probably operative and effective to varying degrees in all four lanthanides. The liquidus temperature can be calculated using the Le Chatelier-Shreder [84] relationship as shown in Equation 3-14. The Le Chatelier-Shreder equation draws a link between the liquidus temperatures and the activity of species.

$$T_{i,liq} = \frac{\Delta_{fus}H_i T_{fus,i}}{\Delta_{fus}H_i - RT_{fus,i}ln(a_i)} \qquad (3\text{-}14)$$

In equation 3-14, the $T_{i,liq}$ is the liquidus temperature of species i which is a function of the enthalpy of fusion and activity of species i. Using this equation, it is possible to calculate liquidus temperature. For the systems LiCl-KCl-CsCl-$RECl_3$ salt mixtures tested for this work, it would be challenging to use this equation since there are four species that need to be considered; LiCl, KCl, CsCl, and $RECl_3$. Of these four species, the activity of only one species, $RECl_3$ is known from the electrochemical measurements made in this project. One way to look at this equation intuitively is to consider the system as a pseudo binary system made of LiCl-KCl-$RECl_3$ and CsCl, since the liquidus temperatures shows a depression from the baseline liquidus temperature of the LiCl-KCl-$RECl_3$ system. Now when CsCl is added to the ternary salt mixture, the activity of the LiCl-KCl-$RECl_3$ will decrease since its mole fraction decreases. In terms of equation 3-1, this implies that the value of a_i decreases. This implies that the term $\ln(a_i)$ is a larger negative number. This means that the denominator in equation 3-1 is larger causing the term, $T_{i,liq}$, on the left hand side to be smaller. This is consistent with the observations reported in this work. But actual calculation of the liquidus temperatures requires knowledge of the activity of the LiCl-KCl-$RECl_3$ this may be

possible to calculate using the Gibbs-Duhem equation if CsCl activity is known. But data is not available for activity coefficient of CsCl in these salt mixtures. So, this equation is useful for explaining the effect of CsCl addition but not for predicting the effect.

Consider the observed phase behavior as a possible consequence of coordination chemistry. In general, lanthanides are known to be present in the molten salt in an octahedral network structure of the form $LnCl_6^{3-}$. Alkali metals are known to be effective network breakers of increasing power going from Li to Cs. When an alkali metal like Cs is added to a molten salt mixture, the octahedral structure is broken down to incorporate the additional Cl^- ions into the coordination shell of the $LnCl_3$ ions. The degree to which the network structure is broken is governed by the ease with which the alkali cation releases their Cl^- ions. Cs^+ releases its Cl^- ions with a greater efficiency and hence is considered a better structure breaker [85]. This propensity of the Cs^+ ions to break the network structure in molten salts may play an important role in the observed phase diagram behavior. First looking at the LiCl-KCl-CsCl-$LaCl_3$ mixtures, two important observation can be made. First, at the low CsCl concentration of 0.70 mol %, the peak of the low temperature endothermic event is small and does seem to get bigger with increasing $LaCl_3$ concentration. Another observation is that for the LiCl-KCl-CsCl-$LaCl_3$ mixtures with 1.40 mol% CsCl, the peak of the low temperature endothermic event is much more prominent than the comparable peaks for mixtures with 0.70 mol % CsCl. It is clear from these trends that at high CsCl and high $LaCl_3$ concentrations there seems to be some intermolecular interactions that causes the low temperature endothermic event peaks to be more prominent.

While there have been no other studies to date on the LiCl-KCl-CsCl-$LaCl_3$ systems, there have been a number of studies [85, 86] performed on binary $LaCl_3$-CsCl molten salt mixtures. Okamoto et al. [86] reported that the introduction of CsCl into pure $LaCl_3$ melt cause the coordination number of Cl^- to decrease from 8 to a limiting case of 6 (octahedral structure) with increasing CsCl concentration. This finding concurs with the conclusions that were drawn by Rollet and Salanne [83] that the bigger the alkali earth species the stronger the decrease in the coordination number of anion around cation. The strong propensity of CsCl to break up the structure of $LaCl_3$ should also be present when the $LaCl_3$ is dissolved in LiCl-KCl eutectic salt. The presence of two alkali metals, Li and K, already disrupts the structure of $LaCl_3$ to a certain extent. However, the introduction of CsCl likely aggravates these disruptions further. This would be the reason for the change in behavior of the LiCl-KCl-$LaCl_3$ system when CsCl is introduced from a coordination chemistry standpoint.

Interestingly, Okamoto et al. [86] also noted that based on related works [86, 87] that other trivalent metal ions show different behavior when mixed with alkali halides. Ions smaller than La^{3+}, like Y^{3+} or Dy^{3+}, which form six coordinate chloride crystals, appear not to change their coordination number on dilution in alkali chlorides. This indicates that not even all lanthanides behave identically underscoring the complexity of these studies in drawing meaningful interpretations. The closely related system of $NdCl_3$-ACl (A = Li, Na, K, Cs) is much harder to comment on since it has been studied by only a handful of authors [88,89,90]. The $NdCl_3$ also shows an octahedral structure with $NdCl_6^{3-}$ ions [88] in the presence alkali ions like Cs^+. The reason this system behaves vastly different from the $LaCl_3$

system is not well understood from the existing open literature. For the $GdCl_3$-ACl system, again an octahedral $GdCl_6^{3-}$ structure has been reported in the literature [91, 92]. Though no studies are present on the $GdCl_3$-CsCl system, studies on the $GdCl_3$-KCl [91] and $GdCl_3$-LiCl-KCl [92] systems exist. It is hard to conclude much from either of these two studies on the possible interactions of CsCl with $GdCl_3$. However, on the phase diagram behavior and the general interaction of lanthanides with CsCl some information can be hypothesized. In the phase diagrams, a lower temperature peak is observed only at high CsCl and low $GdCl_3$ concentrations. This indicates that if CsCl does break the network structures of $GdCl_3$, it is probably more effective at high Cs/Gd ratios. $CeCl_3$ is also known to be present in the octahedral coordination in molten salts [93]. However, there is no published literature for the $CeCl_3$-alkali chloride interactions. However, given the similarity between the behavior of $CeCl_3$ and $LaCl_3$ systems, it may be presumed that both of these systems behave similarly. In the above discussion, it is recognized that the explanations and potential conclusions may be incomplete. However, given the complex nature of the systems studied here and the unique behavior of each rare earth, it is hard to ascertain the exact causes for the various phenomenon observed and reported here**.**

3.3.6. Conclusions

The solidus and liquidus temperatures for four quaternary salt systems were measured and reported. These systems were the LiCl-KCl-CsCl-$RECl_3$ (RE = La, Nd, Ce, and Gd) mixtures. It was observed that the presence of CsCl causes a slight depression in the liquidus temperature for all of the four rare earth chloride mixtures when compared to the corresponding ternary system liquidus temperatures in the absence of any CsCl. The $LaCl_3$ and $CeCl_3$ quaternary system (with CsCl) manifests a peritectic behavior as opposed to eutectic behavior of ternary systems (no CsCl). The $GdCl_3$ quaternary system shows a peritectic behavior only in a limited concentration windows, at low $GdCl_3$ and high CsCl concentrations. The $NdCl_3$ system shows a eutectic behavior throughout the concentrations range tested in this work, albeit with a slight depression in the liquidus temperatures in the presence of CsCl.

4. Solubility prediction model

In order to monitor the pryroprocessing process and optimize its design, thermodynamic assessment of actinides and lanthanides in LiCl-KCl molten salt is significantly needed. Even though several systems have been assessed, such as LiCl-KCl-$CeCl_3$ [94,95] and LiCl-KCl-UCl_3 [96], as one of the important lanthanide, $GdCl_3$ in LiCl-KCl has not been evaluated. In the present work, thermodynamic properties of LiCl-KCl-$GdCl_3$ are being considered and evaluated. Two-sublattice model for ionic liquid was applied to LiCl-$GdCl_3$, and KCl-$GdCl_3$ binary systems primarily to model their Gibbs energies. The experimental data used includes the phase information and enthalpy of mixing from literature. Assessment of LiCl-KCl was directly from our previous work [97]. The ternary system of LiCl-KCl-$GdCl_3$ was extrapolated based on the binary systems by applying Kohler-Toop asymmetric formulism [98]. After that, the solubility of $GdCl_3$ in the typical molten LiCl-KCl used in pyroprocessing were derived from the optimized results.

4.1. Database for LiCl-KCl-$GdCl_3$ system

The LiCl-KCl system has been widely studied and assessed in our previous work [97]. For the KCl-$GdCl_3$ system, Korshunov et al. [99] studied it by experiments and reported three intermediate compounds, KGd_3Cl_{10}, K_2GdCl_5, and K_3GdCl_6. Frenzel [100] restudied the system later and claimed that the first compound is KGd_2Cl_7 but not KGd_3Cl_{10}. Sefert et al. [101] then performed a more detailed study by calorimetric and EMF method. They confirmed the existence of KGd_2Cl_7 and investigated all the enthalpy, entropy, and Gibbs energy information of each intermediate compound. However, few studies were focus on the LiCl-$GdCl_3$ system. The only one we found was Chaogui Zheng et al. [102] (in Chinese). They studied the system by differential thermal analysis and x-ray diffraction methods. An intermediate compound of Li_3GdCl_6 with two structures was reported with a transition temperature of 373 ^{0}C. For the LiCl-KCl-$GdCl_3$ system, no phase or structure studies found in the literature. They were extrapolated from binary systems based on Kohler-Toop asymmetric formulism preliminarily without considering the ternary interactions.

4.2. Thermodynamic modeling

In the present work, a two-sublattice model [103,104] was applied to describe the excess Gibbs energy of liquid. The model separates anions and cations into different sublattices. Since KGd_2Cl_7 divides the KCl-$GdCl_3$ system into two pseudo-binary system, here it was treated as a neutral species in anionic sublattice to deal with the short-range ordering. Now the model is indicated by

$$(K^+, Li^+, Gd^{3+})_p : (Cl^-, KGd_2Cl_7)_q$$

The parenthesis represents different lattices and the colon is used to separate them. In every parenthesis, there is a constituent array resided in the sub-lattice. p and q are the site numbers in the corresponding lattice and given by

$$p = y_{Cl^-} \tag{4-1}$$

And

$$q = y_{K^+} + y_{Li^+} + 3y_{Gd^{3+}} \tag{4-2}$$

where y_i is the site fraction of a particular species i on the corresponding sublattice. The molar Gibbs energy of liquid phase now is

$$\begin{aligned} G_m^{Liq.} &= y_{Li^+} y_{Cl^-} {}^0G^{Liq.}_{Li^+:Cl^-} + y_{K^+} y_{Cl^-} {}^0G^{Liq.}_{K^+:Cl^-} + y_{Gd^{3+}} y_{Cl^-} {}^0G^{Liq.}_{Gd^{3+}:Cl^-} \\ &+ {}^0G^{Liq.}_{KGd_2Cl_7} + RT[\,p(y_{Li^+} lny_{Li^+} + y_{K^+} lny_{K^+} + y_{Gd^{3+}} lny_{Gd^{3+}}) \\ &q(y_{Cl^-} lny_{Cl^-} + y_{KGd_2Cl_7} lny_{KGd_2Cl_7})] + {}^E G_m^{Liq.} \end{aligned} \tag{4-3}$$

where ${}^0G^{Liq.}_{Li^+:Cl^-}$, ${}^0G^{Liq.}_{K^+:Cl^-}$ ${}^0G^{Liq.}_{Gd^{3+}:Cl^-}$, ${}^0G^{Liq.}_{KGd_2Cl_7}$ are the standard molar Gibbs energy of LiCl, KCl, $GdCl_3$, and KGd_2Cl_7 in liquid status, respectively. The Gibbs energy of the end members were from Thermo-Calc Software SGET database v5.2 [105]. ${}^E G_m^{Liq.}$ is the molar excess Gibbs energy. In the manner of Muggianu formalism [106], it was given by

$$\begin{aligned} {}^E G_m^{Liq.} &= y_{Cl^-}(y_{K^+} y_{Li^+} L^{Liq.}_{K^+,Li^+:Cl^-} + y_{K^+} y_{Gd^{3+}} L^{Liq.}_{K^+,Gd^{3+}:Cl^-} + y_{Li^+} y_{Gd^{3+}} L^{Liq.}_{Li^+,Gd^{3+}:Cl^-}) \\ &+ y_{Cl^-} y_{KGd_2Cl_7}(y_{K^+} L^{Liq.}_{K^+:Cl^-,KGd_2Cl_7} + y_{Li^+} L^{Liq.}_{Li^+:Cl^-,KGd_2Cl_7} + y_{Gd^{3+}} y_{KGd_2Cl_7} L^{Liq.}_{Gd^{3+}:Cl^-,KGd_2Cl_7}) \\ &+ y_{Cl^-} y_{KGd_2Cl_7}(y_{K^+} y_{Li^+} L^{Liq.}_{K^+,Li^+:Cl^-,KGd_2Cl_7} + y_{K^+} y_{Gd^{3+}} L^{Liq.}_{K^+,Gd^{3+}:Cl^-,KGd_2Cl_7} \\ &+ y_{Li^+} y_{Gd^{3+}} L^{Liq.}_{Li^+,Gd^{3+}:Cl^-,KGd_2Cl_7}) + y_{K^+} y_{Li^+} y_{Gd^{3+}} y_{Cl^-}(L^{Liq.}_{K^+,Li^+,Gd^{3+}:Cl^-} \\ &+ y_{KGd_2Cl_7} L^{Liq.}_{K^+,Li^+,Gd^{3+}:Cl^-,KGd_2Cl_7}) \end{aligned} \tag{4-4}$$

These interaction parameters L for both binary and ternary interactions could be expressed as concentration and temperature dependent. For example, binary interaction parameter $L^{Liq.}_{K^+,Gd^{3+}:Cl^-}$ can be expanded as a Redlich-Kister polynomial [107]

$$L^{Liq.}_{K^+,Gd^{3+}:Cl^-} = \sum_{v=0}^{n} {}^v L^{Liq.}_{K^+,Gd^{3+}:Cl^-}(y_{K^+} - y_{Gd^{3+}})^v \tag{4-5}$$

And ternary one, for example, can be

$$L^{Liq.}_{Li^+,K^+,Gd^{3+}:Cl^-} = y_{Li^+} L_{Li^+:Cl^-} + y_{K^+} L_{K^+:Cl^-} + y_{Gd^{3+}} L_{Gd^{3+}:Cl^-} \tag{4-6}$$

Then linear dependence on temperature is applied to these parameters like

$$ {}^v L = a_v + b_v T \tag{4-7}$$

a_v and b_v are the parameters that will be optimized during the calculation. Since there are no heat capacity data for the intermediate compounds, their standard Gibbs energies are written according to Neumann–Kopp rule [108] as, for example,

$$ {}^{0}G^{state}_{K_mGd_nCl_{m+3n}} = m\,{}^{0}G^{state}_{KCl} + n\,{}^{0}G^{state}_{GdCl_3} + A + BT \quad (4\text{-}8) $$

where "state" stands for liquid or solid. A and B are variables related to the enthalpy and entropy of formation of the intermediate compound $K_mGd_nCl_{m+3n}$, respectively. These values were optimized according to experimental data.

4.3. **Results and discussion**

The parameter optimization was carried out in the PARROT module of CALPHAD software Thermo-Calc [109] by minimizing the sum of squares of errors through iterations. Data collected from the references and Thermo-Calc were edited into an experimental data file to be used as the input. After obtaining the Gibbs energy expressions for different phases in the system, phase diagrams were calculated and plotted accordingly in the POLY module of the same software. Figure 4-1 and Figure 4-2 shows the calculated phase diagrams of KCl-$GdCl_3$ and LiCl-$GdCl_3$, respectively. It can be observed that the calculated results agree well the experiments. The phase transitions of Li_3GdCl_6 is also captured. The LiCl-KCl phase diagram was taken directly from our previous work [97]. Then using the Kohler-Toop asymmetric formulism, the ternary phase diagram of LiCl-KCl-$GdCl_3$ was assessed as Figure 4-3. The liquidus projection at 723, 773, and 823 K is plotted. The optimized parameters are shown in Table 4-1.

Table 4-1: Optimized parameters for the LiCl-KCl-$GdCl_3$ system

Phase	Parameters
Solid	${}^{0}L_{Li^+,K^+:Cl^-} = 17467.15$
	${}^{0}G^{s}_{KGd_2Cl_7} = {}^{0}G^{s}_{KCl} + 2\,{}^{0}G^{s}_{GdCl_3}$ -18846.53-47.50T
	${}^{0}G^{s}_{K_2GdCl_5} = 2\,{}^{0}G^{s}_{KCl} + {}^{0}G^{s}_{GdCl_3}$ -53651.49-2.63T
	${}^{0}G^{s}_{K_3GdCl_6} = 3\,{}^{0}G^{s}_{KCl} + {}^{0}G^{s}_{GdCl_3}$ -23242.96-57.50T
	${}^{0}G^{s}_{\alpha-Li_3GdCl_6} = 3\,{}^{0}G^{s}_{LiCl} + {}^{0}G^{s}_{GdCl_3}$ -12145.00+18.65T
	${}^{0}G^{s}_{\beta-Li_3GdCl_6} = 3\,{}^{0}G^{s}_{LiCl} + {}^{0}G^{s}_{GdCl_3}$ -4631.07+7.02T
Liquid	${}^{0}L_{Li^+,K^+:Cl^-} = $-17523.74
	${}^{0}L_{Gd^{3+},Li^+:Cl^-} = 28551.95-62.54T$
	${}^{1}L_{Gd^{3+},Li^+:Cl^-} = $-24743.15+26.14$T$
	${}^{0}L_{K^+,Gd^{3+}:Cl^-} = $-123452.61+54.18$T$
	${}^{1}L_{K^+,Gd^{3+}:Cl^-} = 11659.96$
	${}^{0}G^{l}_{KGd_2Cl_7} = {}^{0}G^{l}_{KCl} + 2\,{}^{0}G^{l}_{GdCl_3}$ -2675.41-54.62T

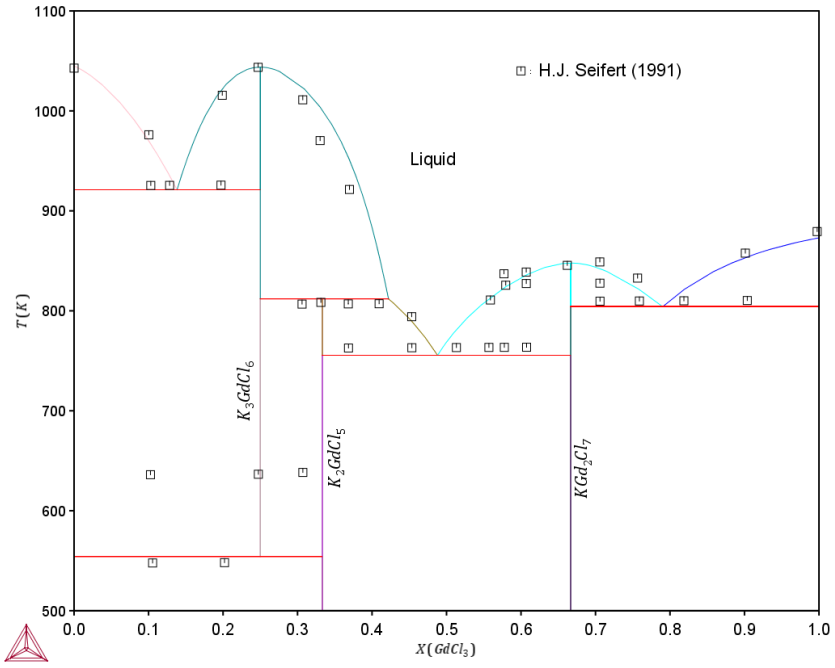

Figure 4-1: The calculated phase diagram of KCl-$GdCl_3$ system

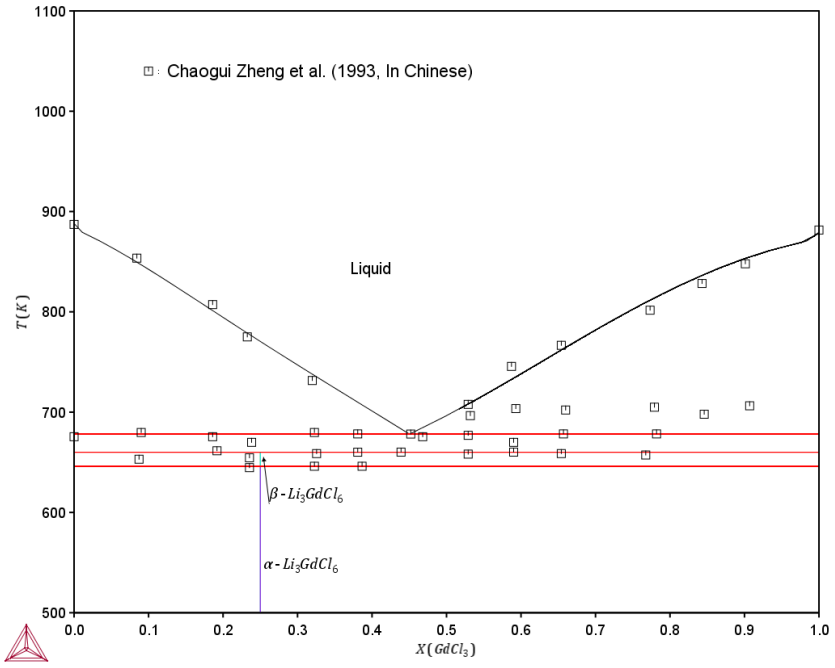

Figure 4-2: The calculated phase diagram of LiCl-$GdCl_3$ system

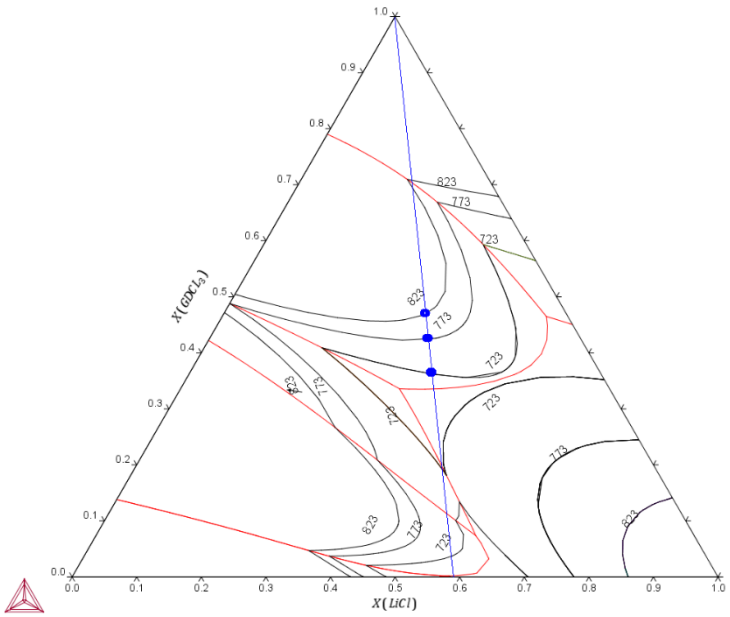

Figure 4-3: The calculated liquidus projection for LiCl-KCl-$GdCl_3$ system

The blue line stands for the compositions with $x(\mathrm{LiCl}):x(\mathrm{KCl})=0.586:0.414$. The dots represent where $GdCl_3$ starts to precipitate, which should be the limit of solubility of $GdCl_3$ in LiCl-KCl eutectic salt at different temperatures. The mole fractions of $GdCl_3$ at these positions are list in Table 4-2. Generally, the solubility S_{GdCl_3} in the unit of mole fraction can be expressed by [110]

$$\log S_{GdCl_3} = a + \frac{b}{T} \tag{4-9}$$

which is used to fit the calculated data in Table 4-2. Figure 4-4 shows the fitting result, which gives the correlation of

$$\log S_{GdCl_3} = 0.4783 - \frac{661.8}{T} \tag{4-10}$$

Table 4-2: Solubility of $GdCl_3$ at different temperatures

T (K)	723	773	823
Solubility (mole fraction)	0.363	0.425	0.469

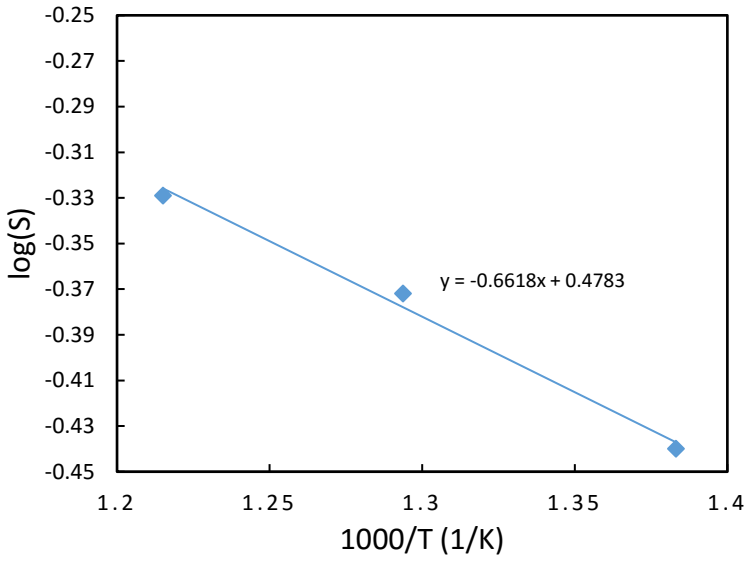

Figure 4-4: Calculated solubility of $GdCl_3$ in LiCl-KCl eutectic and the fitting curve

4.4. **Conclusions**

Thermodynamic assessment for the LiCl-KCl-$GdCl_3$ ternary system has been carried out by CALPHAD method using two-sublattice model. From the optimized phase diagram, the solubility of $GdCl_3$ in LiCl-KCl eutectic was obtained. Other interesting thermodynamic properties could be derived from it as well. This study will help to evaluate the salt status and $GdCl_3$ properties during pyroprocessing and will also contribute to evaluating other salt systems with more components.

5. Electrolysis model

Electrolysis have been studied extensively in the past including experiments and model developments. In order to get a better understanding of the processing, Tomczuk et al [111] carried out experiments using liquid anode and solid cathode to study the recovery of U and Pu during the electrorefining. Johnson [112] studied the transfer and distribution of metallic fuel between liquid alloy and molten salt based on the thermodynamic equilibria at two phases. Kobayashi et al [113] developed a multicomponent electrorefining model according to the diffusion control in a fixed diffusion layer. Zhang [114] proposed another model assuming the reaction equilibrium on the electrode surface. Comparatively, this model accounts for more details in the processing, such as flows condition, surface area change, and solubility limits of solutes. There are also other models supported by commercial software, such as ANSYS and COMSOL [115,116,117]. In addition to electrorefining, molten salt clean-up processing is another area needed to be studied since there are still some actinides, rare earth, and active fission products left in removed molten salt. In order to maximize the actinide recycle and minimize the volume of waste, molten salt needs to be cleaned up before disposal or being re-used [118]. Rare earth and actinides drawdown by electrolysis is a potential method to achieve the object. Kwon et al [119] studied the salt clean-up with U and Ce using solid cathode. They found that almost all of the material would deposit on the cathode with long enough time however the current efficiency decreases with time. Tylka [120] investigated a model based on reaction equilibrium and Nernst' equation. This model considers the changes in electrolyte composition and can predict the potential needed to accomplish a desired level of separation.

Previous studies show that many models have been proposed to study the steps in pyroprocessing; however most of them only focused on the diffusion control but missed the kinetic processing on the electrode surface. They have the ability to predict the main features of the electrorefining but generally cannot capture the effect of chemical and electrochemical processing. In the present study, we constructed a new deposition model in LiCl-KCl molten salt considering both of diffusion control and activation control. In this model, Butler-Volmer equation used to describe the reaction at the electrode surface was applied to the boundary conditions to solve the one dimensional diffusion equation. The model predicts the deposition of U and Np on solid cathode successfully.

5.1. Methodology

When ions An+ deposit on the solid cathode, the reaction can be expressed by

$$A^{n+} + ne^{-} \rightleftharpoons A \tag{5-1}$$

Diffusion equation for one dimensional dynamics without convection is :

$$\frac{\partial c_{A^{n+}}}{\partial t} = D_{A^{n+}} \frac{\partial^2 c_{A^{n+}}}{\partial^2 x} \tag{5-2}$$

where $c_{A^{n+}}$ is the concentration of A^{n+}, x is the distance, $D_{A^{n+}}$ is the diffusion coefficient of A^{n+}. Initially, concentration everywhere is the same, thus we have

$$c_{A^{n+}}(t=0,x) = c^0_{A^{n+}} \tag{5-3}$$

where $c^0_{A^{n+}}$ is the initial concentration. The current density in the cathode is due to the reduction of RE^{3+}. According to Butter-Volmer equation, the value can be expressed by

$$i = nFk^0[c^S_{A^{n+}} \exp\left(-\frac{(1-\alpha)nF\eta}{RT}\right) - \sigma c^S_A \exp\left(\frac{\alpha nF\eta}{RT}\right)] \tag{5-4}$$

where F is Faraday constant, k^0 is standard rate constant, $c^S_{A^{n+}}$ and c^S_A are surface concentrations of A^{n+} and A metal on the electrode surface, respectively, α is the charge transfer coefficient, σ is the ratio of forward constant to the backward constant and has the unit of cm^{-1}. Its value was taken to be 1 in all the calculation. Actually, it has little effect on the simulation results. R is gas constant, T is temperature in Kelvin, n is the number of electrons involved, and η is over potential defined by

$$\eta = E - E^{ap}_{A^{n+}/A} \tag{5-5}$$

where E is the potential applied and $E^{ap}_{A^{n+}/A}$ is the apparent potential of A^{n+}/A, which is

$$E^{ap}_{A^{n+}/A} = E^0_{A^{n+}/A} + \frac{RT}{nF} ln\gamma \tag{5-6}$$

where $E^0_{A^{n+}/A}$ is the standard potential and γ is the activity coefficient. Thus, the generation rate and consumption rate of A and A^{n+} can be expressed by the equations below, respectively [121].

$$R_{A,+} = \frac{i}{nF} \tag{5-7}$$

$$R_{A^{n+},-} = \frac{i}{nF} \tag{5-8}$$

The ion flux of A^{n+} to the electrode surface can be expressed by

$$R_{A^{n+},+} = D_{A^{n+}} \frac{\partial c_{A^{n+}}}{\partial x}|_{x=0} \tag{5-9}$$

Then the concentration change of A^{n+} on the surface of electrode is

$$\delta_l \frac{\partial c_{A^{n+}}}{\partial t} = R_{A^{n+},-} - R_{A^{n+},+} \tag{5-10}$$

where δ_l is the thickness of the surface layer, in which the concentration changes to balance the materials mass. Also due to the reaction, the surface concentration change of A metal on the cathode is

$$\frac{\partial c^S_A}{\partial t} = R_{A,+} = \frac{i}{nF} \tag{5-11}$$

At the at end of diffusion layer, the concentration equals bulk concentration, which gives us

$$C_{end} = c^0_{A^{n+}} \tag{5-12}$$

Combining those equations above, we will have one initial condition and two boundary conditions. Accordingly, the diffusion equation could be discretized and calculated numerically. There are two modes of the electrolysis, namely potential control and current

control. They correspond to the chronoamperometry (CA) and chronopotentiometry (CP), respectively in experiments. The model would be applied to these two situations below.

5.2. Chronoamperometry – Constant potential electrolysis

For the CA method, the step potential was given to monitor the variation of current. The initial and two boundary conditions are

Initial condition:

$$c_{A^{n+}}(t=0,x) = c^0_{A^{n+}} \tag{5-13}$$

Boundary conditions:

$$\delta_l \frac{\partial c_{A^{n+}}}{\partial t} = nFk^0\left[c^s_{A^{n+}} \exp\left(-\frac{(1-\alpha)nF\eta}{RT}\right) - \sigma c^s_A \exp\left(\frac{\alpha nF\eta}{RT}\right)\right] + D_{A^{n+}} \frac{\partial c_{A^{n+}}}{\partial x}|_{x=0} \tag{5-14}$$

$$C_{end} = c^0_{A^{n+}} \tag{5-15}$$

when the surface concentration is obtained, the current can be calculated by Eq. 5-4. The model was applied to simulate the CA process of $GdCl_3$ in LiCl-KCl-$GdCl_3$ system with 3 wt% at 723 K. The applied potentials were set to -3.267, -3.287, and -3.307 V vs. Cl_2/Cl-. The unknown parameters include δ_l, k^0, and α. For the parameter vector

$$p = [\delta_l] \tag{5-16}$$

The squared residuals could be expressed in terms of this vector

$$S(\mathbf{p}) = \sum_{i=1}^{l} [sim_i(\mathbf{p}) - \exp_i]^2 \tag{5-17}$$

where l is the number of the experimental data points. The nonlinear least squares algorithm of Trust Region [122] was used to search the *3*-dimensional parameter space to find the optimum values that minimized the squared residuals. The parameters obtained are shown in Table 5-1 and the fitting results are show in Figure 5-1. Table 5-1 shows that the surface layer increase as the step potential decrease. Figure 5-1(a)(b)(c) show that model predicts the current change very well. With each applied potential, the current decreases rapidly at the beginning and then varies very slowly with time. It could be seen by the concentration profile shown in Figure 5-1(d). The surface concentration is equal to bulk concentration initially but suddenly decreases to a small value, which results in the slow variation of the current because of the depletion of reactant on the surface.

Table 5-1: Parameters obtained from CA fitting

Applied Potential	δ_l
-3.267	0.0032
-3.287	0.0048
-3.307	0.0052

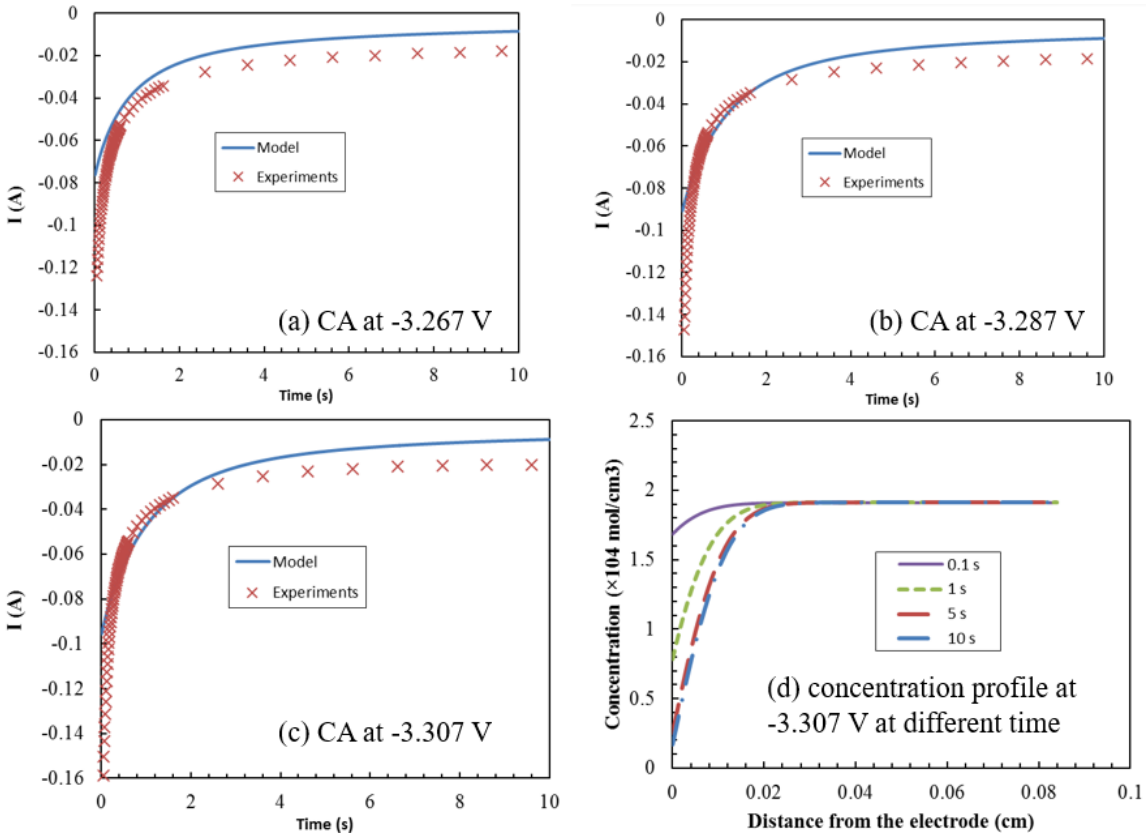

Figure 5-1: Comparison of CA simulation with experiment data at (a) -3.267 V (b) -3.287 V (c) -3.307 V. (d) Concentration profile at the electrode surface at different time.

5.3. Chronopotentiometry – Constant current electrolysis

For the CP method, the step current was given to monitor the variation of potential. The initial and two boundary conditions now are:

Initial condition:

$$c_{A^{n+}}(t = 0, x) = c^0_{A^{n+}} \tag{5-18}$$

Boundary conditions:

$$\delta_l \frac{\partial c_{A^{n+}}}{\partial t} = \frac{i}{nF} + D_{A^{n+}} \frac{\partial c_{A^{n+}}}{\partial x}|_{x=0} \tag{5-19}$$

$$C_{end} = c^0_{A^{n+}} \tag{5-20}$$

After obtaining the surface concentration, the potential can be calculated by Eq. 5-4. It is a reverse process compared with CA method. The CP data of $GdCl_3$ in LiCl-KCl-$GdCl_3$ system with 3 wt% at three temperatures, namely 723, 773, and 823 K was used to validate the model. The applied current is 0.001 A. The δ^l is fitted again due to the different temperature being used. Table 5-2 lists the optimized surface layer and it is showed that the thickness of the surface layer decrease as temperature increase. Figure 5-2(a)(b)(c) shows the results from three different temperature. They indicate that the simulation

predicts the potential change accurately. The potential decreases rapidly at the beginning but then varies slowly with the time. As in the CA, the phenomenon can be explained by the concentration profile. As shown in Figure 5-2(d), the surface concentration decreases with time. According to the Nernst equation

$$E = E^{ap}_{A^{n+}/A} + \frac{RT}{nF} lnx \tag{5-21}$$

The potential will decrease with the depletion of reactant on the surface. Also, the decrease of the decreasing rate explained the rapid step of the potential at the beginning.

Table 5-2: Optimized parameter for CP

	723 K	773 K	823 K
δ^I	0.023	0.009	0.0054

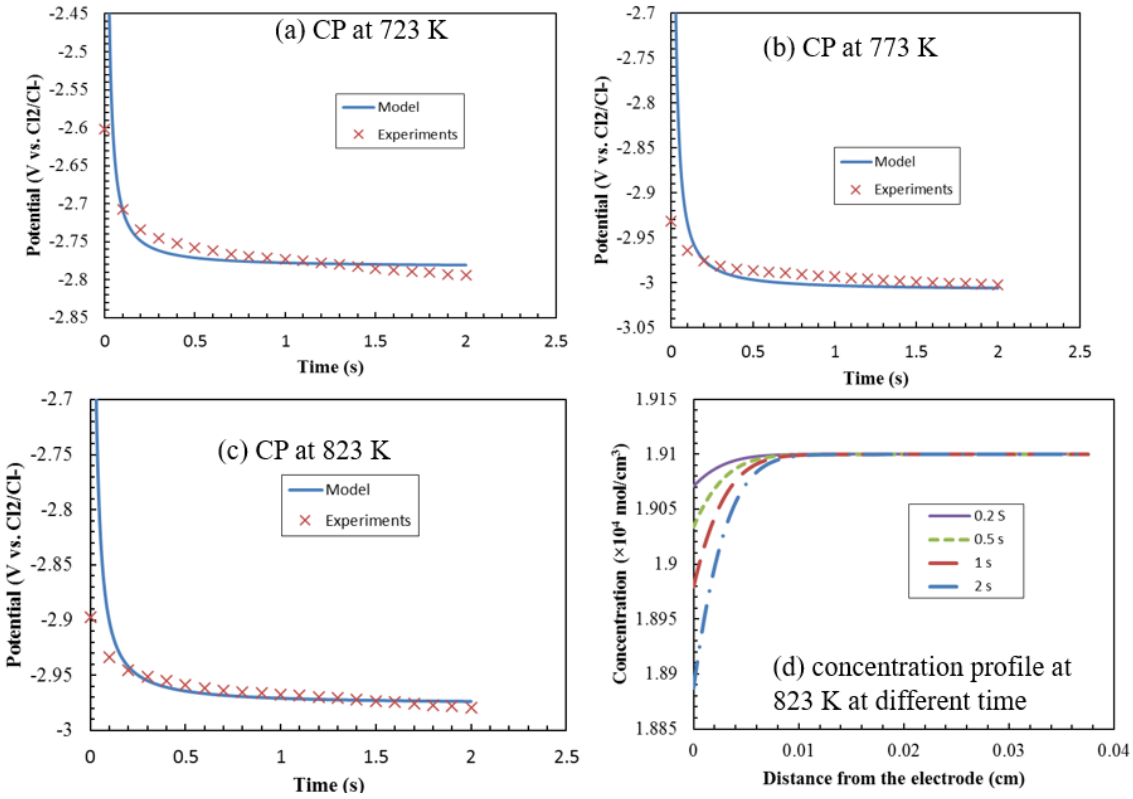

Figure 5-2: Comparison of CP simulation with experiment data for 3 wt% GdCl3 at (a) 723 K (b) 773 K (c) 823 K. (d) Concentration profile at the electrode surface at different time.

5.4. Conclusions

In this section, a model combining the kinetics and diffusion process was developed to simulate the CP and CA process. The result indicates the feasibility and robustness of this model. It is worth mentioning that the current in this model is only calculated by Butler-Volmer equation. Unlike the previous model [123,124], the diffusion current is not

necessarily equal to the current due to the Butler-Volmer equation. A “surface layer” was set here with the thickness of δ^l, therefore the concentration can be altered if the amount of the consumed ions is different with the ion diffusing into the electrode. In the future, this property may be used to study the diffusion control and activation control properties of a system. The model development can not only investigate the fundamental properties of elements in molten salt but can also instruct the design and optimization of the electrolysis device for the used fuel reprocessing.

6. **Summary**

In present study, various electrochemical techniques are applied to study the fundamental properties of La, Gd, and Nd in LiCl-KCl eutectic salt with and without fission product chloride CsCl in temperature range from 723 K to 823 K and RE concentration range from 1 wt % to 9 wt%. These include the determination of the diffusion coefficient, activity coefficient, and apparent potential by the analysis of experimental cyclic voltammogram data, analysis of diffusion coefficients from chronocoulumetry and chronopotentiometry data, and the measurement of the exchange current density and charge transfer coefficient by electrochemical impedance spectroscopy, liner polarization, Tafel plot, and proposed electrode kinetic simulation method.

Temperature and concentration dependency of apparent potential and diffusion coefficient are being examined. In general, apparent potential tends to increase with temperature linearly and to decrease with concentration linearly in the investigated concentration range with the only exception being Nd^{3+} for which the apparent potential increases linearly as concentration increases. All obtained diffusion coefficients follow the Arrhenius relation with temperature, but in terms of concentration dependency, no clear relation is found with La while the increasing in Nd and Gd concentration results in lower value of diffusion coefficient. The diffusion coefficient calculated by the BET model agrees within 35% difference from the value with Gd using conventional method (Berzins-Delahay equation) and within 61% difference from La with conventional method. In conventional method, it is assumed that the reaction is reversible. However, in this research, both La and Gd are found to be quasi-reversible during the reaction. Specifically, the reversibility parameter for La is very close to the irreversible reaction criteria while Gd's reversibility parameter is in the middle of quasi-reversible reaction criteria. In BET model, the kinetic of the reaction is considered, hence, the reversibility of the reaction does not affect the analysis. This explains the greater discrepancy found between BET model and conventional method for La since the reaction is closer to irreversible, where the assumption for conventional method does not hold true anymore. The concentration dependence of activity coefficient and diffusion coefficient of La(III) in LiCl-KCl eutectic are studied using molecular dynamics simulation method to enhance the understanding. Compared to the experimental values of La(III), the simulations showed similar trends but relatively higher activity coefficients and diffusion coefficient at higher concentrations.

The analysis of exchange current density in investigated salt systems using the conventional methods such as Tafel, LP, and EIS methods can lead large deviation of exchange current density and inconsistency of charge transfer coefficient. These three methods are commonly used due to their convenience. However, the origin of these methods are based on the electrode kinetic equations with the assumption of no mass transfer effect. An electrode kinetic model including the mass transfer effect is developed to accurately calculate exchange current density of La^{3+} and Gd^{3+}. In this research, it is found that the exchange current density increases linearly with temperature and follows a relation $k_0 nF[C]^{1-\alpha}$ with concentration where α is charge transfer coefficient and k_0 is standard reaction rate constant. The obtained rate constant follows the Arrhenius law.

CALPHAD method using two-sublattics model is also applied to assess the thermodynamic property for complex molten salt system. LiCl-KCl-$GdCl_3$ ternary system is selected as an example and the phase diagram is optimized using the proposed model. Form the optimization results, the solubility of $GdCl_3$ in LiCl-KCl eutectic is obtained. This method will help to evaluate the salt status and RE properties during pyroprocessing and will also contribute to evaluating other salt systems with more components.

The developed correlations and values are integrated into a kinetic model to predict electrolysis process. The model considers both the diffusion in electrolyte and Faraday process on the electrode surface. A surface layer is included in the model to account for the fact that diffusion current is not necessarily equal to the current due to the Butler-Volmer equation. The model was validated by our experiment with both constant current and constant potential electrolysis. The model gives insights on the reaction mechanism and can be used to predict efficiency of RE drawdown from LiCl-KCl salt.

The activity coefficients of chlorides of La, Nd, Ce, and Gd in LiCl-KCl eutectic salt are also studied using the emf method. The results also indicate extremely low activity coefficient in the range of 10^{-3} –10^{-6} for these REs. Compared to the activity coefficient from CV analysis, these values are generally 1 order of magnitude higher, corresponding to a difference of tens of millivolts for the apparent potential. Such magnitude of difference has also been observed from existing literature data from different researchers using various methods. By comparing the activity coefficient of these four REs, it is found the activity of rare earth chlorides in LiCl-KCl increases exponentially with their ionic size in the salt. Correlations between the activity and ionic size at three concentrations are developed which can be used to calculate the activity of any rare earth chlorides between lanthanum (Z= 57) to gadolinium (Z = 64) in concentration range of 1–2.5 mol %. Activity of $LaCl_3$, $CeCl_3$, and $GdCl_3$ in LiCl-KCl-CsCl melts are also measured at different $RECl_3$ concentrations and several CsCl concentrations. It is found that the presence of CsCl does affect the activity coefficient of $LaCl_3$ but the role is complex. Additions of CsCl up to 1.92 mol % showed little influence on the activity coefficient of $CeCl_3$ while the presence of CsCl decreases the activity coefficient of $GdCl_3$. A novel process using a galvanic couple between a cathode basket made of stainless steel and a Gd rod is investigated in LiCl-KCl-UCl_3-$MgCl_2$. The process shows rapid reduction of UCl_3 to U and $MgCl_2$ to Mg without any co-reduction of $LaCl_3$, $NdCl_3$, or $CeCl_3$ because of the higher standard potential of Gd^{3+}/Gd. Benefits of this process include passive operation, short processing times, removal of actinides as metals, and high selectivity for actinides relative to rare earths.

The phase behaviors of four quaternary LiCl-KCl-CsCl-$RECl_3$ (RE = La, Nd, Ce, and Gd) salt systems are also studied. The solidus and liquidus temperatures are measured by differential scanning calorimetry (DSC). The presence of CsCl causes a slight depression in the liquidus temperature for all of the four rare earth chloride mixtures when compared to the corresponding ternary system liquidus temperatures in the absence of any CsCl. The $LaCl_3$ and $CeCl_3$ quaternary system (with CsCl) manifests a peritectic behavior as opposed to eutectic behavior of ternary systems (no CsCl). The $GdCl_3$ quaternary system shows a peritectic behavior only in a limited concentration windows, at low $GdCl_3$ and high CsCl concentrations. The $NdCl_3$ system shows a eutectic behavior throughout the concentrations

range tested in this work, albeit with a slight depression in the liquidus temperatures in the presence of CsCl.

7. **Reference**

[1] Nuclear Energy Data 2016, OECD&NEA, NEA No. 7300, 2016

[2] Fuel, Spent Nuclear. Accumulating Quantities at Commercial Reactors Present Storage and Other Challenges. GAO-12-797, US Government Accountability Office, 2012.

[3] "Spent Fuel Reprocessing Options", IAEA-TECDOC-1587, August 2008.

[4] Tucek, Kamil. Neutronic and burnup studies of accelerator-driven systems dedicated to nuclear waste transmutation. Diss. Fysik, 2004.

[5] Simpson, Michael F. Developments of spent nuclear fuel pyroprocessing technology at idaho national laboratory. No. INL/EXT-12-25124. Idaho National Laboratory (INL), 2012.

[6] Inoue, Tadashi, Tadafumi Koyama, and Yasuo Arai. "State of the art of pyroprocessing technology in Japan." Energy Procedia 7 (2011): 405-413.

[7] Song, Kee-Chan, et al. "Status of pyroprocessing technology development in Korea." Nuclear engineering and technology 42.2 (2010): 131-144.

[8] Boussier, H., R. MALMBECK, and G. MARUCCI. "Pyrometallurgical Processing Research Programme "PYROREP". Final Technical Report." European Community (2003).

[9] Cipiti, Benjamin B., et al. "Modeling and design of integrated safeguards and security for an electrochemical reprocessing facility." Sandia National Labs, Albuquerque (2012).

[10] Simpson, Michael F. "Developments of Spent Nuclear Fuel Pyroprocessing Technology at Idaho National Laboratory." Idaho National Laboratory Idaho Falls Idaho 83415 (2012).

[11] Li, S. X., and M. F. Simpson. "Anodic process of electrorefining spent nuclear fuel in molten LiCl-KCl-UCl3/Cd system." Proc. 13th Int. Symp. Molten Salts. 2002.

[12] Yoon, Dalsung. "Electrochemical Studies of Cerium and Uranium in LiCl-KCl Eutectic for Fundamentals of Pyroprocessing Technology." (2016).

[13] Hoover, Robert Oaks. Uranium and Zirconium Electrochemical Studies in LiCl-KCl Eutectic for Fundamental Applications in Used Nuclear Fuel Reprocessing. Diss. University of Idaho, 2014.

[14] An Experimental Study of Molten Salt Electrorefining of Uranium Using Solid Iron Cathode and Liquid Cadmium Cathode for Development of Pyrometallurgical Reprocessing

[15] Williamson, M. A., and J. L. Willit. "Pyroprocessing flowsheets for recycling used nuclear fuel." Nuclear Engineering and Technology 43.4 (2011): 329-334.

[16] Martin, Sean, et al. "Physical and Electrochemical Properties of Molten LiCl-KCl Salt for Used Fuel Reprocessing." International Pyroprocessing Research Conference. 2012.

[17] Zhang, Jinsuo. "Electrochemistry of actinides and fission products in molten salts—Data review." Journal of Nuclear Materials 447.1 (2014): 271-284.

[18] Kuznetsov, S. A., et al. "Electrochemical behavior and some thermodynamic properties of UCl4 and UCl3 dissolved in a LiCl-KCl eutectic melt." Journal of The Electrochemical Society 152.4 (2005): C203-C212.: 169-172

[19] Fusselman, S. P., et al. "Thermodynamic properties for rare earths and americium in pyropartitioning process solvents." Journal of the Electrochemical Society 146.7 (1999): 2573-2580.

[20] Masset, Patrick, et al. "Thermochemical properties of lanthanides (Ln= La, Nd) and actinides (An= U, Np, Pu, Am) in the molten LiCl–KCl eutectic." Journal of Nuclear Materials 344.1 (2005): 173-179.

[21] Castrillejo, Y., et al. "Solubilization of rare earth oxides in the eutectic LiCl–KCl mixture at 450 C and in the equimolar CaCl 2–NaCl melt at 550 C." Journal of Electroanalytical Chemistry 545 (2003): 141-157.

[22] Lantelme, Frédéric, and Youssef Berghoute. "Electrochemical Studies of LaCl3 and GdCl3 Dissolved in Fused LiCl-KCl." Journal of the Electrochemical Society 146.11 (1999): 4137-4144.

[23] Shirai, Osamu, et al. "Thermochemical properties of the intermetallic compounds in the lanthanum–cadmium system." Journal of nuclear materials344.1 (2005): 142-145.

[24]. Tang H, Pesic B (2014) Electrochim. Acta 119:120-130

[25] Samin, Adib, et al. "Estimation of key physical properties for LaCl 3 in molten eutectic LiCl–KCl by fitting cyclic voltammetry data to a BET-based electrode reaction kinetics model." Journal of Nuclear Materials 475 (2016): 149-155.

[26] Marsden, K. C., and B. Pesic. "Evaluation of the electrochemical behavior of CeCl3 in molten LiCl-KCl eutectic utilizing metallic Ce as an anode." Journal of The Electrochemical Society 158.6 (2011): F111-F120.

[27] Castrillejo, Y., et al. "Use of electrochemical techniques for the study of solubilization processes of cerium–oxide compounds and recovery of the metal from molten chlorides." Journal of Electroanalytical Chemistry 522.2 (2002): 124-140.

[28] Iizuka, Masatoshi. "Diffusion Coefficients of Cerium and Gadolinium in Molten LiCl-KCl." Journal of the Electrochemical Society 145.1 (1998): 84-88.

[29] Kim, Tack-Jin, et al. "Study on electrodeposition of Ce (III) at a tungsten electrode in a LiCl-KCl molten salt solution." International Journal of Electrochemical Science 8 (2013): 9180.

[30] Vandarkuzhali, S., et al. "Investigation on the electrochemical behavior of neodymium chloride at W, Al and Cd electrodes in molten LiCl-KCl eutectic." Electrochimica Acta 145 (2014): 86-98.

[31] Caravaca, C., G. Cordoba, and M. J. Tomas. "Strontium and barium precipitation as carbonates in molten eutectic LiCl-KCl." 9th International Topical Meeting on Research Reactor Fuel Management 10-13 April 2005, Budapest, Hungary. 2005..

[32] Fukasawa, Kazuhito, et al. "Electrochemical and spectrophotometric study on neodymium ions in molten alkali chloride mixtures." Journal of Alloys and Compounds 509.16 (2011): 5112-5118.

[33] Castrillejo, Y., et al. "Electrochemical extraction of samarium from molten chlorides in pyrochemical processes." Electrochimica Acta 56.24 (2011): 8638-8644.

[34] Cordoba, G., and C. Caravaca. "An electrochemical study of samarium ions in the molten eutectic LiCl+ KCl." Journal of Electroanalytical Chemistry572.1 (2004): 145-151.

[35] Castrillejo, Y., et al. "Cathodic behaviour and oxoacidity reactions of samarium (III) in two molten chlorides with different acidity properties: The eutectic LiCl–KCl and the equimolar CaCl 2–NaCl melt." Electrochimica Acta97 (2013): 120-131.

[36] Kim, Tack-Jin, et al. "Elucidation of electrode reaction of EuCl 3 in LiCl-KCl eutectic melts through CV curve analysis." Bulletin of the Korean Chemical Society 32.3 (2011): 863-866.

[37] Bermejo, M. R., et al. "Cathodic behaviour of europium (III) on glassy carbon, electrochemical formation of Al 4 Eu, and oxoacidity reactions in the eutectic LiCl–KCl." Journal of Electroanalytical Chemistry 603.1 (2007): 81-95.

[38] Bermejo, M. R., et al. "The electrochemistry of gadolinium in the eutectic LiCl–KCl on W and Al electrodes." Journal of Electroanalytical Chemistry588.2 (2006): 253-266.

[39] Bermejo, M. R., et al. "Electrochemistry of terbium in the eutectic LiCl–KCl." Electrochimica Acta 53.16 (2008): 5106-5112.

[40] Kim, Bong Young, et al. "Electrochemical and spectroscopic investigations of Tb (III) in molten LiCl–KCl eutectic at high temperature." Electrochemistry Communications 12.8 (2010): 1005-1008.

[41] Castrillejo, Y., et al. "Electrochemical behaviour of dysprosium in the eutectic LiCl–KCl at W and Al electrodes." Electrochimica acta 50.10 (2005): 2047-2057.

[42] Tang, Hao, and Batric Pesic. "Electrochemistry of ErCl 3 and morphology of erbium electrodeposits produced on Mo substrate in early stages of electrocrystallization from LiCl–KCl molten salts." Electrochimica Acta 133 (2014): 224-232.

[43] Castrillejo, Y., et al. "Electrochemical behaviour of erbium in the eutectic LiCl–KCl at W and Al electrodes." Electrochimica acta 51.10 (2006): 1941-1951.

[44] Peng, C. A. O., et al. "Electrochemical behaviour of erbium and preparation of Mg-Li-Er alloys by codeposition." Journal of Rare Earths 29.8 (2011): 763-767.

[45] Yang, Ling, and Robert G. Hudson. "Some Investigations of the Ag/AgCl in LiCl-KCl Eutectic Reference Electrode." Journal of The Electrochemical Society 106.11 (1959): 986-990.

[46] Matsuda, Hiroaki, and Yuzo Ayabe. "Theoretical analysis of polarographic waves. I. Reduction of simple metal ions." Bulletin of the Chemical Society of Japan 28.6 (1955): 422-428.

[47] Berzins, Talivaldis, and Paul Delahay. "Oscillographic polarographic waves for the reversible deposition of metals on solid electrodes." Journal of the American Chemical Society 75.3 (1953): 555-559.

[48] Bard, Allen J., et al. Electrochemical methods: fundamentals and applications. Vol. 2. New York: Wiley, 1980.

[49] Samin, Adib, Evan Wu, and Jinsuo Zhang. "The thermodynamic and transport properties of GdCl3 in molten eutectic LiCl-KCl derived from the analysis of cyclic voltammetry signals." Journal of Applied Physics 121.7 (2017): 074904.

[50] Brunauer, Stephen, Paul Hugh Emmett, and Edward Teller. "Adsorption of gases in multimolecular layers." Journal of the American chemical society60.2 (1938): 309-319.

[51] Wang, Yafei, Prediction of Fundamental Data of Fission Products in Molten Salt and Liquid Electrode for Electrochemical Separation, Master Thesis, The Ohio State University, Colmbus, OH (2017)

[52] Gueshi, Tatsuro, Koichi Tokuda, and Hiroaki Matsuda. "Voltammetry at partially covered electrodes: Part I. Chronopotentiometry and chronoamperometry at model electrodes." Journal of Electroanalytical Chemistry and Interfacial Electrochemistry 89.2 (1978): 247-260.

[53] Rose, M. A., M. A. Williamson, and J. Willit. "Determining the Exchange Current Density and Tafel Constant for Uranium in LiCl/KCl Eutectic." ECS Electrochemistry Letters 4.1 (2015): C5-C7.

[54] A.J. Bard, L.R. Faulkner, “Electrochemical methods: fundamentals and applications”, second edition, John Wiley & Sons, Inc. 2001.

[55]Shaoqiang Guo, Evan Wu, Jinsuo Zhang, “Exchange current density of Gd(III)/Gd reaction in LiCl-KCl eutectic and fundamental analysis of errors caused by various methods”, submitted to Electrochimica Acta.

[56] Yoon, D., and S. Phongikaroon. "Electrochemical Properties and Analyses of CeCl3 in LiCl-KCl Eutectic Salt." Journal of The Electrochemical Society 162.10 (2015): E237-E243.

[57] Yoon, Dalsung, and Supathorn Phongikaroon. "Measurement and Analysis of Exchange Current Density for U/U 3+ Reaction in LiCl-KCl Eutectic Salt via Various Electrochemical Techniques." Electrochimica Acta (2017).

[58] Brett, CHRISTOPHER MA, Oliveira Brett, and A. M. Electrochemistry. "Principles, Methods, and Applications." (1993): 427.

[59] Matsuda, Hiroaki, and Yuzo Ayabe. "Theoretical analysis of polarographic waves. I. Reduction of simple metal ions." Bulletin of the Chemical Society of Japan 28.6 (1955): 422-428.

[60] Masset, Patrick, et al. "Electrochemical behaviour of neptunium in the molten LiCl–KCl eutectic." Journal of Electroanalytical Chemistry 603.2 (2007): 166-174.

[61] Tang, Hao, and Batric Pesic. "Electrochemical behavior of LaCl 3 and morphology of La deposit on molybdenum substrate in molten LiCl–KCl eutectic salt." Electrochimica Acta 119 (2014): 120-130.

[62] Tang, Hao, and Batric Pesic. "Electrochemical behavior of LaCl 3 and morphology of La deposit on molybdenum substrate in molten LiCl–KCl eutectic salt." Electrochimica Acta 119 (2014): 120-130.

[63] Tang, Hao, and Batric Pesic. "Electrochemical behavior of LaCl 3 and morphology of La deposit on molybdenum substrate in molten LiCl–KCl eutectic salt." Electrochimica Acta 119 (2014): 120-130.

[64] C. Caravaca, G. Cordoba, M.J. Tomas, Electrochemical Study of Europium Trichloride in Molten Eutectic LiCl-KCl (2005)

65 H. Tang, B. Pesic. J. Electrochem. Soc. 161 (2014) D429.

66 A. Lasia. Electrochemical Impedance Spectroscopy and Its Applications; Springer-Verlag New York, 2014, pp. 91.

[67] P. Delahay (Ed.), New Instrumental Methods in Electrochemistry. Theory, Instrumentation, and Applications to Analytical andPhysical Chemistry, Interscience, New York, 1954.

[68] Kuznetsov, S. A., and M. Gaune-Escard. "Kinetics of electrode processes and thermodynamic properties of europium chlorides dissolved in alkali chloride melts." Journal of Electroanalytical Chemistry 595.1 (2006): 11-22.

[69] Allen M P, Tildesley D J. Computer simulation of liquids[M]. Oxford university press, 1989.

[70] Croteau T, Patey G N. Structures and rearrangements of LiCl clusters[J]. The Journal of chemical physics, 2006, 124(24): 244506-244506.

[71] IUPAC. Compendium of Chemical Terminology, 2nd ed. (the "Gold Book"). Compiled by A. D. McNaught and A. Wilkinson. Blackwell Scientific Publications, Oxford (1997). XML on-line corrected version: http://goldbook.iupac.org (2006-) created by M. Nic, J. Jirat, B. Kosata; updates compiled by A. Jenkins. ISBN 0-9678550-9-8.

[72] Frenkel D, Smit B. From algorithms to applications[J]. 1996.

[73] http://lammps.sandia.gov

[74] S. Plimpton, Fast Parallel Algorithms for Short-Range Molecular Dynamics, J Comp Phys, 117, 1-19 (1995).

[75] Y. Wang, W. Zhou, J. Zhang, Investigation of concentration-dependence of thermodynamic properties of lanthanum, yttrium, scandium and terbium in eutectic LiCl-KCl molten salt, Journal of Nuclear Materials, 478 (2016) 61-73.

[76] K. Sridharan, NEUP Project 09-780, Final Report, 2012.

[77] T. Gutknecht, *M.S. Thesis*, University of Idaho, 2012.

[78] Shirai, O.; Uozumi, K.; Iwai, T.; Arai, Y., *Analytical Sciences/Supplements* **2002,** *17icas*, i959-i962.

[79] P. Bagri, T. Bastos, M. F. Simpson, *ECS Transactions* 75 (2016) 489–495.

[80] P. Bagri, M. F. Simpson, *Journal of The Electrochemical Society* 164 (2017) H5299–H5307.

[81] P. Bagri and M.F. Simpson, Measurement of the Activity of Rare Earth Chlorides (Ce, Nd, La, Gd) in LiCl-KCl Eutectic Salt, *Electrochimica Acta*, v.259, 1120-1128 (2018).

[82] J.-B. Shim, T. Kim, G. Kim, S. Kim, S. Paek, D. Ahn, S. Lee, Uranium recovery tests using rare earth metals in LiCl-KCl molten salt, *International Pyroprocessing Research Conference*, 2016.

[83] P. Bagri, C. Zhang, M. F. Simpson, Journal of Nuclear Materials 493 (2017) 120 – 123.

[84] V. Danek, *Physico-chemical analysis of molten electrolytes*, Elsevier, 2006.

[85] W. J. Glover, P. A. Madden, *Journal of Chemical Physics* 121 (2004) 7293–7303.

[86] Y. Okamoto, S. Suzuki, H. Shiwaku, A. Ikeda-Ohno, T. Yaita, P. A. Madden, *Journal of Physical Chemistry* A 114 (2010) 4664–4671. PMID: 20225902.

[87] T. Inoue, Y. Sakamura, M. Gaune-Escard, *Nato Science Series* 52 (2002) 249.

[88] T. Fujii, T. Nagai, N. Sato, O. Shirai, H. Yamana, *Journal of alloys and compounds* 393 (2005) L1–L5.

[89] G. Photiadis, B. Brresen, G. Papatheodorou, *Journal of the Chemical Society*, Faraday Transactions 94 (1998) 2605–2613.

[90] K. Fukasawa, A. Uehara, T. Nagai, T. Fujii, H. Yamana, *Journal of Nuclear Materials* 414 (2011) 265–269.

[91] A. Chrissanthopoulos, G. Papatheodorou, *Physical Chemistry Chemical Physics* 2 (2000) 3709–3714.

[92] Y. Okamoto, H. Shiwaku, T. Yaita, S. Suzuki, M. Gaune-Escard, *Journal of Molecular Liquids* 187 (2013) 94–98.

[93] H. Matsuura, S. Watanabe, T. Sakamoto, T. Kanuma, K. Naoi, M. Hatcho, N. Kitamura, H. Akatsuka, A. Adya, T. Honma, et al., *Journal of alloys and compounds* 408 (2006) 80–83.

[94] M. He, G. Lu, Z. Kang and Y. Zhang. "Thermodynamic assessment of the LiCl–KCl–CeCl 3 system." *Calphad* 49 (2015): 1-7.

[95] T. Shujian, L. Qingfan, L. Shixiang and Z. Chaogui. "Phase diagram of the ternary system CeCl 3–KCl–LiCl."*Journal of alloys and compounds* 274.1 (1998): 142-147.

[96] S. Ghosh, B.P. Reddy, K. Nagarajan and K.H. Kumar. "Experimental investigations and thermodynamic modelling of KCl–LiCl–UCl 3 system." *Calphad* 45 (2014): 11-26.

[97] Zhou, Wentao, and Jinsuo Zhang. "Thermodynamic evaluation of LiCl-KCl-PuCl 3 system." *Journal of Alloys and Compounds* 695 (2017): 2306-2313.

[98] Pelton, Arthur D. "A general “geometric” thermodynamic model for multicomponent solutions." *Calphad* 25.2 (2001): 319-328.

[99] B.G. Korshunov, D.V. Drobot, Zh. Neorg. Khim. 10 (1963) 939

[100] Frenzel, J. "Zur existenz von KGd3Cl10." *Inorganic and Nuclear Chemistry Letters* 6.4 (1970): 371-373.

[101] Seifert, H-J., and J. Sandrock. "Ternäre Chloride in den Systemen ACl/EuCl3 (A= Na Cs)." *Zeitschrift für anorganische und allgemeine Chemie* 587.1 (1990): 110-118.

[102] 郑朝贵, and 赵仲冬. "GdCl3—LiCl 及 GdCl3—PbCl2 二元系相图的研究." *稀土* 14.1 (1993): 65-66.

[103] M. Hillert, B. Jansson, B. Sundman. "A two-sublattice model for molten solutions with different tendency for ionization." *Metallurgical Transactions A* 16.1 (1985): 261-266.

[104] B. Sundman. "Modification of the two-sublattice model for liquids." *Calphad*15.2 (1991): 109-119.

[105] Thermo-Software SGTE Substances Database v5.2. Accessed in August, 2017

[106] Y. M. Muggianu, M. Gambino, J. P. Bros, Enthalpies of formation of liquid alloys, *J. Chim. Phys*., 72 (1975): 83–88

[107] O. Redlich and A.T. Kister. "Algebraic representation of thermodynamic properties and the classification of solutions." *Industrial & Engineering Chemistry* 40.2 (1948): 345-348.

[108] H. Kopp. "Investigations of the specific heat of solid bodies."*Philosophical Transactions of the Royal Society of London* (1865): 71-202.

[109] J.O. Andersson, T. Helander, L. Höglund, P. Shi and B. Sundman. "Thermo-Calc & DICTRA, computational tools for materials science." *Calphad* 26.2 (2002): 273-312.

[110] J. Zhang. "Kinetic model for electrorefining, part II: Model applications and case studies." *Progress in Nuclear Energy* 70 (2014): 287-297.

[111] Tomczuk, Zygmunt, et al. "Uranium transport to solid electrodes in pyrochemical reprocessing of nuclear fuel." Journal of the Electrochemical Society 139.12 (1992): 3523-3528.

[112] Johnson, Irving. "The thermodynamics of pyrochemical processes for liquid metal reactor fuel cycles." Journal of Nuclear Materials 154.1 (1988): 169-180.

[113] Kobayashi, Tsuguyuki, and Moriyasu Tokiwai. "Development of TRAIL, a simulation code for the molten salt electrorefining of spent nuclear fuel."Journal of alloys and compounds 197.1 (1993): 7-16.

[114] Zhang, Jinsuo. "Kinetic model for electrorefining, part I: Model development and validation." Progress in Nuclear Energy 70 (2014): 279-286.

[115] Bae, Judong, et al. "Numerical assessment of pyrochemical process performance for PEACER system." Nuclear Engineering and Design 240.6 (2010): 1679-1687.

[116] Kim, K. R., et al. "Multi physics modeling of a molten-salt electrolytic process for nuclear waste treatment." IOP Conference Series: Materials Science and Engineering. Vol. 9. No. 1. IOP Publishing, 2010.

[117] Srihari, B. Krishna, et al. "Modeling the molten salt electrorefining process for spent metal fuel using COMSOL." Separation Science and Technology just-accepted (2015).

[118] Simpson, Michael F., et al. "Selective reduction of active metal chlorides from molten LiCl-KCl using lithium drawdown." Nuclear Engineering and Technology44.7 (2012): 767-772.

[119] Kwon, S. W., et al. "A Study on a Salt Clean-up with Solid Cathode-Perforated Ceramic Container." (2008).

[120] Tylka, Magdalena M. “Actinide and Lanthanide Recovery via Electrolysis to Enable Salt Recycle” 2013 FCRD Annual meeting

[121] Zhang, Jinsuo. "Parametric studies of uranium deposition and dissolution at solid electrodes." Journal of Applied Electrochemistry 44.3 (2014): 383-390.

[122] Conn, Andrew R., Nicholas IM Gould, and Ph L. Toint. Trust region methods. Vol. 1. Siam, 2000.

[123] Cumberland, Riley M., and Man-Sung Yim. "Development of a 1D transient electrorefiner model for pyroprocess simulation." Annals of Nuclear Energy71 (2014): 52-59.

[124] Seo, Seungjin, Sungyeol Choi, and Byung Gi Park. "Transient modeling of spent nuclear fuel electrorefining with liquid metal electrode." Journal of Nuclear Materials 491 (2017): 115-125.

Appendix A. Data from literatures

Table A - 1: Apparent potential of La^{3+}/La in molten LiCl-KCl salt.

T (K)	Apparent potential (V) (versus Cl_2/Cl^-)			
	Fussleman [19]	Masset [20]	Castrillejo [21]	Tang[24]
673	-3.1804		-3.159	
693				-3.139
698	-3.1637			
723	-3.1462		-3.124	-3.114
733		-3.126		
753				-3.089
773			-3.095	
783				-3.064
813				-3.04
Molar Fraction	0.0001-0.01	0.00764	0.00281	0.00201

Table A - 2: Apparent potential (E^{ap}) of La^{3+}/La in molten LiCl-KCl salt [22].

T(K)	E^{ap}/V	T(K)	E^{ap}/V	T(K)	E^{ap}/V
647	-3.159	**652**	-3.157	**642**	-3.162
695	-3.128	**690**	-3.131	**691**	-3.134
751	-3.101	**741**	-3.106	**729**	-3.106
802	-3.068	**812**	-3.070	**812**	-3.058
869	-3.037	**858**	-3.032	**862**	-3.039
Molar Fraction	0.00152		0.0035		0.0078
T(K)	**E^{ap}/V**	**T(K)**	**E^{ap}/V**	**T(K)**	**E^{ap}/V**
653	-3.146	**647**	-3.158	**651**	-3.148
698	-3.125	**695**	-3.129	**689**	-3.128
741	-3.102	**755**	-3.090	**742**	-3.102
815	-3.068	**812**	-3.063	**815**	-3.056
868	-3.026	**869**	-3.025	**866**	-3.023
Molar Fraction	0.01		0.0132		0.0181

Table A - 3: Apparent potential (E^{ap}) of La^{3+}/La in molten LiCl-KCl salt [25].

T(K)	Apparent potential (V) versus Cl_2/Cl^-		
773 K	-3.157	-3.194	-3.307
Molar Fraction	0.00222	0.00623	0.01529

Table A - 4: Apparent potential of Ce^{3+}/Ce^0, Pr^{3+}/Pr^0 in LiCl-KCl salt.

T(K)	Apparent potential (V) versus Cl_2/Cl^-				
	Ce^{3+}/Ce [19]	Ce^{3+}/Ce [21]	Ce^{3+}/Ce [26]	Pr^{3+}/Pr [19]	Pr^{3+}/Pr [21]
673	-3.1323	-3.125	-3.135	-3.1187	-3.123
698	-3.1154			-3.1024	
723	-3.0984	-3.092	-3.106	-3.085	-3.097
748				-3.0562	
773		-3.054	-3.076	-3.0463	-3.06
823		-3.018	-3.046		-3.029
873		-3.017			
923		-2.987			
973		-2.957			
Molar Fraction	0.0001-0.01	0.00372	0.011	0.0001-0.01	0.0028

Table A - 5: Apparent potential of Nd^{3+}/Nd, Nd^{3+}/Nd^{2+}, Nd^{2+}/Nd in LiCl-KCl salt.

T (K)	Apparent potential (V) versus Cl_2/Cl^-								
	Nd^{3+}/Nd [20]	Nd^{3+}/Nd [21]	Nd^{3+}/Nd [30]	Nd^{3+}/Nd [32]	Nd^{3+}/Nd^{2+} [30]	Nd^{3+}/Nd^{2+} [32]	Nd^{2+}/Nd [20]	Nd^{2+}/Nd [30]	Nd^{2+}/Nd [32]
673		-3.151							
723		-3.105	-3.093	-3.127	-3.058	-3.122		-3.11	-3.142
733	-3.113						-3.073		
748			-3.079		-3.049			-3.094	
773		-3.079	-3.065		-3.039			-3.078	
798			-3050		-3.029			-3.061	
823		-3.055							
Molar Fraction	0.0254	0.0044	0.0025	0.0047	0.0025	0.0047	0.0254	0.0025	0.0047

Table A - 6: Apparent potential of Sm^{3+}/Sm^{2+}, Eu^{3+}/Eu^{2+}, Tb^{3+}/Tb^{0}, Er^{3+}/Er^{0} in LiCl-KCl salt.

T(K)	Apparent potential (V) versus Cl_2/Cl^-					
	Sm^{3+}/Sm^{2+} [34]	Sm^{3+}/Sm^{2+} [35]	Eu^{3+}/Eu^{2+} [31]	Tb^{3+}/Tb^{0} [39]	Tb^{3+}/Tb^{0} [40]	Er^{3+}/Er^{0} [42]
673	-2.09			-3.067		
683						-3.047
693				-3.054		
698			-0.864			
723	-2.04	-2.099	-0.848	-3.038		-3.018
748			-0.817	-3.023		
773	-2		-0.8	-3.012		-2.982
813						-2.956
823	-1.98			-2.982		
873	-1.93					
887					-2.83	
Molar Fraction	0.00225	0.00372	0.00385	0.0036	0.00297	0.0044

Table A - 7: Apparent potential (E^{ap}) of Gd^{3+}/Gd in LiCl-KCl salt [22].

T(K)	E^{ap}/V	T(K)	E^{ap}/V	T(K)	E^{ap}/V
650	-3.078	**673**	-3.059	**649**	-3.074
679	-3.062	**726**	-3.026	**699**	-3.045
717	-3.040	**772**	-2.997	**748**	-3.017
765	-3.011	**820**	-2.969	**795**	-2.988
808	-2.981	**868**	-2.936	**842**	-2.957
841	-2.959				
Molar Fraction	0.00172		0.0026		0.00344
T(K)	**E^{ap}/V**	**T(K)**	**E^{ap}/V**	**T(K)**	**E^{ap}/V**
651	-3.070	**656**	-3.067	**658**	-3.065
699	-3.041	**675**	-3.057	**701**	-3.040
747	-3.011	**698**	-3.045	**743**	-3.013
772	-2.999	**742**	-3.015	**783**	-2.987
795	-2.983	**783**	-2.986	**826**	-2.959
842	-2.952	**825**	-2.960	**853**	-2.942
		868	-2.932	**867**	-2.934
Molar Fraction	0.00688		0.01		0.0144

Table A - 8: Activity coefficient of $NdCl_3$, $SmCl_3$ in LiCl-KCl salt.

T (K)	Activity coefficient (logγ)					
	$NdCl_3$ [20]	$NdCl_3$ [21]	Nd(III)/Nd(Al) [30]	Nd(III)/Nd(Cd) [30]	$SmCl_3$ [34]	$SmCl_3$ [35]
673					-3.931	
698			-12.1	-8.9	-3.617	
723		-3.516	-11.5	-8.8		-4.35
733	-4.0969			-8.6		
748			-10.9			
773			-10.4	-8.4	-3.446	
823		-3.355			-3.347	
873					-3.111	
Molar Fraction	0.0254	0.00448	0.0025	0.0025	0.00225	0.00372

Table A - 9: Activity coefficient of $LaCl_3$, $CeCl_3$, $PrCl_3$ in LiCl-KCl salt.

T(K)	Activity coefficient (logγ)				
	$LaCl_3$ [24]	$CeCl_3$ [26]	$CeCl_3$ [27]	$CeCl_3$ [28]	$PrCl_3$ [21]
673		-1.721			
693	-0.692				
723	-0.645	-1.853	-2.49	-2.699	-2.517
753	-0.6				
773		-1.744			
783	-0.555				
813	-0.53				
823		-2.009	-2.43		-2.129
873		-2.07			
923		-2.119			
973		-2.159			
Molar Fraction	0.00201	0.011	0.00566	0.00189	0.00285

Table A - 10: Activity coefficient of $EuCl_3$, $GdCl_3$, $TbCl_3$, $ErCl_3$ in LiCl-KCl salt.

T(K)	Activity coefficient (logγ)				
	$EuCl_3$ [31]	$GdCl_3$ [31]	$GdCl_3$ [28]	$TbCl_3$ [39]	$ErCl_3$ [42]
673				-4.99	
683					-4.746
693				-4.87	
698	-3.092				
723	-2.977	-2.586	-3.769	-4.76	-4.579
748	-2.767			-4.64	
771		-2.332			
773	-2.661			-4.61	-4.394
813					-4.311
822		-2.312		-4.39	
873		-2.291			
Molar Fraction	0.00385	0.0045	0.00234	0.0036	0.00443

Table A - 11: Diffusion coefficient of La^{3+}, Pr^{3+} in LiCl-KCl salt.

T (K)	Diffusion coefficient (10^{-5} cm^2s^{-1})				
	La^{3+} [20]	La^{3+} [22]	La^{3+} [24]	Pr^{3+} [19]	Pr^{3+} [21]
653				0.68	0.6
673				0.8	0.72
693			1.22		
698				0.97	0.89
723	1.47	0.8			
724				1.17	1.1
733			1.7		
763			2.1		
773				1.61	1.57
813			2.88		
Method	CV	CV	CV	CP	Convolution
Molar Fraction	0.00763	0.00293	0.00201	0.00284	0.00284

Table A - 12: Diffusion coefficient of Ce^{3+}, Nd^{3+}, Nd^{2+} in LiCl-KCl salt.

T(K)	Diffusion coefficient (10^{-5} cm^2s^{-1})						
	Ce^{3+} [26]	Ce^{3+} [26]	Ce^{3+} [29]	Ce^{3+} [28]	Nd^{3+} [20]	Nd^{3+} [30]	Nd^{2+} [30]
653	0.47	0.53					
673				0.694			
698				0.853			
723					1.1	0.28	0.98
724				1.04			
748						0.45	1.38
773	0.99	1.96	1.71	1.53		0.54	1.69
798						0.76	2.03
973	2.76						
Method	CV	CP	CP	CP	CV	CV	CV
Molar Fraction	0.0111	0.0111	0.00377	0.00189	0.0254	0.0025	0.0025

Table A - 13: Diffusion coefficient of Sm^{3+} in LiCl-KCl salt.

T(K)	Diffusion coefficient (10^{-5} cm^2s^{-1})					
	Sm^{3+} [34]	Sm^{3+} [34]	Sm^{3+} [34]	Sm^{3+} [35]	Sm^{3+} [35]	Sm^{3+} [35]
673	0.41	0.63	0.36	0.41	0.45	0.48
698					0.54	
723	0.76	0.95	0.51	0.7	0.75	0.75
773	1.3	1.41	0.98	1.04	1.01	1.18
823	1.6	1.83	1.7	1.13	1.19	1.15
873	2.7	2.14	2.05			
Method	CV	Semi-integral	CP	CV	CP	Convolution
Molar Fraction	0.00225	0.00225	0.00225	0.00372	0.00372	0.00372

Table A - 14: Diffusion coefficient of Eu^{3+}, Eu^{2+} in LiCl-KCl salt.

T(K)	Diffusion coefficient (10^{-5} cm^2s^{-1})						
	Eu^{3+} [31]	Eu^{3+} [31]	Eu^{3+} [36]	Eu^{3+} [37]	Eu^{3+} [37]	Eu^{3+} [37]	Eu^{2+} [37]
673				0.425	0.457	0.421	0.432
698	0.1	0.2					
723	0.12	0.29		0.583	0.578	0.592	0.565
748	0.15	0.49		0.75	0.751		0.773
773	0.2	0.59	0.92	0.93	0.889	0.897	0.951
823				1.16	1.122	1.19	1.13
Method	Convolution	CP	CV	CV	CP	CA	CV
Molar Fraction	0.00385	0.00385	0.00037	0.00377	0.00377	0.00377	0.00377

Table A - 15: Diffusion coefficient of Gd^{3+} in LiCl-KCl salt.

T (K)	Diffusion coefficient (10^{-5} cm^2s^{-1})					
	Gd^{3+} [28]	Gd^{3+} [28]	Gd^{3+} [28]	Gd^{3+}[31]	Gd^{3+}[31]	Gd^{3+}[31]
675	0.526	0.59	0.558			
723				0.31	0.88	0.64
725	0.815	0.873				
770	1.14	1.08	1.02			
773				0.53	1.15	1.18
822				1.09	1.65	1.83
824		1.59	1.17			
873				1.28	2.22	
Method	CP	CP	CP	CV	Convolution	CP
Molar Fraction	0.001	0.002	0.0004	0.0045	0.0045	0.0045

Table A - 16: Diffusion coefficient of Tb^{3+}, Dy^{3+}, Er^{3+} in LiCl-KCl salt.

T(K)	**Diffusion coefficient (10^{-5} cm^2s^{-1})**						
	Tb^{3+} [39]	Tb^{3+} [40]	Dy^{3+} [41]	Er^{3+} [42]	Er^{3+} [43]	Er^{3+} [44]	Er^{3+} [44]
673	0.414		0.69				
683				0.59	0.559		
693	0.492		0.81				
698				0.68	0.632		
723	0.626		1.03				
733				0.95	0.825		
748	0.754		1.24				
773	0.89		1.47	1.29	1.087		
813				1.9	1.394		
823	1.23		2				
873						2.01	2.75
887		2.06					
Method	CP	CV	CP	CP	CP	CV	CP
Molar Fraction	0.0036	0.003	0.00466	0.0044	0.0037	0.0084	0.0084

Appendix B. Publication list

- Peer-reviewed journal papers
    1. S. Guo, E. Wu, J. Zhang, Exchange current density of Gd(III)/Gd reaction in LiCl-KCl eutectic and analysis of errors caused by various method, Electrochimica Acta, 259 (2018) 253-261.
    2. P. Bagri, M.F. Simpson, Activity Coefficient of Gadolinium(III) Chloride in Molten LiCl-KCl Eutectic Salt and its Dependence on Cesium Chloride Concentration using EMF Measurements, Journal of the Electrochemical Society, 164 (2017) H5299-H5307.
    3. P. Bagri, M.F. Simpson, Determination of Activity Coefficient of Lanthanum Chloride in Molten LiCl-KCl Eutectic Salt as a Function of Cesium Chloride and Lanthanum Chloride Concentrations Using Electromotive Force Measurements, Journal of Nuclear Materials, 482 (2016) 248-256.
    4. P. Bagri, C. Zhang, M.F. Simpson, Galvanic reduction of uranium(III) chloride from LiCl-KCl eutectic salt using gadolinium metal, Journal of Nuclear Materials, 493 (2017) 120-123.
    5. A. Samin, E.Wu, J. Zhang, The role of correlations in the determination of thetransport properties of LaCl3 in high temperature molten eutectic LiCl–KCl, Radiochimica Acta, 105 (2017) 649-656.
    6. A. Samin, E. Wu, J. Zhang, The thermodynamic and transport properties of GdCl3 in molten eutectic LiCl-KCl derived from the analysis of cyclic voltammetry signals, Journal of Applied Physics 121 (2017): 074904.
    7. Yixing (Kevin) Shen, Jinsuo Zhang, E-pO2– diagram for rare earth elements in molten salt, Journal of Rare Earths, 35 (2017) 187-192.
    8. Yafei Wang, Wentao Zhou, Jinsuo Zhang, Investigation of concentration-dependence of thermodynamic properties of lanthanum, ytttium, Scandium and terbium in eutectic LiCl-KCl molten salt, Journal of Nuclear Materials, 478 (2016) 61-73.
    9. Adib Samin, Zhonghang Wang , Erik Lahti, Michael Simpson, Jinsuo Zhang, Estimation of key physical properties for LaCl3 in molten eutectic LiCleKCl by fitting cyclic voltammetry data to a BET-based electrode reaction kinetics model, Journal of Nuclear Materials, 475 (2016) 149-155.
    10. Adib Samin, J. Zhang, A multi-scale study of the adsorption of lanthanum on the (110) surface of tungsten, Journal of Applied Physics, 120 (2016) 045305.

- Conference papers
    1. P. Bagri, T. Bastos, M. Simpson, Electrochemical Methods for Determination of Activity Coefficients of Lanthanides in Molten Salts, ECS Transactions, October 3-7, 2016, 75(15), 603-608.
    2. P. Bagri, M.F. Simpson, Determination of the Activity of Neodymium(III) in molten eutectic LiCl-KCl using Electrochemical Methods, Proceedings of the Annual Meeting of the American Nuclear Society, June, 2016.
    3. Y. Wang, W. Zhou, J. Zhang, Activity coefficient of rare earth elements in eutectic LiCl-KCl, ANS summer Conference, June, 2016.

4. E. Wu, J. Zhang, Multi-Component Model for Actinides and Rare Earths Drawdown for Molten Salt Clean Up using Liquid Bismuth, ICAPP-2016, April 18-21, 2016.

- Presentations
    1. P. Bagri, T. Bastos, and M. Simpson, Electrochemical Methods for Determination of Activity Coefficients of Lanthanides in Molten Salts
    2. P. Bagri, M.F. Simpson, Determination of the Activity of Neodymium(III) in molten eutectic LiCl-KCl using Electrochemical Methods, Proceedings of the Annual Meeting of the American Nuclear Society, New Orleans, LA, June 11-16, 2016.
    3. Y. Wang, W. Zhou, J. Zhang, Activity coefficient of rare earth elements in eutectic LiCl-KCl, ANS summer Conference, New Orleans, LA, June 11-16, 2016.
    4. E. Wu, J. Zhang, Multi-Component Model for Actinides and Rare Earths Drawdown for Molten Salt Clean Up using Liquid Bismuth, ICAPP-2016, San Francisco, CA, April 18-21, 2016.

- Thesis
    1. Evan Wu (Ph.D), Integrated Study of Rare Earth Drawdown by Electrolysis for Molten Salt Recycle, The Ohio State University, 2017
    2. Yafei Wang (M.S.), Prediction of Fundamental Data of Fission Products in Molten Salt and Liquid Electrode for Electrochemical Separation, The Ohio State University, 2017
    3. Prashant Bagri (Ph.D), Measurement of Thermodynamic Properties of Rare Earth Chlorides in Molten LiCl-KCl Eutectic Salt for Waste Minimization from Pyrochemical Processing of Spent Nuclear Fuel, University of Utah, 2017.